Re-establishing the beast: An investigation into the spatiotemporal evolution of the Y5 phase of the Taupō 232 ± 10 CE eruption, New Zealand

Sarah Joanne Tapscott

A thesis submitted in partial fulfilment of a
Philosophiae Doctor degree in Earth Science

Supervisors:

Prof. Gert Lube
Prof. Colin J.N. Wilson

Volcanic Risk Solutions
School of Agriculture and Environment
Massey University, New Zealand

August 2023

Abstract

Plinian eruptions are sustained, high-energy explosive eruptions that generate buoyant plumes that reach >20 km into the atmosphere. They often produce devastating pyroclastic density currents (PDC) along with widespread tephra fall out, with significant hazards to communities around the volcanoes. Current computational modelling of Plinian eruptions considers generalized steady versus unsteady column regimes as the explanation for the formation of coeval buoyant Plinian plumes and intraplinian PDCs; however, natural eruption scenarios indicate that these regimes can oversimplify the interpretation of both PDC and plinian fall deposits.

The large-Plinian Y5 phase of the Taupō 232 ± 10 CE eruption has an exceptionally widespread and well-preserved deposit that incorporates fall and coeval PDCs. Despite an extensive dataset in place for the Y5, there remain conflicting views on the interpretation of its deposit regarding eruption and sedimentation dynamics. Original studies by Walker (1980) considered the Y5 as a single eruptive unit from the perspective of the widespread fall deposit, without consideration of the intraplinian, coeval Early Flow Units (EFU) identified by Wilson & Walker (1985). Walker's study determined that the Y5 phase involved a Plinian plume ~50 km high. Bedding characteristics in the fall deposit were considered in detail by Houghton et al (2014), who used their qualitative observations to propose the presence of 26 subunits within the Y5 fall deposited by a fluctuating plume influenced by strong changes in wind direction. Houghton et al.'s study brought the plume height down to (35 – 40 km) and denoted a vent location ~6 km SW of that proposed by Walker (1980). This Ph.D. research presents a comprehensive quantitative dataset of the deposit characteristics in the vertical stratigraphy of the upper phreatoplinian Y4 deposit, and the coeval fall and PDC deposits of the Plinian Y5 phase of the Taupō eruption. The dataset is used to reconstruct the spatiotemporal evolution of the Y5 phase and improve our understanding of Plinian eruption dynamics and sedimentation.

Detailed sample collection and analysis was conducted on proximal to medial deposit exposures, whose vertical stratigraphy encompass the final stage of the Y4 (Y4-G), the Y5 fall deposit and its coeval Early Flow Units (EFU). Samples were analysed for grain size distributions, componentry, and juvenile textural characteristics. It is demonstrated that foreign lithic lithologies and their time-relative abundance in relation to other deposit characteristics play an important role in informing vent location, the evolution of the conduit and the nature of generation of erupted facies (i.e., PDC and fall). In this study, foreign lithics were subdivided by their inferred stratigraphic depth of origin below the lake floor into: F1) pre-232 ± 10 CE volcanic material (~0 – 400 m), F2) predominantly Huka Group sediments, minor Whakamaru ignimbrite and hydrothermally altered material (~400 – 3000 m), and F3) plutonic microdiorites and granitoids (>4000 m) At the boundary between the Y4-G and Y5 deposits, a decrease in obsidian abundance of c. 30 wt.%, along with an increase in F2 lithics of c. 20 wt.%, and a drop in pumice vesicularity by c. 30 % indicate a distinct change in vent location between the Y4 and Y5 phases. F2 lithologies in the Y4 differ significantly from those in the Y5, but coincide with those of the plinian Y2 deposit, suggesting similar regions of crustal excavation for Y5 and Y2 and imply a vent location comparable to that of the Y2 phase.

Vertical variations in the abundance and relative proportions of different juvenile and lithic pyroclasts, in pyroclast textures and pumice densities identified in the Y5 fall deposit,

following the initial clearing of the vent, define three successive stages within a relatively steady, continuous eruption. These stages are: 1) the continuous excavation of the conduit at relatively low mass eruption rate shown through higher lithic:pumice ratios, finer overall grain size and higher pumice densities compared to later stages of the Y5; 2) increasing mass eruption rate towards a climax with relatively steady conduit erosion coinciding with deepening fragmentation, exhibited in increasingly larger grain sizes and relatively lower total lithic abundances, yet higher relative proportions of F2 and F3 lithics; and 3) a moderate decrease in mass eruption rate and the acceleration of conduit erosion (shown through a rapid increase in F1 abundance and decreasing grain size), promoting the potential early onset of caldera collapse that led to the Y6 ignimbrite producing blast event. Vertical bedding features in the Y5 fall deposit are shown to be laterally discontinuous and pinch out over length scales of 10^1-10^3 m. This precludes the possibility that coarse-fine fluctuations were caused by mass partitioning of material during partial column collapse, or by variations in wind direction. Instead, I suggest that the bedform features identified in the Y5 deposit result from gravitational instabilities in the umbrella cloud, sedimenting as tephra swathes.

Additionally, the intraplinian EFUs were differentiated by their characteristics into two main types: Type 1 centimetre to metre thick, massive, pink-orange to cream coloured, coarser grained deposits that are topographically confined; and Type 2 decimetre to centimetre thick, massive to moderately stratified, white-grey, finer grained deposits that have mounted topography. The anomalously high proportion of ash (<10 μm at 4 – 27 wt.%) in the EFU deposits, in conjunction with a lack of evidence for enrichment of dense clasts (i.e., lithics and crystals), indicates that there was minimal to no mass partitioning that would be expected in the case of partial column collapse. In addition, the inferred high particle concentration of the Type 1 flows and their high temperature emplacement indicates that the materials that propagated to form the EFU PDCs is likely to have originated from lower heights around the jet where entrained air had limited effect to cool the mixture. A lack of variation in the proportion of lithic types and juveniles between Type 1 and Type 2 with relative height compared to the Y5 fall suggests that the EFU are a product of one generation mechanism and that the deposit types 1 and 2 represent contrasts in relative volume, runout distance, and/or topographical constraints on runout of individual flows. The EFU are entirely contained within fall activity and become more abundant, voluminous and/or increase in flow mobility with increasing mass eruption rate during the Y5 phase. The generation mechanism for the EFU PDCs strongly aligns with the modelling and field observations for gargle dynamics, where a dense sheath formed by recycled pre-existing material in a basin-like vent structure develops on an eruptive jet. This dense sheath produces PDCs simultaneous with a sustained plinian column that occurs seemingly without interruption. Similarities can be drawn with deposits from other, historical large-Plinian eruptions such as the Bishop Tuff, 0.76 Ma and Novarupta, 1912, which also involved phases of coeval fall and PDC deposition analogous to the Y5 and EFUs, and were likely produced through gargle dynamics.

This study has shown that through the detailed, quantitative characterisation of deposit features in plinian eruption deposits involving coeval fall and PDCs, the temporal changes in eruptive behaviour, conditions at source and the nature of sedimentation can be identified. Interpretations indicate that the Y5 phase of the Taupō 232 ± 10 CE eruption was a large, steady, and extremely powerful eruption beyond the general depiction of a ‘standard’ Plinian event. Using quantitative analysis such as this may help build upon our knowledge base of the eruption and sedimentation dynamics of large Plinian eruptions by providing a field-

based foundation for the reconstruction of the spatiotemporal evolution of such events. This is intended to provide a pathway for the amalgamation of field data and computational eruption models, ultimately improving our ability to forecast and mitigate explosive eruption hazards at similar volcanoes globally.

To my family, for their never-ending support.

Film photograph of my primary location, LARRY (a.k.a. Exposure D; Figure 4.2), taken with my late Grandad's camera.

Explanation of COVID-19 Impacts

MASSEY UNIVERSITY
TE KUNENGA KI PŪREHUROA
UNIVERSITY OF NEW ZEALAND

GRADUATE RESEARCH SCHOOL

Note for Examiners
Explanation of COVID-19 Impacts

Thank you for taking the time to examine this thesis, which has been undertaken during the Covid- 19 pandemic. The New Zealand Government's response to Covid-19 includes a system of Alert Levels which have impacted upon researchers. Our University's pandemic plan applied the Government's expectations to our research environment to ensure the health and safety of our researchers, however, research was impacted by restrictions and disruptions, as outlined below.

For a six-week period from March 26 to April 27 2020, New Zealand was placed under very strict lockdown conditions (Level 4 – Lockdown), with students and staff unable to physically access University facilities, unless they were involved in essential research related to Covid-19. All field work ceased and data collection with humans was restricted to online methods, if appropriate. The restrictions were partially lifted on April 27, but students and staff were not generally allowed back into University facilities until May 13.

Ongoing disruptions have also been encountered for some students due to uncertainties over the potential for future Covid-19-related restrictions on activities, and a Covid-19 cluster outbreak based in Auckland in New Zealand on 12 August 2020 led to the imposition of rolling Level 2 (Reduce) and Level 3 (Restrict) conditions until 23 September 2020. Auckland campus based students remained on Level 2 until 7 October 2020. This Alert Level system continues to be utilised throughout 2021.

These changing Alert Levels have meant that some research students had experimental, clinical, laboratory, field work, and/or data collection or analysis interrupted, and consequently may have had to adjust their research plans. For some students, the impacts of Covid-19 stretched far beyond the lockdown period in April/May 2020, as they may have had to significantly revise their research plans.

Overseas travel is not permitted by the University and restrictions have been placed on the New Zealand borders which are closed to non-New Zealand citizens and permanent residents. This meant that international students who were based offshore at the time of lockdown, were unable to return to New Zealand. A small number of offshore students were provided permission to return to New Zealand in early 2021. Many students have also suffered from anxiety and stress-related issues, and have had financial impacts, meaning their research progress has been significantly delayed.

This form, as completed by the supervisor and student, outlines the extent that the research has been affected by Covid-19 conditions.

Approved by DRC 10/Feb/2021
DRC 21/02/03

Please consider the factors listed below in your assessment of the work.

This statement has been prepared by the candidate's supervisor in consultation with the student and has been endorsed by the relevant Head of Academic Unit.

Student Name: Sarah Tapscott ID Number: [redacted]

Supervisor Name: Gert Lube Date: 11-Apr-23

Thesis title: Re-establishing the beast: An investigation into the spatiotemporal evolution of the Y5 phase of the Taupō 232 ± 10 CE eruption, New Zealand

Considerations to be taken into account. Note: This statement will remain in the final copy of the thesis which will be available from the Massey University Library following the examination process.

During 2020, 2021 and 2022, national lock downs and Covid-19 restrictions had an impact predominantly on the field and laboratory aspects of this research. Access to facilities on campus at Massey University was denied during level 4 and level 3 lock downs. Level 2 allowed restricted access to laboratories and offices, when needed, however field work was denied. The following outlines the dates during which Massey University (Manawatu) was under specific lock down levels:

LEVEL 4:
26 Mar 2020 - 27 Apr 2020;
18 Aug 2021 - 31 Aug 2021

LEVEL 3:
28 Apr 2020 - 13 May 2020;
01 Sept 2021 - 07 Sept 2021

LEVEL 2:
14 May 2020 - 08 Jun 2020;
12 Aug 2020 - 21 Sept 2020;
15 Feb 2021 - 17 Feb 2021;
28 Feb 2021 - 06 Mar 2021;
08 Sept 2021 - 02 Dec 2021

Level 1 occurred at all other times.

Typical field season in New Zealand is between October to May so much of the restrictions effected the ability to access the field. The confirmation examination for the author was completed on 20 Feb 2020, field and laboratory work expected to be undertaken to move forward with the research following this was therefore significantly delayed.

Author contracted Covid-19 on the 30 Mar 2022 and was required to isolate for 7 days in addition to isolation of housemates (3 days prior), totalling 10 days.

Signed, confirming this is a fair reflection of the impact of Covid-19 on this research.

Student Sarah Tapscott Digitally signed by Sarah Tapscott Date: 2023.04.11 16:50:42 +12'00'

Supervisor Gert Lube Digitally signed by Gert Lube Date: 2023.04.12 09:37:05 +12'00'

Head of Academic Unit (or nominee) Diane Pearson Digitally signed by Diane Pearson Date: 2023.04.12 08:00:03 +12'00'

Table of Contents

List of Figures ..... **xii**

List of Tables ..... **xv**

Abbreviations ..... **xvi**

Terminology ..... **xvii**

Acknowledgements ..... **xx**

1 Introduction **1**
1.1 Introduction 1
1.1.1 Research objectives and approach 2
1.1.2 Thesis outline 4
1.2 Background Information 5
1.2.1 Plinian eruptions and their products 5
1.2.2 The Taupō Volcanic Zone 20
1.2.3 The Taupō 232 ± 10 CE eruption 24

2 Methodology **34**
2.1 Field work 34
2.1.1 Sample collection 34
2.2 Analytical methods 36
2.2.1 Grain size analysis 36
2.2.2 Componentry analysis 38
2.2.3 Density analysis 39
2.2.4 Thin sections and textural characterisation 43

3 The transition between the phreatoplinian Y4 and Plinian Y5 phases of the Taupō 232 CE eruption **44**
3.1 Introduction 44
3.1.1 The Taupō 232 CE eruption: Y4 and Y5 phases 45
3.2 Data 46
3.2.1 Stratigraphy of the Y4-Y5 transition zone 46
3.2.2 Isopach maps 50
3.2.3 Grain size characteristics 51
3.2.4 Componentry 53
3.2.5 Pumice density 59
3.3 Discussion 60
3.3.1 The nature of the Y4-G and the onset of Y5 60
3.3.2 Vent transitioning between the Y4 and Y5 eruption phases 62
3.3.3 Implications for the vent location of the Y5 phase 63
3.4 Conclusions 65

4 Reconstructing the temporal evolution of the large Plinian Y5 phase of the Taupō 232 CE eruption 66
4.1 Introduction 66
4.1.1 The Y5 phase of the 232 CE eruption 67
4.2 Data 69
4.2.1 Deposit characteristics 69
4.2.2 Maximum clast size 71
4.2.3 Grain size 71
4.2.4 Componentry 74
4.2.5 Pumice types 77
4.2.6 Pumice density and porosity 79
4.2.7 Lithic types 82
4.2.8 Additional field observations and bedform correlations 85
4.3 Discussion 86
4.3.1 Onset of the Y5 eruption 86
4.3.2 Temporal evolution of the Y5 eruption 87
4.3.3 Temporal evolution of conduit stability 88
4.3.4 Temporal evolution of fragmentation and conduit flow conditions 91
4.3.5 Implications for the interpretation of plinian deposits 94
4.4 Conclusions 99

5 Co-plinian pyroclastic density currents: The relationship of the Early Flow Units to the Taupō Y5 plinian fall deposit 101
5.1 Introduction 101
5.1.1 The Early Flow Units 104
5.2 Data 106
5.2.1 Stratigraphy and general distribution of the Early Flow Units 106
5.2.2 Granulometry 112
5.2.3 Pumice density 115
5.2.4 Componentry 116
5.3 Discussion 120
5.3.1 The relative timing of the Early Flow Units 120
5.3.2 Transport regime of the Early Flow Units 127
5.3.3 The nature and generation of the Early Flow Units 130
5.4 Conclusions 134

6 Discussion 136
6.1 A review of the vent location for the Y5 phase: Implications for the vent configuration of the Taupō 232 CE eruption 137
6.2 The interpretation of plinian deposits 143
6.2.1 Introduction 143
6.2.2 The use of lithic lithologies in understanding time-variant progressions during an eruption 145
6.2.3 Complexities in the vertical stratigraphy of plinian deposits 149
6.3 Generation and dynamical controls of intraplinian PDCs 151
6.3.1 Introduction 151
6.3.2 Intraplinian PDC case studies and implications for interpretations of eruption dynamics 156
6.4 Reestablishing the beast: A spatiotemporal model of the Y5 eruption 160

6.5 Modelling of Plinian eruptions: Uses and limitations 163
6.6 Implications for hazard management and mitigation 165

7 Conclusions 167
7.1 Specific findings of this study 167
7.2 Opportunities for future research 169
7.2.1 Further investigation into transitional vent dynamics 169
7.2.2 Further investigation into the Y5 fall, EFU and other intraplinian PDC deposits 169
7.2.3 Are the features of the Y5 phase seen in other Plinian eruptions globally? 170
7.2.4 Implications for modelling of Plinian eruptions 170

References 172

Appendix A: Exposure Locations 193

Appendix B: Samples 194

Appendix C: Grain Size Distributions 197

Appendix D: Exposure D Full Componentry 208

Appendix E: 1 phi Componentry 214

Appendix F: Pycnometry 217

Appendix G: Porosity 221

Appendix H: Pumice Type Density 223

Appendix I: Density Suites 226

Appendix J: Isopachs 252

Appendix K: MP ML 254

Supplementary Material: Figure 4.13 repeated 257

List of Figures

Figure 1.1 Schematic of the eruptive processes during a Plinian eruption 8

Figure 1.2 Example of sedimentation by gravitational instabilities during the 2010 eruption of Eyjafjallajökull 12

Figure 1.3 Example of a portion of a plinian fall deposit from the Y5 phase of the Taupō 232 ± 10 CE eruption 15

Figure 1.4 Example of interbedded plinian fall and ignimbrite from the Y5 phase of the Taupō 232 ± 10 CE eruption 18

Figure 1.5 The Taupō Volcanic Zone (TVZ) 22

Figure 1.6. Exposure of the Taupō eruption deposits, showing layers Y2 through to Y6 25

Figure 1.7 The location of the three vents described for the various eruptive phases of the Taupō 232 ± 10 CE eruption 28

Figure 2.1 Map showing locations of exposures A – H investigated in this study 35

Figure 3.1 Map and field photos of locations A – E investigated in this study 47

Figure 3.2 Isopachs defined for the Y4-G Lower, Middle and Upper, and Y5-Base units 51

Figure 3.3 Grain size distributions at Exposure D 53

Figure 3.4 Ash content, median grain size and sorting of the box samples taken 54

Figure 3.5 Examples of lithic components F1, F2 and F3 55

Figure 3.6 The ratios of, a) obsidian to pumice (O:P), b) F2 to pumice (F2:P) and c) F2:F1 with stratigraphic height in exposure D 57

Figure 3.7 The relative abundance of components in wt.% from grain sizes 2 to -4ϕ in exposure D 58

Figure 3.8 The abundance of 1 phi components (num%) with stratigraphic height for exposures A to E 59

Figure 3.9 Examples of lithic clasts from the Y2, Y4-G and Y5 fall deposits 61

Figure 4.1 Map of the studied field area with the location of exposure D noted 70

Figure 4.2 Photograph and stratigraphic column of exposure D 72

Figure 4.3 Distribution of the maximum lithic (ML) and maximum pumice (MP) sizes with stratigraphic height 73

Figure 4.4 Ash content, median grain size and sorting of exposure D 74

Figure 4.5 The total abundance of pumice, lithic, crystal and composite pumice components with stratigraphic height at exposure D 76

Figure 4.6 Photograph and SEM backscatter images of a CP clast 77

Figure 4.7 Photograph and SEM backscatter images of microvesicular (J1), macrovesicular (J2) and sheared (J3) pumices 78

Figure 4.8 Total abundance of pumice components (J1, J2, J3) with stratigraphic height in exposure D 79

Figure 4.9 The distribution of bulk pumice density and bulk vesicularity of pumices with stratigraphic height in exposure D 80

Figure 4.10 Density and porosity distributions of pumice components. 81

Figure 4.11 Examples of the lithic components from the Y5 deposit 83

Figure 4.12 The total abundance of lithic components with stratigraphic height in exposure D 84

Figure 4.13 Photographs and associated stratigraphic columns of exposures taken at logarithmic distances. Examples of bedform correlations shown 90

Figure 4.14 The total abundance of components in each grain size fraction from -4 to 2 ϕ for all sampled intervals at exposure D 93

Figure 4.15 Distal exposure (UTM 60S 509825 5711483) of the Y5 deposit, courtesy of C. J. N. Wilson 95

Figure 4.16 Examples of sedimentation by gravitational instabilities, storms showing precipitation streaks, and hail swathes 98

Figure 5.1 Map of the Early Flow Units (EFU) extentand locations of exposures A - H 107

Figure 5.2 Slide photograph provided by C. J. N. Wilson of the exposure created by the clearing of State Highway 1 108

Figure 5.3 Exposures A, B, D, G and F investigated in this study 111

Figure 5.4 The interbedded plinian fall and ignimbrite at Exposure H 113

Figure 5.5 Grain size distribution examples of Type 1 and Type 2 EFU deposits 114

Figure 5.6 Abundance of ash for the Type 1 and 2 EFU deposits from all exposures and distal ash beds of Exposure G 115

Figure 5.7 Density distributions of pumices from exposures D, G, and H with stratigraphic height 117

Figure 5.8 Example of a composite pumice (CP) fragment 118

Figure 5.9 The total abundance of composite pumices (CP) in Unit Y5 at Exposure D with stratigraphic height 119

Figure 5.10 Examples of deposit characteristics, in this case the ratio of F:J clasts with height, used to define the three eruptive stages of phase Y5 124

Figure 5.11 Stratigraphic columns showing the ratio of F2:F1 with height in the three eruptive stages of phase Y5 125

Figure 5.12 The three stages of phase Y5, correlated between the stratigraphic columns of each of the exposure locations in relation to the reference Exposure D 126

Figure 5.13 The F2:J ratio of EFU ignimbrite and Y5 fall material with relative height 128

Figure 5.14 The F1:J ratio and F2:F1 ratio of EFU and Y5 fall with relative height 129

Figure 5.15 Classification of PDC deposits with the transport factor '$T_{de\text{-}di}$" in relation to their volume, from Breard et al. (2018) 131

Figure 6.1 The location of the three vents proposed for the various eruptive phases of the Taupō 232 ± 10 CE eruption as revised in this study..... 138

Figure 6.2 Map showing the locations of the original Y5 vent location determined by Walker (1980) and the location revised by Houghton et al. (2014)..... 139

Figure 6.3 Isopachs defined for the Y4-G Lower, Middle and Upper, and Y5-Base units 142

Figure 6.4 The F2:J ratio of EFU ignimbrite and Y5 fall material with relative height 148

Figure 6.5 Photographs and associated stratigraphic columns of exposures taken at logarithmic distances. Examples of bedform correlations shown..... 150

Figure 6.6 Schematic of the EFU generation by gargle dynamics in early and late stages of the eruption. 154

Figure 6.7 Schematic of the partial column collapse model modified from Gilchrist & Jellinek (2021) 155

Figure 6.8 The three stages of phase Y5, correlated between the stratigraphic columns of each of the exposure locations in relation to the reference Exposure D. .. 157

Figure 6.9 Schematic diagram of the three transient stages of phase Y5 162

List of Tables

Table 1.1 Phases of the Taupō 232 ± 10 CE with their deposit types, summary of details regarding main eruption conditions and deposit features, and the relevant literature. 29

Table 2.1 Classification of tephra size classes 36

Abbreviations

Locations and Stratigraphic Units

TVZ Taupō Volcanic Zone
VTTS Valley of Ten Thousand Smokes

Taupō 232 ± 10 CE Eruption
Y1 Initial Ash
Y2 Hatepe Plinian
Y3 Hatepe Ash
Y4 Rotongaio Ash
Y5 Taupō Plinian
Y6 Taupō Ignimbrite
EFU Early Flow Units

Eruption Dynamics & Parameters

MDR Mass Discharge Rate
NBL Level of Neutral Buoyancy
DRE Dense Rock Equivalent
SW Sediment Wave
ESA Enhanced Settling Annulus

Grain Size Parameters

GSD Grain Size Distribution
wt.% Weighted Percent
ϕ Phi (logarithmic scale)
μ Mean
Md_{ϕ} Median
σ_I Sorting
MP Maximum Pumice
ML Maximum Lithic

Componentry Parameters

wt.% Weighted Percent
num% Number Percent (point count)
J1 Microvesicular Pumice
J2 Macrovesicular Pumice
J3 Sheared Pumice
O Obsidian
F1 Shallow Foreign Lithics
F2 Intermediate Foreign Lithics
F3 Deep Foreign Lithics
C Crystal
CP Composite Pumice

Density & Porosity Parameters

Pycnometry
vol% Volume Percent
V Volume of a Cylinder
h Height of a Cylinder
r Cylinder Radius
h_0 Distance penetrated during zero-volume baseline
h_t Distance penetrated with the sample
φ_{bulk} Total/Bulk Porosity (vol%)
φ_{conn} Connected Porosity (vol%)
φ_{iso} Isolated Porosity (vol%)
V_{bulk} Bulk Volume (g cm^{-3})
V_{skel} Skeletal Volume (g cm^{-3})
δ_{sol} Solid Density (g cm^{-3})

Archimedes' Principle
ρ Density (g cm^{-3})
m Mass (g)
v Volume (ml)
SG_c Specific Gravity of the Clast
w_a Weight of the clast in air (g)
w_w Weight of the clast in water (g)
w_b Weight of the ballast (g)
ρ_c Density of the clast (g cm^{-3})
ρ_w Density of water (g cm^{-3})
V Vesicularity (%)
ρDRE Dense Rock Equivalent value (g cm^{-3})

Textural Parameters

Ca Capillary Number
ϵ Strain Rate
R Bubble Radius
μ Melt Viscosity
σ Surface Tension

Pyroclastic Density Current Parameters

PDC Pyroclastic Density Current
$T_{av/ma}$ Non-dimensional ratio of timescales
V_g Vertical upward gas velocity (aggrading dense flow region)
C_{bed} Particle volumetric concentration (aggrading dense flow region)
C_{ac} Particle volumetric concentration (basal portion of ash-cloud surge)
V_s Settling velocity of particles (above dense flow region)
$T_{de\text{-}di}$ Empirical PDC transport parameter
$d_{s,1/2}$ Sauter Mean Diameter (half runout distance)
A Inundation Area
V Deposit Volume
L Runout Distance
D32 Sauter Mean
μ_{ϕ} Geometric Mean (ϕ)
σ_{ϕ} Standard Deviation (ϕ)

Other

SiO_2 Silica
^oC Degrees Celsius
NZFM New Zealand Forest Managers Ltd.
LPA Laser Particle Analyser
SEM Scanning Electron Microscope
BCE Before Current Era
CE Current Era
Ma Mega Annum (million years)
Ka Kilo Annum (thousand years)
UTM Universal Transverse Mercator
Cal Calibrated

Terminology

Aeolian “Produced or carried by the wind” (Cambridge Advanced Learner’s Dictionary & Thesaurus)

Buoyancy “The ability that something has to float on a liquid or in the air” (Collins Dictionary)

Caldera “A large basin-shaped volcanic depression with a diameter many times larger than included volcanic vents; may range from 2 to 50 km across. Commonly formed when magma is withdrawn or erupted from a shallow underground magma reservoir. The removal of large volumes of magma may result in loss of structural support for the overlying rock, thereby leading to collapse of the ground and formation of this type of large depression. Calderas are different from craters, which are smaller, circular depressions created primarily by explosive excavation of rock during eruptions.” (USGS Volcano Hazards Program Glossary 2016)

Caldera complex Cluster of craters or surface depressions resulting from collapse of underlying magma chamber roof during withdrawal of magma within a volcanic region (Carrigan 2000)

Collapse (plume) When the initial momentum is not sufficient to carry a plume up to the point of buoyancy inversion, it cannot sustain the plume and it therefore collapses to form a pyroclastic flow (Carazzo et al. 2008)

Componentry “Study of the abundances of different individual particle types in a pyroclastic deposit” (Houghton et al. 2000a).

Computational/ numerical model A mathematical model that represents natural systems and their interactions through a system of complex equations. Numerical models are often implemented on a computer in a simulation that shows how the model behaves over time, with a resulting graphical output visualisation (Bokulich & Oreskes 2017)

*Entrainment “*The process of picking up and carrying along” (Carey & Bursik 2015)

Eruption column “The ascending, vertical part of the mass of erupting debris and volcanic gas that rises directly above a volcanic vent. Higher in the atmosphere, columns usually spread laterally into plumes or umbrella clouds.” (USGS Volcano Hazards Program Glossary 2016)

Fragmentation “The transition from a continuous melt with a dispersed gas phase to disconnected parcels of bubbly melt within a continuous gas phase” (Cashman et al. 2000)

Gravitational instability “Instability of a dynamic system in which gravity is the restoring force” (McGraw-Hill Dictionary of Scientific & Technical Terms 2003)

Hazard “Geomorphological, geological, or environmental processes, phenomena, and conditions that are potentially dangerous or pose a level of threat to human life, health, and property, or to the environment” (Komac & Zorn 2013)

Hazard model Used to quantify the scale, frequency and source of a hazard through numerical modelling: important for risk assessments and reducing impacts (Doyle et al. 2019)

Ignimbrite. “Welded or unwelded, pumiceous, ash-rich deposit of pyroclastic density currents” (Freundt et al. 2000)

Intensity “The emission rate of an eruption” (Walker 1980)

Isopach “Line joining points of equal thickness in a deposit” (Houghton et al. 2000a)

Isopleth “Line joining points where the sizes of the largest clasts are the same” (Houghton et al. 2000a)

Juvenile Pyroclast derived from fresh magma during an eruption

Lithic Dense clasts derived from either accidental or foreign (wall rock) material, or juvenile magma

Magnitude “The total volume of an eruption” (Walker 1980)

Multiphase volcanic jet Mixture of ash and pyroclasts suspended in gas ejected from, and located in the region just above, the eruptive vent (Bercovici & Michaut 2010)

Particle aggregation “Processes leading to the formation of clusters of particles during transport in an eruption plume” (Houghton et al. 2000b)

Phreatomagmatic Volcanic eruption that involves the interaction of hot magma with water at, or near, the Earth’s surface, causing explosive conversion of water to steam which then fragments magma into small pieces (Carey & Bursik 2015)

Phreatoplinian Phreatomagmatic eruption that has a deposit dispersal area and volume, and eruption column height similar to a Plinian eruption, yet a much finer and more complex grain size distribution (Self & Sparks 1978)

Plinian A typically dry, explosive eruption with a high discharge rate and powerful, convecting column reaching more than 20 km high (Walker & Croasdale 1971)

plinian The deposit resulting from a Plinian eruption with a high content of juvenile pumiceous material that is typically coarse grained, has a wide dispersal and tends to be homogeneous through its thickness (Walker 1973)

Pyroclast A particle or rock that has been produced directly by volcanism, owing size and shape to fragmentation in an explosive eruption (Fisher 1966)

Pyroclastic density current “A particulate gaseous volcanic flow moving along the ground” (Freundt et al. 2000)

Stratigraphy/stratigraphic “Concerned with all characters and attributes of rocks as sequentially timed layers and their interpretation in terms of mode of origin and geologic history. The arrangement of strata signifies chronologic order of sequence.” (USGS Volcano Hazards Program Glossary 2016)

Tephra “The collective term for those particles of varying components ejected from the vent into the atmosphere during a volcanic eruption” (Bonadonna et al. 2015a).

Turbulence “Chaotic fluid movement (normal to direction of flow), or deviation of flow from laminar. Turbulent flow characterises streamflows but not debris flows or sediment-rich hyper concentrated flows” (Vallance 2000)

Umbrella cloud A laterally spreading cloud that transports a large volume of tephra rapidly away from a volcano in all directions (Constantinescu et al. 2021)

Volcaniclastic “A body of rock that is composed of fragments of volcanically derived rocks or minerals that were then transported some distance from their place of origin.” (USGS Volcano Hazards Program Glossary 2016)

Acknowledgements

I'd like to take this opportunity to express my gratitude to the people who have been instrumental in the successful completion of this research.

Firstly, I would like to acknowledge Ngāti Tūwharetoa for the privilege of conducting my research on the lands around Lake Taupō.

Thank you to my two supervisors, Prof. Gert Lube and Prof. Colin Wilson.

Gert – thank you for your never-ending excitement and enthusiasm about my project and the data I produced. Your commitment to helping me achieve the best work I could did not go unnoticed and is so very appreciated. I will forever be grateful to you for allowing me to work on a project that encompassed so many different aspects of volcanism that I have been interested in for years.

Colin – thank you for being a voice of reason, master speed editor, and for the many entertaining one-liners. The immense amount of knowledge and wisdom you imparted over the years was instrumental to the completion of this project and continued to motivate my enthusiasm and interest for volcanology.

Thank you to my examiners Dr. Stuart Mead, Dr. Adrian Pittari and Prof. Nobuo Geshi for spending their time thoroughly reviewing my thesis and providing valuable recommendations and engaging discussion.

Thank you to NZ Forest Managers, Timberlands Ltd., and Wairakei Estates for permitting my access to areas within their forestry and farmland operations. Particular appreciation goes to Julz (NZFM), Aaron (Wairakei Estates), and Michelle and Jess (Timberlands). Special thanks also go to Toby (Timberlands), who went above and beyond, organising access to an excavator for a portion of my field work. Many thanks also to Bubs for his support of my project and the many connections he has helped me make.

Thank you to the many field and lab companions I had throughout the years – Anja, Hannah, James, Lucas, Ermanno, and Joel, your comradery and hard work helping me dig holes, collect and analyse samples is greatly appreciated. Special thanks to Anja for the countless hours of frustration spent over making thin sections of my pumices.

To my fellow comrades and colleagues from Volcanic Risk Solutions and Massey University for your support, words of wisdom and companionship. To Kate and Tara for their endless support and assistance with the administration required for this project. Dr. Mary K. Butwin, thank you for your help navigating the world of weather systems and meteorology, and the entertaining snaps throughout the years. To Jason and the Scorpion Gym crew, for providing me with a safe space to let out all the PhD frustrations and for keeping me sane, active and distracted from the many hours of work I needed to do. To Bogi, Hannah, Shannen, Sarouen, Lilly, and Ash for their friendship, support and adventures over the years, I couldn't have gotten through it all without you – especially the final few months. I am forever grateful. To the 8 Worcester Street crew over the years, I have so many fantastic memories in that house. Particular shout out goes to Nico, Paul and Marija for the discussions, kitchen dance sessions, backyard boot camps, and more that got us all through the Covid Lockdown together. To The Farmer's, for their support over the final months of my thesis writing. To

the many friends I have made in Palmerston North and New Zealand throughout this experience, thank you for your support and making Palmy feel like home. There are so many people I would like to thank that I could probably take another page to acknowledge everyone, so for those people who have been a positive source of encouragement and support through stories, adventures, smiles, food, music, camping, diving, and more, I thank you. I would, however, like to give a particular shout out to Lucas, Daniel, Danny, Carmen, Kate, Andrea, Stephen, and Jerry.

To my friends around the globe.

Thank you to Laura Pioli, Greg Valentine, Josef Dufek, Erik Breard, Roberto Sulpizio, and Mark Jellinek for their helpful and interesting discussions.

And lastly, but certainly not least – to my family. Thank you for your unconditional support. I could not have done this without your love and encouragement. Thank you for helping me spread my wings and chase my dreams.

This research was funded through the Eruption or Catastrophe: Learning to Implement Preparedness for future Supervolcano Eruptions (ECLIPSE) program, Volcanic Risk Solutions at Massey University, and by a Massey University Doctoral Research Scholarship.

1 Introduction

1.1 Introduction

The eruption dynamics and sedimentation behaviour of large-scale Plinian eruptions, and the destructive hazards they present to communities and the environment, are an important aspect of current research in volcanology (e.g., Walker 1980, 1981a; Carey & Sigurdsson 1989; Spence et al. 2004; Rose & Durant 2009; Wilson et al. 2011, 2014; Biass et al. 2017; Geshi 2020; Constantinescu et al. 2021). Plinian eruptions are sustained, high-energy explosive eruptions that generate bouyant plumes that reach >20 km into the atmosphere and often produce devastating pyroclastic density currents along with widespread tephra fall out (Walker & Croasdale 1971; Sparks 1976; Wilson 1976; Walker 1980, 1981; Walker et al. 1980a; Self & Rampino 1981; Carey & Sigurdsson 1989; Sparks et al. 1997; Branney et al. 2002; Komorowski et al 2013; Cioni et al. 2015; Dufek 2016; Trolese et al. 2019; Lube et al. 2020; Constantinescu et al. 2021). Current computational modelling of Plinian eruptions considers generalized steady versus unsteady column regimes as the explanation for the formation of plumes that occur with coeval, intraplinian pyroclastic density currents (e.g., Branney & Kokelaar 2002; Di Muro et al. 2004; Burgisser et al. 2005; Kaminski et al. 2005; Carazzo et al. 2014, 2015, 2020; Dufek 2016; Gilchrist & Jellinek 2021). Natural eruption scenarios, such as those developed from detailed field studies for the eruptions of Bishop Tuff, 0.76 Ma and Novarupta, 1912 (Wilson & Walker 1985; Fierstein & Hildreth 1992; Wilson & Hildreth 1997; Houghton et al. 2004; Fierstein & Wilson 2005; Hildreth & Fierstein 2012), indicate that these regimes do not capture the complexity of processes presented in the pyroclastic density current and plinian fall deposits. Field data is not readily available in a format that allows it to inform input and boundary conditions of Plinian eruptions, and eruption scenario models are biased toward the steady versus unsteady column regimes. The limited number of detailed, quantitative field studies and incomplete simulation scenarios restrict our understanding of the processes involved in the spatiotemporal evolution of large Plinian eruptions and their consequent hazard impacts.

This research aims to improve our understanding of the eruptive processes involved during large Plinian eruptions that involve coeval plinian fall and pyroclastic density current generation. I focus on the large-Plinian Y5 phase of the Taupō 232 ± 10 CE eruption, which has an exceptionally widespread and well-preserved deposit (Walker 1980; Wilson & Walker 1985; Houghton et al. 2010, 2014). Although the Y5 is very well studied (Healy 1964; Walker 1980; Wilson 1981; Wilson & Walker 1985; Houghton et al. 2010, 2014; Mitchell et al. 2018), there remain conflicting views on the interpretation of its deposit regarding eruption and sedimentation dynamics. Walker (1980) originally considered the Y5 unit as a single eruptive unit from the perspective of the extensive fall deposit. He, however, did not consider the presence and relevance of the intraplinian, coeval flow units (Wilson & Walker 1985). Bedding characteristics in the Y5 deposit were also only briefly contemplated by Walker (1980) yet were investigated in detail by Houghton et al. (2014) who used their observations to propose the presence of 26 subunits within the Y5 fall deposit. The correlation of these subunits, however, was based on a qualitative investigation and the quantitative basis for the resulting dispersal directions of the subunits was not presented. Here, I present a detailed quantitative dataset of the physical properties in the vertical stratigraphy at selected proximal to medial exposures within the Y5 deposit. I aim to build upon our knowledge base of the eruption and sedimentation dynamics of large Plinian eruptions by providing a field-based foundation for the reconstruction of the spatiotemporal evolution of such events. This is intended to provide a pathway for the amalgamation of field data and computational eruption models, ultimately improving our ability to forecast and mitigate explosive eruptive hazards at similar volcanoes globally.

1.1.1 Research objectives and approach

A principal hypothesis for this thesis is proposed as follows:

A quantitative characterisation of the variation in deposit features (e.g., granulometry, componentry, and textural characteristics of juveniles) with stratigraphic height in plinian eruption deposits that involve coeval fall and PDCs can be used to identify temporal changes in eruption behaviour, conduit dynamics and sedimentation. This will provide a foundation to reconstruct the spatiotemporal evolution of Plinian eruptions and constitute the basis for the amalgamation of field studies and computational eruption modelling.

To test this hypothesis, three research objectives have been defined:

***Objective 1*:** Characterise the nature of vent transition and onset of large Plinian phases during multiphase eruption sequences.

Goals

- Create a detailed, quantitative database of deposit characteristics across the transition between the phreatoplinian Y4 and plinian Y5 deposits in terms of granulometry, components with specific focus on lithic lithologies, and pumice densities.

- Constrain the vent location for the Y5 phase of the Taupō 232 ± 10 CE eruption.

- Determine whether the transition was 1) a function of eruptive power at a single vent, 2) variation in vent condition from wet to dry at a single vent, or 3) a shift in the vent position from a wet dry environment.

***Objective 2*:** Reconstruct the temporal evolution of a plinian fall deposit through detailed quantitative analysis of deposit features with respect to changes in conduit, plume, and sedimentation dynamics.

Goals

- Create a detailed, quantitative database of deposit characteristics in the vertical stratigraphy of the Y5 fall deposit in terms of granulometry, variations in lithic lithologies and pumice textures and their relative abundance, and pumice densities and porosity. Use this to characterise the dynamics of the conduit and sedimentation from the umbrella cloud.

- Interrogate the lateral correlatability of bedding characteristics in the Y5 fall deposit to aid the interpretation of eruption and plume dynamics from deposit data.

***Objective 3*:** Reconstruct the relative timing and source dynamics of coeval, intraplinian PDC events during Plinian eruptions.

Goals

- Use deposit features in fall and related PDC deposits to define the lateral correlation of PDCs and their relative timing with respect to the fall.
- Characterise and determine the nature of generation of the types of PDCs generated during the Y5 phase of the Taupō 232 ± 10 CE eruption using deposit characteristics.
- Contrast the Y5 scenario with other Plinian case studies from New Zealand, and globally to open opportunities for the amalgamation of field studies and computational eruption modelling.

1.1.2 Thesis outline

This thesis is composed of seven chapters, with eleven appendices presenting a collection of specific data sets. *Section 1.2* is a review of the current literature regarding the understanding of Plinian eruptions, their products, and the details of the Taupō 232 ± 10 CE eruption. *Chapter 2* outlines the general details of the methodologies used to address the aforementioned research objectives. Chapter specific methodology details are further explained in each research chapter. The nature of vent transitioning between the Y4 and Y5 phases of the Taupō 232 ± 10 CE eruption is detailed in *Chapter 3*, including a critical review of the vent location for the Y5 phase. *Chapter 4* addresses the eruption and sedimentation dynamics of the large Plinian Y5 phase in terms of detailed quantitative analyses of deposit characteristics, reconstructing its temporal evolution. Building upon the eruption dynamics of the Y5 phase, *Chapter 5* then investigates the relationship of the coeval Early Flow Units to the Y5 Plinian plume and explains the relative timing and nature of the flows. *Chapter 6* discusses the data sets as a whole, suggests a revised vent configuration for the Taupō 232 ± 10 CE eruption, and develops a new spatiotemporal reconstruction of the Y5 phase, with implications for the amalgamation of field studies and computational modelling. A summary of the main conclusions is presented in *Chapter 7*.

1.2 Background Information

1.2.1 Plinian eruptions and their products

Plinian eruptions are sustained, quasi-steady, high-energy explosive eruptions that generate buoyant, convective multiphase plumes of pyroclasts (most commonly silicic for the juvenile fraction), magmatic gas and entrained air that reach >20 km into the atmosphere (Walker & Croasdale 1971; Wilson 1976; Walker 1980, 1981a; Carey & Sigurdsson 1989; Sparks et al. 1997; Constantinescu et al. 2021). They comprise some of the most destructive natural phenomena on Earth. Plinian eruption columns spread laterally as gravity currents into an umbrella cloud once the plume attains conditions of neutral buoyancy relative to the adjacent ambient air, which results in an exceptionally widespread tephra fallout (Walker 1980, 1981a; Carey & Sigurdsson 1989; Constantinescu et al. 2021). During an eruption, the column will partially or completely collapse if buoyancy of the erupting mixture is not achieved and produce short-lived pulses or sustained, ground hugging pyroclastic density currents (PDCs) that disperse around the vent (Sparks 1976; Walker et al. 1980b; Self & Rampino 1981; Branney & Kokelaar 2002; Komorowski et al. 2013; Cioni et al. 2015; Dufek 2016; Trolese et al. 2019; Lube et al. 2020).

Modern historical Plinian eruptions are classified based on varying levels of geophysical data and satellite remote sensing observation in addition to eye-witness accounts (e.g., Mt Pinatubo, 1991; Mt St Helens 1980). The classification of historical events that predate the development of abundant geophysical observations (e.g., Vesuvius, 79 CE; Krakatau, 1883; Novarupta, 1912) is reliant on eye-witness accounts in addition to analysis of resulting deposits. In the case of pre-historical events (e.g., Taupō, 232 ± 10 CE; Minoan Eruption, 1613 ± 13 BCE), eruption classification is exclusively reliant on deposit characteristics. Few instrumentally recorded historical plinian eruptions have occurred and direct observations and measurements are still rare in the field of volcanology. Therefore, research into understanding the dynamics and sedimentation of large-scale Plinian events is still often dependent on investigating the characteristics of their deposits in relation to the parental eruption cloud and conduit using field investigation, and analogue and numerical modelling. In this section, I present a summary of the current understanding of the dynamics and sedimentation of Plinian eruptions and the resulting deposit features.

Eruption plume and cloud dynamics

The strength of a volcanic plume is controlled by the mass discharge rate (MDR), the temperature, composition and volatile content of the magma, vent and conduit geometry, and advection by atmospheric winds (Sparks et al. 1997; Bonadonna et al. 1998; Woodhouse et al. 2013; Cioni et al. 2015; Cashman & Rust 2016). The height of the plume relies greatly on the heat transfer from particles to entrained air and is therefore sensitive to the total mass and grain size distribution (GSD) within the plume, creating buoyant, convective momentum by which the plume rises (Cioni et al. 2015; Cashman & Rust 2016). Variations in the MDR or other parameters controlling the eruption dynamics generally take place over longer time scales than those of the processes that control magma ascent, fragmentation, and plume development, which results in a sustained, quasi-steady eruption column (Cioni et al. 2015). If the maximum height that a strong plume rises to is greater than the level of neutral buoyancy (NBL; *Figure 1.1*) the plume will collapse back to the NBL and propagate laterally as a density current, forming an umbrella cloud that has a geometry dependent on atmospheric wind (Bursik et al. 1992; Baines & Sparks 2005; Costa et al. 2013; Cashman & Rust 2016; Constantinescu et al. 2021).

Plume modelling suggests that for a volcanic plume to become buoyant, concentrations of >1 mm particles should be in minor quantities due to the effects of thermal disequilibrium between gas and large particles (Woods & Bursik 1991; Lherm & Jellinek 2019), the sedimentation of large particles (Girault et al 2014; Lherm & Jellinek 2019), and the recycling of particles (Veitch & Woods 2002; Lherm & Jellinek 2019). It is assumed that fine ash-rich columns are more likely to ascend higher into the atmosphere; however, these columns are also more likely to collapse due to reduced entrainment rates and mixing (Jessop & Jellinek 2014; Lherm & Jellinek 2019). Volcanic plume models often simplify the dynamical controls of multiphase volcanic jets, however, by ignoring the turbulent entrainment of the atmosphere (e.g., Kaminski et al. 2005; Carazzo et al. 2006), limiting knowledge regarding the effect of turbulence on the sedimentation dynamics of large volcanic clouds. Current studies suggest that the rate of entrainment and mixing of the atmosphere into volcanic jets comprised of gas and particles (juvenile, cognate, and lithic material) determines the buoyancy and/ or collapse dynamics of a plume, based predominantly on the physical properties of the mixture such as density and grain size (Turner 1969, 1986; Woods 1995, 2010; Kaminski et al. 2005; Cioni et al. 2015; Lherm &

Jellinek 2019; Gilchrist & Jellinek 2021). Modelling of Plinian plumes indicate that variations in conduit geometry, magma properties, MDR and fragmentation style may cause steady state conditions to shift and hinder convective buoyancy, potentially causing partial- to total-collapse of the column, generating PDCs, discussed below.

Pyroclastic density currents

Pyroclastic density currents (PDCs) are one of the most destructive and hazardous phenomena of explosive volcanism. They can be short-lived pulses or sustained, ground hugging, gravity-controlled hot currents of particles and gas that are produced during eruption processes such as collapse of eruptive plumes, direct magmatic blasts, and caldera-collapse scenarios, and have the potential to rapidly transport material for many kilometers (Sparks 1976; Walker et al. 1980a; Self & Rampino 1981; Branney & Kokelaar 2002; Clarke et al. 2002; Belousov et al. 2007; Komorowski et al. 2013; Cioni et al. 2015; Dufek 2016; Trolese et al. 2019; Lube et al. 2020). Investigations into their deposits have outlined two endmembers of PDC behaviour, which are pyroclastic flows (concentrated) and pyroclastic surges (dilute). Flows are typically dominated by gas-particle transport with high particle volume concentrations of several tens of percent, while surges have lower bulk concentrations of typically less than one volume percent (e.g., Sparks 1976; Wilson 1985; Wilson & Houghton 2000; Lube et al. 2020).

In the case of large-scale Plinian eruptions that generate high, buoyant eruption plumes, there are two widely accepted interpretations for the generation and dynamical controls of PDCs: partial- or total column collapse. If positive buoyancy of the erupting mixture cannot be achieved because of its physical properties, variations in conduit geometry, mass discharge rates and/ or fragmentation styles, the column will partially or completely collapse. Partial column collapse is commonly recognized as the transitional regime between a sustained column and total collapse conditions and is marked by column unsteadiness where large-volume annular sediment waves descend periodically from the jet-plume transition height (*Figure 1.1*), producing pulsating PDCs (Turner 1969, 1986; Woods 1995, 2010; Neri et al. 2002; Kaminski et al. 2005; Carey & Bursik 2015; Cioni et al. 2015; Lherm & Jellinek 2019). Models of such scenarios indicate that the erupted mixture is expected to be partitioned between the buoyant umbrella cloud and collapsing sediment waves. This partitioning can result in the finer size fractions of the erupted mixture preferentially being winnowed into the umbrella cloud and PDCs spreading as relatively dilute flows (Gilchrist & Jellinek 2021).

Column collapse regimes have traditionally been interpreted to be the sole generators of PDCs when associated with Plinian eruptions; however, this view places unwarranted limitations on the understanding of real-world scenarios.

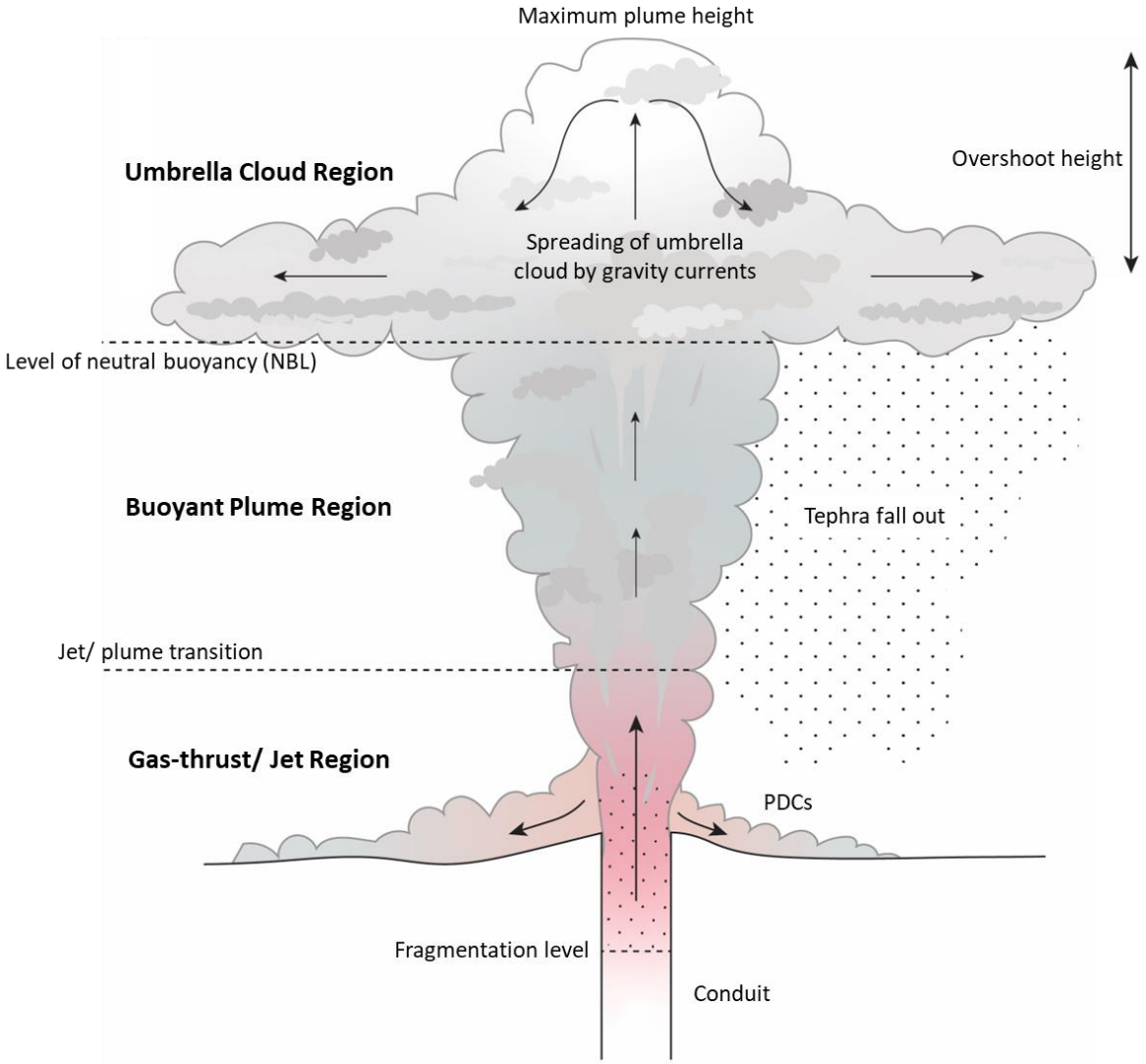

Figure 1.1 Schematic of the eruptive processes during a Plinian eruption, from fragmentation in the conduit to atmospheric dispersal as the umbrella cloud spreads by gravity currents at the level of neutral buoyancy. The three mechanically distinct regions from which tephra sedimentation (fall out and PDCs) occurs are noted in bold. Modified from Rowell et al. (2022).

Studies of the coeval emplacement of plinian fall and PDC deposits, such as in the Novarupta, 1912 eruption (Hildreth & Fierstein 2012, for overview), have outlined the complexities in PDC generation. In this example, field studies showed that PDCs, both dilute

and concentrated, could undergo little to no ascent with the coexisting Plinian column which, contrary to partial collapse models, was never fully interrupted (Fierstein & Hildreth 1992; Houghton et al. 2004; Fierstein & Wilson 2005). Numerical multiphase simulations Valentine & Cole (2021) were used to model such behaviour, termed "gargle dynamics" (cf. Wilson & Hildreth 1997), as a process in which debris-filled vent structures cause large portions of the venting materials to become trapped, resulting in an eruption jet needing to penetrate its own earlier ejecta. When preexisting ejecta interact with the erupting mixture and form a dense sheath along the margins of the erupting jet (Houghton et al. 2004; Hildreth & Fierstein 2012; Valentine & Cole 2021), overloaded annular zones within the jet region fail to rise sufficiently with the jet (Wilson & Walker 1985; Fierstein & Hildreth 1992; Wilson & Hildreth 1997; Houghton et al. 2004; Hildreth & Fierstein 2012; Valentine & Cole 2021). Collapse or diversion of this material can occur at all heights along the sheath on the outer edge of the jet, producing concentrated, highly fluid PDCs (Fierstein & Wilson 2005; Valentine & Cole 2021), while the Plinian plume continues uninterrupted. These field observations and models show that generalised steady versus unsteady column regimes can oversimplify the interpretation of both PDC and plinian air fall deposits in natural eruption scenarios, yet they are still the most accepted explanation for PDCs generated simultaneously with fall deposition.

Tephra fragmentation and sedimentation

Magma fragmentation is the breakup of a continuous volume of magma into pyroclasts. Primary fragmentation can occur due to rapid expansion, decompression or quenching of melt (Cashman & Rust 2016). In the case of dry, rhyolitic eruptions, where minimal to no external water interacts with the magma, fragmentation mostly occurs by brittle fracture due to rapid expansion from bubble nucleation and growth (Sparks 1978; Cashman 2004; Cashman & Rust 2016). Fragmentation may also be initiated or enhanced when magma interacts with external water, encouraging increased fragmentation efficiency due to steam explosivity as the water violently expands on contact with the magma (Smith 1998; White 1996; Austin-Erickson et al. 2008). This fragmentation style is known as phreatomagmatic activity and, when associated with large-scale eruptions, the term phreatoplinian is sometimes adopted to describe the related eruption style (Self & Sparks 1978; Houghton et al. 2000a). Secondary fragmentation will also occur as particles are broken down further due to collision or abrasion within a volcanic plume and can result in an abundance of very fine

ash particles (Dufek & Manga 2008; Rose & Durant 2009; Cashman & Rust 2016). Grain size distributions (GSD) may be used to classify eruptions, using methods by Walker (1973) and Pyle (1989), in terms of their magnitude and intensity (Pyle 2015). Typically, GSDs of plinian deposits are polymodal, due to the density variations of sedimented clasts with similar fall velocities (Cioni et al. 2015). The fall deposits associated with phreatoplinian eruptions commonly have finer GSDs and poor sorting comparative to their dry plinian counterparts due to:

1. Increased efficiency of fragmentation during magma-water interaction producing higher proportions of fine material; and,

2. The aggregation of ash due to increased external water content (Self & Sparks 1978; Walker 1981b; Smith 1998; White 1996; Van Eaton & Wilson 2013; Houghton et al. 2015).

Tephra is the collective term for particles of varying components ejected from the vent. The components consist of juvenile (material newly erupted from a molten state during an eruption, i.e., pumice, obsidian, and crystals) and foreign (i.e., wall rock, older pumice, obsidian, or crystals, and/ or lava) particles. These particles have variable densities, and each can span from metre-sized blocks and bombs, ejected as short-range ballistics, to micron sized particles transported to global scales by atmospheric winds (Sparks et al. 1997; Bonadonna et al. 2015a; Cioni et al. 2015).

During an explosive eruption, tephra sedimentation and fall deposits are generated from three spatially overlapping, yet mechanically distinct regions, as outlined by Houghton et al. (2000a):

1. Jet or gas-thrust region (*Figure 1.1*) –material is ejected from the vent at high velocities driven primarily by expansion of gases;

2. Buoyant/convective region (*Figure 1.1*) –thermal flux determines the height of buoyant rise of the mixture; and,

3. Umbrella cloud region (*Figure 1.1*) –the eruption plume spreads laterally as a gravity current, at altitudes controlled by atmospheric stratification and ambient winds.

Models infer that most sedimentation occurs in regions directly under the leading edge of the cloud, with atmospheric diffusion causing sedimentation beyond this point (Carey & Sparks 1986; Constantinescu et al. 2021). The distance of atmospheric transport in the umbrella cloud, however, is accomplished by flow of the cloud as a density current, and atmospheric diffusion is of secondary importance. The sedimentation regimes of tephra are complex, likely occurring at all positions under the umbrella cloud, and depend greatly on plume dynamics and the terminal velocities of particles, as well as the total grain size distribution within the plume, gravitational instabilities and turbulence, and clast aggregation (e.g., Fierstein & Nathenson 1992; Bonadonna et al. 1998, 2015a, b; Durant et al. 2009; Carazzo & Jellinek 2013; Cioni et al. 2015; Manzella et al. 2015; Cashman & Rust 2016).

As mentioned previously, the various tephra components ejected from a vent during an eruption have a range of densities and sizes, properties that greatly influence the fall out conditions of individual clasts. Juvenile fragments can be dense or vesicular due to the variable amounts of bubbles and crystals present in a silicate melt prior to and during an eruption (Cashman 2004; Cashman & Rust 2016). Juvenile fragments in plinian eruptions are commonly dominated by highly vesicular pumice clasts and ash-sized pumice and glass shards (Cioni et al. 2015). Crystals formed in the magma chamber prior to eruption (phenocrysts) are transported to the surface in the ascending melt and are typically dense. Both the phenocrysts and glassy, vesicle-poor juvenile fragments are classically ash sized, yet phenocrysts tend to sediment from a volcanic plume more rapidly due to their higher densities. Similarly, wall rock material is preferentially sedimented (Cashman & Rust 2016) as a result of the higher densities and typically larger sizes of these clasts. According to Carazzo & Jellinek (2012), in general, particles that are larger than 250 μm – 1 mm located high in the atmosphere will settle individually while finer particles are likely to settle collectively, with the primary control on the residence time of tephra in the atmosphere being the settling velocity of particles. Ash particles <100 μm often settle due to either particle aggregation or elutriation processes, or gravitational instabilities, which can reduce tephra residence time in the atmosphere and cause premature sedimentation (Walker 1981b; Talbot et al. 1994; Bonadonna et al. 2015a). This can significantly reduce the amounts of fine ash transported to distal regions in the umbrella cloud.

Gravitational instabilities have been noted to increase the sedimentation rate of fine ash particles via preferential pathways (Carazzo & Jellinek 2013). These pathways, termed

'fingers', are protrusions of particles that reach the ground more rapidly than individually settling particles and have been identified in eruptions such as Soufrière Hills 1997, Montserrat; Mt. Ruapehu 1996, New Zealand; and Eyjafjallajökull 2010, Iceland (e.g., *Figure 1.2*: Bonadonna et al. 2015a). Manzella et al. (2015) noted that the fingers enhance sedimentation of fine ash, providing a plausible explanation for near source fine ash deposition. Studies such as those described above, however, have predominantly focused on smaller scale explosive eruptions. In larger scale eruptions, sedimentation is expected to be dominated by individual particle settling due to coarser median grain sizes (Bursik et al. 1992; Carrazzo & Jellinek 2012). It is recognized that the fine ash portion of such eruptions is difficult to assess due to prolonged atmospheric suspension and therefore median grain sizes of large eruption plumes may be overestimated. This increases the possibility that large-scale explosive eruptions occur within the particle boundary layer regime that promotes gravitational instabilities and finger driven sedimentation (Carrazzo & Jellinek 2012). During such powerful events, larger variations in grain sizes, stronger convection, and greater variations in densities in proximal to medial regions of the umbrella cloud could also result in instabilities that preferentially sediment predominantly coarser grained pyroclast packages (Bonadonna et al. 1998, 2015a, b; Cioni et al. 2015; Houghton & Carey 2015). There is, however, a lack of modelling regarding this scenario.

Figure 1.2 Example of sedimentation by gravitational instabilities during the 2010 eruption of Eyjafjallajökull, from Manzella et al. (2015).

Deposit characteristics

Deposits of both fall and PDC origin generally provide a great opportunity for analysis and interpretation for the purpose of identifying stratigraphic correlations through isochronous marker beds, determining eruptive parameters, and reconstructing eruption dynamics (e.g., Walker 1971, 1973, 1980, 1981a, b; Bond & Sparks 1976; Wilson et al. 1980; Wilson 1985, 1993; Sigurdsson & Carey 1989; Blake et al. 1992; Wilson & Hildreth 1997). Umbrella clouds can rapidly transport large volumes of tephra in the atmosphere while, in the case of intraplinian PDCs and total column collapse, flows transport dilute to dense concentrations of material along the ground in proximal to medial distances. Therefore, large-scale explosive eruptions result in complex tephra sedimentation patterns and can manufacture considerable uncertainties when used to estimate eruption source parameters (Constantinescu et al. 2021). Large-scale eruptions are predominantly prehistoric with few occurring in modern times (Geshi 2020) and real-time observations are scarce. Detailed field analysis is therefore required to improve the interpretation and understanding of these events for the purposes of eruption reconstructions, with applications to hazard mitigation and risk assessment for future events.

Large scale deposit characteristics, such as spatial extent and thickness variations, can be attributed to a combination of eruption and transport conditions (Houghton et al. 2000a; Scollo et al. 2008; Cashman & Rust 2016). The thickness and maximum grain size of tephra deposits tend to decrease with distance from source (Thorarinsson 1967; Houghton et al. 2000a; Cashman & Rust 2016; Constantinescu et al. 2021), reflecting the generalized preferential and continuous deposition of particles with distance. The spatial extent of a deposit is often attributed to the MDR and plume height, and/or variations in atmospheric wind strength and direction (Sparks et al. 1997; Houghton et al. 2000a; Bonadonna et al. 2015a, b). Tephra deposit dispersal geometry is highly dependent on the wind field at the time of eruption, with deposit elongation occurring in the direction of the wind. Variations in dispersal may result from variability in wind directions at different altitudes during a sustained eruption characterised by changes in MDR, or from the change in wind direction during different eruption pulses, producing juxtaposed lobes of various dispersal that are difficult to separate as they grade into one another at their margins (Sparks et al. 1997; Cioni et al. 2015). By measuring the thickness and maximum clast sizes at various sites within a deposit, representative isopachs and isopleths, respectively, can be identified (Sparks et al.

1997; Pyle 1989; Houghton et al. 2000a; Cashman & Rust 2016). From these measures, the total deposit volume can be estimated (Pyle 1989) and tephra trajectories ascertained, respectively (Cashman & Rust 2016). There are several complexities that can affect isopach and isopleth measurements, however, which can be difficult to account for if a deposit is not well-preserved. These include:

1. Secondary thickening caused by aggregation and premature fine particle deposition,
2. Variations in umbrella cloud elongation at different atmospheric levels,
3. Changes in wind direction during the eruption,
4. Coeval deposition with PDCs causing complex thinning relationships and mixing of different source material (Houghton et al. 2000a), and
5. Erosion from PDCs due to scouring (Cioni et al. 2015).

Fall deposits commonly exhibit variations in stratification and fluctuations in grain size and components with height (e.g., *Figure 1.3*), especially in proximal to medial regions, providing insight into eruption and transportation dynamics. Sustained eruptions are typically interpreted to be characterized by deposits that lack well defined bedding planes, whereas distinct units of contrasting grain size and/or components are indicative of a periodic, inconsistent eruption (Houghton et al. 2000a; Houghton & Carey 2015). For example, beds of fine ash are often interpreted as either time breaks in the eruption allowing fines that persist in the atmosphere to settle, or as the result of rain flushing or gravitational instabilities (Walker 1981b, Talbot et al. 1994; Bonadonna et al. 2015a). Crossbedding and/or pinch-and-swell features within layers are interpreted to indicate coeval deposition with flow units and/or co-ignimbrite plumes. Grading and contrasts of grain size within a deposit may be interpreted as fluctuations in the eruption intensity, as a stronger plume is more likely to transport coarse material to greater distances, or it may indicate shifts in wind direction and strength (Houghton et al. 2000a; Houghton & Carey 2015). Tephra deposits produced by dry plumes often exhibit volcanologically good sorting and a systematic decrease in clast size with distance from the vent. Aeolian fractionation in distal deposits also produces changes in relative proportions of components due to variable densities of the clasts. However, in proximal regions deposits are thick, coarse-grained, and lithic-rich compared to their distal counterparts, and are moderately to poorly sorted due to the

simultaneous sedimentation of tephra from varying regions in the eruptive column (Houghton et al. 2000a; Cioni et al. 2015). As fall deposits blanket the landscape, it is also common for tephra to roll, slide or avalanche down steeper surfaces (Duffield et al. 1979), causing overthickening or misrepresentation of the true stratigraphical profile.

Figure 1.3 Example of a portion of a plinian fall deposit from the Y5 phase of the Taupō 232 ± 10 CE eruption at Exposure D (discussed in this thesis; UTM 60S 428674E 5706559N.). Note the fluctuation in, for example, grain size with stratigraphical height in the profile.

Products from Plinian-related PDCs are defined as ignimbrites, which are a pumiceous, ash-rich, poorly sorted mixtures of tephra that may drape over pre-existing stratigraphy, modify the landscape, or build new landscapes in the largest examples (Smith 1960; Sparks 1976; Walker et al. 1980; Fisher & Schmincke 1984; Wilson 1986; Cas & Wright 1987; Freundt et al. 2000; Branney & Kokelaar 2002). Ignimbrites can vary from metres to hundreds of metres thick and can be massive or contain a wide range of sedimentary structures such as sharp to diffuse stratification, cross bedding, erosional surfaces, grading patterns and particle fabrics (Wilson 1981; Branney & Kokelaar 2002). High velocity, low volume flows can often surmount topography and the resulting ignimbrites are generally decimetre to metres thick and show massive to stratified, cross bedded internal structures. Low velocity, high volume flows are commonly topographically confined and deposit ignimbrites that are massive and up to tens of metres thick (Sparks et al. 1997; Wilson 1981; Branney & Kokelaar 2002). Sequential deposition by both concentrated and dilute PDCs can result in ignimbrite packages up to hundreds of metres, where the boundaries between individual flows may be obscure in proximal to medial regions (Wilson 1981). Complete or incipient welding of ignimbrites can occur when emplaced at high temperature of at least 600 ºC, based on estimates for the onset of sintering in rhyolitic compositions (e.g., Boyd 1961; Grunder et al. 2005; Quane & Russell 2005).

In proximal regions, fall deposits may be eroded or overthickened by PDCs due to scouring or deposition, respectively (Cioni et al. 2015). Deposits may also contain interbedding of ignimbrites with fall sequences (e.g., *Figure 1.4*), which can indicate complexities in column behaviour from instabilities in buoyant convection and/ or gargle dynamics. In general, plinian deposits have been categorised into three types: simple plinian deposits, simple-stratified plinian deposits, and multiple plinian deposits. Simple plinian deposits are most common and are inferred to develop through sedimentation from a steady eruption plume and are typically massive, or reversely graded if there is an increase in MDR (Cioni et al. 2015; Houghton & Carey 2015). Stratigraphical isochrons are laterally distinct in these types of deposits as vertical changes in sedimentological features do not differ with distance from vent, allowing correlations to be made between exposures.

The commonly accepted notion is that partial collapse of an eruptive column may produce simple-stratified plinian deposits. These deposits are typified by proximal to medial interbedding of ignimbrite within a fall deposit from a single eruptive event that may have

numerous partial collapse episodes (Walker 1980; Cioni et al. 2015; Houghton & Carey 2015). The boundaries between individual flow units, however, may sometimes be obscured due to rapid emplacement succession (Wilson & Walker 1985). With distance, the alternating fall-PDC beds become a massive plinian fall deposit due to the limited runout distance of PDCs. Past this runout limit, or when directionally restricted PDCs occur, eruption modelling suggests that column collapse is recorded in atypical sedimentological deposit features, such as finer grained beds at relative levels, because partial mass partitioning into PDCs results in a decrease in convective column height (e.g., Neri et al. 2002; Di Muro et al. 2004; Carazzo et al. 2015; Cioni et al. 2015; Houghton & Carey 2015). When sedimentation rates of the two processes are similar, hybrid, poorly sorted deposits of coarse and fine material exists. If fallout dominates, a poorly sorted deposit of coarse pumice with an anomalous amount of ash occurs (Walker 1971; Cioni et al. 2015). Sedimentation dominated by PDCs will produce poorly sorted, ash rich ignimbrites with minor large pumice or impact pumice (Walker 1971; Cioni et al. 2015). The generalized partial collapse interpretation, however, does not consider gargle dynamics and the synchronous emplacement of plinian fall deposits and ignimbrite (or other PDC deposits), where currents undergo little to no ascent with the coexisting Plinian column, which in turn also undergoes no height diminution that is reflected in the subsequent fall deposits (Fierstein & Hildreth 1992; Wilson & Hildreth 1997; Houghton et al. 2004; Valentine & Cole 2021). In this case, it is possible that plinian fall deposits may show few or no characteristics assumed to be associated with partial mass partitioning, whilst still being proximally interbedded with PDC deposits, highlighting the oversimplification that may result from categorizing deposits in this manner.

Multiple plinian deposits are produced by distinct eruption pulses that deposit under different atmospheric and/or eruptive conditions, yet rapidly enough such that erosion or reworking does not occur between fallout beds. These deposits are typified by internal boundaries that indicate changes in, for example, eruption mass discharge at source, conduit stability, contrasting explosive styles, complex magma mixing, a compositionally zoned magma chamber or tapping of various sources (Lirer et al. 1973; Sparks et al. 1981; Walker 1981a; Sigurdsson & Carey 1989; Blake et al. 1992; Rosi et al. 1999; Polacci et al. 2001; Cioni et al. 2015; Houghton & Carey 2015).

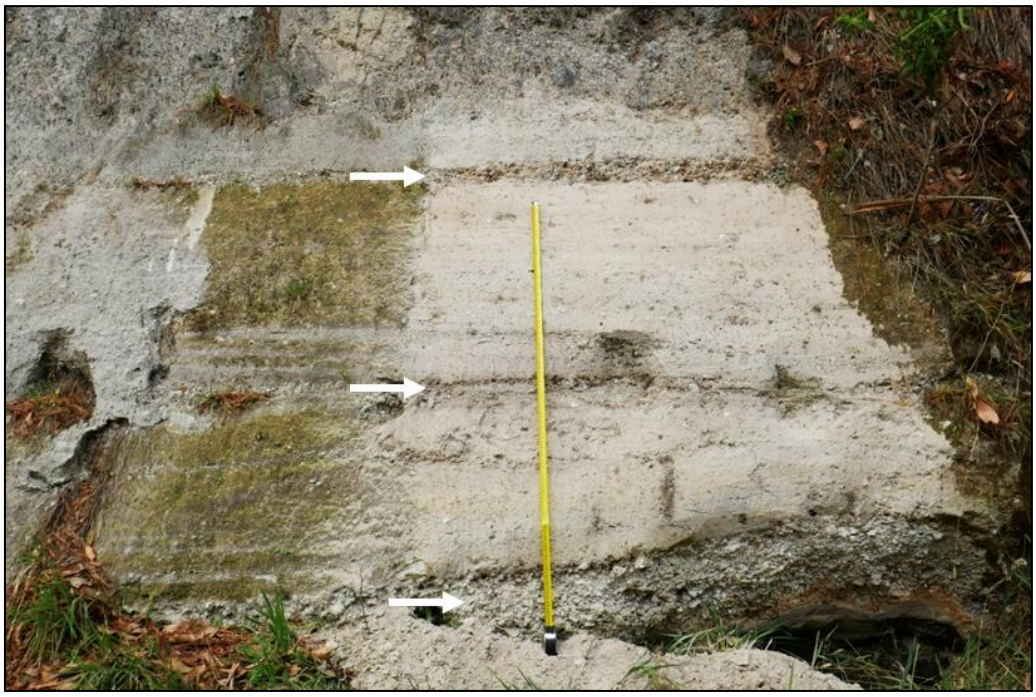

Figure 1.4 Example of interbedded plinian fall and ignimbrite from the Y5 phase of the Taupō 232 ± 10 CE eruption. Fall marked by white arrows. Location is Exposure H discussed in this thesis, at coordinates UTM 60S 414727E 5715310N. Measuring tape is extended to 150 cm.

The small-scale properties of tephra fall deposits are attributed to the various clast components present, which give insight into processes such as fragmentation, column transport and density fractionation of clasts. For plinian deposits, components are generally split into classes of juvenile pumice, obsidian, and crystals, and foreign lithics (wall rock, lava and other erupted material from pre-existing deposits) based on vesicularity, morphology and lithology.

Juvenile pumice clasts have vesicularities that highlight the history of degassing in explosive eruptions, and shapes that signify their origin and transport history (Cashman 2004; Houghton et al. 2000a). For example, pumice clasts in plinian deposits exhibit a narrow range in vesicularity populations, with bulk vesicularities typically between 65 – 85 vol%, and textural variability (e.g., clast and vesicle morphology) indicative of the fragmentation of highly viscous magmas (Houghton & Wilson 1989; Polacci et al. 2003; Cioni et al. 2015). The high MDR of plinian eruptions also requires maintained high magma ascent velocities in the conduit which, in conjunction with the high viscosity of silicic magmas, creates boundary layers along the conduit walls, reducing drag effects during magma ascent. Shearing of magmas in these boundary layers results in stretching of vesicles and produces

a large proportion of tube pumice in plinian deposits (Polacci et al. 2003; Dingwell et al. 2016; Cioni et al. 2015; Ohashi et al. 2020). Phenocrysts (crystals) within juvenile pumices provide insight into the residence conditions in the magma chamber which has implications for the eruption dynamics (Houghton et al. 2000a). The crystal content of pumice is considered representative of the magmatic crystal content at the time of eruption, and free crystals are often released when the magma is fragmented to particles finer than the largest phenocryst (~2 mm; Walker 1980). Considering the higher density of crystals versus pumice particles of the same size, crystals will generally fall close to the source than the pumice particles due to aeolian fractionation in the umbrella cloud. Based on these assumptions, the crystal concentration method developed by Walker (1980) has allowed for inferences to be made regarding the volumes of deposits by estimating the total mass of free crystals, with implications for estimates of plume height.

Foreign lithic and pumice clasts are derived from the conduit wall and existing products of previous eruptions. When the local stratigraphy is known, fragmentation depths and conduit behaviour can be inferred from the type of wall rock lithic present in the deposit. Variations in composition and relative abundance of lithic clasts throughout the vertical profile of a deposit provides the potential to constrain conduit and eruptive dynamics, as demonstrated in studies such as Hildreth & Mahood (1985), Barberi et al. (1989), and Hanson et al. (2016). These studies provided insight into factors such as:

- Conduit wall stability,
- Vent location or opening of new vents,
- Widening of the vent,
- Variations in fragmentation depth; and
- Lateral dimension and length of the conduit.

For example, beds enriched in shallow-level wall rock lithics in a plinian deposit are often interpreted to represent phases of vent widening (Cioni et al. 2015).

Volcanic hazards

Constituting one of the most powerful natural phenomena on Earth, Plinian eruptions have the potential to cause widespread havoc on communities in terms of health issues, impacts on critical infrastructure, and agriculture. PDCs are one of the most destructive and

hazardous phenomena of explosive volcanism, with the potential to rapidly transport hot debris for many kilometres. Human exposure to even minor PDCs can cause fatalities by heat and dynamic pressure damage (Spence et al. 2004; Geshi 2020). Critical infrastructure – here defined based on Wilson et al. (2014) as energy sector infrastructure, water supply and wastewater networks, transportation routes, communications, and urban areas – may be severely damaged or hindered by the destructive potential of PDCs or by ashfall deposition. For example, fine ash particles suspended in the atmosphere may hinder air traffic for prolonged periods, or network lines for power and communication can sustain significant damage from PDCs or fall deposition (Rose & Durant 2009; Wilson et al. 2014; Biass et al. 2017; Geshi 2020). Cardiorespiratory illness in both humans and animals can result from exposure to ultra-fine ash (<10 μm) and aerosols suspended in the atmosphere (Horwell & Baxter 2006; Rose & Durant 2009; Geshi 2020). Tephra accumulation on agricultural land can cause severe damage by covering the land and constricting water supplies as well as having direct health implications on livestock (Rose & Durant 2009; Wilson et al. 2011; Biass et al. 2017; Geshi 2020). Globally, the injection of large amounts of ultra-fine ash and aerosols into the atmosphere can have long term impacts of the global climate system (Rampino & Self 1982, 1984; Rampino et al. 1988; Self et al. 2004; Sparks et al. 2005; Self 2006, 2015; Geshi 2020). Therefore, it is imperative to increase our scientific and societal understanding of large-scale Plinian eruptions to further develop risk assessment, and hazard management and mitigation planning for communities living around such volcanoes, globally.

1.2.2 The Taupō Volcanic Zone

The Taupō Volcanic Zone (TVZ: *Figure 1.5*), located within the Taupō-Hikurangi arc-trench system of New Zealand's North Island, is a volcanic arc formed by the westward subduction of the oceanic Pacific Plate beneath the continental crust of the Australian Plate (Cole & Lewis 1981; Cole 1990; Villamor & Berryman 2001; Spinks et al. 2005; Wilson & Rowland 2016; Villamor et al 2017). It is globally one of the most active silicic volcanic regions and is a major focus of Quaternary volcanism in New Zealand (Wilson et al. 1995; Houghton et al. 1995; Spinks et al. 2005). Crustal thinning, in association with major transtensional lineaments, provides an environment for high quantity magma storage in the crust, ultimately favouring large volume eruptions with associated subsidence and caldera formation (Wilson et al. 1984, 2009). The central TVZ has erupted dominantly rhyolitic magma and minor high-

alumina basalt, with at least 25 caldera forming ignimbrite eruptions identified (Wilson et al. 2009). These eruptions have occurred predominantly from the major caldera volcanoes; namely, Rotorua, Okataina, Kapenga, Mangakino, Ohakuri, Whakamaru, Reporoa and Taupō. All but Mangakino have formed in the past 350 ka, denoted as the young TVZ (*Figure 1.5*; Wilson et al. 1995, 2009; Gravley et al. 2007). Rhyolitic eruptions (>15000 km^3 bulk volume, typically 70 – 77 % SiO_2) initiated at approximately 1.9 Ma, the past 65 ka of which has seen highly frequent activity from both the Okataina and Taupō volcanic centres (*Figure 1.5*; Houghton et al. 1995; Eastwood et al. 2013; Chambefort et al. 2014; Milicich et al. 2020). From the Taupō Volcano, this includes the massive 530 km^3 magma Oruanui eruption at 25.5 ka and 28 individual eruptions since, including the 232 CE Taupō eruption (35 km^3 magma) ─ the most recent explosive event at Taupō and one of the most powerful explosive eruptions globally for the past 7000 years (Self 1983; Wilson & Walker 1985; Wilson 1993, 2001; Hogg et al. 2012, 2019; Vandergoes et al. 2013). It is the latter event that is considered in detail in this thesis.

Pre-Taupō 232 ± 10 CE eruption stratigraphy lithologies

As mentioned in *Section 1.2.1*, understanding the stratigraphy at a volcano can have implications for interpreting the temporal evolution and dynamical controls of a volcanic conduit during an eruption. Here I discuss the stratigraphy at Taupō volcano with implications for the characterisation of lithic lithologies addressed throughout this study.

Banded and spherulitic rhyolite and obsidian lavas or domes represent extrusions associated with eruptions at Taupō with compositions indistinguishable from the pyroclastic deposits documented in the area from activity over the past 12 ka. (Chernet 1987; Cole et al. 1998; Sutton et al. 2000; Barker et al. 2015). One group of andesites in the area was likely transported as alluvium or lahars into Lake Taupō basin, evident through similar geochemical fingerprints to andesites that originate in the Tongariro Volcanic Centre. Dacites and other geochemically distinct andesites likely formed during eruptions in the central TVZ (Chernet 1987; Cole et al. 1998). Pumices below the Taupō 232 ± 10 CE deposit are likely derived from the >200 m thick, 25.4 ka Oruanui deposit and the succeeding eruption suite (units Ψ, Ω, A – X from Wilson 1993; Cole et al. 1998). Post-Oruanui (inclusive) stratigraphy is here estimated to be situated at depths ranging from 0 – 400 m below the surface, based predominantly on thickness estimates of the Oruanui deposit,

although the thickness estimates are from outside the Oruanui caldera, and succeeding eruption suite (Wilson 1993; Bibby et al. 1995; Cattell et al. 2016; Rosenberg et al. 2020).

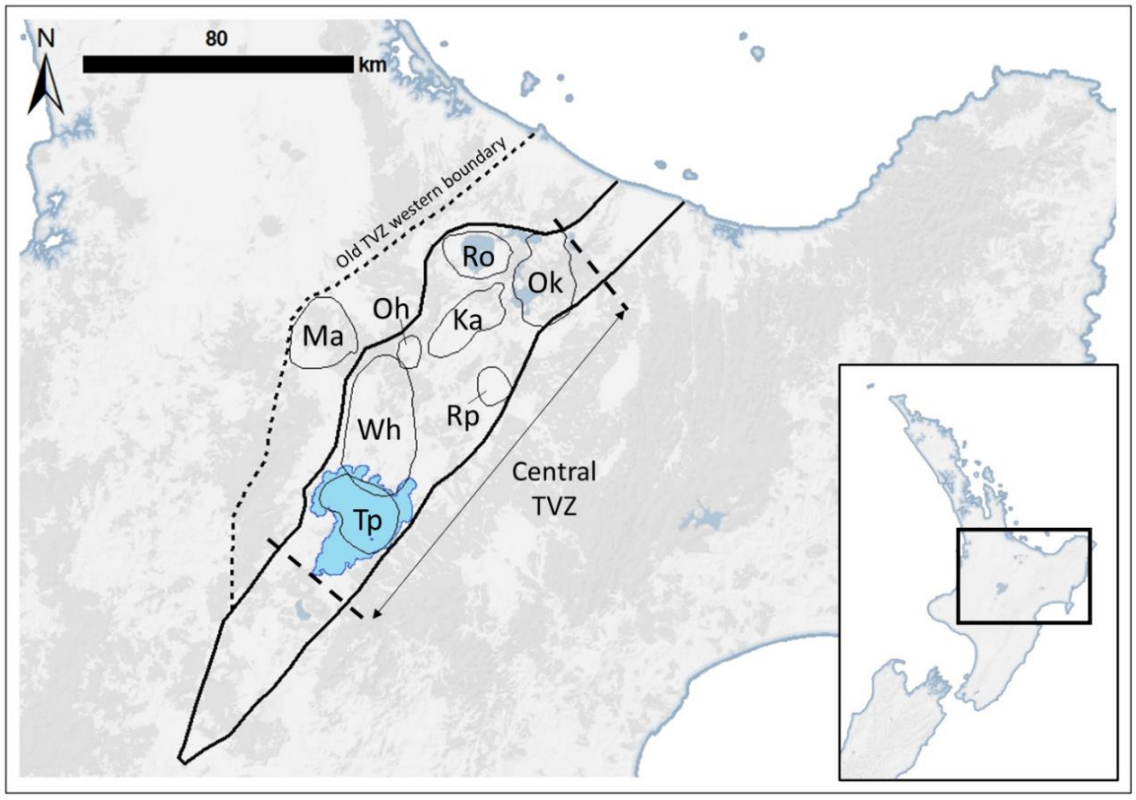

Figure 1.5 The young Taupō Volcanic Zone (TVZ), outlined in a solid black line, with the major calderas identified within the central TVZ. Ro: Rotorua; Ok: Okataina; Ka: Kapenga; Rp: Reporoa; Oh: Ohakuri; Wh: Whakamaru; Tp: Taupō; and Ma: Mangakino (located within the old TVZ western boundary). Inset shows the location within the North Island, New Zealand. Modified from Wilson et al. (1995) and Gravley et al. (2007).

The Huka Group includes all deposits above the 350 ka Whakamaru Group ignimbrites and below the 25.4 ka Oruanui eruption deposit (Cattell et al. 2016; Rosenberg et al. 2009, 2020). It is comprised of the lower, 400 – 1200 m thick Wairoa Formation and the upper, 150 – 300 m thick Huka Falls Formation. Predominantly, the Wairoa Formation includes thickly bedded, unwelded and welded ignimbrites, and reworked volcaniclastic and lacustrine sediments. The Huka Falls Formation is dominated by massive to thinly bedded siltstone, sandstone, and lapilli tuff (Cattell et al. 2016). Overall, the Huka Group is comprised of the following dominant facies:

- Moderately consolidated, massive to thinly bedded, brown silt and fine sand, sometimes mixed or interbedded with lithologically variable sand and pebbles;
- Fine to medium pumice and lithic lapilli volcaniclastic tuffs ranging from grey-white, fine tuff to coarse sand, with no significant clast content, to grey-white and green, fine to coarse sand with matrix supported, angular, medium lapilli-sized pumice and lithic clasts;
- White, grey, green and brown breccias with self-supported, poorly sorted, angular clasts up to cobble size and of either single or mixed lithologies;
- Massive, fractured to intact, coherent hypocrystalline lavas, often flow banded with strong alteration of contact zones (Cattell et al. 2016).

The Whakamaru Group ignimbrites are estimated to be ~1000 m thick based on drillhole data in the Wairakei area (Rosenberg et al. 2020). They are comprised of several units of crystal rich, typically grey or green (hydrothermally altered), welded ignimbrite (Wilson et al. 1986; Chernet .1987; Rosenberg et al. 2020).

Here I estimate the pre-Oruanui sediments and volcaniclastic facies to be between ~400 – 3000 m below surface. This estimate is based on maximum stratigraphic thickness estimates of the Huka Group and Whakamaru Group, combined (Chernet 1987; Cattell et al. 2016; Rosenburg et al. 2020).

Plutonic microdiorites and granitoids are rare accessory lithics within recent Taupō pyroclastic deposits. These clasts are defined by their microcrystalline, equigranular nature and are not considered primary (co-magmatic) xenoliths from the existing magma chamber (Chernet 1987). Fine grained granitoids are considered to be crystallized portions of silicic magma chambers from earlier activity (Chernet 1987; Brown et al. 1998), while the microdiorites are interpreted to be intrusive equivalents of high alumina basalts (Brown et al. 1998). Here I estimate depths of >4000 m below surface for the origin of plutonic intrusive rocks as crystallised magma must be present below the volcaniclastic and sedimentary facies previously mentioned (~400 – 3000 m), yet above the likely depth of the existing magma chamber below the Taupō Caldera Complex (~5 km; Chernet 1987; Brown et al. 1998; Cole et al. 1998; Rosenburg et al. 2020; Barker et al. 2021). Comparisons may also be drawn with the Ngatamariki intrusive complex, which are plutonic rocks encountered

by geothermal well drilling in the Ngatamariki area, NE of Lake Taupō, at >2500 m below surface (Chambefort et al. 2014).

1.2.3 The Taupō 232 ± 10 CE eruption

The 232 ± 10 CE eruption of the Taupō Volcanic Centre (Taupō eruption within this section) was a large-scale multiphase event that produced three phreatomagmatic ash deposits, two plinian fall deposits (one coevally with minor ignimbrite) and an extremely widespread ignimbrite (*Table 1.1*) (Baumgart 1954; Baumgart and Healy 1956; Healy 1964; Walker 1980, 1981a, b; Walker et al. 1980a, b, 1981; Froggatt 1981; Froggatt et al. 1981; Wilson 1985, 1993; Wilson & Walker 1985; Talbot et al. 1994; Smith & Houghton 1995a, b; Houghton et al. 2010, 2014; Hogg et al. 2012, 2019; Mitchell et al. 2018; Nisbet 2019; Walters 2020; Lowe & Pittari 2021). The Taupo eruption was considered by Wilson & Walker (1985) to comprise seven parts, but the last of these (emplacement of the floated giant pumices from growth of domes beneath the re-forming lake) is now separated out on the basis of an inferred time break. Wilson (1993) thus labelled the main explosive part of the eruption as eruption Y and the dome extrusion as eruption Z (*Table 1.1*), with an inferred time gap of years to about a decade (see also Barker et al. 2016).

The base of the eruptive products consists of a uniformly fine grained, pumiceous ash with a maximum observed thickness of ~65 cm (Wilson & Walker 1985; Nisbet 2019), denoted as unit Y1 (*Table 1.1*; *Figure 1.6*). The eruptive volume of the layer is ~0.015 km^3 and it resulted from a minor phreatomagmatic event that produced a column of no more than ~10 km high and a visible dispersal of ~20 – 25 km from the vent (Wilson & Walker 1985).

Following the phase Y1 activity, activity shifted abruptly to a dry phase, erupting the 6 km^3 Hatepe Plinian pumice fall deposit denoted unit Y2 (*Table 1.1*; *Figure 1.6*; Walker 1981a). This layer in the study area is composed predominantly of coarse pumice and is generally free of fine ash, with the exception of some ash beds interpreted to be the products of rain flushing and low-density, low energy PDCs (Walker 1981a; Wilson & Walker 1985; Talbot et al 1994; Walters 2020). Y2 exceeds ~2 m thickness proximal to Lake Taupo and has been identified as far as the east coast of New Zealand (Walker 1981a; Wilson & Walker 1985).

Succeeding unit Y2 is the 2.5 km^3 Hatepe phreatoplinian ash (unit Y3; *Table 1.1*; *Figure 1.6*), which is a pale grey or commonly denoted "putty colour" (Healy 1964; Self & Sparks

1978; Walker 1981b). This fine ash-dominated, poorly sorted unit displays poorly developed decimetre-scale bedding, exhibits thicknesses of >2 m proximal to Lake Taupo and is identified as far as the east coast of the North Island (Walker 1981b; Wilson & Walker 1985; Smith 1998). The eruption and deposition of unit Y3 was controlled by the presence of large-quantities of external water (i.e., proto-Lake Taupō) that increased fragmentation efficiency and resulted in both premature fall out of finer grained material and generation of dilute, proximal PDCs (Smith 1998).

Figure 1.6. Exposure of the Taupō eruption deposits, showing layers Y2 through to Y6, located at UTM 60S 430455E 5710938N. Basal layer Y1 is also present at this deposit; however, it is buried by debris in this image. Author for scale (168 cm tall); photograph by H. Walters.

A possible time break in the eruption was proposed to follow phase Y3, represented by a distinctive erosional gullying surface likely caused by running water prior to deposition of

the succeeding unit Y4 (Walker 1981b; Smith 1998). This time break, however, was short (or possibly negligible) as conformable drapes of units Y3 and Y4 on branch moulds show that unit Y3 was not disturbed in many areas prior to deposition of unit Y4 (Walker 1981b, figure 7). The phreatoplinian Rotongaio ash (unit Y4; *Table 1.1*; *Figure 1.6*) was deposited through numerous distinguishable eruptive spasms, as predominantly very fine grained ash, rich in dense pumiceous and non-vesicular obsidian fragments. Originally interpreted to have been deposited as a "wet, cohesive mud" (Walker 1981b; Wilson & Walker 1985), producing a dark grey unit with a very high portion of sub-millimetric material and fine parallel bedding structures, the unit was revised to have occurred as a sequence of fall material and low-energy PDCs (Smith 1998). Unit Y4 in total has a volume of 0.8 km^3, estimated from isopach data of the subunits A-G identified by Smith (1998).

The succeeding Taupō Plinian deposit (unit Y5) is one of the most widely dispersed (*Table 1.1*; *Figure 1.6*; Walker 1980; Wilson & Walker 1985) and well preserved large plinian fall deposits in the world. It is, in most cases, used as a textbook example for Plinian eruptions throughout modern literature and is a major focus of this thesis. Unit Y5 phase is identified in sediment cores taken 90 km offshore in both Hawkes Bay and Bay of Plenty (Froggatt et al. 1981) and extending 220 km downwind on land (Healy 1964). However, its total volume, and therefore eruptive parameters, such as dispersive power and mass eruption rate (Houghton et al. 2014), are still contested. Original studies conducted by Walker (1980) calculated a bulk volume of 24 km^3 based on the aeolian concentration of crystals, given that the large quantities of free crystals found in the deposit on land implied that large quantities of fine vitric ash erupted were blown out to sea. The common isopach volume method (Pyle 1989) is relatively unreliable for use on the Y5 deposit due to the intense erosion caused by the succeeding pyroclastic flow, effecting measured thicknesses (Walker 1980). Walker estimated that material finer than 250 μm made up ~80 % of the total mass of the deposit, most of which has been lost at sea (Wilson & Walker 1985). Given the coarseness of the deposit, this was used to estimate an eruptive column of ~50 km in height, requiring a steady state eruption at ~10^6 m^3 s^{-1} of magma (Walker 1980; Wilson & Walker 1987). This method, however, treats the Y5 unit as a single eruptive unit and does not take into account the layering of coarse and fine material identified by Walker (1980) and, more recently, Houghton et al. (2014).

Following a re-examination of Y5, Houghton et al. (2014) subdivided the unit into 26 internal stratigraphical layers. The subunits were qualitatively characterised by shifts in one or more deposit parameters, such as variations in grain size, changes in pumice morphology or foreign lithic abundance (Houghton et al. 2014). The resulting data were used to suggest that the total fall deposit isopachs defined by Walker (1980) had in fact been exaggerated by a shift in wind direction resulting in a variably layered deposit. This inference then effects estimates of eruptive parameters, for example, ultimately lowering the estimated plume height to ~35 – 40 km (Houghton et al. 2014).

Within a region encompassing approximately 15 km from the vent, the Y5 fall deposit is interbedded with ignimbrite flow units, named the Early Flow Units (EFUs; *Table 1.1*), which are rich in fine material (<10 μm at 2.6 – 6.5 wt.%: Wilson 1981; Wilson & Walker 1985). The most proximal of these units are massive, up to ~10 metres thick, and are pink to orange-brown in colour, suggesting thermal oxidation (Wilson 1981; Wilson & Walker 1985). The proximal EFU were interpreted to have been emplaced by highly concentrated, low energy flows coeval with the unit Y5 fall deposit, generated by the diversion of material directly from a basin-like vent (cf. gargle dynamics, *Section 1.2.1*; Wilson 1981; Wilson & Walker 1985). In more distal regions, the EFU are massive to moderately stratified, decimetres to metres thick, and white to grey in colour (Wilson 1981; Wilson & Walker 1985). The distal EFU were interpreted as high energy, low concentration flows that have been generated by discrete column collapse events correlating with extreme increases in discharge rates (Wilson 1981; Wilson & Walker 1985). Up to twelve units totalling >40 m thick were recognised proximal to the vent, and three thin units at distal locations, all separated by several coarse air-fall layers.

Drastic changes in the eruption conditions then resulted in the blast-like emplacement of the Taupo ignimbrite (Y6; *Table 1.1*: Wilson 1981; Wilson 1985; Wilson & Walker 1985), during which a highly energetic PDC travelled to ~80 ± 10 km from vent and eroded significant portions of the underlying deposits (in particular, the unit Y5 fall layer). This event is inferred to have been caused by either an intense increase in discharge rate, which would limit the capabilities of forming a stable Plinian plume, or the widening of the vent due to erosion leading to a blast event or triggered by the onset of caldera collapse (Wilson 1981; Wilson 1985; Wilson & Walker 1985).

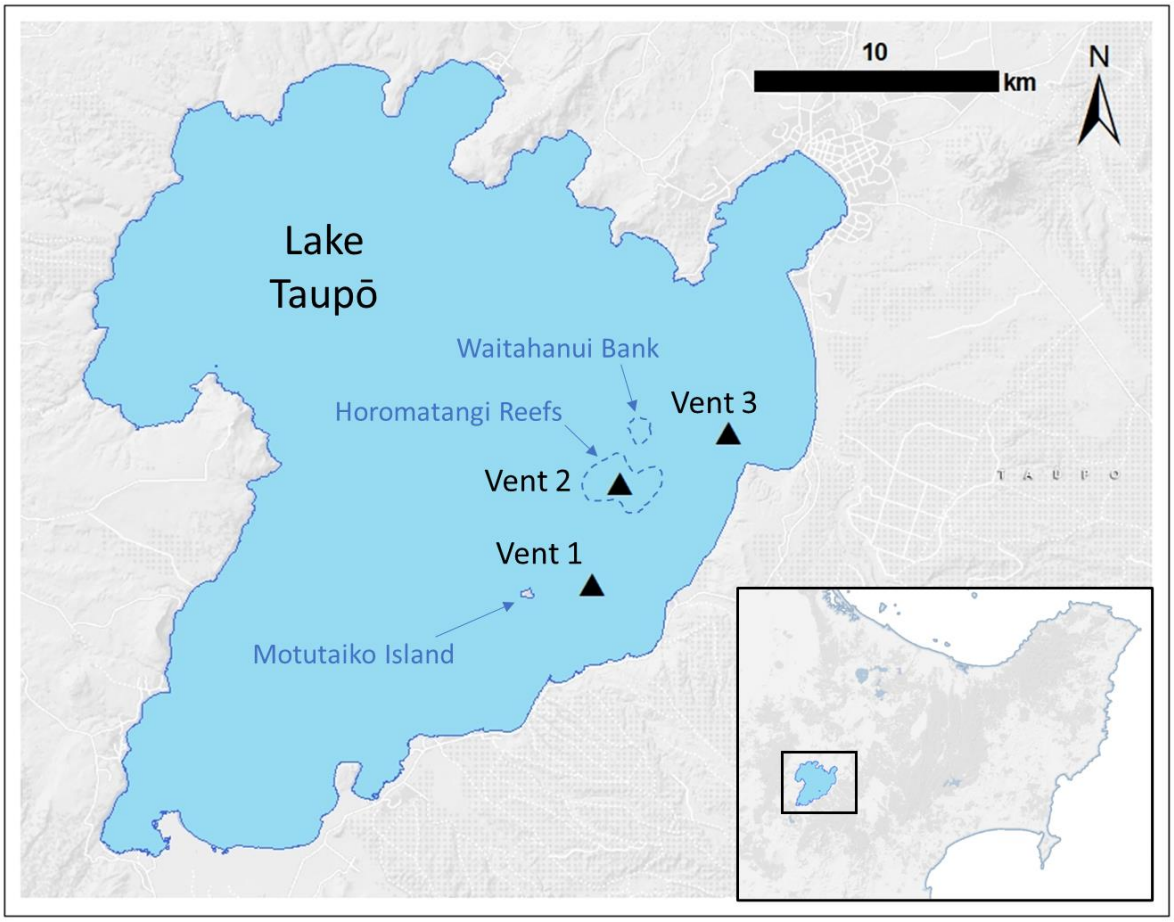

Figure 1.7 The location of the three vents described for the various eruptive phases of the Taupō 232 ± 10 CE eruption. Vent 2 is the original location for the single source model at the (younger) Horomatangi Reefs (Walker 1980). Vent 1 is the currently accepted vent site for the Y1 and Y3 phases of the eruption, while Vent 3 is accepted to have produced Y4. Vents 1 and 2 are the debated vent loci for Y2 and Y5, where Y2 was revised to originate from Vent 1 by Smith & Houghton (1995) and Y5 revised to Vent 1 by Houghton et al. (2014). Waitahanui Bank, produced by eruption Z, is noted, as is Motutaiko Island.

Walker (1980) proposed a single-source model for the Taupō eruption sequence, with the vent located at the (younger) Horomatangi Reefs (Wilson & Walker 1985) within Lake Taupō. Currently, however, a multiple source model is an accepted contributor to the contrasting eruptive styles in the various phases of the Taupō 232 ± 10 CE eruption (Smith & Houghton 1995a; Houghton et al. 2010) where the vents occur along a NNE-SSW lineation passing in proximity to the Horomatangi Reefs, which are interpreted to post-date the 232 ± 10 CE event (Wilson 1993). Detailed isopach and isopleth mapping by Walker (1981b) placed the Y2 (*Table 1.1*) vent also in proximity to the (younger) Horomatangi Reefs, also thought to be coincident with the vent location of the Y5 phase (*Figure 1.7*; Walker 1980). Smith & Houghton (1995) and Smith (1998) later revised this vent location

to once comparable with that for the Y1 and Y3 phases based on the assumption that the vesiculated magma of these phases was like that of the Y2 phase deposits and therefore discharged from a similar source, in sharp contrast to the poorly vesiculated ejecta of unit Y4. Detailed mapping of the Y3 and Y4 deposits (Smith & Houghton 1995a; Smith 1998) however, confidently places these vents at locations SW and NE of the Horomatangi Reefs, respectively (*Figure 1.7*). Houghton et al. (2014) recently proposed a new vent location for the Y5 phase ~6 km SW of the originally proposed vent, at a position comparable to that of the Y3 vent. This inference was based on observed internal variations of grain size within the vertical stratigraphy of the Y5 deposit, where isopach measurements (although the data were not presented in Houghton et al. 2014) based on qualitative correlations of sub-units resulted in deviations in dispersal directions from that originally determined by Walker (1980).

Table 1.1 Phases of the Taupō 232 ± 10 CE with their deposit types, summary of details regarding main eruption conditions and deposit features, and the relevant literature.

Phase	Deposit Type	Details	References
Eruption Z	Lava domes	Post-Y dome building event inferred to have produced the Horomatangi Reefs and Waitahanui Bank. Floated pumiceous rhyolite blocks evident on eastern edge of Lake Taupō. Volume 0.28 km^3.	Wilson & Walker 1985; Wilson 1993; Barker et al. 2016
Y6 (Taupō ignimbrite)	Ignimbrite	Drastic change in eruption conditions from Y5 (vent widening or increased discharge rate). Deposit extent of ~80 ± 10 km from vent. Eruptive volume of 30 km^3 of pumice and ash. Immensely destructive and eroded significant portions of underlying deposits.	Walker et al. 1980a; Froggatt 1981; Froggatt et al. 1981; Walker et al. 1981; Wilson 1981; Wilson 1985; Wilson & Walker 1985; Houghton *et al.* 2010
Y5 & EFU (Taupō Plinian and coeval Early Flow Units)	Ignimbrite	Intraplinian pyroclastic flow units identified within the proximal Y5 fall deposit. 15 km dispersal from vent. High proportion of fines (<10 µm at 2.6 – 6.5 mass%). Pink, red or orange brown colour and incipient welding suggests high temperature emplacement. 12 proximal units totalling >40 m thickness, 3 thin distal units. Separated by several coarse airfall layers.	Wilson 1981; Wilson & Walker 1985; Houghton et al. 2010
	Plinian	Definitively larger grain size than the Y2 at any given distance from vent. Poorly defined stratification of interbedded coarser-finer	Healy 1964; Walker 1980; Wilson & Walker 1985;

		layers results in two contrasting interpretations:		Houghton et al. 2010, 2014; Mitchell et al. 2018
		Singular dispersal axis: The deposit as a whole unit. Eruptive volume of 24 km^3. 80% of total mass is <250 µm, lost at sea. Column height exceeding 50 km and steady state eruption at ~10^6 m^3s^{-1} DRE.	Multiple dispersal axes: 26 internal stratigraphical subunits with separate dispersal axes. Affected by strong shifts in wind direction. Column heights between 31 – 37 km. Fine grained layers either from lower mass discharge or phreatomagmatic fragmentation: column heights ~25 km.	
Y4 (Rotongaio Ash)	Phreatomagmatic	Composed predominantly of dense pumice and obsidian ash that fell as a "wet, cohesive mud". Dark grey in colour with a high proportion of sub-mm material and fine bedding structures. Minor PDCs and reworking is noted. Eruptive volume of 1.3 km^3.		Healy 1964; Froggatt 1981; Walker 1981b; Wilson & Walker 1985; Smith & Houghton 1995a, b; Houghton et al. 2010
Y3 (Hatepe Ash)	Phreatomagmatic	Pale grey, "putty-coloured" fine ash with poorly developed bedding and max. observed thickness of 200 cm. Eruptive volume of 2.5 km^3.		Healy 1964; Froggatt 1981; Wilson & Walker 1985; Smith & Houghton 1995a, b; Houghton et al. 2010
Y2 (Hatepe Plinian)	Plinian	Relatively coarse pumice, free of fine ash except minor intraplinian rain flushed ash beds. Max. observed thickness of 200 cm. Eruptive volume of 6 km^3, eruption column est. 30 km high.		Healy 1964; Wilson & Walker 1985; Froggatt 1981; Walker 1981a, b; Wilson & Walker 1985; Talbot et al. 1994; Houghton et al. 2010; Mitchell et al. 2018; Walters 2020
Y1 (Initial Ash)	Phreatomagmatic	Generally fine grained, pumiceous ash with max. observed thickness of 65 cm. Eruptive volume of 0.015 km^3, eruption column ≤10 km high and 20 – 25 km deposit extent from vent.		Wilson & Walker 1985; Nisbet 2019

Critical review of aspects of the 232 ± 10 CE eruption

Although the Taupō 232 ± 10 CE eruption is extensively studied (*Table 1.1* and references therein), there are several discrepancies that should be noted regarding the interpretation of various elements of the eruption. These discrepancies are part of what this thesis is aimed at addressing and are as follows.

1. The vent location for the Y2 phase of the eruption, as shown by Smith & Houghton (1995a), is comparable to that identified for the Y1 and Y3 phreatomagmatic phases (*Figure 1.7*). This interpretation was solely based on the assumption that the Y2 material was discharged from the same vent as Y1 and Y3 phases, in contrast to the gas-poor magma of the Y4 eruption. This view can be challenged by the detailed isopach and isopleth data gathered by Walker (1981a), which place the vent in proximity to the Horomatangi Reefs area and do not align with a vent site located as far SW as proposed by Smith & Houghton (1995a).

2. Previously, the pumice fall bed from the Y5 phase has been treated as a unitary deposit (Walker 1980) with only minor consideration for the coevally emplaced Early Flow Unit (EFU) ignimbrite and subtle coarse-fine fluctuations in the fall deposit. Wilson & Walker (1985) proposed that the thicker, proximal flows, with higher temperatures and lower emplacement velocities, were generated as material was diverted at the base of the eruption column. The distal, smaller volume, and high emplacement velocity units were interpreted to result from episodes of partial column collapse, which roughly correlated with distinct finer bands in the Y5 fall deposit (Wilson 1981; Wilson & Walker 1985). Studies regarding the Y5 plinian deposit have tended to neglect the relationship between the fall and EFUs (e.g., Walker 1980; Houghton et al. 2014) which potentially oversimplifies interpretations of the Y5 phase of the eruption and its fall deposit. Further detailed analysis of the properties of the EFUs and their stratigraphical relationship with the Y5 plinian fall deposit is therefore required as generation of the EFUs may play an important role in understanding the behaviour and consequent sedimentation dynamics of the coeval large-scale buoyant plume.

3. Although the Y5 phase is well studied (*Table 1.1* and references therein), there is a lack of detailed quantitative investigation into vertical variations in the deposit

characteristics. As previously mentioned, it has been treated primarily as a uniform deposit with only brief mention of observed internal variations in the vertical stratigraphy (Walker 1980; Wilson & Walker 1985). Observations made by Wilson & Walker (1985) roughly correlated the finer bands in the deposit with partial column collapse episodes related to the distal EFU, as mentioned above. A more detailed investigation into these internal variations has also remained relatively qualitative (Houghton et al. 2014), where field observations were used as the basis for complex correlations between subtly variable 'sub-units'. Issues arise here where isopleth measurements (not presented in that work) based on the qualitative correlations of sub-units have resulted in extraordinarily subtle differences in individual dispersal directions. In addition, when comparing the consequent calculations of column heights for each sub-unit (35–40 km) to that of the similarly sourced Waimihia eruption (42 km high column: Carey & Sigurdsson 1989), of note is that the Waimihia is observably finer grained than the Y5 deposit at any given distance from source along their respective dispersal axes. This situation is contradictory, as the more powerful of the two events would be assumed to display the coarser grain size when observed at similar distances from source. Therefore, it may be appropriate to seek another explanation for the internal vertical variation identified within the Y5 stratigraphy.

4. The Y5 vent location proposed by Houghton et al. (2014), based predominantly on the dispersal directions of the qualitative sub-units mentioned previously, has been inferred to occur in proximity to Motutaiko Island. This vent site is ~6 km SW of the originally proposed Horomatangi Reefs location proposed by Walker (1980) through whole deposit isopach and isopleth measurements. The new vent location is comparable to those of the Y1 and Y3 phases of the Taupō eruption and thus, in addition to the lack of supporting data in Houghton et al. (2014), several factors suggest that this vent location is not accurate. Motutaiko Island is a ~7000-year-old rhyolite dome (Wilson 1993), which lies at the margin of the caldera collapse area following the Taupō eruption (Davy & Caldwell 1998). In the case of the vent location proposed by Houghton et al. (2014), it seems unlikely that the rhyolite dome would remain following the plinian Y5 eruption and that an event of this magnitude would occur on the rim of the subsequent caldera. Additionally, the low-energy

proximal EFU ignimbrite, interpreted to have erupted from the same vent location as the Y5 fall deposit (Wilson 1981, Wilson & Walker 1985), is distributed about an area well north of the Houghton et al. (2014) proposed vent (Wilson & Walker 1985) and is more consistent with the original Walker (1980) vent site. Therefore, further quantitative investigation is required to verify the location of the Y5 eruption vent.

2 Methodology

2.1 Field work

The field strategy for this study was to identify, characterise, and sample exposures of Y5 fall, Early Flow Unit (EFU) and upper Y4 (henceforth Y4-G, based on Rn-G as defined by Smith 1998 and Smith & Houghton 1995a) deposits at proximal to medial distances from source (defined in *Chapters 3 – 5*). An extensive field campaign was conducted predominantly within the Kaingaroa Forest (Timberlands Ltd), Taupo Forest (New Zealand Forest Managers) and Wairakei Estate farm blocks. The Y5 fall deposit was identified at 45 sections: 12 exposures included distinct layers of Y4-G and the EFUs were identified in 9 outcrops, existing either as single or multiple flow-unit deposits. The deposits, produced by various volcanic processes, and their internal characteristics were distinguished based on identification in existing studies (e.g., Walker 1980; Wilson 1981; Wilson & Walker 1985; Smith & Houghton 1995a; Smith 1998), and their distinctive grain sizes, componentry, presence of flow textures and matrix, and other characteristic sedimentological markers like those described in *Table 1.1* (for more detail, see *Chapters 3 – 5*).

At 9 selected sections (labelled A to H; *Figure 2.1*; *Appendix A*), detailed notes were taken describing the sedimentological features, and individual units (in the case of various deposit types, e.g., fall and PDC) and/or separate bedform features (in the case of continuous variation of grain size or components) were defined for discrete sampling. Samples were collected for further physical analysis purposes, as described below. See *Appendix B* for a list of samples from each exposure. Note that coordinates of exposures discussed throughout this thesis are in the map projected Universal Transverse Mercator (UTM) system, modelled with the World Geodetic System WGS84 ellipsoid.

2.1.1 Sample collection

Bulk sampling of layers

For use in grain size analyses, component counting and density analyses, the nine exposures (*Figure 2.1*) were continuously box sampled according to individual deposit type layers and/or variations in bedform features. Samples were systematically taken from the top to base of the exposure to avoid collapse and contamination from above layers. Samples were

excavated carefully from each layer, with amount roughly determined by observed grain size. Larger samples were taken for coarser units, whereas smaller samples were required for finer units, to gain proper representation of the overall grain size distribution without making excessive work for the subsequent laboratory procedures.

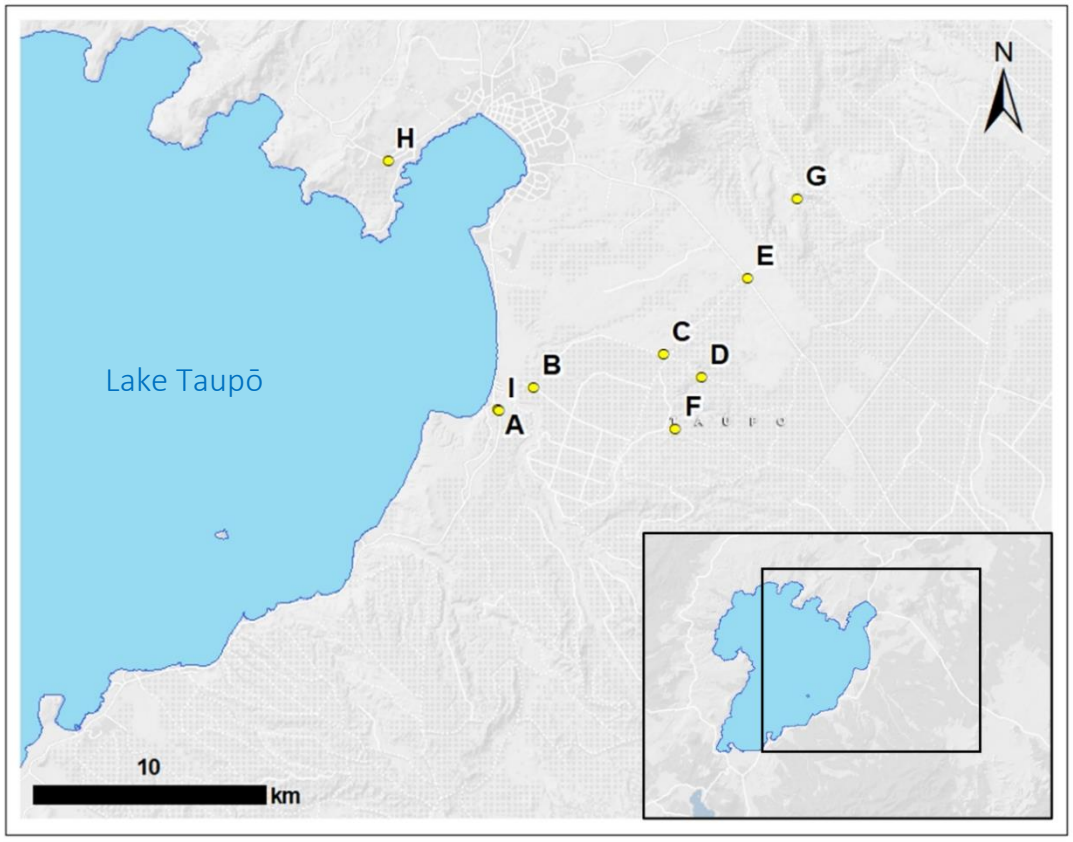

Figure 2.1 Map showing locations of exposures A – H investigated in this study (see Appendix A for coordinates list) in relation to Lake Taupō (inset). Note Exposures A and I are in close proximity to each other.

Clast bulk density sampling

At three exposures (D, G and H; *Figure 2.1*), for each defined layer where possible, 100 juvenile pumice clasts between 8 – 32 mm (cf. Houghton & Wilson 1989) were collected for use in clast bulk density analyses. Vesicle populations at this size are best preserved from the time of magma fragmentation and ensure minimal influence of post-fragmentation expansion while still allowing clasts to fit onto a subsequent thin section (Houghton & Wilson 1989; Shea et al. 2010). Basal, fine-grained units did not have adequate numbers of juvenile pumice within this size range and were therefore mostly disregarded; however,

where juvenile pumices within this size range were minimal, as many pumices were collected as possible to obtain an averaged comparative density value.

2.2 Analytical methods

2.2.1 Grain size analysis

Wet and dry sieving

Grain sizes in this study use the logarithmic phi scale originally defined by Krumbein (1934, 1938) as:

$$\phi = -log2d$$

where ϕ is the phi size of a particle and d is the diameter of the particle/sieve mesh in mm (Tanner 1969; Boggs 2006). Table 2.1 shows the classification for tephra size classes in their relation to both phi and metric size (White & Houghton 2006). In this thesis, grain size terminology uses the nomenclature of White and Houghton (2006), and descriptive terms (i.e., median, mode and sorting) follow those defined by Folk and Ward (1957).

Table 2.1 Classification of tephra size classes in relation to both phi and metric grain size. From White & Houghton (2006).

Grain size (ϕ)	Grain size (mm)	Tephra size class
>4	<0.0625	Extremely fine ash
3 – 4	0.0625 – 0.125	Very fine ash
2 – 3	0.125 – 0.25	Fine ash
1 – 2	0.25 – 0.5	Medium ash
0 – 1	0.5 – 1	Coarse ash
-1 – 0	1 – 2	Very coarse ash
-2 – -1	2 – 4	Fine lapilli
-4 – -2	4 – 16	Medium lapilli
-6 – -4	16 – 64	Coarse lapilli
< -6	>64	Block/ bomb

The exception here is the definition for total ash abundance. Total ash is defined in this thesis as material <1 mm, based on the separation between high and low Stokes number particles. The Stokes number demonstrates that, due to particle inertia, the size and concentration of

pyroclasts determines the momentum exchange and mass transfer properties of entrainment eddies in eruption columns (Crowe et al. 1995; Burgisser et al. 2005; Jessop & Jellinek 2014; Lherm & Jellinek 2019). The purpose of this deviation is for ease of potential numerical modelling following this research.

Manual sieving of material (coarser than 2 ϕ)

Samples collected at all sites were prepared for grain size analysis based on the observed grain size properties in the field. Predominantly coarse-grained samples with approximately <20 % observed ash proportion were dried at ~45 ºC and gently hand sieved at 1 ϕ intervals for sizes larger than and including 2 ϕ. The hand sieving cut off at 2 ϕ is to avoid pumice breakage and generation of fines due to abrasion and material finer than 2 ϕ was set aside for laser particle analysis. Careful dry sieving was preferred for these samples over wet sieving as the fine ash was not observed to coat larger pumices or be packed within vesicles, and reduced the time spent on sample processing. Samples with approximately >20 % observed fine ash were not dried and were processed initially by wet sieving. Material finer than 2 ϕ was washed with deionized water through a sieve, with fines smaller than 2 ϕ set aside for laser particle analysis. The material coarser than 2 ϕ was then dried at ~45 ºC and subsequently dry sieved as per previous. Wet sieving was chosen for these samples to minimize both the higher proportion of low-density fines becoming airborne and being lost from the sample, and the manual generation of fines due to abrasion. Separated grain sizes were weighed and normalised to the overall weighted percent of the sample.

Laser particle analysis (finer than 2ϕ)

Material finer than 2 ϕ was analysed using the Horiba Partica LA 950V2 Laser Scattering Particle Size Distribution Analyser (LPA) in the School of Agriculture and Environment. This instrument measures the particle range at 0.25 ϕ intervals from 2 – 10 ϕ using two light-source wavelengths: 1) long wavelength for coarse particles (>0.01 µm) and 2) short wavelength for fine particles (<0.01 µm). The analysis was conducted using a measuring routine based on the Fraunhofer approximation, thereby removing the requirement of a refractive index for the light-source wavelengths and discarding data for particles smaller than 2 µm (i.e., clay grade). Prior to LPA measurements, the samples were dried at ~45 ºC and split using a riffle splitter to give a representative aliquot of ~10–20 g. Each measurement was conducted a minimum of three times to obtain a representative average of grain size values for the finer than 2 ϕ portion of each distribution.

Once completed, the data gathered from the combined sieving and LPA measurements of each sample were processed and compiled using the open-source particle analysis software GRADISTAT (Blott & Pye 2001). This calculated various statistical grain size parameters, for example, mean (μ), median (Md), and sorting (σ) values arithmetically (μm), geometrically (μm) and logarithmically (ϕ) per sample (e.g., Krumbein 1938; Inman 1952; Folk & Ward 1957). Here, the methods of Folk & Ward (1957) are used for all grain size parameter calculations. Detailed results are found in *Appendix C*.

2.2.2 Componentry analysis

All deposits were characterised by pyroclast assemblage alongside grain size distribution, with a focus on the textural characteristics of juvenile pumice and glass, the distinct lithologies of foreign lithic clasts, and crystal concentrations. The ratios of these three components are strongly influenced by fragmentation mechanisms and eruption characteristics. Here, terminologies are defined as follows:

- *Juvenile*: Material produced by fragmentation of the original magma during the Y5 eruption, i.e., pumice, obsidian, crystals;
- *Lithic*: Clasts of foreign origin excavated from the conduit walls during fragmentation, or from the surface at the onset of eruption; i.e., wall rock, older pumice, obsidian and crystals;
- *Composite pumice*: Clasts of welded Early Flow Unit material which have various pumices amalgamated within a distinct, pink-orange, oxidised pumicious matrix, also often including fragments of lithic material;
- *Obsidian:* In this study, obsidian is volcanic glass produced from rapid cooling of the juvenile Y5 magma, foreign obsidians are classified within the lithic components;
- *Crystals*: Juvenile crystals of predominantly plagioclase, pyroxene and titanomagnetite, foreign crystals are classified within the lithic components.

Point counting

Point counting was conducted on samples from exposures A – H. Exposure D was selected, based on its central location in the thickest isopach (Walker 1980) and strong preservation

of thickness and deposit features, to be a reference exposure for the Y5 fall deposit and all grain size classes 2 ϕ and larger from each sampled layer were analysed. This was to investigate both variations of component ratios with grain size, and to gain an overall weight percentage of components for each layer in the deposit (discussed further below). For correlation purposes, the seven other exposures were selected for point counting of the 1 ϕ fraction from all sampled layers. This grain size was considered representative for further analysis as it is present in all deposit types (including airfall and PDC), is large enough to permit identification of foreign lithologies and juvenile clast textures, and contains all components as described below.

To gain appropriate representation, a minimum of 300 clasts were split from grain size classes, using a riffle splitter where necessary (logarithmic grain size scale results in lower clast numbers as grain size increases). Component classes identified were 1) juvenile pumice, subdivided into three groups based on observed vesicularity and degree of shearing (J1 microvesicular, J2 macrovesicular, and J3 sheared); 2) juvenile obsidian (G); 3) lithics, subdivided into 3 groups based on lithologies that infer the depth of origin within the crust (F1 shallow, F2 intermediate, and F3 deep); 4) composite pumices with minor lithic inclusions (CP); and 5) free crystals identified based on colour, transparency and habits (C). Component classes are discussed in relevant further detail in *Chapters 3 – 5*.

Individual component classes were normalized to the total number of clasts counted within each grain size class and number percentages were calculated for comparisons between sampled layers. Detailed results are found in *Appendices D and E*.

Weight percent

The weights of all component classes in each full phi grain size class from 2 ϕ and larger for Exposure D were obtained. Each of these measurements were then normalized to each associated grain size class, and then subsequently normalized to the associated layer inclusive of all grain sizes. This was done to obtain a time-variant mass distribution estimation of components within the conduit during the eruption.

2.2.3 Density analysis

Two density analysis methods were used in this study to gain a proper representation of pumice type densities. Where possible, clast selection followed methods outlined in

Houghton & Wilson (1989) by which a minimum of 100 clasts between 8 – 32 mm in size are analysed. For all analyses, clasts were cleaned using an ultrasonic bath in batches until the water was clear and fine ash was removed from the pumice vesicles. Clasts were subsequently dried at ~45 ºC for >24 hours and then weighed. Here, terminologies are defined as follows:

- *Envelope/ bulk density*: The density of a clast when vesicle spaces are included in the volume measurement;
- *Skeletal density*: The ratio of the melt to the sum of the volumes of melt and isolated vesicles within the clast;
- *Solid density*: The density of the crushed pumice;
- *Isolated porosity*: The ratio of vesicles not connected to the vesicle network to the volume of melt;
- *Connected porosity*: The ratio of vesicles connected to the vesicle network to the volume of melt;
- *Total porosity*: The ratio of vesicles to the volume of melt.

Pycnometry

Envelope density was measured on at least 100 pumices between 4–8 mm sieve sizes from each component class (J1, J2, and J3) using a Micrometrics GeoPyc pycnometer (see *Appendix F*), which automatically measured the volume and density of a clast by displacement of the solid medium DryFlo. It has a high degree of flow ability and is able to closely pack around the surface of a clast without invading vesicle space. An initial blank reading was conducted where the DryFlo medium is compacted within the GeoPyc cylinder, and a zero-volume baseline was established prior to each individual clast. Subsequently, clasts were then placed in the cylinder and the DryFlo is compacted inclusive of the clast. The displacement volume was then calculated using the formula for the volume of a cylinder of height (h):

$$V = \pi r^2 h$$

where r is the cylinder radius and $h = h_0 - h_t$ ($h_0$is the distance penetrated during zero-volume baseline and h_t is the distance penetrated with the sample). Archimedes' Principle was applied to calculate the volume and density of each clast. Runs were repeated a minimum of three times for statistical reliability.

From the bulk density distributions, clasts were selected from the mean, 10th and 90th percentile bins for each pumice type. These were then further analysed using a helium pycnometer to obtain skeletal density, porosity, and solid density of each clast. The helium pycnometer uses the volume-pressure relationship of Boyle's Law to measure volume by inert gas displacement. The clast was placed into a sealed cup of known volume, which in turn was put into a sample chamber. Helium gas was then admitted into the sample chamber and a reference chamber of known volume, and the skeletal volume was then calculated from the differential pressure. Density was then calculated by dividing the sample weight by the measured volume. A minimum of three runs for each clast were completed to gain a statistically representative average density. A blank calibration was completed at the beginning of the session using a non-porous sphere of known volume.

To completely quantify the porosity of the clasts, the solid volume and density of each clast needed to be calculated. Following measurements of skeletal density, clasts were crushed using an agate mortar and pestle into a fine powder and dried at ~45 ºC. The volume of powder was then measured, and density calculated, using the methods described previously for skeletal density.

The total (φ_{bulk}), connected (φ_{conn}) and isolated (φ_{isol}) porosities were then determined (see *Appendix G*) using the bulk volume (V_{bulk}), skeletal volume (V_{skel}) and solid density (δ_{sol}), following calculations from Klug & Cashman (1996), Klug *et al*. (2002) and Wright *et al*. (2009):

$$\varphi_{bulk} = \left(1 - \left(\frac{V_{bulk}}{\delta_{sol}}\right)\right) \times 100$$

$$\varphi_{conn} = \frac{V_{bulk} - V_{skel}}{V_{bulk}}$$

$$\varphi_{iso} = \varphi_{bulk} - \varphi_{conn}$$

Archimedes' Principle for clast bulk density and vesicularity

Clast bulk density and vesicularity measurements were obtained using methods outlined in Houghton & Wilson (1989) and Shea et al. (2010). A total of 100 clasts, where possible, were collected for the three pumice types (J1, J2, J3; *Appendix H*) and for each appropriate density suite (Exposures D, G, and H, described further in *Chapters 4 and 5*; *Appendix I*), cleaned of fine ash using an ultrasonic bath and dried at ~45 ºC in preparation for weighing of individual clasts in both air and water.

Based on the Archimedes' Principle, the buoyant force exerted on a clast submerged in water is equal to the weight of the water displaced by that clast. In laboratory conditions (1 atm pressure and water at 4 ºC), 1 ml of water is ~1 g, hence the clast volume can be calculated and therefore, in conjunction with the weight of the clast in air, the density of the clast can be determined.

Density is calculated by dividing the mass of a clast by its volume, as follows:

$$\rho = m/v$$

where, ρ is the density ($g\ cm^{-3}$), m is the mass (g), and v is the volume (ml).

Individual clast densities were obtained by weighing the clast in air to ±0.01 g. The clasts were each then sprayed with *Selleys Watershield Water Repellent* and left to dry for 24 hours according to product instructions to render a waterproof barrier, sealing vesicles in the clasts. It was considered unnecessary to reweigh the clasts following this procedure as the spray resulted in inconsequential weight change (±0.001 g). Clasts were then weighed in water. If the clast floated, it was weighed down with a small ballast weight, the submerged weight of which was also recorded and subtracted from the measured weight.

The specific gravity of each clast was calculated using the following equation:

$$SG_c = w_a w_a - [w_w - w_b]$$

where, SG_c is the specific gravity of the clast, w_a is the weight of the clast in air (g), w_w is the weight of the clast in water (g), and w_b is the weight of the ballast (g).

Using the SG_c, the density of each clast was calculated using the equation:

$$\rho_c = SG_c \rho_w$$

where, ρ_c is the density of the clast (g cm^{-3}) and ρ_w is the density of water (g cm^{-3}).

Density was then converted to bulk vesicularity using:

$$V = 100(\rho DRE - \rho_c)\ \rho DRE$$

where V is the vesicularity (%) and ρDRE is the dense rock equivalent value (g cm^{-3}).

The dense rock equivalent, or DRE, is based on a non-vesicular juvenile clast of tephra. For this study, 2.4 g cm^{-3} was used based on both results obtained using the GeoPyc and from densities given by Manville et al. (2009).

2.2.4 Thin sections and textural characterisation

Thin sections were made of J1, J2 and J3 pumice clasts within the mean, 10th and 90th percentile density bins as defined in *Section 2.2.3* for qualitative textural characterisation and comparison. Two clasts from each pumice type were selected from the mean density bins and thin sectioned in directions both parallel and perpendicular to the orientation of vesicle elongation. A single clast from each pumice type was selected from the 10th and 90th percentile density bins and thin sectioned parallel to the orientation of vesicle elongation. An additional thin section was made of a piece of composite pumice to qualitatively investigate the nature of the groundmass and textural variability in pumice fragments within the clast. The thin sections were then polished and carbon coated to obtain back scattered electron images using an FEI Quanta 200 Scanning Electron Microscope at the Manawatu Microscopy and Imaging Centre, Massey University.

3 The transition between the phreatoplinian Y4 and Plinian Y5 phases of the Taupō 232 CE eruption

3.1 Introduction

Investigations into pyroclastic deposit characteristics, such as variations in granulometry, componentry and clast density, have predominantly focused on the interpretation of eruptive styles (i.e., changes between phreatomagmatic, plinian and ignimbrite-forming activities) in sequences from single source events (e.g., Lirer et al. 1973; Sparks et al. 1981; Houghton & Wilson 1989; Carey & Sigurdsson 1989; Sigurdsson & Carey 1989; Scasso et al. 1994; Rosi et al. 1999, 2001; Polacci et al. 2001; Klug et al. 2002; Sulpizio et al. 2010). Fewer studies have explored the transitional dynamics between multiple sources during eruptive events (e.g., Sparks & Wilson 1990; Wilson & Hildreth 1997; Pfeiffer 2001; Houghton et al. 2010), and there is a need for detailed quantitative analyses of deposit characteristics across the transitions to further our understanding of complex, multi-vent eruptions. Original studies of the Taupō 232 ± 10 CE eruption considered a single source model for the sequence, with the vent located at the Horomatangi Reefs within Lake Taupō (Walker 1980; Wilson & Walker 1985). More recently, however, the varying phases (see *Table 1.1*) are considered to have occurred from multiple sources along a NE-SW alignment that passes through the later-formed Horomatangi Reefs (Wilson 1993; Smith & Houghton 1995a; Houghton et al. 2010). Successive units Y4 and Y5 of the Taupō 232 ± 10 CE eruption are individually well studied examples of phreatoplinian and plinian eruption deposits (Self & Sparks 1978; Walker 1980, 1981a; Wilson & Walker 1985; Smith & Houghton 1995a, b; Smith 1998; Houghton et al. 2010, 2014; Mitchell et al. 2018), respectively, but limited in-depth analysis has been conducted on the nature of transition between them (Smith 1998). Here I provide a detailed quantitative investigation into the physical properties of pyroclasts across the transition between these two deposits to understand the transitional vent behaviour and the mechanisms that influence changes in eruptive style during such large-scale events.

3.1.1 The Taupō 232 CE eruption: Y4 and Y5 phases

The Taupō 232 ± 10 CE eruption produced three phreatomagmatic ash-rich deposits, two plinian fall deposits one coevally with minor ignimbrite, and an extremely widespread ignimbrite (refer to *Chapter 1*, *Table 1.1*). Phase 4 (Y4) is a widely dispersed, very fine-grained unit composed of multiple beds resulting from numerous individual explosive events at source (Walker 1981b; Smith 1998). With focus on the final stage of the Y4 eruption phase (labelled Rn-G by Smith (1998), herein referred to as Y4-G), it was inferred that there was an increase in magma discharge rate, lowering the water:magma ratio and resulting in a short lived, drier 'plinian-style' period of activity where discrete pyroclasts were deposited from a high plume (Smith 1998). Prior to the Y4-G phase there was inferred to be near-continuous presence of water at the vent, resulting in intense fragmentation yielding very fine-grained material by steam explosivity while deposition, especially near-vent, was a combination of vent-derived density currents and fine particle aggregate fallout (Walker 1981b; Smith 1998).

Phase 5 (Y5) is the larger of the two Plinian phases, is one of the most widely dispersed plinian fall deposits documented (Walker 1980) and is well preserved in proximal to medial zones of the deposit. Its typically white, coarse lapilli pumice deposit sits distinctively atop the grey phreatoplinian Y4 deposit (see *Table 1.1*; *Figure 3.1*), indicating an abrupt change in eruptive style where discharge changed from gas-poor magma with fragmentation driven by magma-water interaction, to the very rapid discharge of actively vesiculating magma (Walker 1981b; Smith 1998). As noted by Smith (1998), the cause of this abrupt change remains unclear and detailed analysis of the basal Taupō Y5 plinian deposit is needed to reconstruct the spatiotemporal evolution of vents as well as changes in magma fragmentation conditions during the transition. Here I present a comprehensive analysis of the variation in pyroclast properties in proximal to medial stratigraphical profiles from the upper Y4 and lower Y5 deposits through granulometry, componentry and textural investigation to provide insights into this transition.

3.2 Data

3.2.1 Stratigraphy of the Y4–Y5 transition zone

To investigate the nature of the transition between units Y4 and Y5, five exposures were selected (*Figure 3.1*, exposures A – E) that span from proximal to medial zones semi-parallel to the depositional axis of the final stage of the Y4 eruption established by Smith & Houghton (1995a). These exposures also sit within the proximal to medial regions of the overall Y5 deposit dispersal (*Figure 3.1*; Walker 1980) where the azimuths of the Y4 and Y5 dispersal axes are comparable (cf. Houghton et al. 2014). In this study, I use the vent location for unit Y4 proposed by Smith & Houghton (1995). The Y5 source location is more controversial; however, this study agrees with the original vent location determined by Walker (1980; cf. Houghton et al. 2014). This decision is predominantly based on the relative deposit dispersal axis mapped by Walker (1980), which contradicts the dispersal axes of internal sub-units established by Houghton et al. (2014) through isopach measurements based on qualitative correlations. In addition, the Houghton et al. (2014) vent location (*Figure 3.1*) is in proximity to the older Motutaiko Island (Wilson 1993), the existence of which is questionable as it would be expected to be destroyed during such a powerful event. Further evidence and reasoning for using the Walker (1980) vent location for this study is discussed in *Section 3.3.3*.

The transition zone was identified based on the sharp contact between the pumice lapilli-bearing, obsidian-rich, 'plinian-like' Y4-G layer (Smith & Houghton 1995a), and the succeeding fine-ash bearing, yellow-brown, foreign lithic- (henceforth lithic-) rich bed that signifies the onset of the Y5 eruption phase (Smith 1998; Houghton et al. 2014). The deposits were continuously box sampled from the base of unit Y4-G to the lower portion of unit Y5, which incorporates both Y5 airfall pumice or Early Flow Unit (EFU) pyroclastic density current (PDC) facies varying at each exposure. Sample thicknesses varied based on either sharp or subtle vertical changes in deposit type (e.g., PDC or fall), grain size and/or abundances of wall rock lithics. Each of the five exposures contain unit Y4-G, the basal ash-rich unit of unit Y5 (herein Y5-Base) and the succeeding airfall, as outlined below (*Figure 3.1*).

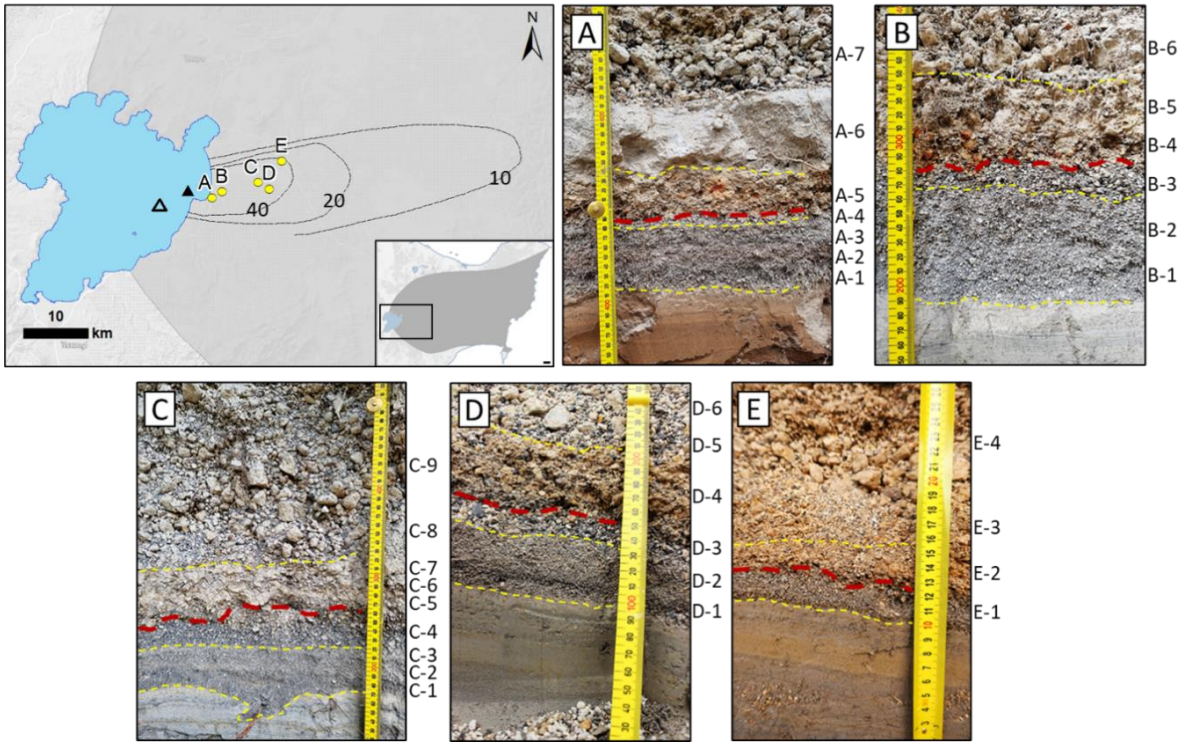

Figure 3.1 Map and field photos of locations A – E marked by yellow dots within the Smith (1998) Y4-G isopachs (in mm). Grey area in main map and inset defines the Y5 deposit extent (Walker 1980). The Y4 vent is indicated with a black triangle, the Walker (1980) Y5 vent with an open triangle. Scale bar is 10 km. Red dotted line in the field photos indicates the boundary between the Y4 & Y5 deposits. Y4-G sits between the lower yellow dotted line and the boundary. The onset of Y5 is outlined by the boundary and upper yellow dotted line. Above is Y5 airfall and a PDC at exposure A. Box samples collected are identified on the left of each image.

A) The most proximal location, Exposure A, has a ~90 mm thick section of Y4-G that overlies the very fine-grained bulk of the Y4 deposit. Four primary zones can be identified within the Y4-G layer based predominantly on grain size variations, the grain size descriptions of which align with those outlined in *Table 1.1*; *Chapter 1*. The lower ~30 mm (sample A-1, *Figure 3.1*) is a grey, massive, medium to coarse grained ash and fine lapilli (up to ~4 mm) zone with minimal extremely fine ash (<63 µm at ~4.8 wt.%). This is followed by ~20 mm of grey-brown, coarse ash to fine lapilli averaging 0.5 – 1 mm, with a visible increase in extremely fine ash content to ~6 wt.% (A-2). ~25 mm of grey, coarse ash, fine lapilli with ~5 wt.% extremely fine ash succeeds this (A-3). The Y4-G unit is topped with ~15 mm of fine to medium lapilli-sized dense pumice and obsidian with no visible fine ash (sample A-4; *Figure 3.1*). A sharp contact (to ±5 mm) separates this lapilli bed from the succeeding ~40 mm yellow-brown, extremely fine-ash dominated (~28 wt.%), lithic

rich bed with medium to coarse lapilli pumice that defines the Y5-Base unit (A-5). Red oxidized (jarositic) clasts are present in the Y5-Base. Succeeding this is an 80 mm thick white, extremely fine-ash rich PDC deposit (44 wt.% <63 µm: A-6) with pumices up to ~30 mm concentrated in the basal 40 mm. Above is the pumice fall deposit of the Y5 eruption with pumices up to ~35 mm long (A-7; *Figure 3.1*).

B) At exposure B, 110 mm of Y4-G succeeds the fine-grained portion of the Y4 deposit. The lower 90 mm of unit Y4-G can be separated into two normally graded, coarse ash to fine lapilli, obsidian-rich layers with ~3 wt.% extremely fine ash at the base, moderately increasing in abundance with height to 3.5 wt.% (samples B-1, 40 mm thick and B-2, 50 mm thick, respectively; *Figure 3.1*). Obsidian and dense pumice fragments are on average 2–4 mm in size. The upper ~20 mm of the Y4-G is a coarser band of obsidian and pumice (average 2–5 mm, maximum lengths of 8–9 mm; B-3). This is capped by a moderately undulating contact (to ±5 mm) with a 20 mm layer rich in jarositic clasts (~10 %) and with an orange/cream-coloured ash matrix (B-4). Obsidian clasts, like those seen in the unit below, are still present in this layer, but pumices are coarser (8–15 mm) and visibly more vesicular. Pumice sizes increase up to 20 mm in the succeeding 30 mm layer and with no jarositic clasts present, while the extremely fine ash content increases to 24 wt.% (B-5). Above this unit is the ash poor (1.6 wt.% <63 µm), coarse lapilli Y5 plinian fall layer (B-6; *Figure 3.1*).

C) Exposure C has 90 mm of Y4-G material. The lower 20 mm is coarse ash to fine lapilli sized with maximum pumice fragments of ~3 mm, averaging <1 mm. Of this 20 mm unit, the lowermost 15 mm has lower extremely fine ash content (~5.5 wt.%) and consists of predominantly coarse ash-sized dense pumice and obsidian clasts (sample C-1; *Figure 3.1*). A 5 mm band with ~8 wt.% extremely fine ash is noted above this (C-2). The following 30 mm of material (C-3) is like the previous; however, it is normally graded with minor extremely fine ash content in the lower 5 mm, increasing with height, averaging ~8 wt.%. The succeeding layer is a distinct 40 mm band of coarse ash to fine lapilli obsidian and pumice, with maximum clast sizes reaching 8–10 mm and containing <1.5 wt.% extremely fine ash (C-4). Its upper contact undulates over ~20 mm, and it is followed by the 50 mm extremely fine ash rich, medium lapilli pumice Y5-Base. The Y5-Base unit is cream orange in colour and has 3 distinct layers where the lower and upper layers (C-5 and C-7,

respectively; *Figure 3.1*) are extremely fine ash dominated (33 wt.% and 20 wt.%, respectively), while the middle layer (C-6) contains a higher proportion of fine to medium lapilli pumice (16 wt.% <63 µm). Above the Y5-Base unit is the extremely fine ash poor (<3 wt.%), medium to coarse lapilli plinian fall pumice of the Y5 eruption (C-8 and C-9).

D) Exposure D has 55 mm of Y4-G material. The lowest 10 mm (sample D-1; *Figure 3.1*) is predominantly composed of coarse-ash-sized obsidian and dense pumice fragments while the 25 mm above this (D-2) is similar in composition but with increased extremely fine ash abundance (8 wt.% versus 15 wt.%, respectively). There is then a distinct change in grain size with a relatively sharp contact (±5 mm) to a 20 mm layer of fine lapilli obsidian and dense pumice, where the largest clasts are up to 10 mm in length (D-3). A relatively sharp contact (to ±5 mm) separates the Y4-G units below from the basal extremely fine-ash dominated (21 wt.%), lithic rich Y5-Base unit, which is 50 mm thick at this exposure (D-4). The Y5-Base layer has a distinct orange-brown colour and pumice is predominantly fine lapilli sized (*Figure 3.1*). Another relatively sharp (±5 mm) contact defines the upper boundary of this unit, where the occurrence of the ash-poor (<2 wt.% <63 µm), fine to medium lapilli pumice fall material of Y5 begins (D-5 and D-6).

E) Exposure E is the farthest from source. Y4-G is 25 mm thick and predominantly composed of coarse-ash-sized obsidian and dense pumice particles with ~8 wt.% ash <63 µm (sample E-1; *Figure 3.1*). There is a very subtle reverse grading noted in the unit, where the uppermost 7 mm has a slightly coarser grain size, and the largest particles are approximately 2–5 mm in length. The 7 mm unit is tentatively correlated with the upper coarse-grained layer of Y4-G observed at exposures A – D. The contact with the Y5-Base is sharp to ±7 mm and defined by a distinct change in colour from grey-brown to orange-brown. The base of Y5 (30 mm; E-2) is dominated by extremely fine ash (27 wt.%) with fine lapilli sized pumice and lithics. In contrast to the more proximal sections, the upper contact of the ash-rich base appears to be somewhat gradational (E-3) toward a strong change in grain size to an ash-poor (<2 wt.%), medium lapilli sized pumice deposit (E-4).

3.2.2 Isopach maps

Isopachs were defined for the three layers identified within the Y4-G unit through thickness measurements during field mapping (*Figure 3.2*). Exposures were easily identified in medial to distal regions, while proximal exposures were either buried beneath or eroded by thick proximal ignimbrite of the Y5 coeval Early Flow Units (Wilson & Walker 1985). The layers were distinguished predominantly by laterally consistent, vertical changes in grain size and ash content, and are defined as follows.

- Lower Y4-G is composed of fine lapilli to coarse ash sized dense pumice, obsidian, and lithic shards with a maximum average proximal clast size of 4 mm. In medial regions of the deposit, this unit is predominantly coarse ash grade. This unit is the least widely dispersed of the three, with the 5 mm isopach reaching a maximum distance of 23 km from vent (*Figure 3.2*). Its dispersal is also relatively narrow (~10 km maximum width).

- Middle Y4-G is moderately fine grained with an observably higher quantity of coarse ash (3.7–16.9 wt.% <250 µm compared to 2.8–8.6 wt.% and 1.2–3 wt.% in the lower and upper, respectively) yet is the thickest of the noted layers in all exposures. Its dispersal is wider than that of the lower Y4-G unit at ~12 km (*Figure 3.2*), and although the overall distance reached by the 5 mm isopach is only slightly greater at 24 km, the thicker portions of the unit (10–40 mm) reach comparatively greater distances from source.

- Upper Y4-G is distinctively coarser, with fine lapilli sized clasts of predominantly dense pumice and obsidian averaging 2–5 mm in size in proximal to medial regions with maximum sizes of ~15 mm. It has a very narrow dispersal (~8 km; *Figure 3.2*), yet the greatest downwind extent (the 5 mm isopach reaches 30 km from source). The thickest isopachs (20 and 40 mm) are enclosed about a point several kilometres to the ENE of the vent (*Figure 3.2*).

In addition, the thickness of the ash-rich Y5-Base was measured and isopachs were defined (*Figure 3.2*). The layer exhibits a strongly irregular, multilobate character, with the thickest portion occurring to the NE of the vent.

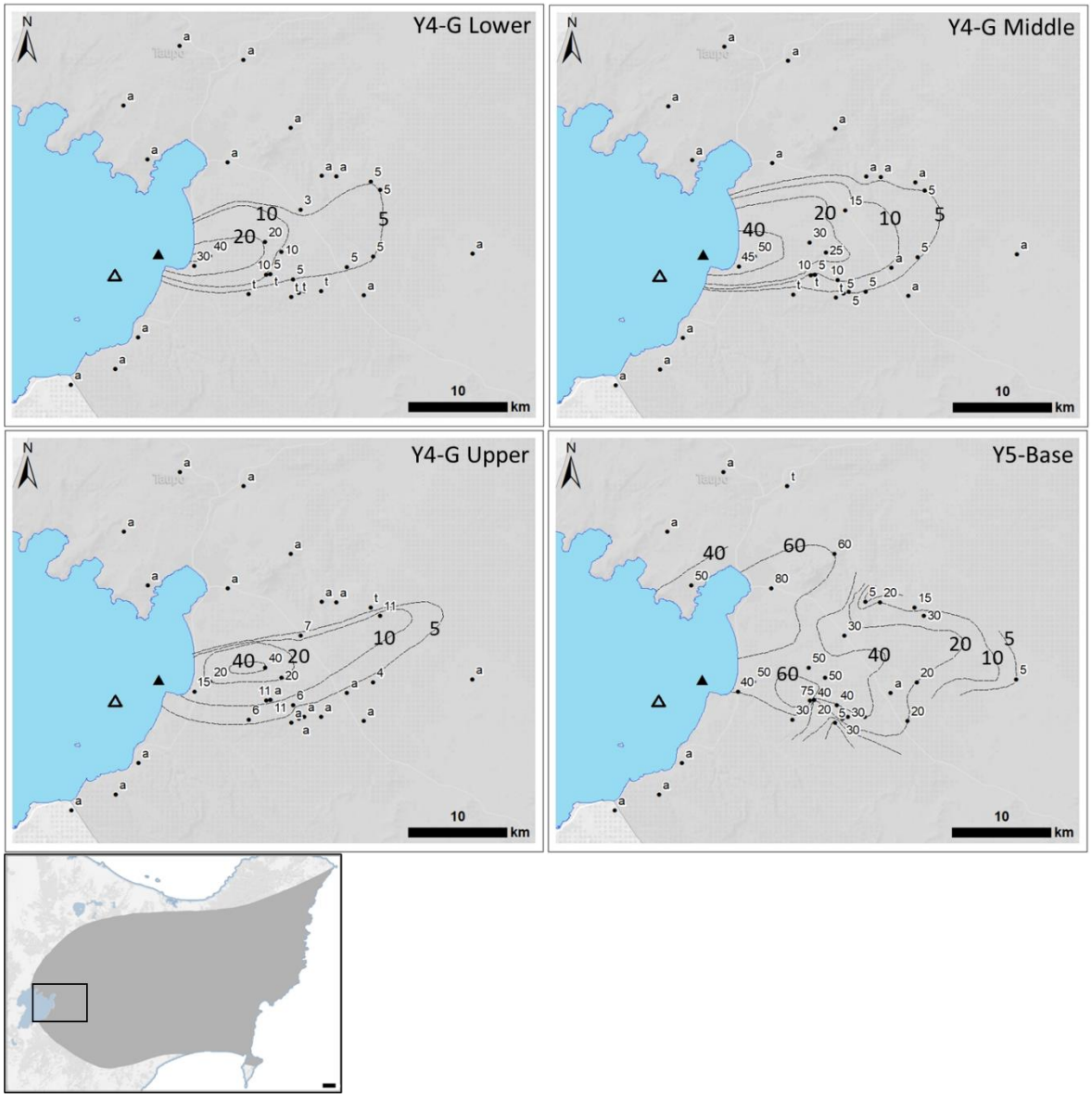

Figure 3.2 Isopachs defined for the Y4-G Lower, Middle and Upper, and Y5-Base units. Black dots show field locations with thicknesses in mm. a is absent and t is a trace (<1 mm) of deposit. Thicknesses of isopachs are in mm (see Appendix J for a list of thicknesses). Scale bars are 10 km. Black triangle is the Smith & Houghton (1995a) Y4 vent and the Walker (1980) vent is an open triangle. Inset below: Grey is the extent of the Y5 deposit on land with black box showing isopach map location.

3.2.3 Grain size characteristics

Grain size analyses were executed by dry sieving size fractions at full phi (ϕ) intervals from the 2 ϕ to -5 ϕ size classes, where ϕ is the -log2 of the given grain size in millimetres (Krumbein 1934). Size fractions >2 ϕ were measured using laser particle analysis (LPA; Horiba Partica LA 950V2). Where fine ash is visibly dominant (e.g., Y5-Base samples), fractions >2 ϕ were first sieved out using water to minimize fine ash losses that might have

been incurred if dry sieving were used. The <2 ϕ fraction was then dried and treated as per the other samples.

The lower Y4-G fall deposits are typically bimodal distributions with most of the material occurring in the coarse fraction (1 ϕ mode) and a minor fine mode at 7 ϕ (e.g., *Figure 3.3*). The coarsest upper layer of the YG-4 fall is generally unimodal (e.g., *Figure 3.3*), with a mode decreasing from -2 ϕ in proximal to 1 ϕ in medial exposures. The Y5-Base deposit samples for each exposure (i.e., A-5; B-4, -5; C-5, -6, -7; D-4; E-2) are also defined by strongly bimodal grain size distributions (e.g., *Figure 3.3*). The fine mode occurs consistently at 7 ϕ whereas the coarse mode gradually decreases in size with distance from the vent from -2 ϕ to 0 ϕ. The Y5 fall samples are dominantly unimodal distributions (e.g., *Figure 3.3*) with modes occurring ≤-2 ϕ, while the PDC unit from exposure A is bimodal, with a fine mode at 7 ϕ and a skewed coarse mode at -5 ϕ.

When comparing the total ash abundance (<1 mm, see *Chapter 2, Section 2.2.1*) with that of the extremely fine ash (<63 μm), I see specific groupings of the various deposition material (*Figure 3.4*). The Y5 fall samples have the lowest total- and extremely-fine-ash contents. The Y4-G Upper samples exhibit total and extremely fine ash contents only moderately higher than those of the Y5 fall deposit samples (*Figure 3.4*). The total ash abundance of the lower and middle Y4-G samples systematically increase with distance from source. The Y5-Base samples show no systematic increase in ash content with increasing distance from source and span the range of ash content between the fall units and the A-6 PDC (*Figure 3.4*).

Median grain size (Md_ϕ) and sorting (σ_I) statistics, calculated according to Folk & Ward (1957), also show strong relative groupings in *Figure 3.4*. Both Y4-G and Y5 fall samples are well-sorted deposits distinguished by a clear difference in Md_ϕ: Y4-G samples are finer grained (c. -2 >Md_ϕ >2 ϕ) than those of the Y5 (c. -3 >Md_ϕ >-1 ϕ; *Figure 3.4*). The ash-rich Y5-Base deposits span the range of sorting between the fall unit and PDC (A-6) samples, with coarser overall Md_ϕ (c. -2 to 1 ϕ) than the PDC and Y4-G samples. *Figure 3.4* shows that σ_I values of the Y4-G units remain relatively consistent (0.8 to 1.8 σ_I) both with stratigraphic height and lateral distance, and there is no significant trend identified in sorting efficiency with distance from source. Σ_I becomes poor in the Y5-Base intervals and PDC deposits, ranging between ~2 and 5, while the Y5 fall intervals encompass similar degrees

of sorting to those of the Y4-G fall (*Figure 3.4*). In general, the Md_ϕ values increase with increasing stratigraphical height across all deposits, disregarding PDC unit A-6.

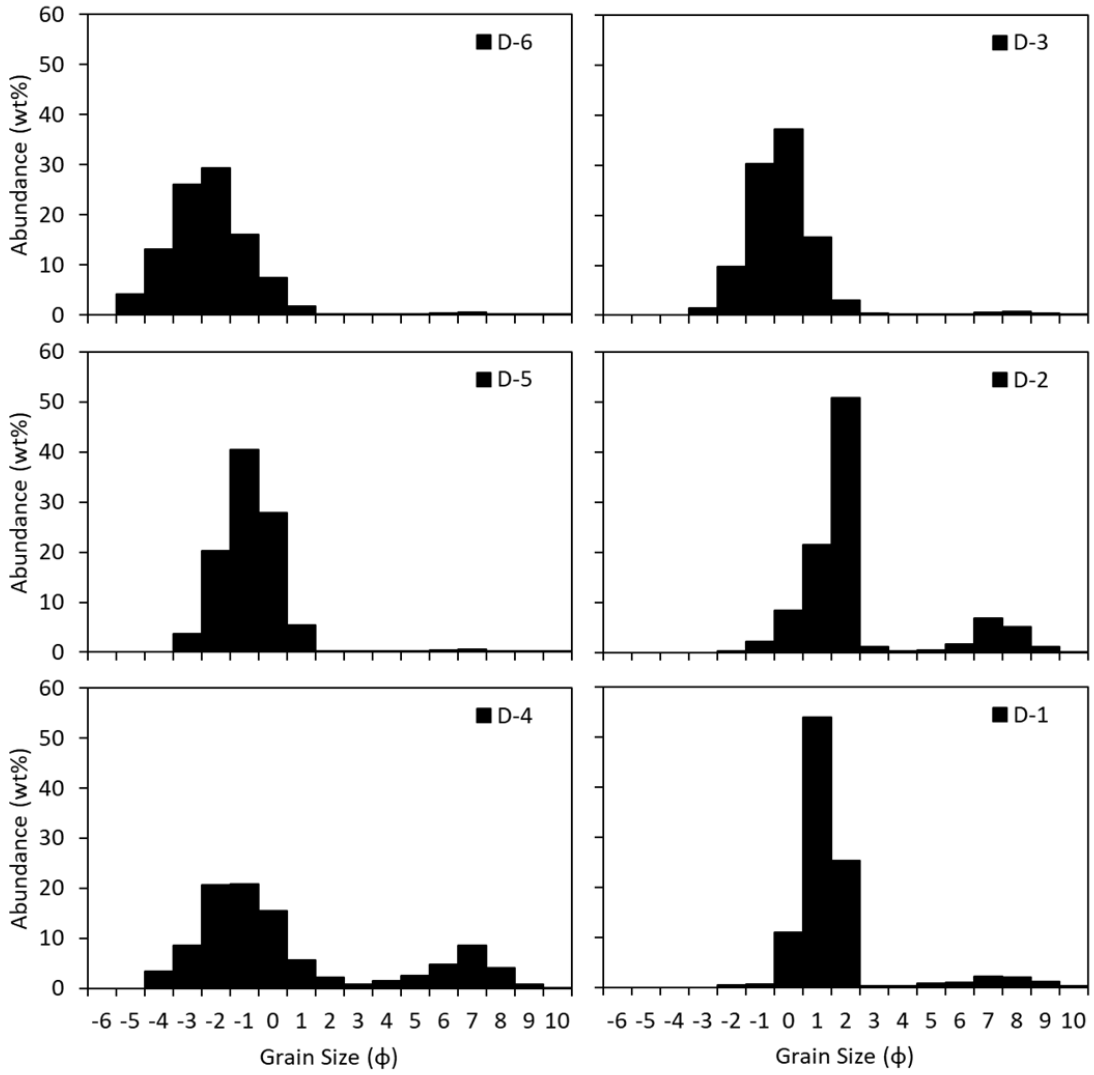

Figure 3.3 Grain size distributions (in wt.% of full ϕ grain sizes) at Exposure D across the transition zone (Y4-G = D1-3; Y5 base = D-4; Y5 fall = D-5, 6).

3.2.4 Componentry

To compare the relationship of components from proximal to medial exposures A – E, the relative point count abundance (num%) of components in the 1 ϕ size fraction was determined for all box samples within each exposure. The relative abundance of components in each full ϕ size class <2 ϕ was also determined for all box samples taken from within the

selected exposure D. Components were divided into four broad classes of: 1) pumice; 2) wall-rock lithic (henceforth, lithic); 3) crystal; and 4) obsidian. The pumices are variably vesicular, with little to no alteration. There is a significant observed difference in pumice

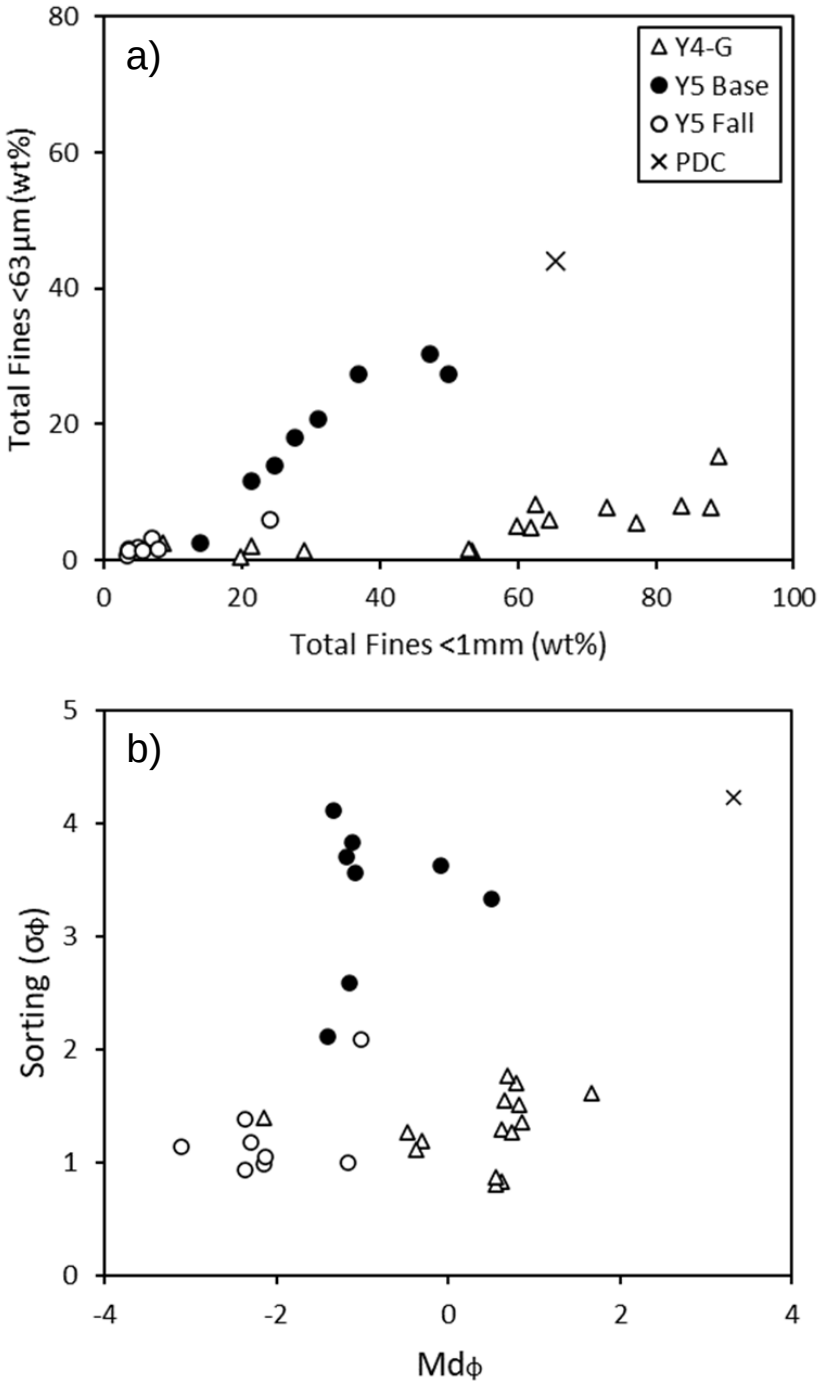

Figure 3.4 a) Total fines <1 mm versus extremely fine ash content <63 um, both in wt.%. b) Median grain size versus sorting (both in phi) of the box samples taken.

types within the Y4-G deposit compared to those in the Y5, where Y4-G pumices are significantly less vesiculated (46 %) with qualitatively thick bubble walls. Pumices in the Y5 deposit are highly vesicular (~74 – 78 %), white in colour, with varying degrees of vesicle elongation. Lithics encompass all non-juvenile components, including pre-232 CE rhyolite lavas, and pumice (i.e., Chernet 1987; Wilson 1993; Cole et al. 1998), fragments of pre-Oruanui volcaniclastics and sediments (i.e., Chernet 1987; Cattell et al. 2016), and plutonic microdiorites and granitoids (i.e., Chernet 1987; Brown et al. 1998; Cole et al. 1998; *Figure 3.5*). Lithic pumice was distinguished from juvenile pumice based on rounded, non-angular edges due to erosion and varying degrees of invasive alteration. Juvenile crystals are dominantly plagioclase and pyroxene, with minor titanomagnetite. Juvenile obsidians were determined as such based on the presence of fresh, conchoidal fracture surfaces and the lack of alteration or surface-adhesive ash.

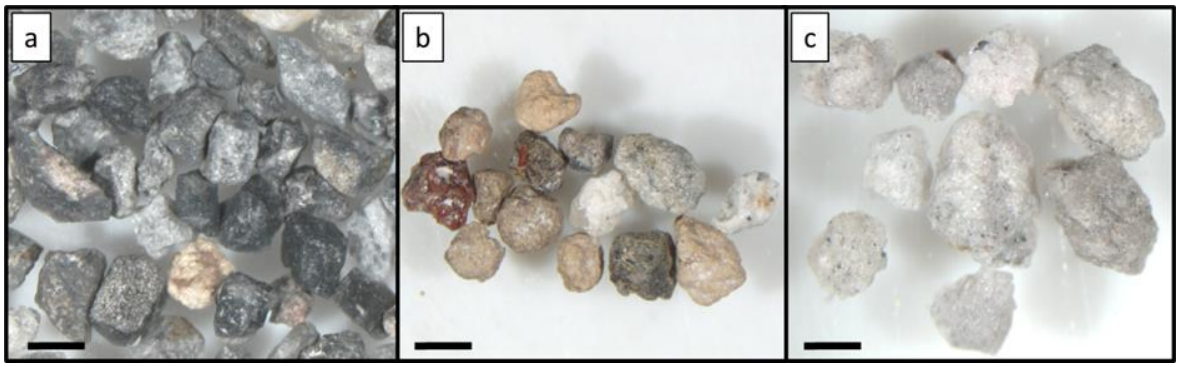

Figure 3.5 Examples of lithic components from the Y4-Y5 deposits: a) F1 shallow lithics, predominantly rhyolite lavas, b) F2 moderate depth sediments, hydrothermally altered material and volcaniclastics, c) F3 deep plutonic intrusives. All scale bars are 2 mm.

Lithic types were subdivided by their inferred stratigraphic depth of origin based on previous investigations of the TVZ (i.e., Chernet 1987; Brown et al. 1998; Cole et al. 1998; Cattell et al. 2016). Three broad groups are defined, labelled F1, F2 and F3 (*Figure 3.5a – c*).

- F1 lithics are predominantly rhyolite lava fragments with typically minor to no alteration, except for hydrothermally altered jarositic ‘rusty’ fragments, and are sometimes spherulite-bearing and/or flow banded. Pervasively altered pumices are a minor component and are micro- to macro-vesicular, rounded clasts that range in colour from pink and light yellow to dark orange/brown. Obsidians are also present

and are primarily red and black with rounded edges, minimal conchoidal fracturing and commonly abraded surfaces with attached fine ash. The altered pumice and obsidian are considered to products of previous eruptive activity of the Taupo area (e.g., Chernet 1987; Cole et al. 1998). Pre-232 CE, post-Oruanui (inclusive) stratigraphy is here estimated to be situated at depths of ~0 – 400 m below the surface based predominantly on thickness estimates of the Oruanui deposit and succeeding eruption suite (Chernet 1987; Wilson 1991; Cole et al. 1998; Rosenberg et al. 2020; *Figure 3.5a*).

- F2 lithics are dominated by the shallower lacustrine formed sediments and volcaniclastics of the Huka Group as used by Cattel et al. 2016 (*Figure 3.5b*), comprised of silts, volcaniclastic tuff, monomict and polymict breccias and coherent lavas with strong alteration rims. Minor abundances of deeper seated, Whakamaru-group ignimbrite material are noted in the F2 class, as well as green, hydrothermally altered pumices and obsidian. Pre-Oruanui eruption products are estimated to originate from ~400 – 3000 m depths, based on maximum stratigraphic thickness estimates of the Huka Group and Whakamaru Group, combined (Chernet 1987; Cattell et al. 2016; Rosenberg et al. 2020; *Figure 3.5b*).

- F3 include intrusive microdiorites and granitoids (*Figure 3.5c*), are defined by their microcrystalline, equigranular nature, and are not considered primary from the magma chamber (Chernet 1987). Granitoids are regarded as crystallised portions of silicic Quaternary TVZ magma chambers, while microdiorites are considered intrusive equivalents of high alumina basalts from the central TVZ (Brown et al. 1998). Plutonic microdiorites and granitoids are assumed to originate from depths >4000 m below surface as crystallised magma chambers must occur stratigraphically below the volcaniclastic and sedimentary facies of F1 and F2, yet above the likely depth of the existing magma chamber of the Taupō Caldera Complex (~5000 m; Chernet 1987; Brown et al. 1998; Cole et al. 1998; Rosenberg et al. 2020; Barker et al. 2021; *Figure 3.5c*).

For exposure D, the total relative abundance of components in each sampled interval was calculated by normalizing the weighted percent (wt.%) of components in each grain size to the measured weight of that grain size and then collated for each component class. There is

a 32 wt.% drop in the overall abundance of obsidian clasts at the boundary between samples D-3 and D-4, with the ratio of obsidian to pumice sharply decreasing with height at this boundary (*Figure 3.6*). This is also highlighted in *Figure 3.7*, which shows the distribution of components across grain sizes -4 to 2 ϕ in exposure D. It is noted that obsidian abundance typically diminishes in the size fractions coarser than -2 ϕ (*Figure 3.7*). There is a noticeable increase in the total amount of lithics (39 wt.% to 57 wt.%) from D-3 to D-4, which then wanes upward as pumice becomes the dominant component at 60 wt.% in D-6. There is a particular trend in the F2 components across the deposit boundary, where the overall abundance increases by ~19 wt.% with the ratio to both pumice and F1 clasts also exhibiting a sharp upward shift from D-3 to D-4 (*Figure 3.6*). The increase in F2 is significant across almost all grain sizes between the Y4-G and Y5 units, however these clasts are typically not present within the coarsest size fraction of each sample (*Figure 3.7*). It can also be noted that overall, the F1 lithics show a gradual reduction in abundance toward the Y4-Y5 deposit boundary, being relatively lower in Y5 as compared to Y4-G (*Figure 3.6* and *Figure 3.7*).

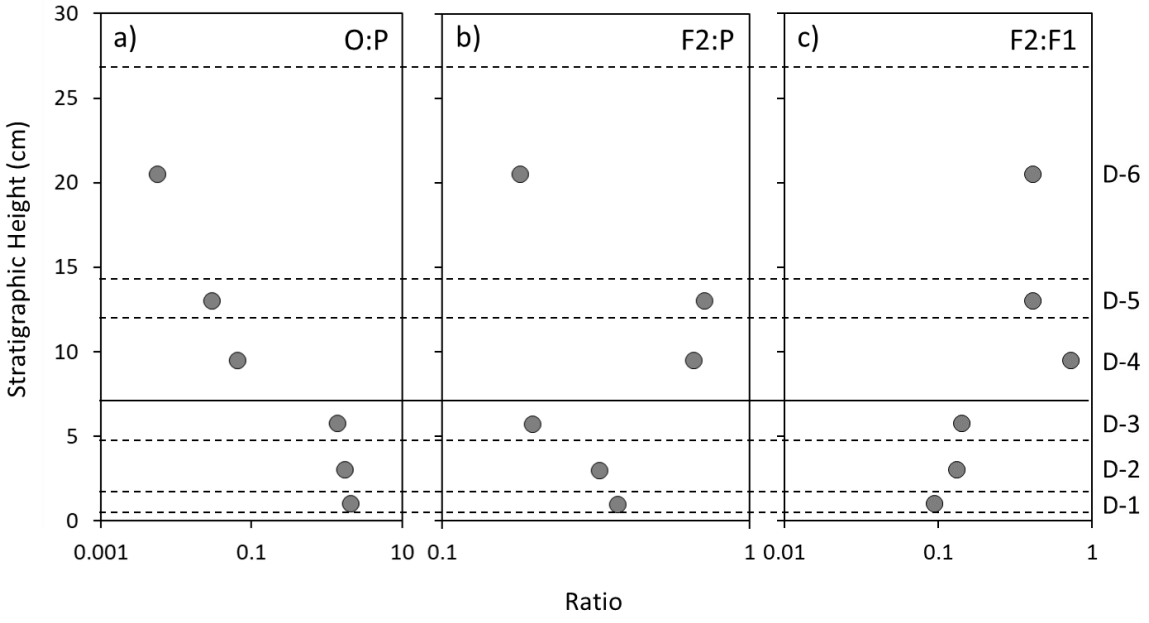

Figure 3.6 The ratios of, a) obsidian to pumice (O:P), b) F2 to pumice (F2:P) and c) F2:F1 with stratigraphic height in exposure D. Box sample numbers are noted on the right. The boundaries between samples are shown by the dotted black lines. The solid black line shows the Y4/ Y5 boundary.

The same trend can be seen at the boundary between the Y4-G and Y5 deposits within the lateral exposures A – E. *Figure 3.8* shows a clear abundance of obsidian in the Y4-G samples across all exposures, the abundance of which decreases by between 12 – 25 num% at the contact with Y5. I also see that F2 increases by between 6 and 21 num% at this boundary while F1 again decreases relatively steadily (*Figure 3.8*). Within the lower Y5 unit, the range between the F1 and F2 components is significantly narrower than that of the Y4-G, where F1 clasts dominate the lithic componentry. Both pumice and crystal abundances are also noted to increase significantly in Y5 comparatively to the Y4-G deposits (*Figure 3.7*). Interestingly, the distinct increase in F2 at the boundary between the Y4-G and Y5 deposits is accompanied by a clear change in the observed type of F2 components. Y4-G F2 is dominated by fine grained siltstone clasts that are typically cream to light orange pink in colour (*Figure 3.9a*) while F2 lithics in Y5 are predominantly comprised of volcaniclastic breccia with a white to cream tuffaceous matrix (*Figure 3.9b*). Walters (2020) identified similar volcaniclastic breccia material in the Y2 eruption deposits (see *Figure 3.9c, d*).

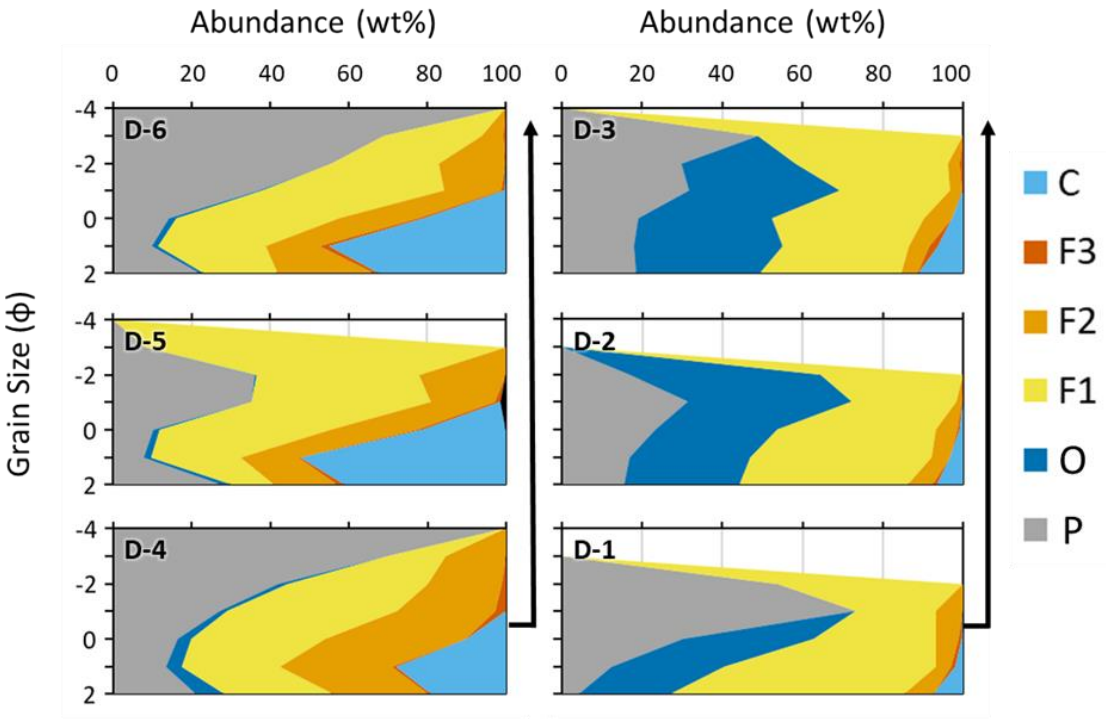

Figure 3.7 The relative abundance of components in wt.% from grain sizes 2 to -4ϕ in exposure D (see Fig. 3.1). Arrows indicate increasing stratigraphic height. P is pumice, O is obsidian, F1 to F3 are shallow to deep lithics (see text) and C is crystals. Sample ID noted in each graph.

3.2.5 Pumice density

Clast density and vesicularity measurements of pumices across the transition zone at exposure D were obtained as per methods outlined in Houghton & Wilson (1989) and Shea et al. (2010). Due to the lack of larger pumices available in sample units D-1, D-2, and D-5, these layers were excluded from this analysis. There was also a relatively small number of pumices within the 8–32 mm size fraction within D-3, therefore measurements were obtained for use as comparative averages, rather than density distributions. The averaged results exhibit a representative density of 1343 ± 21 kg m^{-3} within the Y4-G D-3 and average 636 ± 11 kg m^{-3} in samples D-4 and D-6 above. Although the D-3 pumices are relatively smaller (8–16 mm) than those in the Y5 unit (8–32 mm) due to a lack of larger pumices, they are markedly denser (by ~700 kg m^{-3}) and less vesicular than those in Y5 (45.8 versus 74.5 %, respectively). Therefore, I assume that there is a pumice density contrast between the two eruptive units, as potentially larger (16–32 mm) pumices in the Y4-G are still likely to have significantly higher densities than those of the Y5 deposit based on pumice morphology and observed vesicularity. This inference is also supported by the comparable average Y4 vesicularity measurement of 42 % obtained by Smith (1998).

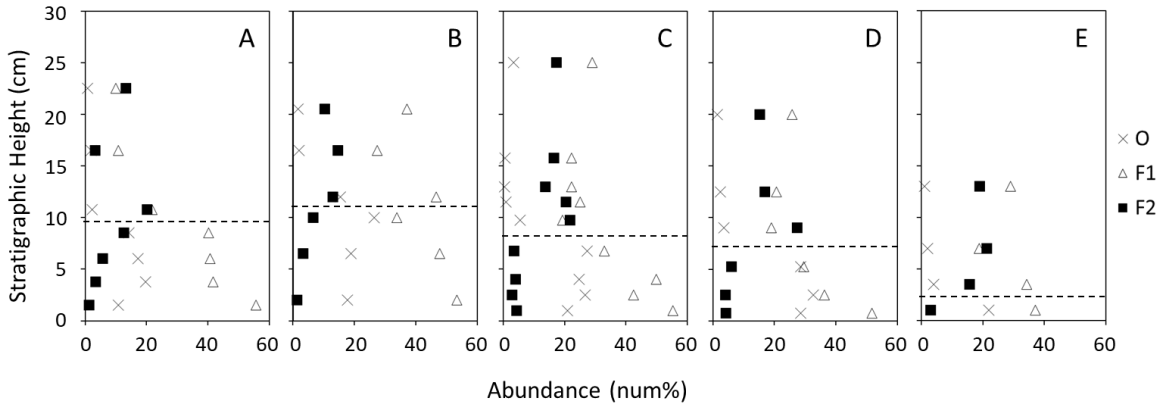

Figure 3.8 The abundance of 1 phi components (num%) with stratigraphic height for exposures A to E. O is obsidian, F1 and F2 are shallow to intermediate depth lithics. The boundary between the Y4 and Y5 units is marked by the dashed black lines.

3.3 Discussion

3.3.1 The nature of the Y4-G and the onset of Y5

Overall, the Y4 deposit consists almost entirely of very fine grained, poorly to non-vesicular, grey juvenile clasts (Smith 1998), whereas the Y5 deposit is dominated by very coarse grained, highly vesicular, white pumice clasts (further details in *Chapter 4*). It is inferred that the Y4 magma resided at shallow levels for some time period and was passively degassed within a separate conduit that restricted magma rise prior to or during the earlier phases of the Taupō eruption (Smith 1998). The final stage of the Y4 phase (unit Y4-G) was described as a 'plinian style' bed dominated by coarse ash and dense pumice lapilli with a mean vesicularity of 42 % (Smith 1998), which is comparable to the 46 % vesicularity value that I obtained. It is assumed to be associated with relatively dry vent and plume conditions compared to the bulk of the Y4, where the early stage Y4 magma interacted with lake water to produce several short-lived, highly unstable eruption plumes (Houghton & Smith 1995a). It can be inferred that external water remained involved during the Y4-G stage; however, did not significantly contribute to the style of particle transport when compared to the earlier bulk of the Y4 deposit, with a more developed plinian-style plume dispersing the erupted, degassed material (Smith 1998).

Based predominantly on isopachs and field observations, I suggest that the Y4-G phase was comprised of three individual pulses. Subtle normally graded layers noted in the analysed sections are consistent with the waning of individual eruptive phases, where the plume height diminishes, and fine ash deposition succeeds the coarser material (*Figure 3.1*). Median grain sizes decrease for all three units with distance from vent, consistent with the preferential fall deposition of coarser, more dense material close to vent, while finer material is transported to greater distances (Walker 1980, 1981b). Isopachs of the three Y4-G pulses show that the dispersal power increased from the lower to upper unit (*Figure 3.2*). There is a lack of evidence for erosion between the Y4-G and Y5 deposits and it can be assumed that proximal measurements of the Y4-G are true thicknesses. A cessation of Y4-G deposition a short time prior to the onset of the Y5 is supported by the sharp boundary between the units and the lack of Y4-G material identified in the lower Y5 deposit. If venting occurred simultaneously for any length of time, it would be expected that cross contamination of pyroclasts would occur in the deposits. In addition, it would be assumed that the lack of fine ash identified in

the Y4-G deposit represents the establishment of the Y5 plume which incorporated remaining near-source atmospheric ash, dispersing it within the growing Y5 plume.

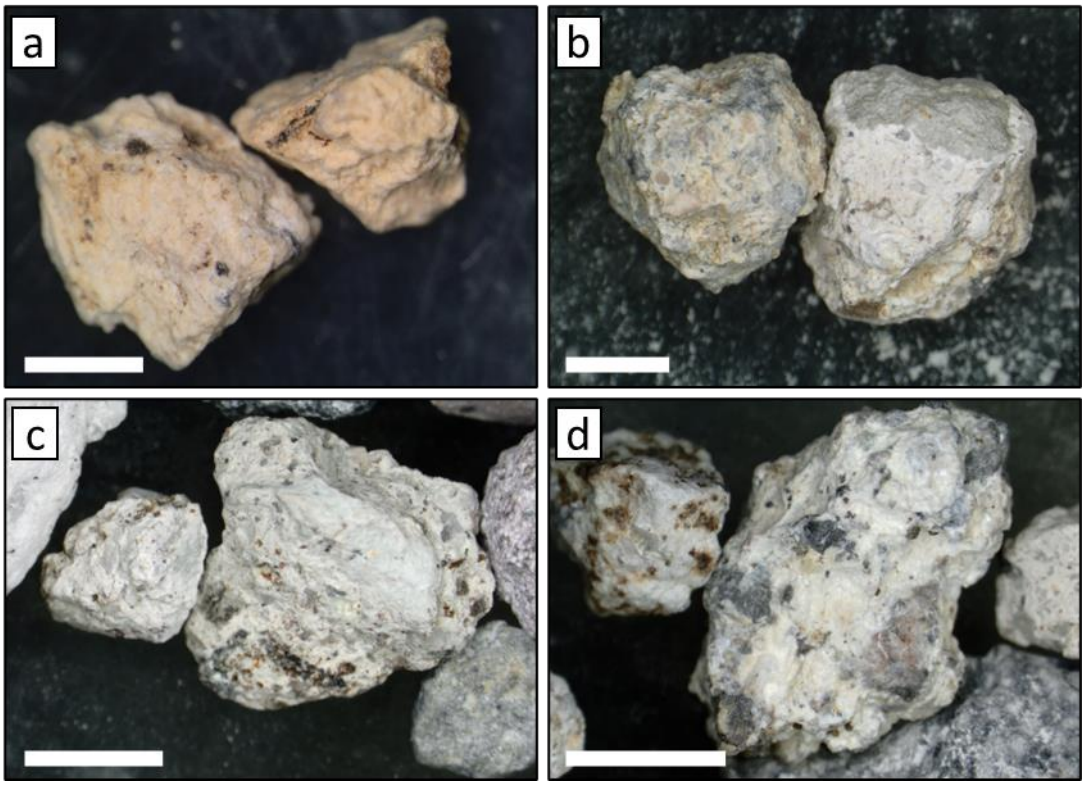

Figure 3.9 Examples of lithic clasts from the Y2, Y4-G and Y5 fall deposits. a) Finer grained silts that dominate the Y4-G F2 lithics; b) volcaniclastic breccias that dominate the Y5 F2 lithics; c, d) similar volcaniclastic breccias documented in the Y2 lithics by Walters (2020). Scale bar is 2 mm.

It has been previously suggested (Smith 1998) that the presence of fine ash in medial to distal sections of the Y4-G unit is possibly related to contamination from the overlying ash-rich base of the Y5 deposit. Field observations, however, show that there is a very distinct change in colour between the two units, where the fine ash portion of the Y4-G deposit is similarly grey to the remainder of the Y4 unit, while the fine ash in the Y5-Base deposit is distinctively cream to orange-brown in colour (*Figure 3.1*). In exposures C and D, especially, the combination of field observations and granulometric data show that the upper fine lapilli sized layer of the Y4-G is distinctly fine ash poor, while the lower layers show an increased abundance of fine ash (*Figure 3.1* and *Figure 3.3*). Since the upper layer is in contact with the basal unit of the Y5, it would be expected to contain the most of any ash contamination. Additionally, the Y4-G layers are notably well sorted like the Y5 plinian pumice (*Figure*

3.3), suggesting that the fine ash material in the Y4-G is in fact a component of the main eruptive plume and not introduced by secondary processes.

The adherence of fine ash to the coarse particles in the Y5-Base unit is inferred to be indicative of the presence of water during the onset of the Y5 eruption, inducing fine particle cohesion. As the topography of the Y5 vent at the time of eruption is unknown, this may suggest that water was present around its periphery in the very initial stages of this eruption phase. This feature, along with others such as the granulometric bimodality of the unit, are comparable to those reported from co-PDC or co-plinian deposits of other explosive eruptions (i.e., Soufriere Hills, Bonadonna et al. 2002; Mt Pinatubo, Dartevelle et al. 2002; Fuego, Rose et al. 2008; Tungurahua, Eychenne et al. 2012). The sharp upper contact and ash-rich nature of Y5-Base suggests that this unit may be a result of peripheral or independent column collapse forming a hybrid PDC-airfall deposit. Another possible scenario arises, however, when looking at the ash rich beds in the lower parts of the Hatepe plinian (Y2) deposit. Like the Group C beds identified by Talbot et al. (1994), the bimodal, ash rich Y5-Base may have instead deposited by elutriation during local rain showers that passed through lower lying ash clouds as lapilli pumice continued to sediment from the early high plume of the Y5 eruption (Talbot et al. 1994; Walters 2020). This scenario is consistent with the irregularity seen in the Y5-Base isopachs (*Figure 3.2*), which show similar distribution behaviour to the Y2 Group C beds defined by Talbot et al. (1994). The irregular dispersal may be related to both rain shower distributions and a dominant south-westerly wind direction rather than vent position, resulting in localized maxima and minima and a deposit with its maximum thicknesses that occur predominantly north-east of the vent.

3.3.2 Vent transitioning between the Y4 and Y5 eruption phases

The abrupt changes identified in eruptive characteristics between the gas-poor magma that fed Y4-G, with fragmentation induced predominantly by magma-water interaction, and the sustained, rapid discharge of actively vesiculating Y5 magma (Smith 1998) can be interpreted to suggest a distinct shift in vent location. The ash- and lithic-rich Y5-Base deposit, which has been interpreted to represent the onset of the Y5 phase (*Figure 3.1*; Smith 1998; Houghton et al. 2014), shows a sharply defined contrast with Y4-G in terms of colour, componentry, grain size and pumice densities (*Figure 3.3*, *Figure 3.6 – Figure 3.8*). Analysis of components implies that the deposition of the Y5-Base was concurrent with a change in

vent position from that of the Y4 phase, where high proportions of lithics, particularly F2 clasts, indicate a vent clearing stage during which a significant quantity of pre-Oruanui volcaniclastic material was excavated (*Figure 3.6 – Figure 3.8*). The lack of obsidian within the Y5 deposit compared to the Y4-G, and the clear change in pumice morphology and vesicularity (~46 % in Y4-G versus ~75 % in Y5) across the boundary indicates that the 'plinian style' pumice erupted at the end of the Y4 was vented from a source unrelated to the Y5 plinian pumice, consistent with the observations by Smith (1998). The separate vent location is also supported by the dispersal directions displayed in the isopachs for all three of the Y4-G layers (*Figure 3.2*), which indicate an origin in the vicinity of the Y4 vent. I cannot, however, rule out that the Y4-G was vented from a partly outgassed dike located between the vents of the Y4 and Y5. Isopachs could be crudely interpreted to define a vent broadly within this vicinity as there is often ambiguity in pinpointing sites based on this technique. The gradual diminution of F1 clasts with height in the Y4-G units at all analysed outcrops (*Figure 3.7*) may suggest either a brief vent opening or vent migration phase at the onset of the Y4-G which, if compared to observations made by Smith (1998) and Smith & Houghton (1995a), is plausible due to the apparent lack of older rhyolite lava lithics found in the earlier phases of the Y4 deposit. A subtle shift in vent location between the 'true' Y4 and Y4-G units may explain the changing eruptive nature from predominantly magma-water interaction driven fragmentation to 'drier' plinian-style fragmentation; however, further detailed investigation is required to test this.

3.3.3 Implications for the vent location of the Y5 phase

The location of the Y5 eruptive vent has previously been inferred to occur in the vicinity of the younger Horomatangi Reefs within Lake Taupō based on isopach and isopleth measurements by Walker (1980; *Table 1.1*). Recently, however, a new proposed vent location has placed the eruption ~6 km SW of the originally proposed vent, in proximity to Motutaiko Island (Houghton et al. 2014), comparable to the vent locations of the Y1 Initial ash and phreatomagmatic Y3 Hatepe ash phases of the 232 CE eruption (Smith & Houghton 1995a). This Y5 vent location was proposed by Houghton et al. (2014) based on observed internal variations within the vertical stratigraphy of the Y5 deposit, where isopach measurements based on qualitative correlations of sub-units resulted in deviations in dispersal directions from that originally determined by Walker (1980: further discussed in *Chapter 4*). In addition to the lack of supporting data in Houghton et al. (2014), other factors

suggest that their proposed vent location is not viable. Motutaiko Island is a ~7000-year-old rhyolite dome (Wilson 1993) which lies at the margin of the caldera collapse following the 232 CE eruption (Davy & Caldwell 1998). In the case of the vent location proposed by Houghton et al. (2014), it is unlikely that the rhyolite dome would remain following the plinian Y5 eruption, or that an event of this magnitude would occur on the rim of the subsequent caldera. I would also expect that, if the island dome was only partially destroyed during the eruption, there would be a significant influx in F1 rhyolite lithics in the Y5-Base, which is contradictory to the trends seen in my data where F1 lithics in fact gradually decrease in abundance from the Y4-G to Y5 deposits. Based on this information, I suggest that the vent location proposed by Houghton et al. (2014) is unlikely to have been the source of the Y5 eruption phase.

It is generally accepted that if the stratigraphy of the vent area is constrained, the types of lithic fragments can aid understanding of the evolution of fragmentation depth (Suzuki-Kamata et al. 1993; Macedonio et al. 1994; Taddeucci & Wohletz 2001; Pittari et al. 2008; Mele et al. 2011; Cioni et al. 2015) and, in the case of Y5, permit inferences to be made regarding vent location. In addition to the increase in overall lithic abundance at the boundary between Y4-G and Y5-Base (*Figure 3.8*), there is a significant influx of F2 type lithics which suggest that new pre-Oruanui eruption material was being excavated. When comparing the F2 lithics in the Y4-G and Y5 deposits, I also note a distinct change in clast type across the boundary zone, with a lack of brecciated volcaniclastics identified in Y4-G (*Figure 3.9*). Similarities have been observed between the F2 lithics in the Y5 and those of Y2 (see Walters 2020, *Figure 3.9*), which may be attributed to analogous regions of crustal excavation and could be used to suggest similar vent locations.

Detailed mapping by Walker (1981a) placed the Y2 vent in proximity to the (younger) Horomatangi Reefs, while Smith & Houghton (1995) revised this vent location to one comparable with that for the Y1 and Y3 phases. This revision, however, was solely based on the assumption that the Y2 material was discharged from the same vent as the vesiculated magma of the Y1 and Y3 phases, in contrast to the gas-poor magma of the Y4 eruption, without sufficient field investigation. Two discrepancies stand out here: 1) the detailed isopleth and isopach data gathered by Walker (1981a) do not align with a vent site located further SW; and 2) Walker (1981a) noted a lack of ballistic material in the Y2 deposit, suggesting a vent location at least a few kilometres from the shoreline of Lake Taupō.

Ballistics have recently been identified within the Y1 ash beds (see *Chapter 6, Figure 6.1*) and, given the size discrepancy between the two eruptions (Wilson & Walker 1985), it is not plausible for the Y2 phase to have occurred from a similar vent location without the occurrence of ballistically emplaced material on land. Similarly, ballistic clasts have also not been identified in the proximal deposits of the Y5 eruption phase (Walker 1980) and therefore rule out the possibility of this south-westerly vent location. Hence, I concur with Walker's (1981a) Y2 vent location and, on the basis of the lithic similarities documented here and in Walters (2020), infer that the Y5 vent was similarly located at the area now occupied by Horomatangi Reefs.

3.4 Conclusions

This study has shown the necessity for detailed quantitative investigation into the physical properties of pyroclasts when looking at transitional vent behaviour in multiple source events. Primarily through the analysis of components in the transitional stratigraphy, I have determined that the change in eruptive style between the phreatoplinian Y4 and plinian Y5 phases of the Taupō 232 ± 10 CE eruption was concurrent with a distinct shift in vent location. The excavation of new volcaniclastic material at the onset of the Y5 phase can be used to suggest similar regions of crustal excavation with those identified previously in the plinian Y2 deposit (Walters 2020) and imply a vent location comparable to that of the Y2 phase determined by Walker (1981a). The sharp contrasts in lithic and pumice types, and obsidian abundance in particular, at the boundary of the Y4 and Y5 deposits points toward a cessation of the Y4 event, with no co-venting occurring at the onset of the Y5. The Y4 eruption shows evidence of sudden termination, where plinian-like pulses of magma-water interaction driven fragmentation mark the final stages of this event, immediately prior to the opening of a new vent and the rapid discharge of actively vesiculating Y5 magma. These results further add to the understanding of transitional vent behaviour in multiple source events and the mechanisms that influence a change in eruptive style during such large-scale events.

4 Reconstructing the temporal evolution of the large Plinian Y5 phase of the Taupō 232 CE eruption

4.1 Introduction

Large-scale Plinian eruptions comprise some of the most destructive natural phenomena on Earth. Eruptive plumes ascend to >30 km height and cause long term stratospheric disturbances, while collapse of all or parts of the column can generate lethal pyroclastic flows. There is still much to learn from the measurable sedimentological and physical characteristics of the deposits to inform on the dynamics of their parental plumes. Sedimentological variations in plinian fall deposits have traditionally been interpreted to reflect strong variations in eruption mass discharge rates at source, magma rheology and fragmentation, and conduit stability (e.g., Sparks et al. 1981; Sigurdsson & Carey 1989; Scasso et al. 1994; Polacci et al. 2001; Taddeucci & Wohletz 2001; Sigurdsson 2003; Sulpizio et al. 2010; Cioni et al. 2015; Cashman & Scheu 2015). Investigations into deposit characteristics such as variations in granulometry, componentry and density have predominantly focused on the interpretation of contrasting explosive styles in an eruptive sequence (i.e., changes between phreatomagmatic, plinian and ignimbrite deposits, e.g., Lirer et al. 1973; Sparks et al. 1981; Houghton & Wilson 1989; Sigurdsson & Carey 1989; Wilson & Houghton 1990; Scasso et al. 1994; Rosi et al. 1999, 2001; Polacci et al. 2001; Taddeucci & Wohletz 2001; Klug et al. 2002; Sigurdsson 2003; Houghton et al. 2010; Sulpizio et al. 2010). Plinian deposits have also been analysed for their compositional traits, where complex magma mixing, a compositionally zoned magma chamber or tapping of various sources have resulted in compositionally variable deposits (e.g., Lirer et al. 1973; Walker 1981a; Blake et al. 1992; Cioni et al. 1995; Rosi et al. 1999; Polacci et al. 2001). There is, however, a lack of investigation into the in-depth stratigraphical variations in deposit characteristics of single, compositionally uniform plinian deposits. For example, Taddeucci & Wohletz (2001) examined changes in granulometry, juvenile characteristics and lithic types to inform the behaviour of phase 1 of the Minoan plinian eruption in terms of conduit stability, development toward climactic eruption and the consequent column collapse. The varying phases of the Minoan eruption are considered to have occurred from

different vent sources (Sparks & Wilson 1990; Pfeiffer 2001), whereas the majority of models investigating deposit characteristics usually look into the evolution of a single source event. Original studies of the Taupō 232 ± 10 CE eruption also considered a single source model for the sequence, with the vent located at the Horomatangi Reefs in Lake Taupo (Walker 1980; Wilson & Walker 1985). Currently, however, a multiple source model is the accepted explanation for the varying phases of the 232 CE eruption (Smith & Houghton 1995a; Houghton et al. 2010) where the vents occur on a NE-SW lineation passing through the site of the younger Horomatangi Reefs. Further investigation is needed to investigate the detailed nature of stratigraphical characteristics within plinian deposits to determine source conditions, understand particle transport and sedimentation and generate a benchmark for use in prospective modelling of natural eruption conditions for a range of likely future eruption scenarios. To do this, I have investigated the deposit characteristics of the compositionally uniform (Dunbar & Kyle 1993; Sutton et al. 1995), large plinian deposit produced during the Y5 phase of the 232 CE eruption. There are currently two contrasting interpretations of this deposit, leading to conflicting assessments regarding the dynamics and behaviour of the eruption: 1) that it occurred as a singular, steady 'ultraplinian' dispersed event (Walker 1980) or 2) that the eruption involved multiple pulses that were influenced by a changing wind direction to produce multiple subunits (Houghton et al. 2014). Through the detailed analysis of deposit characteristics, I aim to add further clarity to the understanding of the behaviour and development of the Y5 eruption.

4.1.1 The Y5 phase of the 232 CE eruption

The Taupō 232 ± 10 CE eruption produced multiple phreatomagmatic ash-rich deposits, two plinian fall deposits coevally with minor ignimbrites, and an extremely widespread ignimbrite deposit (Baumgart 1954; Baumgart & Healy 1956; Healy 1964; Walker 1980, 1981a, 1981b; Froggatt 1981; Wilson 1985; Wilson & Walker 1985; Houghton et al. 2010, 2014). Unit 5 (Y5) of the 232 CE eruption is the larger of the two Plinian phases, is one of the most widely dispersed plinian fall deposits documented (Walker 1980) and is well preserved in proximal to medial zones. It is notably coarse grained when compared to the earlier Plinian Y2 deposit (Hatepe Plinian) and sits distinctively atop the "wet, cohesive mud" (Wilson & Walker 1985) of the phreatoplinian Y4 deposit (Rotongaio ash). The Y5 deposit is interbedded with coevally emplaced ignimbrite (the Early flow units of Wilson & Walker 1985), which has been interpreted to represent a phase of coeval buoyant plume and

partial column collapse. Following and interrupting the Y5 phase, drastic changes in eruption conditions resulted in the immensely destructive outburst that generated the Y6 Taupo ignimbrite, which extended to ~80 ± 10 km from vent and eroded significant portions of the underlying deposits (Wilson & Walker 1985; Wilson 1985). This last event is inferred to have been caused by either an intense increase in discharge rate (which would limit the capabilities of forming a stable plinian plume), or the widening of the vent due to erosion or the onset of caldera collapse, leading to column collapse (Wilson & Walker 1985).

Original studies of the Y5 deposit by Walker (1980) calculated a bulk volume of 24 km^3 based on the aeolian concentration of crystals, given that large quantities of free crystals on land implied that a large proportion of the deposit was represented by fine vitric ash that was blown to sea. The common isopach volume method is relatively unreliable for use on the Y5 deposit due to the erosion caused by the succeeding pyroclastic flow, affecting true total thicknesses (Walker 1980); however, the isopachs are still a reliable indicator of the total deposit extent. Given its coarseness, the Y5 eruption was estimated to have a plume height that exceeded 50 km, occurring as a steady state eruption at ~10^6 m^3 s^{-1} dense rock equivalent (DRE) volume (Wilson & Walker 1985; Wilson & Walker 1987). This method considers the Y5 unit as a single eruptive unit and disregards bedform characteristics and alternating coarse-fine material briefly reported on by Walker (1980), and more recently considered by Houghton et al. (2014). A re-examination of the Y5 deposit by Houghton et al. (2014) derived 26 internal stratigraphical subunits, based predominantly on granulometric features and wall-rock clast abundances. They suggested that the total extent of the deposit defined originally by Baumgart & Healy (1956) and Healy (1964) and refined by Walker (1980), has been exaggerated by a shift in wind direction and the fluctuation of eruptive pulses from columns that reached only between ~35 and 40 km high (Houghton et al. 2014), to produce a variably layered deposit. A new vent site was also proposed through that study, located ~6 km SW of the originally defined site, altering the main direction of deposit axes (*Figure 4.1*).

Although the Y5 eruption has been extensively studied (e.g., Baumgart & Healy 1956; Healy 1964; Walker 1980; Wilson & Walker 1985; Houghton et al. 2010, 2014), there is a lack of detailed quantitative investigation as to vertical variations in deposit characteristics such as granulometry, componentry and the textural features of juvenile material. Observed internal variations within the vertical stratigraphy have been briefly mentioned, but primarily the unit

has been treated as a uniform deposit (Baumgart & Healy 1956; Healy 1964; Walker 1980; Wilson & Walker 1985; Houghton et al. 2010). More detailed investigation into these variations has also remained relatively qualitative (Houghton et al. 2014), where field observations were used as the basis for complex correlations between subtly variable 'sub-units'. Issues arise here where isopleth measurements based on the qualitative correlations of sub-units have resulted in noticeably subtle differences in individual dispersal directions. When comparing the consequent calculations of column heights for each sub-unit (35 – 40 km) to that of the similarly located 3500 BP Waimihia eruption (42 km high; Wilson & Walker 1987), discrepancies are established and the Waimihia deposit is observably less coarse-grained than the Y5 deposit at any given distance from the vent. This is at odds with these column height calculations, as the more powerful of the two events would be assumed to possess the coarser grain size when observed at similar locations. Additionally, the coevally emplaced Early Flow Units (EFU), which have been identified at varying stratigraphic heights in proximal to medial Y5 exposures (Wilson & Walker 1985), have been disregarded in the Houghton et al. (2014) study, and may play an important role in understanding the behaviour of the eruption column and its consequent sedimentation dynamics. Finally, the proposed new vent location apparently lies outside of the caldera produced by the Taupō eruption (Davy & Caldwell 1998; Illsley-Kemp et al. 2021) which is inconsistent with the Y5 event being the second largest phase of the 232 CE eruption sequence. To investigate these discrepancies and add to the knowledge that exists for the Y5 eruption, I use detailed quantitative analyses of deposit characteristics in the vertical stratigraphy and the lateral correlation of bedform features in the deposit to further the understanding of eruption behaviour and sedimentation dynamics in large Plinian eruptions.

4.2 Data

4.2.1 Deposit characteristics

To investigate the variations in the vertical profile of the Y5 fall deposit, an exposed medial section (recently exposed through logging operations) from within the thickest portion of Y5 (Walker 1980) was selected (*Figure 4.1*). This locality satisfies several requirements: 1) there is no evidence of reworking, overthickening, or temporal breaks; 2) it has been

deposited on a relatively flat surface; and 3) it is at a maximum observed thickness for the Y5 deposit in proximity to the overall dispersal axis (Walker 1980).

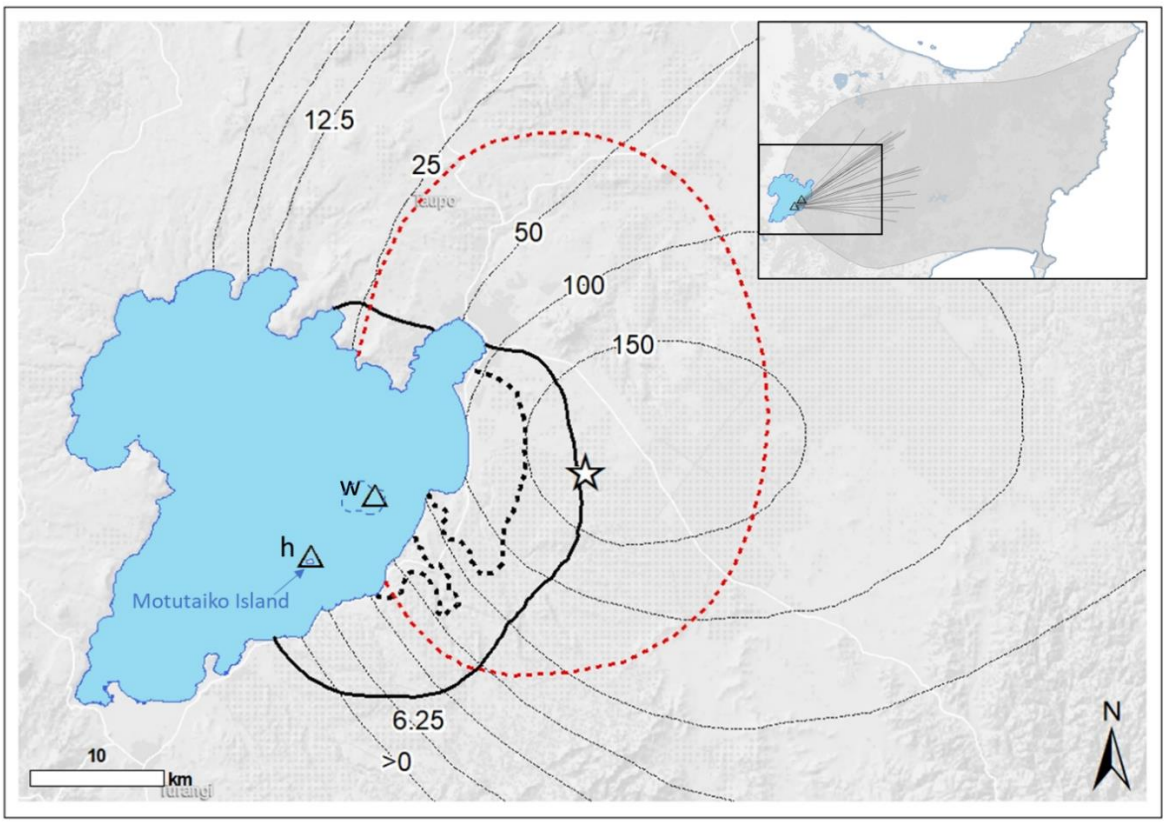

Figure 4.1 Map of the studied field area in context to the whole deposit extent based on Walker (1980), noted in grey in the inset. The grey lines in the inset represent the individual subunit dispersal axes defined by Houghton et al. (2014). The star indicates the selected locality for this study (UTM 60S 428674E 5706559N). Thin, black dotted lines indicate the deposit thickness isopachs with their corresponding measurements in centimetres. The red dotted line is the 64 mm maximum lithic isopleth as defined by Walker (1980). The proximal (thick, black dotted line) and distal (thick, black solid line) extents of the Early Flow Units as identified by Wilson & Walker (1985) are noted. The triangle marked 'W' represents the Walker (1980) proposed vent location and the triangle denoted 'h' represents the Houghton et al. (2014) proposed vent location. Dashed blue line represents the Horomatangi Reefs.

12 bedform features were identified within the deposit at this site, based on fluctuations in grain size and wall-rock clast abundances visible in the field (*Figure 4.2*). Samples were collected from each of these features within the deposit, labelled D-04 at the base to D-15 at the top. D-04 is a distinct fine-ash dominated, yellow-brown bed that is lithic rich with fine-medium lapilli pumice. Red, jarosite 'rusty' oxidized lithics are observed in this unit. It has sharp to 3–5 mm upper and lower contacts and lies atop the lapilli- and obsidian-rich

'plinian-like' G layer of the Y4 (Smith & Houghton 1995a; Smith 1998). Fine ash-depleted airfall begins at D-05, which is lithic rich with coarse ash to fine lapilli sized pumice. Both D-06 and D-07 are also lithic rich, with fine-medium lapilli pumice. They differ in that medium lapilli pumices are yellow stained in D-06 and are of a higher proportion than in D-07, which is predominantly finer grained. The dominance of medium to coarse lapilli pumice begins at D-08, with lithics decreasing in size and abundance. From D-08 to D-15, pumices remain relatively coarse; however, the overall grain size fluctuates. D-10 and D-11 have the coarsest grain size observed, with large pumices (up to 10–12 cm long) dominating the beds with sparse large lithics (up to ~6 cm long). Red, jarosite oxidised lithics are noted to be more abundant in D-12, with the number of lithic components subtly increasing from D-12 to D-14. Lithics are notably more abundant in D-15, with average sizes of ~2 cm. Above this level, the lithic-rich, unconsolidated ground layer of the Y6 ignimbrite (Walker et al. 1981; Wilson & Walker 1982) occurs.

4.2.2 Maximum clast size

The long axes of the five largest pumice and lithic clasts at each sampling interval were measured and averaged to obtain maximum pumice (MP) and maximum lithic (ML) sizes (see Appendix K). Stratigraphic variations in MP and ML are shown in *Figure 4.3*. Following the two basal intervals, two stages of stepwise increase in both MP and ML are noted from D-06 to D-08 and D-09 to D-11, respectively. An additional stage from D-12 to D-15 shows relatively consistent MP values, while ML steadily increases.

4.2.3 Grain size

Grain size data were obtained by dry sieving size fractions at full phi (ϕ) intervals from the 2 ϕ to -6 ϕ size classes, based on the Krumbein (1934) calculation where ϕ is the $-log_2$ of the grain size in mm. Size fractions >2 ϕ were obtained via laser particle analysis (LPA; Horiba Partica LA 950V2). In the case of sample D-04, where fine ash is visibly dominant, fractions >2 ϕ were first sieved out using water to minimize fine ash loss during the dry sieving process. This sample was then dried and treated as per the others. D-04 is defined by a bimodal grain size distribution with modal peaks at 7 ϕ and -1 – 2 ϕ, whereas D-05 to D-15 show coarse-skewed, fine-tail, unimodal distributions with modal peaks ranging from -1 ϕ to -4 ϕ.

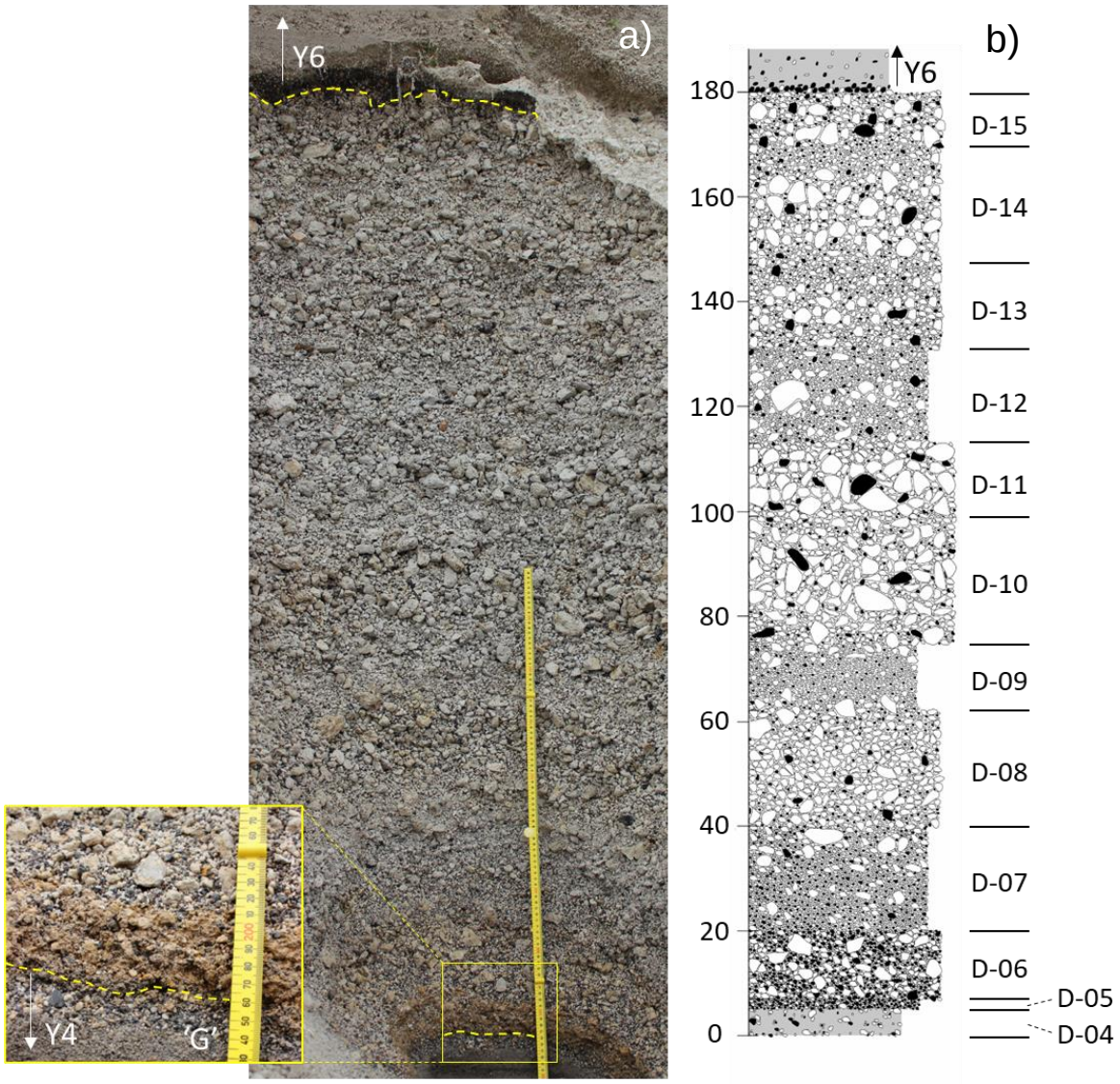

Figure 4.2 a) Photograph of the selected locality with the boundaries between the Y4 (inset) and Y6 deposits identified. Inset: 'G' refers to the final 'plinian-like' G layer of the Y4 phase as defined by Smith & Houghton (1995a). b) Stratigraphic column of the selected locality with each sampled interval marked, where solid grey indicates ash, white is juvenile material and black is lithic material. UTM 60S 428674E 5706559N.

For convenience in description below I use the terms 'total ash' defined as material <1 mm (see *Chapter 2, Section 2.2.1*) and 'extremely fine ash' as <63 µm. Stratigraphical variations in total and extremely fine ash contents (*Figure 4.4*) show a distinct drop in abundance from the ash-rich D-04 (~31 and 21 wt.%, respectively) to D-05 and the remainder of the deposit (averages ~5 and 1.3 wt.%, respectively). *Figure **4.4*** shows that the abundance of total ash in the bulk of the deposit (D-05 to D-14) remains significantly low at <8 wt.% with an extremely fine ash average of 1.3 wt.%. Total ash abundance then increases again at D-15 to 13.1 wt.%, with extremely fine ash remaining low at 1 wt.%.

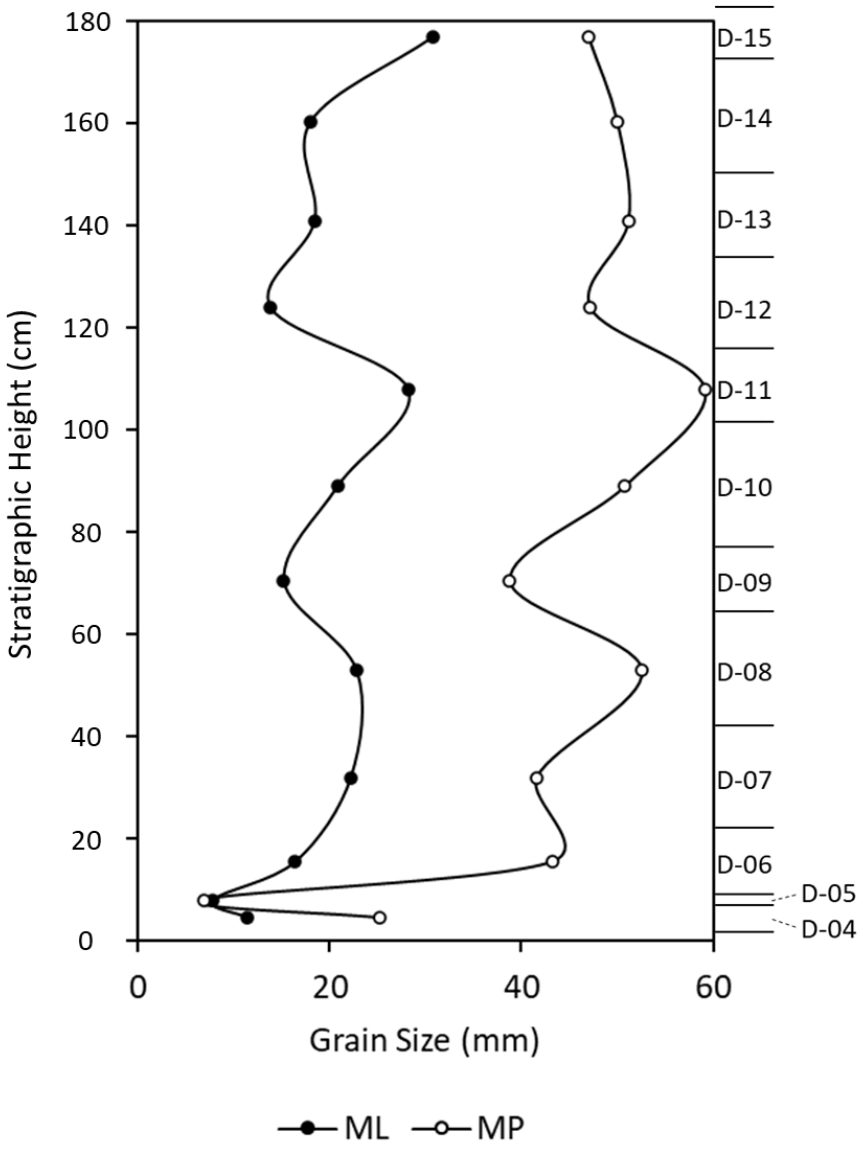

Figure 4.3 Distribution of the maximum lithic (ML) and maximum pumice (MP) sizes in mm with stratigraphic height in the Y5 fall deposit (sampled intervals labelled on the right).

Median grain size (Md_ϕ) and sorting (σ_I) statistics, as defined by Inman (1952), are also shown in *Figure 4.4*. The two basal intervals are relatively fine grained with Md_ϕ of -1 ϕ. A subtle stepwise increase in Md_ϕ is noted, concurrent with MP and ML sizes, from D-06 to D-08 and D-09 to the Md_ϕ maxima (-4 ϕ) at D-11. Md_ϕ then decreases toward D-15. D-04 is poorly sorted ($\sigma_I = 3.\ 6$) compared to the remaining intervals, which are well sorted ($\sigma_I \leq 1.8$; *Figure 4.4*), and I see a faintly defined trend of increased sorting efficiency with increasing Md_ϕ.

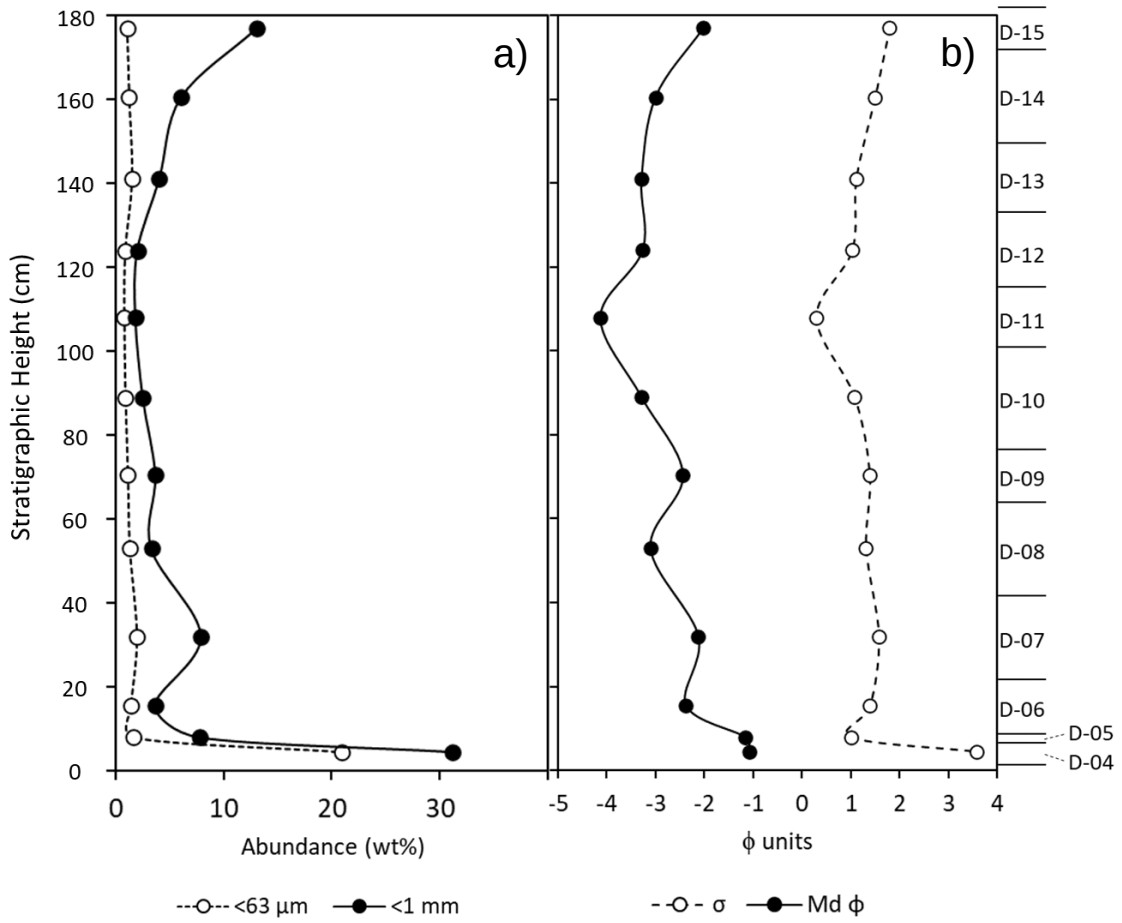

Figure 4.4 a) The abundance of total ash (<1 mm) and extremely fine ash (<63 µm) with stratigraphic height. B) The median grain size (Md_{ϕ}) and sorting (σ_I: Folk & Ward 1957) with stratigraphic height. Sampled intervals labelled on the right.

4.2.4 Componentry

The relative abundance of components in each full ϕ size class <2 ϕ was determined for all sampled intervals. Components were divided into four broad fragment classes of: 1) pumice; 2) wall-rock lithic (henceforth, lithic); 3) crystal; and 4) obsidian. The pumices are variably vesicular, predominantly white to cream coloured with little to no alteration and are the most dominant component of the deposit. Lithics encompass all non-juvenile components, including pre-232 CE rhyolite lavas, foreign crystals derived from older porphyritic lavas, and pumice (i.e., Chernet 1987), fragments of Huka Group sediments (i.e., Chernet 1987; Cattell et al. 2016), and plutonic microdiorites and granitoids (i.e., Chernet 1987; Brown et al. 1998). Juvenile crystals are dominantly plagioclase and pyroxene, with minor

titanomagnetites. Juvenile obsidians were determined based on fresh, conchoidal fracture surfaces and the lack of alteration or surface-adhesive ash.

The total relative abundance of components in each sampled interval was calculated by normalizing the wt.% of components in each grain size to the measured weight of that grain size and then collated for each component class. The assumption is made that, given material >2 ϕ makes up on average <2 wt.% of each sampled interval, the total relative abundance of components <2 ϕ is representative of that for the whole deposited interval.

Obsidian is rare within the Y5 deposit, with the total abundance of 2 wt.% in D-04 diminishing to <1 wt.% in the above sampled intervals. D-04 and D-05 have a distinctly different component distribution than the bulk of the deposit, with higher lithic abundance than pumice (~60 vs. ~30 wt.%, respectively; *Figure 4.5*). In D-06, pumice becomes dominant until D-15, where lithic abundance again increases. Crystals are an overall minor component at <10 wt.% (*Figure 4.5*), however minor fluctuations can be noted coinciding with finer intervals in the Md_{ϕ} distribution (*Figure 4.4*). Higher crystal abundances are noted at D-04, D-05 and D-07, and increase from D-13 to a peak at D-15. From D-06 to D-08, lithics show a distinct decreasing trend from ~37 – 21 wt.%, while pumices increase by ~14 wt.%. Pumice and lithics then remain relatively constant at ~78 wt.% and 15 wt.%, respectively, from D-09 to D-11, before exhibiting fluctuation in abundance from D-12 to D-14 with peak pumice content of ~90 wt.% at D-12.

An additional component type has also been categorized: CP) composite pumices (*Figure 4.6*). These have been rarely described in sub-plinian to plinian eruptions (Taddeuchi & Wohletz 2001; Kuehn 2002; Giachetti et al. 2021) yet seem to be an important component for understanding fragmentation. Giachetti et al. (2021) propose that these agglomerated clasts form during low energy collisions just above the fragmentation zone, where the unfragmented magma sits directly below the fully fluidized gas-pyroclast mixture and individual pyroclasts can sinter together. Another possibility of formation arises specifically for the Y5 phase, where welded EFU material from the vent area is recycled during the eruption. CP clasts are dominantly composed of pumice fragments but may have minor amounts of lithic inclusions <1 mm in size. The pumice fragments range from millimetre to centimetre in size and are sintered within a light orange-red pumiceous matrix, similar in colour to proximal EFU products (Wilson & Walker 1985). Typically a combination of both

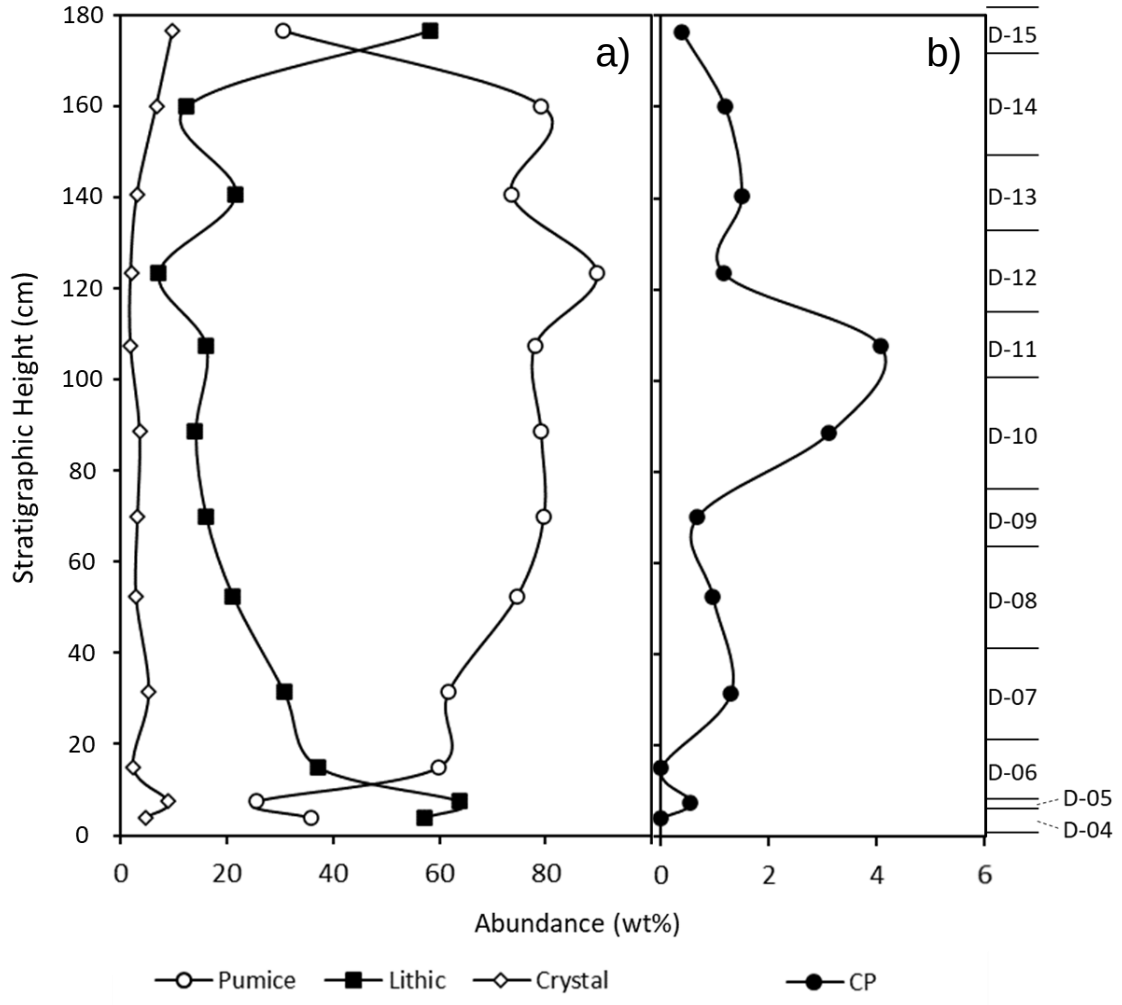

Figure 4.5 a) The total abundance (in wt.%) of pumice, lithic and crystal components with stratigraphic height. b) The total abundance (in wt.%) of composite pumices (CP) with stratigraphic height. Sampled intervals labelled far right. Note the difference in x-axis scale between left and right.

micro- and macrovesicular pumices, the clast inclusions are light cream in colour and the direction of vesicle alignment vary between them (*Figure 4.6*). Individual pumice fragments retain their original vesicle orientations, with directions appearing random between each fragment during amalgamation. The pumiceous matrix material, however, shows fabric distortion around the pumice fragments (*Figure 4.6*). In the overall CP clasts, vesiculation is more prominent in the center of the clasts with larger vesicles evident, becoming smaller toward the outer edges. CP is a sparse component with abundances of <5 wt.% in the whole deposit. There has been no CP clasts identified within D-04 or D-06, and for the remainder of the deposit it is dominant in the coarser grain size fraction concurrent with the Md_{ϕ} distribution (*Figure 4.5*). A trimodal distribution is identified with stratigraphic height and

three main peaks are noted at D-07, D-11 and D-13. D-11 has the highest abundance at ~4 wt.%.

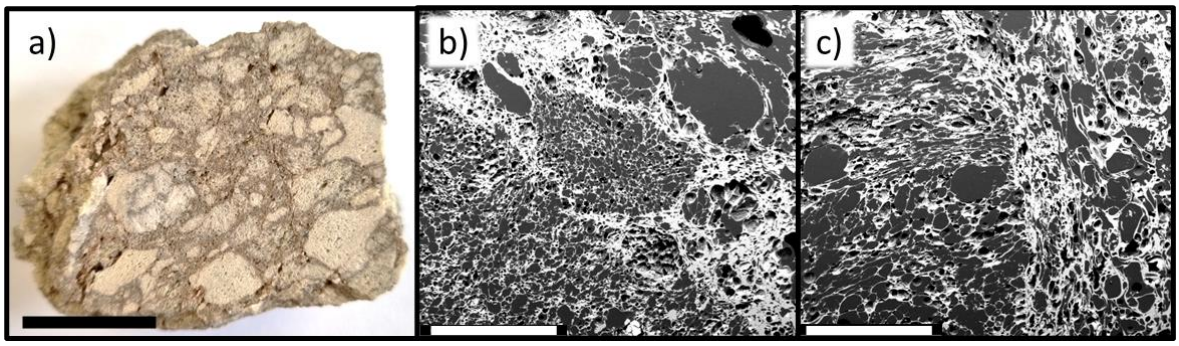

Figure 4.6 a) Cut surface of a composite pumice (CP) clast with black scale bar of 1 cm; b) SEM backscatter image of an ~1 mm sized vesiculated pumice (centre) sintered to a larger vesiculated pumice (bottom left): note the negligible vesiculation in the supporting matrix; c) Sintering of two pumices with contrasting vesicularity orientations. Scale bars in panels b) and c) are 1 mm long.

4.2.5 Pumice types

Pumices were further distinguished according to their observed vesicularity and textural characteristics. Although texturally transitional, three distinct pumice types can be defined: J1) microvesicular pumice; J2) macrovesicular pumice; and J3) sheared/ tubular pumice (*Figure 4.7*). All pumices are white to cream coloured with no pervasive alteration and phenocrysts are relatively rare, estimated by Walker (1980) to occur as 3 wt.% of the pumices. Predominantly, vesicles of the J1 pumices are <100 µm; however, two vesicle populations may be present with clusters of vesicles >100 µm comprising no more than ~25 % of the void space within a clast. Vesicles are spherical to irregular in shape and exhibit minimal coalescence. Shearing is evident, with some vesicles showing zones of elongation. J2 pumices have vesicles predominantly >100 µm with thin bubble walls. They are spherical or irregular to convoluted and exhibit moderate degrees of coalescence. Minor shearing is evident, with some vesicles showing zones of elongation. J3 pumices are strongly sheared, often presenting a visible sheen perpendicular the main axis of shear. Vesicles are predominantly collapsed or elongated due to shearing with only minor zones of larger vesicles remaining. The internal textures of these clasts are complex and, as with J2 clasts, plagioclase phenocrysts may provide points of increased nucleation for vesicles.

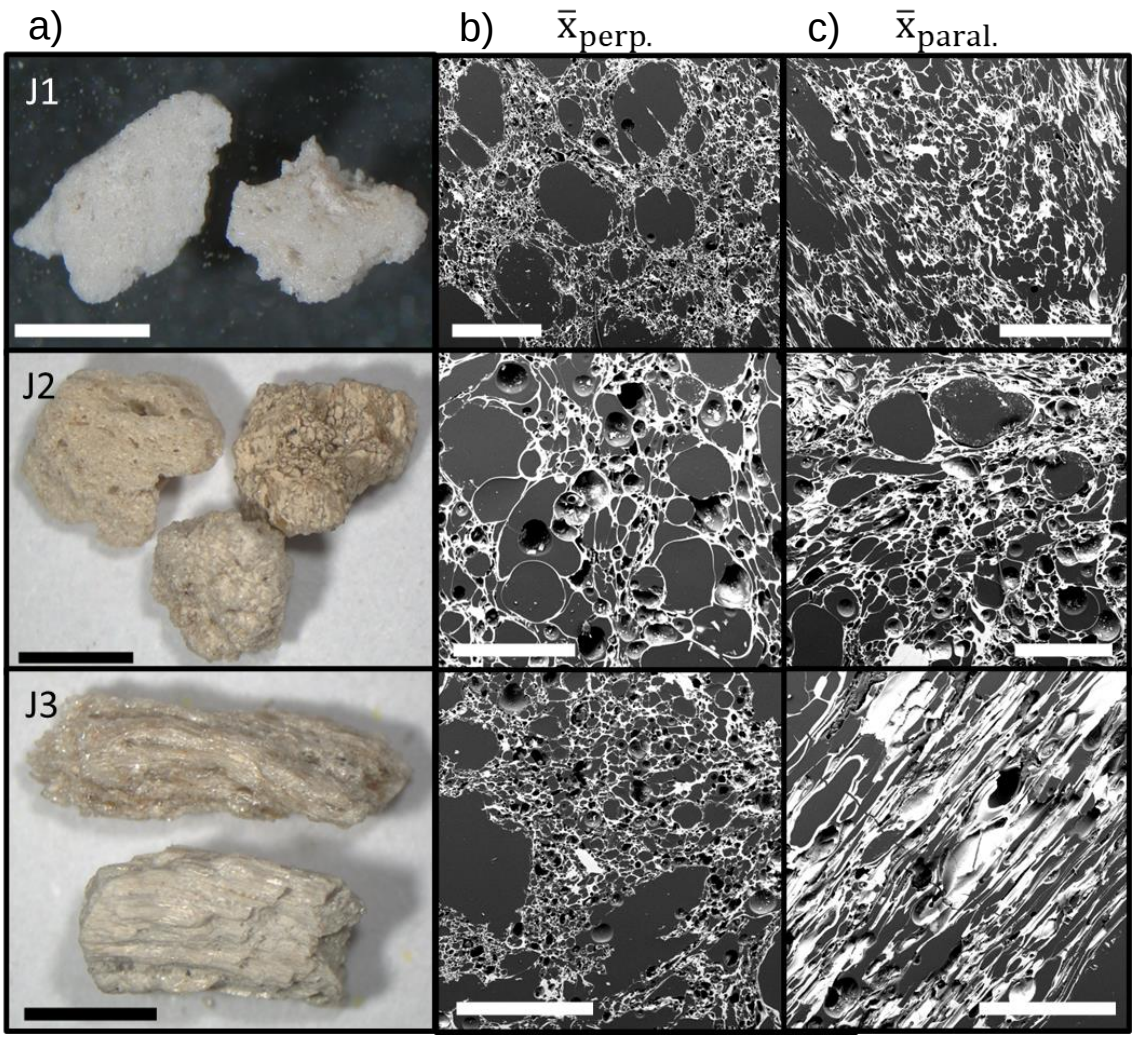

Figure 4.7 a) Examples of microvesicular (J1), macrovesicular (J2) and sheared (J3) pumices where the black bar represents a 2 mm scale. b) Backscattered SEM images of thin sections of the associated pumice type selected from the mean density bin and cut perpendicular to the observed direction of shear. c) Backscattered SEM of thin sections of the associated pumice type selected from the mean density bin and cut parallel to the observed direction of shear. White bars in middle and right represent 500 µm.

The total component abundance for each pumice type was determined as previously and normalized to J1+J2+J3=100 wt.%. J1 pumices dominate the deposit (*Figure 4.8*), while J3 clasts are on average a less significant component, making up <23 wt.% of the pumices. J3 remains low and the range between J2 and J1 abundance is relatively consistent from D-04 to D-07. From D-08 to D-15, J1 pumices consistently decrease in abundance from 67 wt.% to 35 wt.%, while J2 pumices show a stepwise increase. J3 fluctuates throughout this interval (*Figure 4.8*) but shows an overall increase in abundance relative to J1 and J2.

4.2.6 Pumice density and porosity

Pumice bulk density and vesicularity measurements were performed according to methods outlined in Houghton & Wilson (1989) and Shea et al. (2010) on 100 pumices, 16–32 mm in size, collected from each sampled interval except D-05 (due to its fine grain size). Two density populations are identified (*Figure 4.9*) by a distinct shift between D-07 and D-08, where the average bulk densities in the lower and upper populations are 634 ± 9 kg m^{-3} and 568 ± 13 kg m^{-3}, respectively. Peak vesicularity (78 %) occurs at the onset of this shift (D-08) and then wanes with height, contemporaneous with the peak and overall depletion of J1 normalised abundance.

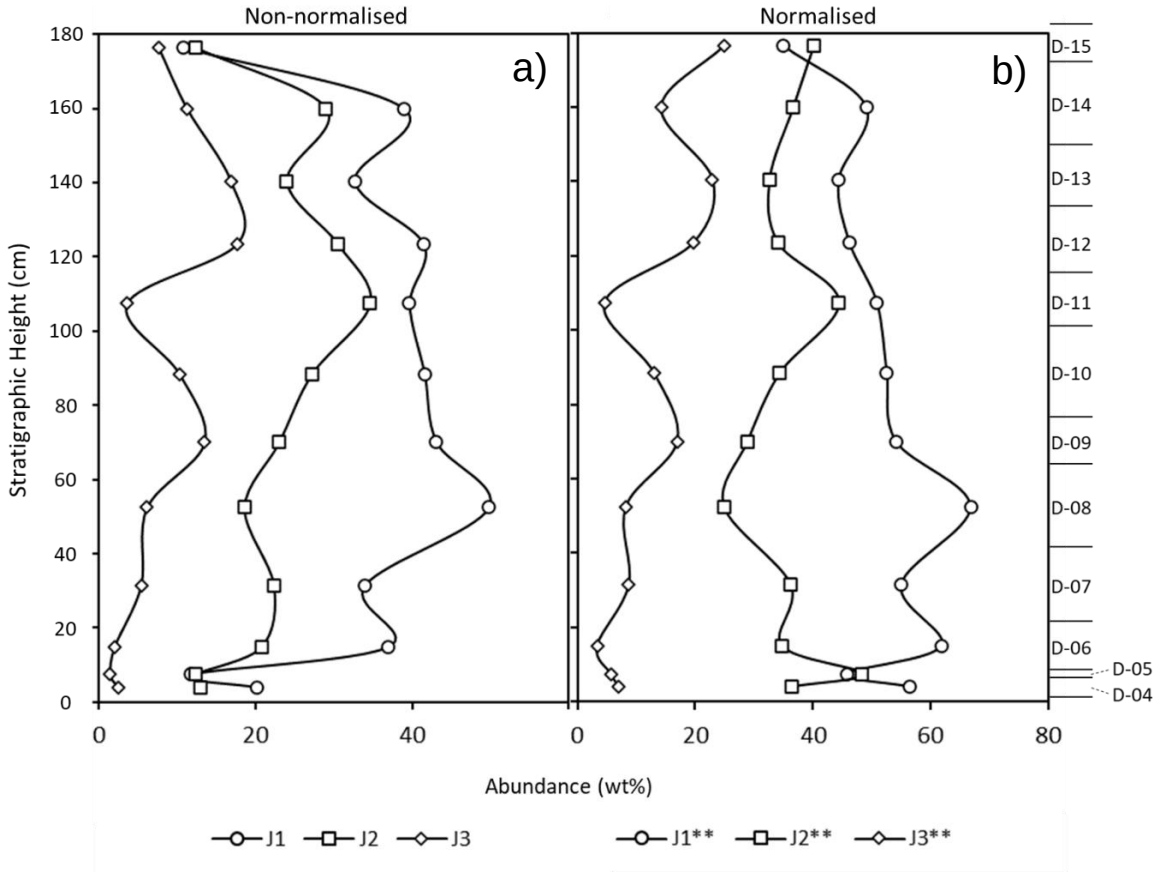

Figure 4.8 a) Total abundance (in wt.%) of pumice components (J1, J2, J3) with stratigraphic height. b) The total abundance (in wt.%) of pumice components normalised to J1+J2+J3=100 wt.% with stratigraphic height. Sampled intervals labelled on the right.

Bulk density measurements were also conducted on pumices from each of the components J1 to J3. For pumices 16 – 32 mm, measurements were obtained according to the methods

of Houghton & Wilson (1989). Pumices were taken from the componentry intervals that had all three types present within this grain size. J1 and J2 are dominant, so to gain a representative quantity of all three pumices, the quantity in each sampled interval was calculated as a normalization to the amount of J3 available. As a result, 100 clasts of each of J1 and J2 were collected and 65 J3 clasts. The variation in bulk density of the pumice types is negligible (*Figure 4.10a*), with average densities differing by only ~14 kg m^{-3}.

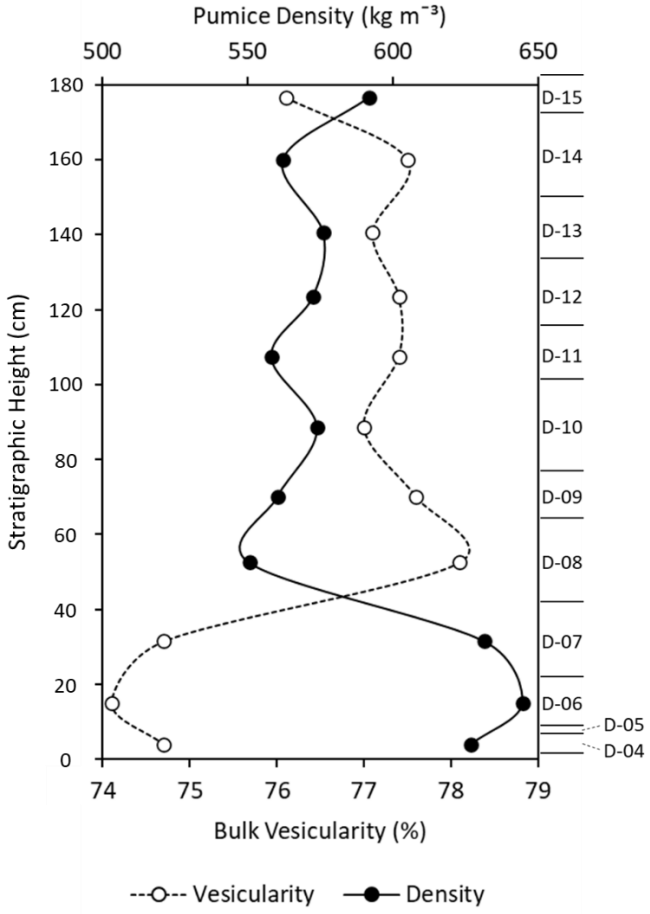

Figure 4.9 The distribution of bulk pumice density (top axis) and bulk vesicularity (bottom axis) of pumices from the 16 – 32 mm size range (based on methods outlines in Houghton & Wilson 1989) with stratigraphic height (sampled intervals labelled far right). Note that L-11 does not have a data point.

For comparison, bulk density measurements were conducted on >100 pumices from each juvenile component type within the 4–8 mm size range using Micrometrics GeoPyc DryFlo pycnometry, which measures the volume and density of a clast by displacement of a solid,

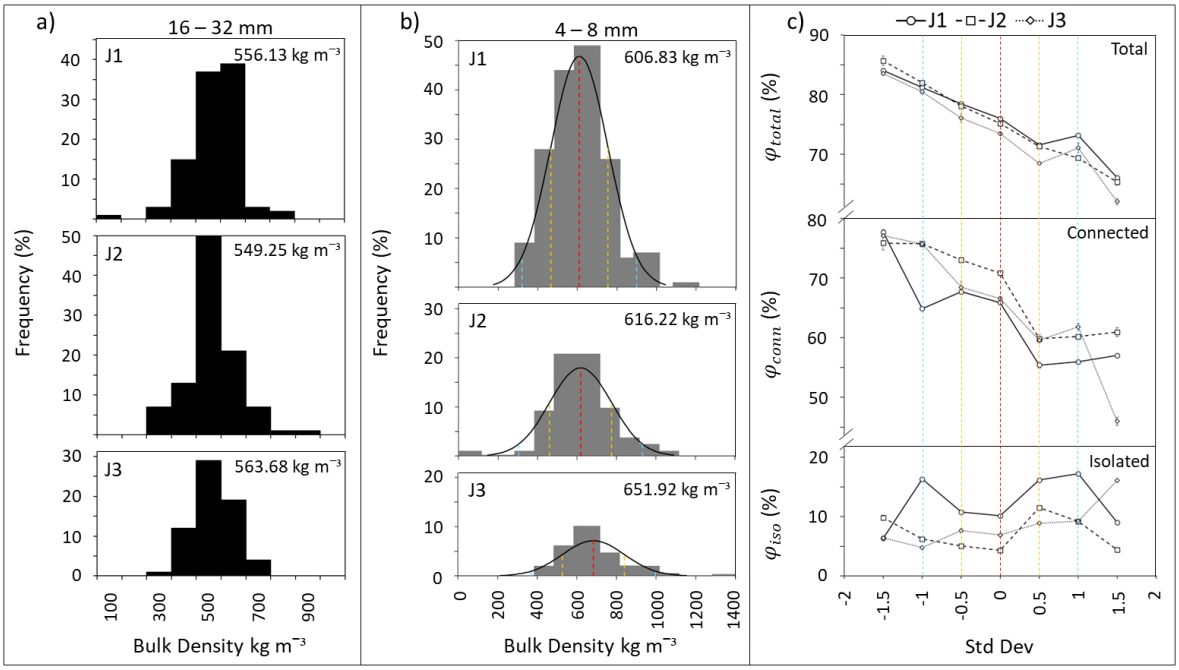

Figure 4.10 a) Bulk density distributions of pumice types from the 16–32 mm size range based on methods outlined in Houghton & Wilson (1989). The mean density for each is noted in the associated top right corners; b) Bulk/ envelope density histogram and bell curve distributions of pumice types from the 4–8 mm size range obtained using Micrometrics GeoPyc DryFlo pycnometry. The mean density for each is noted in the associated top right corners, also indicated by the red dashed line. Yellow and blue dashed lines indicate the ±0.5 and ±1.0 standard deviations of density, respectively; c) The total (top), connected (middle) and isolated (bottom) porosity distributions of each pumice type from the mean (red dashed) and standard deviations (yellow and blue dashed lines) of density as outlined in panel b).

flowable, close-pack medium. Smaller pumice sizes do not capture larger vesicle size populations (Houghton & Wilson 1989); therefore, these measurements show denser values than the 16–32 mm size range. J1 and J2 clasts have similar mean densities and distributed ranges (*Figure 4.10b*), while J3 exhibits a higher mean density of 651 kg m^{-3}. From the pycnometry bulk density distributions of J1 to J3 pumices, clasts were selected from the mean and each ±0.5, 1 and 1.5 density standard deviation (std dev) bins for further analysis of total- (φ_{total}), connected- (φ_{conn}), and isolated-porosity (φ_{iso}) estimations using helium pycnometry (Klug & Cashman 1996; Klug et al. 2002; Wright et al. 2009). The three pumice types show strong negative correlation of φ_{total} and φ_{conn} with increasing density, while φ_{iso} indicates no significant correlation (*Figure 4.10c*). J1≈J2 φ_{total} with J1 clasts only having a higher φ_{total} by <0.1 % for the mean ± 0.5 std dev, while J3 pumices have ~2 % lower φ_{total} values. φ_{conn} is, in contrast, higher in J2 pumices at av. 71 % while J1 and J3 pumices have

low φ_{conn} of ~66 %. J1 pumices also exhibit the highest percentage of isolated vesicles, while J2 has the least at a range of av. 6 %.

4.2.7 Lithic types

Lithic types were subdivided by their inferred stratigraphic depth of origin based on previous investigations of the Taupo area (i.e., Chernet 1987; Brown et al. 1998; Cole et al. 1998; Cattell et al. 2016). Three broad groups are defined (*Figure 4.11*): F1) pre-232 ± 10 CE volcanic material at depths of ~0 – 400 m (Chernet 1987; Wilson 1993; Wilson et al. 2009); F2) Huka Group sediments and minor Whakamaru ignimbrite material and hydrothermally altered clasts from ~400 – 3000 m (Chernet 1987; Cattell et al. 2016); and F3) plutonic microdiorites and granitoids at depths >4000 m (Chernet 1987; Brown et al. 1998). F1 clasts (*Figure 4.11a*) are predominantly rhyolite lava fragments with typically minor to no alteration, except for hydrothermally altered jarositic fragments, and are sometimes spherulite-bearing and/or flow banded. Pervasively stained pumices are a minor component and are micro- to macro-vesicular, rounded clasts that range in colour from pink and light yellow to dark orange/brown. Obsidians are also present and are primarily red or black with rounded edges, minimal conchoidal fracturing and commonly abraded surfaces with adhering fine ash. The altered pumice and obsidian are defined as products of previous eruptive activity of the Taupo area (e.g., Chernet 1987; Brown et al. 1998). F1 clasts dominate the lithic componentry of the Y5 deposit, comprising on average ~73 wt.% of total lithics. F2 clasts are dominated by the shallower lacustrine sediments of the Huka Group as defined by Cattel et al. (2016; *Figure 4.11b*). They are comprised of silts, volcaniclastic tuff, monomict and polymict breccias and coherent lavas with strong alteration rims. Minor abundances of deeper seated Whakamaru ignimbrite material is noted in the F2 class, as well as green, hydrothermally altered pumices and obsidian. Plutonic microdiorites and granitoids (F3; *Figure 4.11c*) are rarer accessory lithics (<8 wt.%) defined by their microcrystalline, equigranular nature and are not considered primary xenoliths from the magma chamber (Chernet 1987). Granitoids are regarded as crystallised portions of historic zoned silicic Quaternary TVZ magma chambers, while microdiorites are considered intrusive equivalents of high alumina basalts from the central TVZ (Brown et al. 1998).

Lithic types were subdivided for each grain size <2 ϕ and it was noted that F1 clasts became more dominant as grain size increased due to their higher resistance to breakage in

comparison to the more fragile F2 and F3 components. Total component wt.% is overshadowed by the abundance of F1 clasts in the coarser fraction (i.e., *Figure 4.12*) and finer grain sizes provide better insight into the overall relationships between lithic component abundances. The size fraction of lithics investigated is therefore important for understanding the evolution, collapse and clearing of the conduit system. In the overall deposit, lithics may be diluted by juvenile fragments at high MDR, or more friable lithics may be overprinted by those that have a higher likelihood of persisting in larger grain sizes. In the case of the Y5 deposit, F2 and F3 clasts are only present in the finer grain sizes as they are more easily fragmented than the durable F1 rhyolitic lavas. This hinders the analysis of the relationships between lithic component abundance and conduit behaviour as, for dominantly coarse-grained deposits, I only see the apparent behaviour of the most durable components. Considering this, the 1 ϕ grain size was selected for comparison of lithic types as this size fraction contained all component types and the inference of low Stokes-number particle-gas coupling suggests that there is little influence of density on preferential sedimentation or gravitational settling for this grain size (Lherm & Jellinek 2019), hence providing a good representation of the behaviour in the conduit.

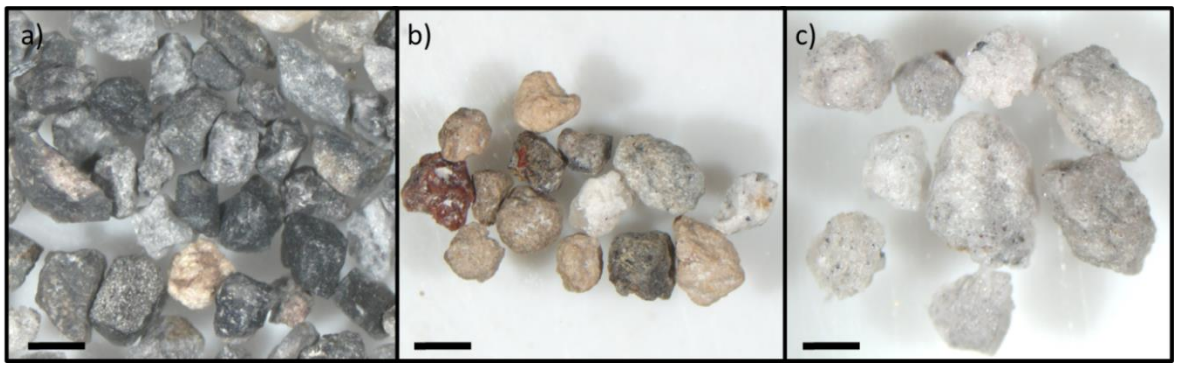

Figure 4.11 Examples of the lithic components from the Y5 deposit: a) shallow-seated F1 fragments; b) F2 Huka Group sediments and volcaniclastics; and c) F3 deep-derived crystalline intrusives. Scale bars are 2 mm. Reproduced from Chapter 3, Fig 3.5.

The 1 ϕ lithic abundances were normalised so that F1+F2+F3=100 wt.%. F2 dominates the lithic fraction at D-04, ~6 wt.% higher than F1 clasts, while F3 abundance is minimal (<2 wt.%; *Figure 4.12*). From D-05, F1 lithics dominate the remainder of the deposit. At D-06 to D-08, I see the range in abundance with height between F1 and F2 narrow, from 32 wt.% to 11 wt.%. F3 clasts show a peak of 5 wt.% at D-06, decreasing to 1 wt.% at D-08.

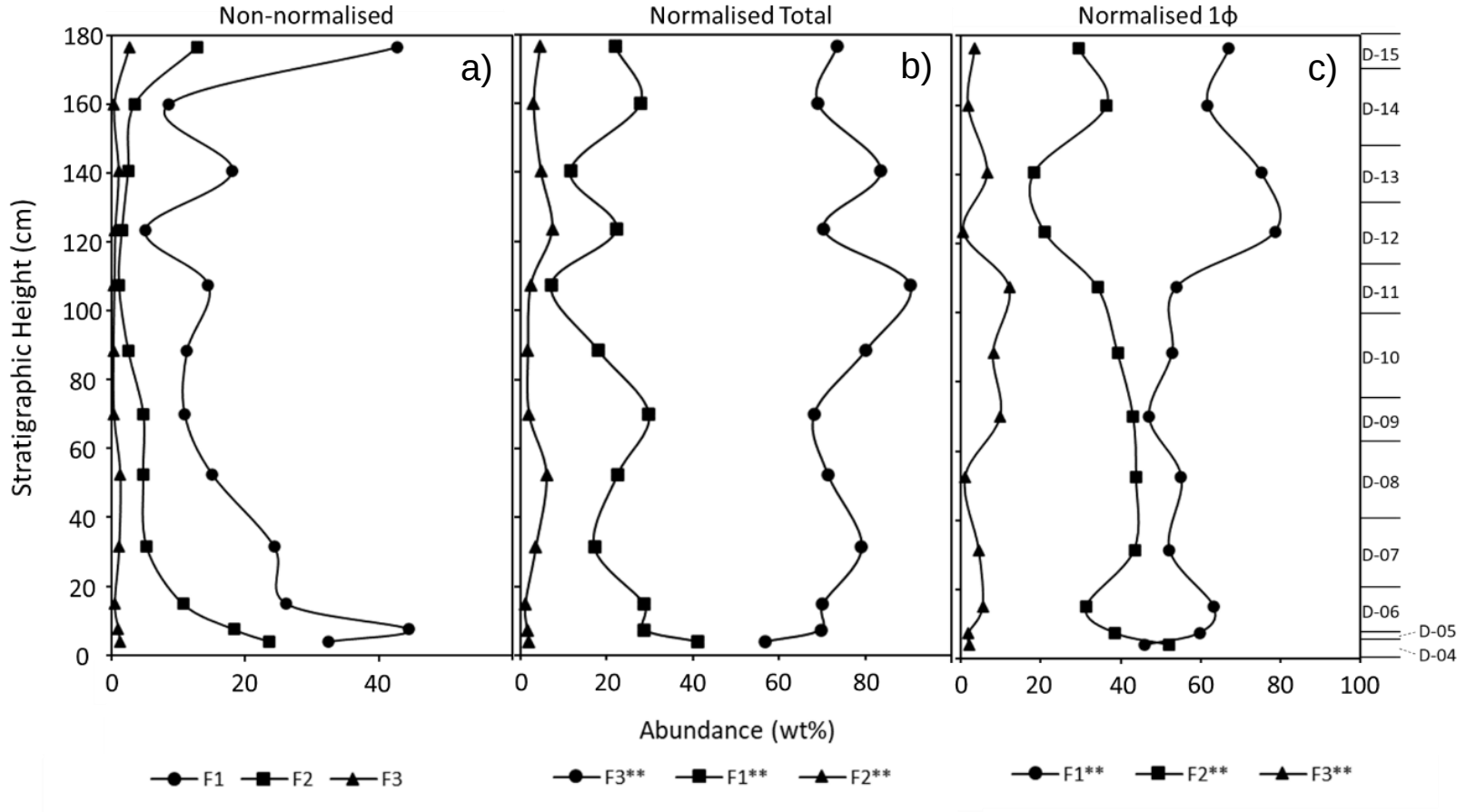

Figure 4.12 a) The total abundance (in wt.%) of lithic components with stratigraphic height. b) The total abundance (in wt.%) of lithic components normalised to F1+F2+F3=100 with stratigraphic height. c) The abundance of lithic components in the 1 ϕ size fraction normalised to $F1_{1\phi}+F2_{1\phi}+F3_{1\phi}=100$ with stratigraphic height. Sampled intervals labelled on the right.

A sudden shift to higher abundances in F3 (av. ~10 wt) from intervals D-09 to D-11 is noted, where D-11 is attributed to the highest overall abundance of F3 (12 wt.%). Simultaneously, the range between F1 and F2 clasts increases, from 4 wt.% at D-09 to 20 wt.% at D-11. The interval from D-12 and D-15 has the overall largest range in abundance between F1 and F2, where F1 dominates the lithic fraction.

4.2.8 Additional field observations and bedform correlations

Extensive field observations were also conducted within the proximal to medial areas of the whole deposit to examine the correlatability of the qualitative sub-units identified by Houghton et al. (2014). Note that the total thickness of the Y5 exposures is variable to an unknown extent, attributed to erosion caused by the deposition of the Y6 ignimbrite. Proximal Y5 deposits and those predominantly in the northern and north-eastern zone of deposition have associated intraplinian PDC deposits, strongly developed proximally, becoming thin ash-rich beds in more medial zones (out to ~15 km of Lake Taupo). D-04 equivalent units are identified to occur up to ~23 km from the Walker (1980) vent site. Both distinct and gradational fluctuations in bedform characteristics in the vertical Y5 stratigraphical profile are identified amongst deposit exposures. These are, however, noticeably difficult to correlate between various outcrops in both proximal and medial regions due to the subtle fluctuations in granulometry and lithic content, which is contradictory to the observations made by Houghton et al. (2014).

To investigate the complexities in lateral correlatability of such bedform characteristics, a series of exposures were studied in the Wairakei Estates area that extended for ~4000 m. At these exposures, the unit Y5 had: 1) relatively uniform thickness, 2) evidence of deposition onto a topographically even landscape and 3) no evidence of reworking or internal erosion (*Figure **4.13***). Exposures were cleared at logarithmically spaced intervals from 0 m up to 64 m distance apart, and then two at 3500 m and 4000 m from starting point. The focus was several bedform features: 1) a boundary with a distinct change in grain size; 2) two bands with gradational fluctuations in grain size; 3) the lower zone of lithic rich air fall; and 4) ash rich distal PDC deposits. As seen in *Figure 4.13*, (1) is defined by a change in grain size from fine grained pumice lapilli to coarser, angular pumice lapilli. This bedform can be confidently correlated over distances of a few metres to almost 100 metres; however, at a few km distance it is noticeably more difficult to discern, and correlation becomes

challenging. Additionally, this distinct feature was identified in an exposure 10 km south-west of the 0 m exposure: however, this feature has not been noted elsewhere in the deposit. Midway in the sequence are gradational bands of predominantly coarse pumice identified as feature (2). These are very noticeable in the initial 1 m extent of *Figure 4.13*, can be confidently correlated up to 2 m, yet beyond this these features become obscure. Lower bedform characteristics (3) and (4) appear to be more uniform through the extent of the observed deposit. Lithic rich zones are identified in the basal zone of each section, interbedded with a relatively well-defined ash band. This ash band does pinch and swell at some locations, as do the lower lithic rich zones, however both features are identifiable in all exposures up to 4000 m apart (*Figure 4.13*).

4.3 Discussion

4.3.1 Onset of the Y5 eruption

The distinct, ash-rich D-04 at the base of the studied locality D is interpreted to represent the onset of the Y5 phase of the eruption and analysis of components suggest that this was concurrent with a change in vent position from that of phase Y4. The high proportion of lithics at the base of the deposit, which are distinctly dominated by F2 components, suggests a vent clearing stage where a significant quantity of pre-Oruanui material was excavated. Similarities have been observed between the F2 lithics in the Y5 and those of the Y2 (Walters 2020), which may be attributed to analogous regions of country rock excavation and could be interpreted to suggest a vent location comparable to that of the Y2 eruption. Further investigations into the behaviour of the vent at the onset of the Y5 and the transitioning phase between the Y4 and Y5 eruptions are considered in *Chapter 3*.

The adherence of fine ash to the coarse particles in the D-04 unit is considered indicative of the presence of water during the onset of Y5. As the topography of the Y5 vent at the time of eruption is not constrained, this may suggest that water existed around its periphery in the initial stages of eruption. This, along with other features such as the granulometric bimodality of the unit, are comparable to those seen in co-PDC or co-plinian deposits of other explosive eruptions (i.e., Soufriere Hills, Bonadonna et al. 2002; Mt Pinatubo, Dartevelle et al. 2002; Fuego, Rose et al. 2008; Tungurahua, Eychenne et al. 2012). We rule out the possibility of the fine ash in the D-04 being a product of co-PDC or co-plinian ash

from the cessation of the Y4, based on the distinct colour difference between the finest ash component in the Y5 and that in the Y4 deposits. Gradational upward waning of ash content would also be expected in this case, as suspended ash in the atmosphere is slowly exhausted and the distinct upper boundary of the D-04 (*Figure 4.2*) again rules out this possibility. The sharp upper contact and ash rich nature of D-04 may instead indicate that this unit may result from peripheral or independent column collapse forming a hybrid PDC-airfall deposit, however another possible scenario arises when looking at ash rich beds in the Hatepe plinian (Y2) deposit. Like the Group C beds identified by Talbot et al. (1994) the bimodal, the ash rich D-04 unit may have deposited due to scavenging during local rain showers that passed through lower lying ash clouds as lapilli pumice has continued to sediment (Talbot et al. 1994; Walters 2020).

4.3.2 Temporal evolution of the Y5 eruption

When looking at proximal to medial regions of the Y5 deposit, it is clear that internal complexities in the vertical stratigraphy vary greatly (e.g., *Figure 4.2*, *Figure 4.13*). Previous interpretations have defined this deposit as a simple plinian deposit (Walker 1980). However, fluctuations in grain size throughout the vertical stratigraphy (Walker 1980; Houghton et al. 2014) as well as the presence of co-plinian PDC deposits in proximal zones (Early flow units of Wilson & Walker 1985), suggest that this deposit may be defined more confidently as a simple-stratified plinian deposit (Cioni et al. 2015). Insights into the granulometric and componentry data gathered across vertical complexities in the purely airfall deposit (D-05 upwards) shows a relatively continuous trend in the eruption progression. Based on the simple interpretation that reverse grading reflects an increase in mass discharge rate (MDR) – that is, as the eruption increases in intensity, and therefore column height, larger pyroclasts are transported to increasingly greater distances (Wilson et al. 1980; Sparks 1986; Mastin et al. 2009; Bonadonna et al. 2015a, b) – the granulometric data allow for generalized assumptions to be made regarding the MDR and plume height of the Y5 eruption. In the Y5 deposit, an overall reverse grading and decrease in ash content toward D-11 suggest a steady increase in eruptive plume height and consequently, MDR, concurrent with interpretations made by Walker (1980; *Figure 4.4*). From here, the plume slowly begins to wane, marked by a normal grading trend and a subtle increase in ash content. MP and ML support this trend, with peak pumice and lithic sizes occurring at D-11, and an increase in both from D-05 to D-11, followed by a lesser clast size from D-12 to D-

15 (*Figure 4.3*). Bed D-15 exhibits another peak in ML and ash content, possibly associated with the onset of conduit collapse in the final stages of the eruption prior to Y6 ignimbrite emplacement, discussed further below.

Bulk vesicularity of the pumices in the vertical profile show that the onset of Y5 (D-04 to D-07), with av. 75 % vesicularity followed by a 3.4 % increase from D-07 to D-08 (*Figure 4.9*), likely involved a narrower conduit, leading to lateral vesicularity gradients in the magma due to boundary effects at the conduit margins (Cioni et al. 2015). This interpretation is also supported by an overall lower abundance of the dominant J1 pumice type in this region.

The relative abundance of lithic components in the deposit informs the evolution, collapse and clearing of the conduit system as a function of conduit erosion and MDR. For example, if MDR decreases, the likelihood of conduit wall collapse increases, which is preserved in a deposit as an increase in shallow-seated lithic abundances (Tadeucchi & Wohletz 2001; Cioni et al. 2015). Conduit widening may also result in a higher abundance of lithics in the deposit; however, if MDR also increases this lithic footprint may be diluted by juvenile material (Varekamp 1993; Tadeucchi & Wohletz 2001). The high lithic:pumice ratio in D-04 and D-05 is interpreted to reflect an initial conduit clearing event (*Figure 4.5*). This is followed by conduit erosion and widening from D-06 to D-07, at lower MDR relative to the bulk of the eruption, where the pumice:lithic ratio changes yet the abundance of lithics remains relatively high. The lithic content then decreases continuously as MDR increases toward climax, consistent with the increase in juvenile content and decrease in crystals. Following this, the fluctuation in the relative abundance of lithics and pumice indicates a likely period of instability within the conduit as the eruption begins to wane toward D-15, where the lithic abundance increases and exceeds the proportion of pumice (*Figure 4.5*), consistent with an episode of conduit wall collapse prior to the Y6 event.

4.3.3 Temporal evolution of conduit stability

Here the types of lithic fragments are considered as an aid to understanding the evolution of fragmentation depth if the existing stratigraphy of the vent area is known (Barberi et al. 1989; Suzuki-Kamata et al. 1993; Macedonio et al. 1994; Taddeucci & Wohletz 2001; Pittari et al. 2008; Mele et al. 2011; Cioni et al. 2015; Houghton & Carey 2015). The total abundance of each of the lithic components, F1 to F3, show an overall domination of F1 clasts, while F2

starts with relatively high abundances, gradually decreasing toward the eruption climax, and F3 remain relatively minor (*Figure 4.12*). It can be noted that the proportion of overall lithics in the analysed locality is likely influenced by the grain size of the deposit. Pumice dominates especially in the coarser zones, and therefore as relative grain size increases, lithic fragments are diluted. Similarly, F1 clasts dominate the larger grain sizes (i.e., *Figure 4.12*, *Figure 4.14*) and the more friable sediments or crystalline components (F2 and F3) are relatively reduced as grain size increases. Therefore, although we see a higher portion of F2 fragments in the lower portion of the deposit (*Figure 4.12*), this may be a by-product of the finer overall grain size, rather than an indicator of deeper fragmentation. To account for this, as mentioned previously, the 1 ϕ grain size was selected to represent the relationships between lithic abundances and the associated conduit dynamics (i.e., *Figure 4.5*, *Figure 4.14*).

The relative vertical abundance of lithics in the 1 ϕ grain size show three main trends (disregarding D-15) which indicates that, within the overall continuous nature of the eruption, several transient stages have occurred. At the onset of phase Y5, F1 and F2 clasts dominate the deposit componentry, with F2>F1, inferred to represent the clearing of the vent as the fragmentation front likely developed at or shallower than the depth of the pre-Oruanui material. Conduit growth and excavation is then marked by a rapid increase in abundance of shallow seated lithics. At the time of D-07, the fragmentation front deepened, and excavation of the shallower conduit decreased, as F1 and F2 abundances generally begin to equalize. The initial phase of conduit clearing and excavation is also supported, as previously mentioned, by the total abundance of non-normalised lithic components in the deposit (*Figure 4.12a*) where F1 and F2 clasts are of a higher proportion at the base of the deposit, slowly decreasing in abundance with stratigraphic height. Similarly, the higher density of pumices and finer grain size in this region indicates the likelihood of a narrower vent and lower MDR than the remainder of the Y5 phase (Cioni et al. 2015). The eruption is then marked by a phase of deepening fragmentation (increased F3) likely associated with the continued excavation of magma and decrease in pressure in the magma chamber toward the climactic part of the eruption (Mullet & Segall 2021). The range of abundance between F1 and F2 clasts remains consistently narrow as F2 sediments slightly decrease with height. This indicates that the erosion rates of relatively unconsolidated material near the surface have diminished, and the fragmentation shock wave is located predominantly at depths associated with the pre-Oruanui sediments. The evidence of this is likely overprinted in the

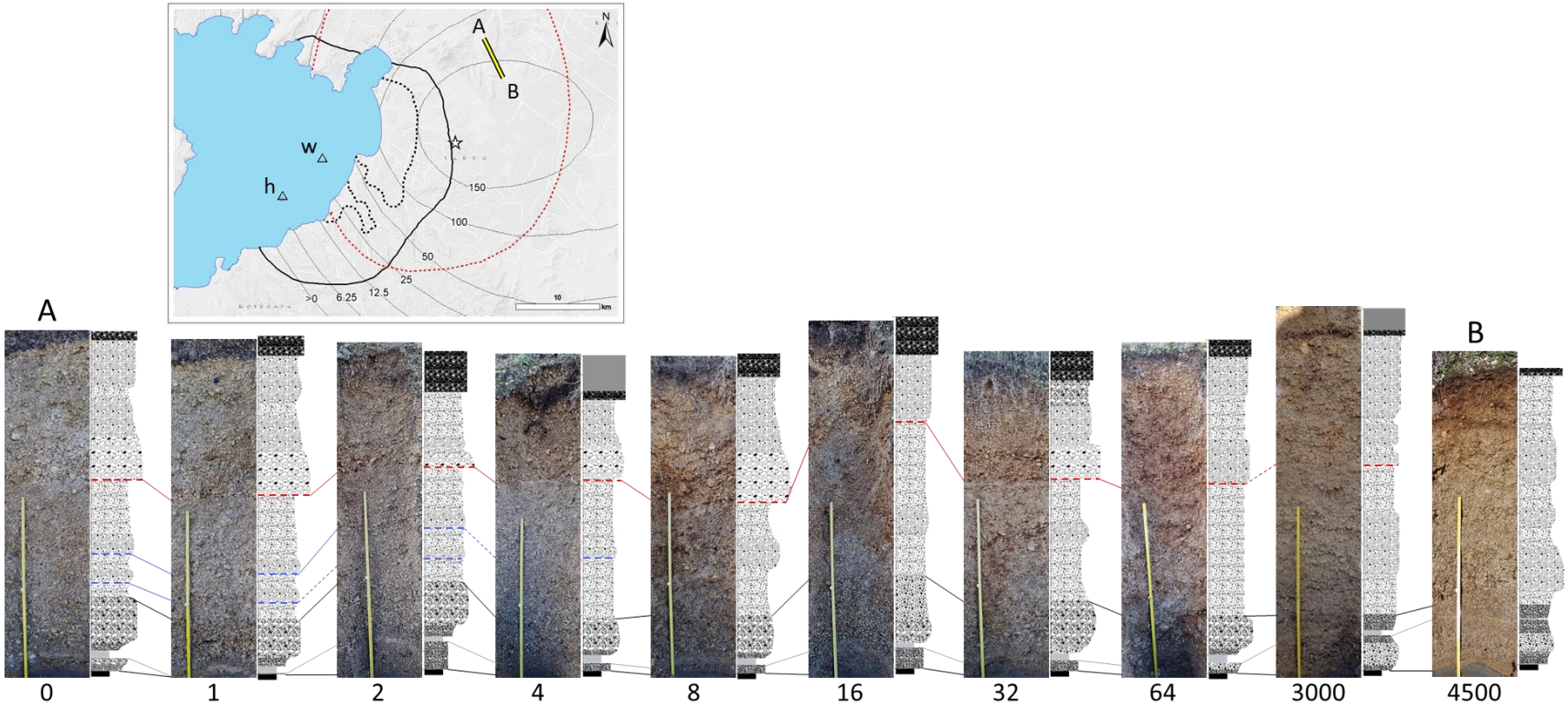

Figure 4.13 Photographs and associated stratigraphic columns of exposures taken at logarithmic distances (indicated at base in meters, starting point 0 m) from cross sectional point A to B in the inset (based on Fig. 2). Solid lines between images shows the correlation possible for the distinct change in grain size, indicated by red dashed lines on the stratigraphic columns, uncertainty is suggested between 64 m and 3000 m by dashed red lines between images. Blue solid lines indicate correlations made between outcrops for features showing transient changes in grain size, indicated by blue dashed lines on the stratigraphic columns, uncertainty is suggested between 1 and 4 m by dashed blue lines between the images. Light grey solid lines show correlations made between outcrops for ash beds (solid light grey in stratigraphic column) with uncertainty shown between 3000 and 4500 m by dashed light grey lines. Black solid lines show the correlations made in all exposures of the upper and lower contacts of the lithic rich zone at the base of the deposit. The black solid base in the stratigraphic column is unit Y4, while the black and solid dark grey upper portion indicates the onset of the Y6 ignimbrite. See Supplementary Material for larger version.

total deposit lithics by the increasing abundance of coarser grained pumices and F1 fragments as the eruption intensified.

The deepening of fragmentation following increased MDR favours inward conduit wall collapse events, commonly toward the end of an eruption (Palladino et al. 2008; Mullet & Segall 2021). The onset of this may be represented initially by a possible accelerated conduit widening phase seen in the increase in shallow seated lithics in the 1 ϕ size fraction of D-12 (from 54 wt.% to 79 wt.%). As mentioned by Tadeucchi & Wohletz (2001), an increase in the rate of conduit widening by erosion is commonly expected to be represented by an overall increase in relative abundance of lithics in the deposit; however, if the MDR is high the lithics will ultimately be diluted by a larger number of juvenile clasts. This is shown in *Figure 4.5*, where pumice abundance peaks at D-12. Accelerated conduit widening is also supported by the field observation of jarositic lithics within the D-12, suggesting significant new F1 material being excavated, as this type of clast was also observed in the initial vent excavation stage. Conduit instability progresses, based on increasing overall abundances of lithics, until a sudden surplus of F1 fragments at D-04. This also correlates with the overall increase in abundance of lithics (*Figure 4.5*, *Figure 4.12*). MDR is likely to decrease with conduit collapse (Taddeucci & Wohletz 2001) and this is shown through the decrease in bulk pumice vesicularity at D-15, the diminishing grain size and smaller MP sizes (Cioni et al. 2015). Assuming that the Y6-forming flow has not eroded a significant portion of the Y5 deposit at this location, these data may be interpreted to represent another stage of accelerated vent widening, or the early onset of conduit collapse that led to drastic changes in eruption conditions causing the Taupo ignimbrite-producing blast event (Wilson & Walker 1981, 1985).

4.3.4 Temporal evolution of fragmentation and conduit flow conditions

The variations in pumice types are predominantly related to their vesicularity style and the range of vesicle elongation or coalescence. The elongation of bubbles is controlled by the capillary number, $Ca = \epsilon R\mu/\sigma$ (Cashman & Mangan 1994), where ϵ is the strain rate, R is bubble radius, μ is melt viscosity and σ is the surface tension. Since the compositions and volatile contents of the 232 CE eruption products remain consistent throughout its progression (Dunbar & Kyle 1993; Sutton et al. 1995), the viscosity of the magma is not expected to change and therefore is not considered to significantly affect development of the

vesicle shapes. There is a negligible difference in densities between the three pumice types, J1, J2 and J3, with averages within only ~14 kg m^{-3} of each other (*Figure 4.10*). The 4–8 mm size fraction has a slightly larger range in densities and does not capture the larger vesicle sizes; however, this is not considered to significantly influence the trends seen as >50 wt.% of pumices in the deposit have sizes greater than 8 mm. Therefore, transport-related sorting resulting from density variations is also excluded as an explanation for the observed trends in pumice type abundances throughout the vertical stratigraphy. It is instead most likely that strain induced vesicle elongation has occurred, where shear stresses increase due to drag in proximity to the conduit walls (e.g., Palladino & Taddeucci 1998; Marti et al. 1999; Taddeucchi & Wohletz 2001; Polacci et al. 2003; Rust et al. 2003; Palladino et al. 2008). Volcanic conduit models suggest that viscous dissipation during high-flux silica eruptions reduces the pressure gradient required for flow resulting in narrow zones of concentrated shear along the conduit margins (Mastin 2005; Costa et al. 2007; Palladino et al. 2008). Based on this, we assume a general cylindrical conduit structure where J3 pumices are produced due to strain related vertical elongation of vesicles at the conduit margins (e.g., Palladino et al. 2008), with the minimal shear stress in the central portion of the conduit contributing to the production of J1 pumices. J2 pumices are considered transitional between the two where coalescence and shear is moderately higher, resulting in comparatively larger, elongated vesicles. Inferences can hence be made regarding magma rise behaviour in the conduit based on vertical variations in pumice types in addition to the previously mentioned data. Generally, as J2 and J3 pumices become gradually more abundant with height in the deposit, we can infer that increasing MDR within an initially narrow conduit has resulted in more pronounced velocity gradients in proximity to the conduit walls, inducing higher shear stresses in the rising viscous magma (i.e., Palladino et al. 2008). Due to the rapid rise rates associated with plinian eruptions (Carey & Sigurdsson 1989; Cioni et al. 2015), J1 pumices are expected to remain at a relatively higher quantity than other pumice types as vesicles do not have sufficient time to grow and coalesce.

In conjunction with trends identified in the lithic components, three transient phases appear within the vertical trends of the pumice types. An initial conduit opening event followed by conduit erosion is indicated by a narrow range between J1 and J2 pumice abundance and minimal J3. The lower abundance of J3 suggests a relatively low MDR at this stage, minimizing magma failure due to vertical elongation strain at the margins and resulting in a

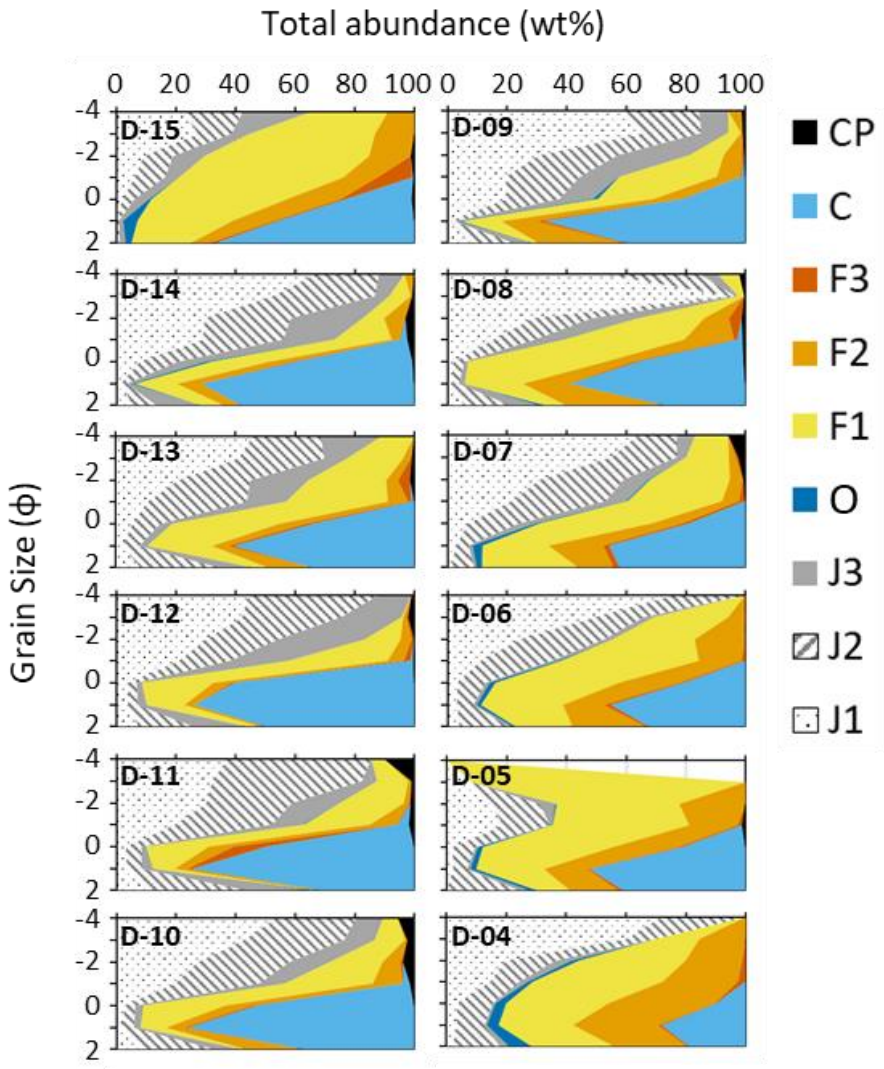

Figure 4.14 The total abundance of components (in wt.%, x-axis) in each grain size fraction from -4 to 2 ϕ (y-axis) for all sampled intervals; where CP: pumice aggregates, C: crystals, F3: deep seated lithics, F2: intermediate depth lithics, F1: shallow seated lithics, G: obsidian, J3: sheared pumices, J2: macrovesicular pumices, and J1: microvesicular pumices.

higher abundance of more vesicular material (J2). This also coincides with a narrower conduit undergoing continuous erosion as indicated by lithic abundance and pumice densities (Cioni et al. 2015; Mullet & Segall 2021). Once the conduit enlargement by erosion has decreased, indicated by a drop in lithic abundance and an increase in J1 abundance due to minimal pressure loss from viscous drag, MDR increases toward the eruption climax. Fragmentation deepens with increasing MDR, promoting higher viscous shear stresses, as evidenced by the increase of J2 and J3 pumices (Palladino et al. 2008; Mullet & Segall 2021). When large volumes of magma are excavated, the pressure in the magma chamber

diminishes and may result in deepening of the fragmentation level (Mullet & Segall 2021). This favours effective inward wall collapse events toward the end of the eruption (Macedonio et al. 1994; Mullet & Segall 2021), the onset of which is evident in D-12 where the range between the three pumice types narrows significantly. Inward wall collapse and consequent increase in viscous shear stress is depicted in a higher abundance of F1 lithics coincident with peak levels of J3 pumices. It is likely that, with reduced magma chamber pressure, increased fragmentation depth and efficient shear stress induced erosion, the early onset of collapse resulted in changing eruption conditions leading to the change between Y5 plinian phase to the catastrophic Y6 ignimbrite event. The large abundance of lithics, higher J2:J1 ratio and lower pumice density in D-15 suggest this significant change to eruption conditions which may signify the onset of the Y6-producing blast event. Further insight into this, however, may be somewhat restricted by erosion of any transitional fall deposits during the Y6 ignimbrite emplacement. The ignimbrite may also have been emplaced too rapidly for the final portions of Y5 fall to be deposited.

Within the Y5 stratigraphy, I see three main phases of CP production, where the highest abundance of these clasts is noted at the climactic point of the eruption (cf. Giachetti et al. 2021). This does not appear to be in direct relationship with increased grain size as compared to the Md_{ϕ}, which varies relatively minimally with height in the deposit, as we see three very distinct peaks in the CP abundance. In-depth study into the origin of these pyroclasts is beyond the scope of this work; however, I postulate that this very distinct component may provide a stratigraphic marker within the Y5 deposit for lateral deposit correlation and understanding of the timing and formation of the EFU in future studies.

4.3.5 Implications for the interpretation of plinian deposits

Through investigations into granulometry, componentry and the textural characteristics of juvenile components, I suggest that the Y5 eruption phase may be less complex than its observable deposit features suggest, constituting a relatively steady, continuous eruption with minor internal transient phases. This notion is supported when observing more distal exposures, such as that in *Figure 4.15* (81 km from the analysed locality), where the upper and lower boundaries of the Y5 deposit are confidently identified from the basal contact onto Y4, and an upper contact to fine-ash-rich material interpreted as fall material related to the Y6 Taupo ignimbrite (pers. comm. C.J.N. Wilson 2022). Three phases are clearly identified:

1) reverse grading in the lower third, consistent with the onset of eruption and increasing vigour during conduit excavation; 2) a relatively massive zone of fine lapilli representing the onset and continuation of relatively steady conduit conditions with a coarser band atop marking the climactic event; and 3) material deposited as the eruption begins to wane, where normal grading is minor and again suggests an abrupt end to the Y5 phase, possibly related to conduit collapse and the initiation of the Y6 ignimbrite event.

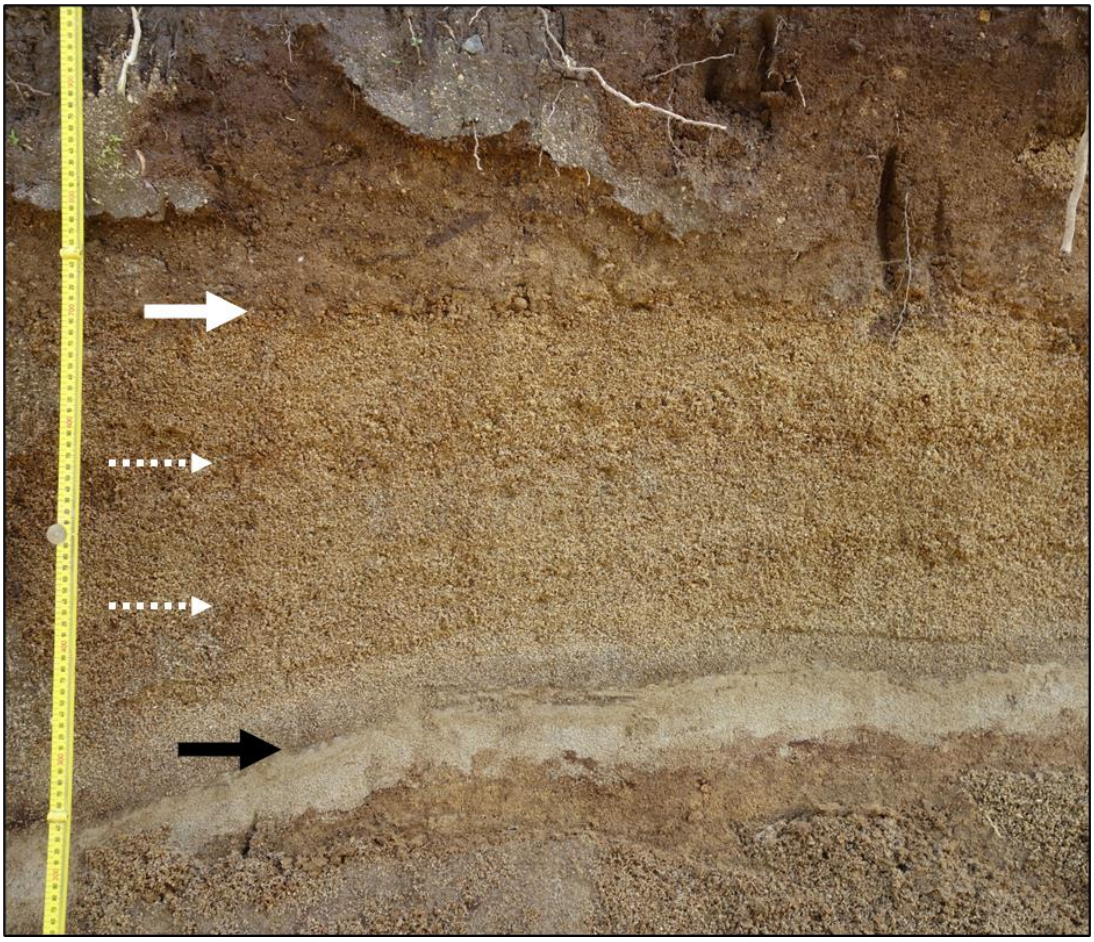

Figure 4.15 Distal exposure (UTM 60S 509825 5711483) of the Y5 deposit, courtesy of C. J. N. Wilson. The black arrow indicates the minor deposit of Y4 material while the solid white arrow shows the onset of the Y6 umbrella cloud deposit. The dashed white lines show the subtle boundaries between the transient phases: evident reverse grading occurs from the Y4 until the lower dashed arrow and the above dashed arrow is indicative of the climactic part of the eruption prior to its subtle waning.

Nevertheless, complexities in the Y5 deposit stratigraphy in proximal to medial areas furnish points of contention in field observations and interpretations. Through observations made of

bedform features in a 4500 m transect of the Y5 deposit (*Figure 4.13*), I have established several uncertainties in lateral correlatability. Lithic-rich zones at the base of the eruption sequence were identified in all exposures and are likely analogous with the conduit excavation phase of the eruption, as reflected in their lateral persistence in medial areas of the deposit. Ash beds observed in the lower portion of the deposit are likely attributed to the flushing of low-lying ash clouds during local rain showers (Talbot et al. 1994; Walters 2020). Due to their nature, and although these features pinch and swell within the lithic rich material, the ash beds are correlatable and are expected to pinch out with distance from vent. Uncertainties arise when investigating the more gradational features in the deposit, such as gradational coarse-fine bands identified in *Figure 4.13*. These coarse-fine bands fade out rapidly laterally over metres and confidence in correlation is limited as there is a lack of noticeable identifiers in such features (e.g., specific lithic types, distinct contacts, or colour variations). Similarly, even more distinct changes in grain size such as that identified in *Figure 4.13* can be correlated up to hundreds of metres, potentially a few kilometres in the Wairakei Estate exposures, but are not persistent at greater distances and a lack of noticeable identifiers again makes correlation difficult. Toward vent the feature with distinct change in grain size (*Figure 4.13*) has been identified up to 10 km distance from the Wairakei Estate exposures, but additional observations have determined this as the extent of its deposition. The seemingly discontinuous nature of bedform features over greater lateral distances makes the identification of sub-unit layering across the dispersal fan of the Y5 deposit unreliable (cf. Houghton et al .2014). This lack of correlatability also precludes the possibility that coarse-fine fluctuations are caused by the partial collapse of the column, temporarily reducing plume height (Walker 1980; Woods & Wohletz 1991; Cioni et al. 2015; Houghton & Carey 2015; Trolese et al. 2019). If this were the case, fluctuations would still be expected to correlate across the dispersal fan at any given stratigraphical height. An alternative explanation is therefore needed for the origin of such bedform structures. Here, I suggest the plausibility of the influence of highly turbulent gas-particle transport on gravitational instabilities resulting in preferential sedimentation from the eruption umbrella cloud (e.g., Carazzo & Jellinek 2013; Bonadonna et al. 2015a; Manzella et al. 2015; Lherm & Jellinek 2019).

Gravitational instabilities have been observed in eruptive clouds from explosive eruptions of many sizes, yet deposit features are still to be attributed to this sedimentation mechanism.

When looking at examples from observed eruptions, it is clear that sedimentation 'streaks' occur as a result of instabilities in the eruptive cloud (e.g., *Figure 4.16a-c*). Instabilities such as these would likely sediment pyroclast packages due to larger variations in grain sizes, stronger convection, and greater variations in densities in proximal to medial regions (Bonadonna et al. 1998, 2015a; Cioni et al. 2015; Houghton & Carey 2015). In distal regions, once preferential settling of coarse, heavier material has occurred, the finer overall grain size would allow for sufficient mingling in the umbrella cloud and/or sedimenting material, resulting in a lack of such sedimentation structures (*Figure 4.15*).

Similarities may be drawn with other examples of polydisperse, fully turbulent gas-particle multiphase flows where the flow and flow turbulence structure are modified by gas-particle feedback mechanisms, strongly affecting particle sedimentation (Burgisser & Bergants, 2002; Lube et al. 2020). In this situation, high Stokes number particles – i.e., particles whose characteristic particle response time (e.g., the particle settling timescale) is lower than the characteristic fluid timescale (e.g., the eddy overturn time) – preferentially migrate and cluster at the margins of coherent turbulence structures. When these (so-called) mesoscale clusters decouple from the peripheries of coherent turbulence structures (or large eddies), they sediment unsupported by turbulence as coherent clusters at terminal fall velocities strongly exceeding the terminal velocity of the coarsest particles contained in a cluster. Mesoscale clusters also sediment at terminal fall velocities far exceeding the terminal fall velocity of the non-clustered and finer-grained particles in the interior of coherent structures. The typical length-scale of mesoscale clusters formed by concentration of high Stokes number particles at eddy peripheries is that of the diameter of the eddy. During sedimentation from the umbrella cloud tens of kilometres high, mesoscale clusters may disintegrate into smaller sub-structures. It is expected that, on the ground, a spectrum of cluster lengths may occur, deposited together with slower background sedimentation from the umbrella cloud.

In the Wairakei Estates exposure, coarse-grained pumice lenses pinch out over length-scales of 10^1–10^3 m. The largest length in this spectrum (a few kilometres) represents a minimum diameter for the largest turbulence structures formed in the umbrella cloud. This is comparable to the expected thickness of the umbrella cloud, where free shear on its upper and lower boundaries is the main driver of turbulence generation. Therefore, decoupling and sedimentation of mesoscale clusters should be considered as a process to explain preferential sedimentation of coarse particles as tephra swathes from Plinian umbrella clouds.

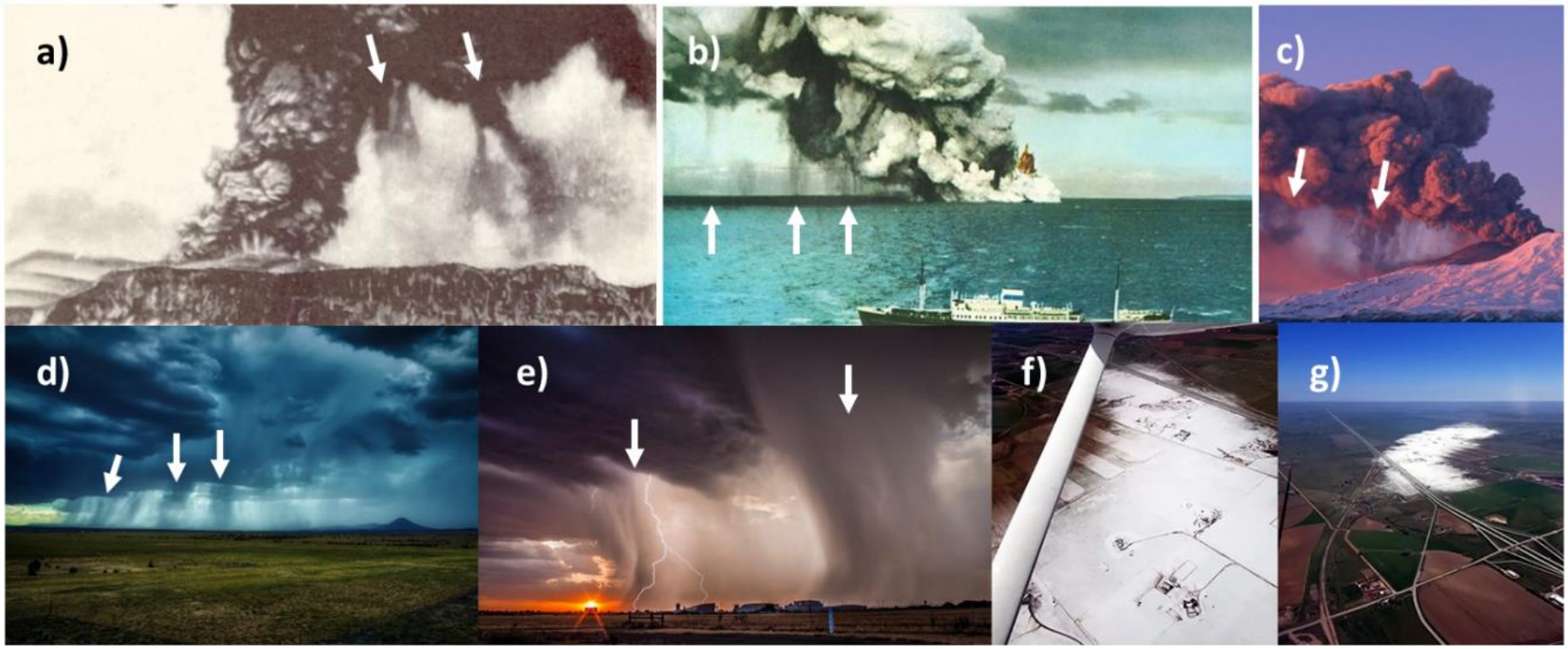

Figure 4.16 a) 1883 Plinian eruption of Krakatau, Indonesia, image from Smithsonian News Service, family archives of R. Breon; b) 1963 phreatomagmatic eruption of Surtsey, Iceland, image from Eimskip; c) 1996 phreatomagmatic eruption of Mt Ruapehu, New Zealand, image by Tui De Roy. Sedimentation instabilities are indicated by arrows in images a – c, d, e) Storms showing precipitation streaks, indicated by arrows. f, g) Small hail swath photographed in Wellington, Colorado: image by Jane Carpenter, First Class Flight Training

Other natural phenomena where related processes occur include hail swathes or rain precipitation produced during storms. Hail or rain rarely falls as a single coherent body below the parent storm cloud, instead falling in streaks like those seen during volcanic eruptions (*Figure 4.16d & e*; Atlas 1963; Basara et al. 2007; Nisi et al. 2018; Knight et al. 2019). The remnants of rain streaks are difficult to identify following deposition, but hailstorms are known to form streaks, or swathes, in which patches of hail are easily identified on the ground surface (*Figure 4.16f & g*; e.g. Charlton & List 1972; Nelson & Young 1979; Schmid et al. 1997; Kunz & Puskeiler 2010; Barrett & Dixon 2012; Gallo et al. 2012; Tuovinen et al. 2015; Nisi et al. 2018). The deposition of hail streaks may thus provide a first-order analogue to the tephra deposition features observed in the proximal to medial regions of the Y5 deposit.

4.4 Conclusions

Through the detailed, quantitative analysis of granulometry, componentry and textural characteristics of juveniles in a selected stratigraphical profile of the Y5 plinian deposit, I have shown that the temporal evolution of this eruption may be less complex than its observable deposit features suggest. I distinguish three transient stages within the relatively steady, continuous eruption of the Y5 following the initial clearing of the vent: 1) the continuous excavation of the conduit at relatively low MDR; 2) increasing MDR with decreased conduit erosion, coinciding with deepening fragmentation, and increased viscous shear, and 3) the acceleration of conduit erosion, promoting the potential early onset of collapse that led to the Y6 ignimbrite-producing blast event. As the deposit has been extensively eroded by the succeeding ignimbrite-forming flow, the final stages of the Y5 phase may still not be fully represented in proximal to medial areas of the Y5 deposit.

Based on observations at a chain of sections spaced over metres to 4 km apart, orientated perpendicular to the dispersal axis, I have established several uncertainties in the lateral correlatability of bedform characteristics in the Y5 stratigraphy. I infer that variations observed in vertical sections are not caused by relatively steady source conditions with shifting wind directions, but instead reflect the sedimentation from the eruption umbrella cloud in the form of gravitational instabilities leading to deposition of tephra swathes. These results have implications for the reconstruction of the temporal evolution of plinian eruptions

worldwide, where correlation of this behaviour to the parent eruption cloud by means of computational modelling may provide improved opportunities for the amalgamation of quantitative field studies and computational based eruption modelling for purposes of hazard prediction and mitigation globally.

5 Co-plinian pyroclastic density currents: The relationship of the Early Flow Units to the Taupō Y5 plinian fall deposit

5.1 Introduction

Pyroclastic density currents (PDCs) are one of the most destructive and hazardous phenomena in explosive volcanism and are associated with a range of eruption styles and magnitudes globally. They can be short-lived or sustained, ground hugging, gravity-controlled hot currents of particles and gas that are produced during eruption processes such as collapse of eruptive plumes, direct magmatic blasts, and caldera-collapse scenarios, and have the potential to rapidly transport hot debris for many kilometers (Sparks 1976; Walker et al. 1980a; Self & Rampino 1981; Branney & Kokelaar 2002; Clarke et al. 2002; Belousov et al. 2007; Komorowski et al. 2013; Cioni et al. 2015; Dufek 2016; Trolese et al. 2019; Lube et al. 2020). There are two end-members of PDC behaviour, as determined from deposit characteristics, which are pyroclastic flows (dense/high particle concentrations) and pyroclastic surges (dilute/lower particle concentrations; e.g., Sparks 1976; Wilson 1985; Wilson & Houghton 2000; Lube et al. 2020). Products from concentrated PDCs where the juvenile component is dominant and pumiceous are termed ignimbrites. Ignimbrites may drape over pre-existing stratigraphy, modify the landscape by infilling valleys, or build new landscapes in the largest examples (Smith 1960; Sparks 1976; Walker et al. 1980a; Fisher & Schmincke 1984; Wilson 1986, 1991; Cas & Wright 1987; Freundt et al. 2000; Branney & Kokelaar 2002). They can vary from metres to hundreds of metres thick and can be massive or contain a wide range of sedimentary structures such as sharp to diffuse stratification, cross bedding, erosional surfaces, grading patterns and particle fabrics (Wilson 1981, 1985; Branney & Kokelaar 2002).

In the case of large-scale Plinian eruptions that generate high, buoyant eruption plumes, there are two widely accepted interpretations for the generation and dynamical controls of PDCs, namely through partial- or total column collapse. In such cases, if positive buoyancy of the erupting mixture cannot be achieved because of its physical properties, variations in conduit geometry, mass discharge rates and/ or fragmentation styles, the column will partially or

completely collapse. Partial column collapse episodes can also be considered to represent the transitional regime of column unsteadiness between a sustained Plinian column and total collapse conditions, with numerical models indicating that this regime produces pulsating, dilute PDCs (Turner 1969, 1986; Woods 1995, 2010; Neri et al. 2002; Kaminski et al. 2005; Carey & Bursik 2015; Cioni et al. 2015; Lherm & Jellinek 2019).

Partial- and total column collapse regimes are useful for the purpose of eruption scenario numerical modelling. To use these interpretations, however, to solely explain the generation of PDCs when associated with Plinian eruptions restricts consideration of real-world scenarios. Recently, Gilchrist & Jellinek (2021) reviewed the existing models of partial column collapse and revisited the characterisation of transitional regimes through analogue experiments using sediment-water mixtures. They proposed that volcanic jets can transition smoothly between buoyant plume, partial collapse and total collapse regimes due to gradually changing source parameters. It was also noted that Plinian eruptions usually occur within the partial collapse regime, with large-volume annular sediment waves descending periodically around the jet column from the fountain-plume transition height. Generally, however, this is not often observed in natural eruption scenarios or deposits. PDCs in this scenario spread radially if the sediment waves are large, or from one side of the enhanced settling annulus if small (Gilchrist & Jellinek 2021). What is not considered in these water-based analogue experiments, however, are the non-linearities of gas-particle mixtures (especially with regard to compressibility and phase behaviour), where there is fundamental contrast between gas-solid and liquid-solid fluid-particle behaviour (e.g., Zenz & Othmer 1960; Davidson & Harrison 1963, 1971; Batchelor 1993; Harris & Crighton 1994; Wilson & Houghton 2000). In analogue experiments of the partial collapse regime, the erupted mixture is expected to partition between the buoyant umbrella cloud and collapsing sediment waves. This partitioning can result in the finer particle size fractions of the erupted mixture preferentially being winnowed into the umbrella cloud (*Chapter 1; Section 1.2.1*) and PDCs spreading as relatively dilute flows (Gilchrist & Jellinek 2021).

Studies of the coeval emplacement of plinian fall and PDC deposits, such as in the Novarupta, 1912 eruption (Hildreth & Fierstein 2012, for overview), have outlined the complexities in PDC generation. In this example, field studies showed that PDCs, both dilute and concentrated could undergo little to no ascent with the coexisting Plinian column which, contrary to partial collapse models, was never fully interrupted (Fierstein & Hildreth 1992;

Houghton et al. 2004; Fierstein & Wilson 2005). Recently, Valentine & Cole (2021) used numerical multiphase simulations to model such behaviour, termed "gargle dynamics" (cf. Wilson & Hildreth 1997), as a process in which debris-filled vent structures cause large portions of the venting materials to become trapped, result in an eruption jet needing to penetrate its own earlier ejecta. Gargling dynamics occur when preexisting ejecta interact with the erupting mixture and form a dense sheath along the margins of the erupting jet (Houghton et al. 2004; Hildreth & Fierstein 2012; Valentine & Cole 2021). This creates overloaded annular zones within the jet region which fail to rise sufficiently with the jet (Wilson & Walker 1985; Fierstein & Hildreth 1992; Wilson & Hildreth 1997; Houghton et al. 2004; Hildreth & Fierstein 2012; Valentine & Cole 2021). Collapse or diversion of this material can occur at all heights along the sheath on the outer edge of the jet, producing concentrated, highly fluid PDCs (Fierstein & Wilson 2005; Valentine & Cole 2021). These field observations and models show that generalised steady versus unsteady column regimes can oversimplify the interpretation of both ignimbrite and plinian air fall deposits in natural eruption scenarios, yet they are still the most accepted explanation for PDCs generated simultaneously with fall deposition. This reliance on numerical models results in limited understanding of the dynamics of intraplinian PDC events and suggests that further research is needed for more accurate modelling of such events.

In the case of a partial column collapse regime, plinian air fall deposits may be accompanied by proximal to medial interbedding of ignimbrites produced by numerous PDC episodes (Wilson & Walker 1985; Wilson & Hildreth 1997; Fierstein & Wilson 2005). With distance, the alternating fall-PDC beds pass into a plinian fall deposit due to the limited runout distance of PDCs. Past this runout limit, or when directionally restricted PDCs occur, column collapse may be recorded in atypical sedimentological deposit features such as fine-grained beds at relative levels if partial mass partitioning into PDCs results in a decrease in convective column height (e.g., Neri et al. 2002; Di Muro et al. 2004). This generalized interpretation, however, does not consider gargle dynamics and the synchronous emplacement of plinian fall deposits and ignimbrite (or other PDC deposits), where currents undergo little to no ascent with the coexisting Plinian column, which in turn also undergoes no diminution that is reflected in the subsequent fall deposits (Fierstein & Hildreth 1992; Houghton et al. 2004; Valentine & Cole 2021). In such cases, it is possible that plinian fall deposits in medial regions may show few or no characteristics assumed to be associated with

partial mass partitioning, whilst still being proximally interbedded with PDC deposits. In the same manner, medial plinian fall deposits may show internal stratification that is in fact unrelated to coevally emplaced PDCs (as discussed in *Chapter 4*). This contrast between model expectations and studies of eruption products highlights the oversimplification that may result from basic categorization of deposits and emphasizes the need for further understanding of the spatiotemporal relationship between Plinian fall deposits and their coevally emplaced PDCs.

5.1.1 The Early Flow Units

The Early Flow Units (EFU) of the Taupō 232 ± 10 CE eruption are the deposits of PDCs that were emplaced coevally with the Y5 plinian fall deposit and provide an opportunity to further investigate the spatiotemporal relationship between Plinian fall deposits and their coevally emplaced PDCs, and the dynamical controls on PDC generation.

The EFUs have previously been interpreted to occur simultaneously with the Y5 Plinian eruption phase and from the same vent location (see also, *Chapter 1; Section 1.2.3*) with a maximum runout distance of ~15 km, predominantly to the E and NE of source (i.e., the downwind sector; Wilson 1981; Wilson & Walker 1985). Initial work by Wilson (1981) differentiated the EFUs according to inferences on flow generation and deposition styles into the proximal and distal EFUs.

There are up to 12 proximal flow units that total ~40 m thickness with run-out and deposition topographically restricted to low lying areas around the eastern side of Lake Taupo (Wilson 1981). Wilson (1981) and Wilson & Walker (1985) suggested the possibility that the proximal flow units, which are typically thicker than the distal flow units, with lower emplacement velocities, were generated as material was diverted at the base of the eruption column in a similar fashion to gargle dynamics. In support of this, the upper 5 m of the proximal EFUs show evidence of incipient welding, which suggests that the material had limited opportunity to cool due to mixing with the atmosphere at greater heights in the eruption column (Wilson 1981). It was also noted that the lack of crystal enrichment and the high content of fine material, particularly <10 μm, in the proximal EFUs reflects the composition and grain size of the primary erupted mass, which supports the interpretation by Walker (1980) that the Y5 eruption column had an unusually high fine ash content (~80 % of erupted material).

The distal EFUs are described as small volume, high emplacement velocity units that mantle topography. They are interpreted to result from episodes of partial column collapse that were roughly correlated with distinct finer bands identified in the Y5 fall deposit (Walker 1980; Wilson 1981; Wilson & Walker 1985). The distal EFUs are interbedded with the Y5 fall deposit and have the occasional observed slightly erosive base (Wilson 1981).

The pumices in the EFUs have broadly similar densities to those in the coeval Y5 deposit (see Houghton et al. 2010). Post fragmentation expansion of vesicles is noted in the cores of some of the pumices, with bubbles being notably more expanded than those in the pumices of the Y5 fall deposit. Houghton et al. (2010) interpreted this to indicate that vent widening occurred, allowing for the unconstrained expansion of vesicles, with the high temperature of the EFU PDCs also influencing vesicle expansion. From this analysis, Houghton et al. (2010) suggested that the EFUs occurred as relatively weakly energetic, concentrated PDCs that resulted from short lived partial column collapses due to fluctuations in mass discharge rate during the Y5 eruption. This disputes Wilson's (1981) initial interpretation regarding the gargling generation mechanism of the proximal EFUs, and the partial column collapse seems to be the generally accepted assumption of formation for the overall EFUs (e.g., Neri et al. 1994; Kaminski & Jaupart 2001; Neri et al. 2002; Gilchrist & Jellinek 2021).

Although the previous works outline the EFUs characteristics (Wilson 1981; Wilson & Walker 1985; Houghton et al. 2010), there is a lack of research development regarding the characteristics and dynamics of the EFUs in recent years, given the advancement in knowledge concerning PDCs through large-scale and analogue experiments, field observations and computational and theoretical models over the past decade (Lube et al. 2020 and references therein). Studies regarding the Y5 plinian deposit also have tended to disregard the relationship between the fall and EFUs (e.g., Walker 1980; Houghton et al. 2014) which potentially oversimplifies the interpretation of the Y5 eruption phase. Detailed analysis of the properties of the EFU deposits and their stratigraphical relationship with the Y5 plinian fall deposit is therefore undertaken here as the EFUs may play an important role in understanding the behaviour and consequent sedimentation dynamics of the large-scale Plinian Y5 event.

5.2 Data

5.2.1 Stratigraphy and general distribution of the Early Flow Units

Following extensive field observations, 6 exposures were selected in medial to distal extents of the EFU deposits, and 3 beyond the runout limit to investigate the characteristics of the PDCs and their relationship with the associated Y5 fall deposit (exposures A – I; *Figure 5.1*). Proximal deposits are either inaccessible or not preserved due to the vent location being situated within Lake Taupō, at closest ~4 km from the shoreline (*Chapter 3, Section 3.3.3*). Here, I do not use the nomenclature defined by Wilson (1981) and refer to deposits of EFUs as Type 1 or Type 2 based on the features identified in the deposits, which may imply individual flow runout distances, discussed in *Section 5.3*.

Type 1 deposits comprise up to ~12 flow units totalling ~40 m thickness near the lake edge (Exposures A and I; Wilson 1981; Wilson & Walker 1985; *Figure 5.2*). Following the work of Wilson (1981) and Wilson & Walker (1985), a large new exposure was created in 1985-86 during realignment of State Highway 1 (*Figure 5.2*) and the presence and number of intercalated fall beds in addition to the nature of the contact between units Y4 and Y5 (*Chapter 3*) became clearly displayed. The Type 1 deposits are massive, poorly sorted, pink-orange to cream coloured and ash-rich (<1 mm ash abundances of ~40–70 wt.%). They can contain large pumice and lithic clasts (up to ~25 cm in size). Type 1 deposits are typically found in topographical low areas ENE to ESE of the vent (*Figure 5.1*) but are observed at elevations up to 575 m above sea level (where modern lake level is 357 m) with maximum runout distances between 10–16 km from source. The Type 2 deposits are variably thick (decimetre to metre scale) and massive to moderately stratified. These units are poorly sorted, white to grey and ash-rich (<1 mm ash abundances of ~65–95 wt.%). Larger pumices (>32 mm) are rare and most clasts between 16–32 mm across occur directly above interbedded fall beds and are thus inferred to be incorporated from the preceding fall deposit layer. The Type 2 deposits have degassing pipes observed in the lower PDC units above fragments of carbonised vegetation. Type 2 deposits are dispersed up to 17 km from vent, spanning N to SSW of the vent (*Figure 5.1*). They show evidence of the parental PDCs climbing topography and are also observed at elevations up to ~575 m (based on extent maps by Wilson 1981 and Wilson & Walker 1985).

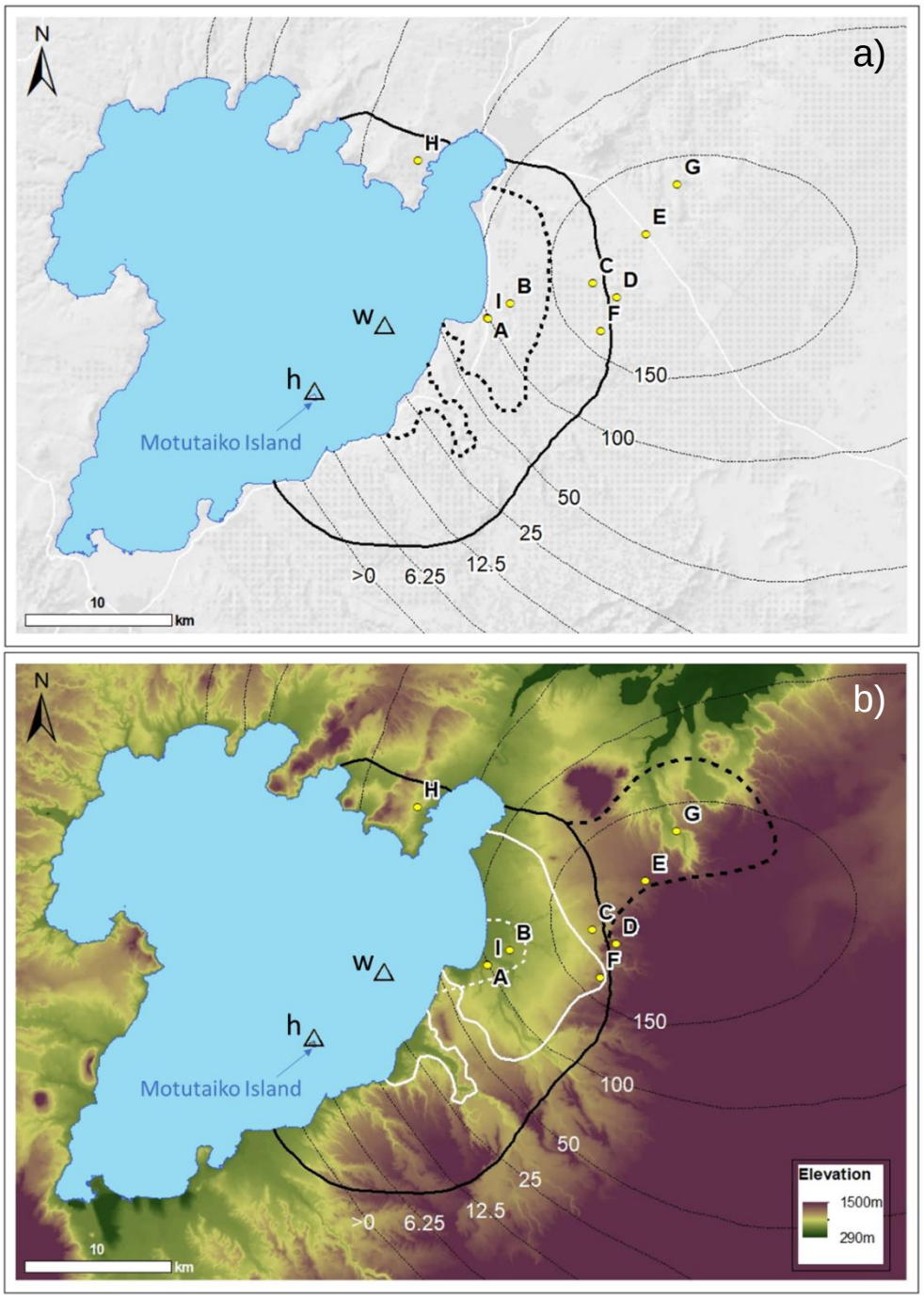

Figure 5.1 a) Map of the Early Flow Units (EFU) extent as determined by Wilson (1981) and Wilson & Walker (1985) with proximal flows marked by thick, dotted lines and distal by a solid line. b) revised maps from this study based on Wilson & Walker (1985). Type 1 EFUs are defined by solid white lines, while the distal Type 2 are defined by the solid black line. The dotted white line indicates the runout of proximal Type 2 flows, while the thick, dotted black line shows the most distal extents of gravity current deposits produced by PDCs. Minimum and maximum elevation is shown in the legend. Exposures A – H are defined by yellow dots. Note that exposures A and I are in very close proximity. The isopachs for the Y5 deposit (Walker 1980) are defined by thin, dotted lines, with associated thicknesses in cm. w: the original vent location for the Y5 phase, as determined by Walker (1980). h: the vent location for the Y5 phase proposed by Houghton et al. (2014).

Variations in the oxidization colour of the ash-rich matrix of the Type 1 and Type 2 deposits show that pink-orange oxidization is dominant in an arc approximately 12 km ESE to ENE of the vent location and progressively diminishes up to the 17 km runout of the Type 2 deposits, particularly to the NNE of vent.

Figure 5.2 Slide photograph provided by C. J. N. Wilson of the exposure created by the clearing of State Highway 1. In proximity to Exposure I, this outcrop shows the thick (up to ~20 m) deposits of the proximal EFU with interbedded layers of Y5 air fall marked by white arrows, where the lowest arrow signifies the contact between the units Y4 and Y5. The dotted white line outlines the strongly erosive basal contact of the Y6 ignimbrite.

The selected exposures for this study were continuously box sampled from the onset of Y5 deposition (refer to *Chapter 2, Section 2.1*) to the upper contact with the Y6 ignimbrite or upper layer of soil. Samples of varying thickness were taken at all locations based on either sharp or subtle vertical changes in sedimentation facies (e.g., PDC or fall), grain size and/or abundances of wall rock lithics (e.g., *Figure 5.3*, *Figure 5.4*). The exception to this was exposures F and I. Exposure F was not entirely sampled due to time restrictions for analytical processing; however, a single EFU was identified in the upper portion of the deposit and was therefore sampled as an eastern distal flow comparative, and the plinian airfall within ~20 cm

of the lower and upper flow contact was also box sampled. Exposure I occurs ~80 m from Exposure A, on the opposite side of Highway 1, and is dominated by thick (up to ~20 m) EFU deposits (*Figure 5.2*). Accessibility to fall deposits and the base of the Y5 deposit here was hindered due to the thickness of the EFUs and therefore only a single representative sample of EFU was taken. Exposure D was selected as a reference locality to compare EFU deposits and their associated airfall with a section of near-complete Y5 deposition that contains no PDC deposits (see *Chapter 4*) for possible time-variant correlation purposes. Key features identified amongst the exposures are defined as follows.

- The lowermost PDCs identified at exposures A and B (*Figure 5.3*) are 80 mm and 250 mm thick, respectively, fine-ash rich, massive, white flow units with relatively sharp upper- and lower-contacts (±10 mm). The initial PDC at Exposure A also contains large (up to ~30 mm) white pumices concentrated in the basal portion of the unit. These PDCs have been defined as Type 2.

- Exposures A and I represent the lowermost portions of relatively proximal (~8 km from source), up to 40 m total thickness EFU deposits with thin (a few tens of cm), interbedded bands of Y5 airfall (*Figure 5.2, Figure 5.3*). Excluding the lowermost flow, all PDCs show features equivalent to those of the Type 1 PDCs.

- At Exposure A a relatively thick (up to 100 cm) zone of red to orange brown thermally oxidised material in the usually dark blue-grey Y4 unit occurs (*Figure 5.3*). This is interpreted to be intense boiling of the water-rich fine-ash in the underlying phreatoplinian Y4 deposit.

- The interbedded Y5 fall material at exposures A and B generally becomes coarser grained (from fine to coarse lapilli) with stratigraphic height and contains abundances of wall rock lithics (between ~15–30 %) that are relatively high when compared to the main Y5 fall deposit just beyond the range of the EFUs.

- Exposures C, D and E lack EFU deposits and are used for time variant correlation with airfall in those exposures with PDCs. Exposure E does, however, contain two ~5 mm fine-ash rich bands at ~17–24 cm from the base of the deposit. These include impact pumice clasts and incorporated airfall and were therefore unable to be individually sampled.

- The EFU deposit at Exposure F (~16 km from source) was originally included in the distal EFU portion of maps by Wilson & Walker (1985; *Figure 5.3*), however upon observation it exhibits traits of Type 1 PDCs. It consists of 190 mm of fine-ash rich, brown to orange, massive PDC deposit with sharp (±15 mm) lower and upper contacts. The lower ~90 mm includes fine lapilli and fragments of carbonized vegetation. The Y6 ignimbrite-producing flow at this exposure has also notably eroded the Y5 fall deposit.

- Exposure G shows predominantly Y5 airfall but contains two undulating 10–20 mm bands of fine-ash rich material (*Figure 5.3*), separated by ~50–100 mm of medium lapilli fall. The upper of the two bands is composed of cream orange coloured ash and contains impacted pumices from the airfall above, while the lower band is composed of grey to white coloured fine ash.

- Exposure H is an ~180 cm thick deposit of predominantly Type 2 PDCs interbedded (and also coevally deposited) with Y5 airfall. The lowermost ~25 cm of the exposure is comprised of coarse lapilli pumice (up to ~60–80 mm long) deposited directly on top of unit Y4. The basal ~5 cm of the Y5 fall deposit contains ~30 % fine ash and is orange to brown in colour. EFU deposits at this exposure total ~130 cm in thickness and contain thin bands (~40–80 mm) of partly disturbed Y5 fall material emplaced between multiple pulses of PDCs (*Figure 5.4*). 20–50 mm pumices are moderately angular in these bands and are mixed with ash content, inferred to be derived from flows occurring simultaneously. The Type 2 PDC deposits at this location are composed of flow units on a decimetre to metre scale, which are massive to moderately stratified, white to grey coloured and ash-rich (up to ~95 % <1 mm). Degassing pipes are identified in the lowermost PDC pulses, as are large fragments (up to 6 cm) of carbonized vegetation (*Figure 5.4*). The upper ~10 cm of this deposit consists of fine to medium lapilli sized Y5 fall which is then succeeded by the lithic-rich basal layer of the Y6 ignimbrite (Wilson 1985).

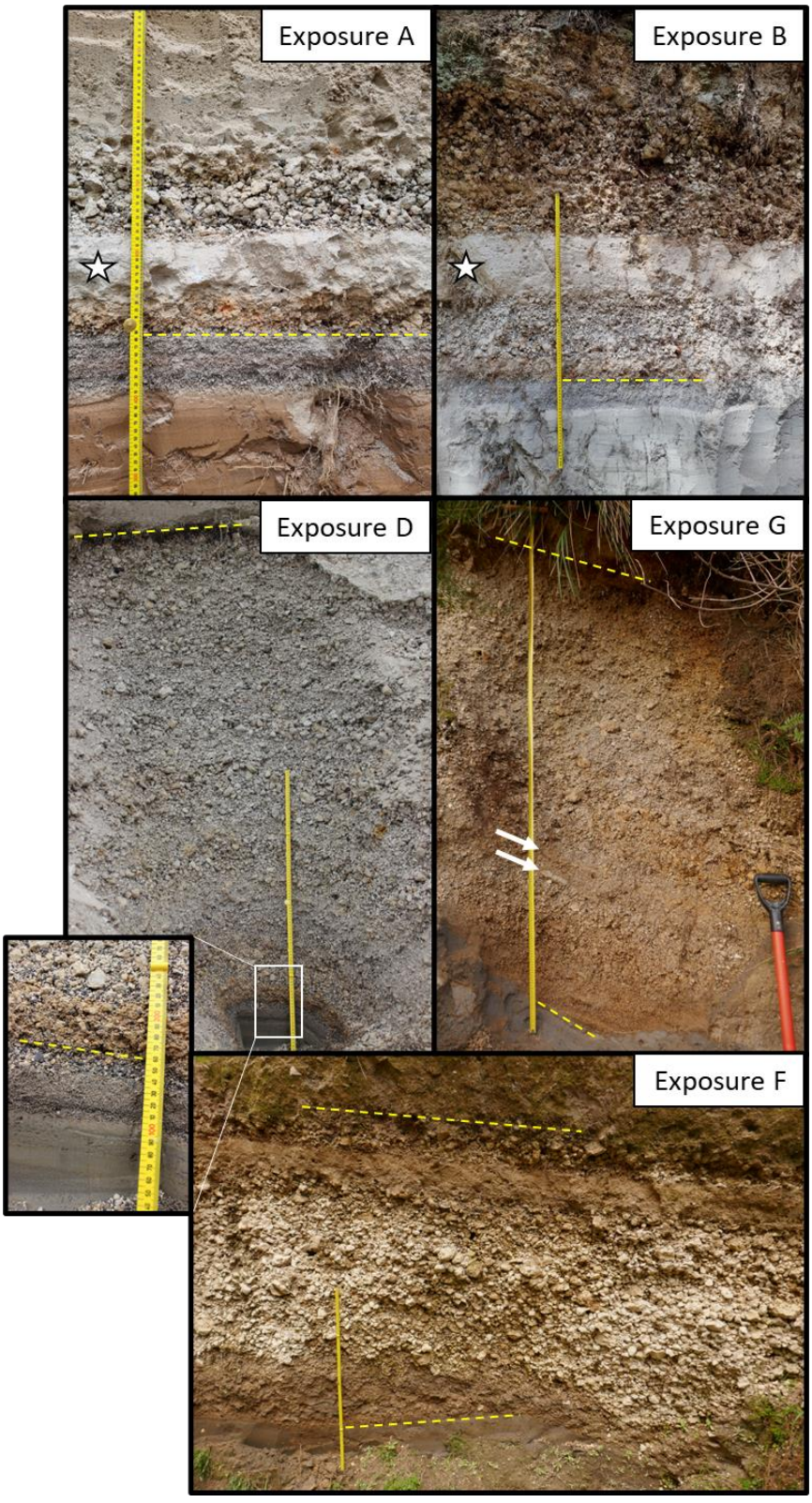

Figure 5.3 Exposures A, B, D, G and F investigated in this study. The yellow dotted line marks either the basal contact with the Y4 or the upper contact with the Y6. The white stars in the images for exposures A and B are the proximal examples of Type 2 EFUs. The white arrows in the Exposure G image indicate the distal ash beds discussed in this study. The inset shows the distinct Y4/Y5 contact at Exposure D.

5.2.2 Granulometry

Grain size analyses were conducted by dry sieving size fractions at full phi (ϕ) intervals from the 2 ϕ to -6 ϕ size classes. Size fractions >2 ϕ were measured using laser particle analysis (LPA; Horiba Partica LA 950V2). Where fine ash is visibly dominant (e.g., EFU and ash-rich facies), fractions coarser than 2 ϕ were first sieved out using water to minimize fine ash losses that might have been incurred if dry sieving were used. The fraction finer than 2 ϕ was then dried and treated as per the other samples.

Y5 fall samples show relatively narrow, unimodal distributions with median grain sizes (Md_ϕ) between 0 – -5 ϕ and are well sorted (typically σ_I <2). Both total-ash and extremely fine-ash contents (<1 mm and <63 µm, respectively) of the Y5 fall deposits are low at <8 wt.% and <3 wt.%, respectively (see *Section 4.2.3*, *Figure **4.4***).

Figure 5.5 shows the grain size distributions of Type 1 and Type 2 PDC deposits at various distances from source. The EFU samples are characterised by polymodal distributions with the Type 1 deposits being typically fine-skewed while the Type 2 are coarse-skewed. Type 1 samples are generally coarser grained with a broad range of Md_ϕ between 3 and -3 ϕ and sorting (σ_I) between 3 - 4, while Type 2 samples have much finer Md_ϕ between 3 and 5 ϕ and a broader σ_I range of 2 - 4. With distance from the source, the extremely fine-ash content in Type 1 deposits decreases by ~19 wt.% over ~8 km, while extremely fine-ash content in the Type 2 samples remains relatively consistent at average 46 wt.% (*Figure 5.5*). The Type 2 flow unit at Exposure A shows an anomalous mode at -5 ϕ, attributed to incorporation of lapilli from the underlying Y5 fall.

The <1 mm and <63 µm contents of the Type 2 samples are greater overall than those of the Type 1 at 65–95 wt.% <1 mm and 40–60 wt.% <63 µm versus 40–75 wt.% <1 mm and 15–40 wt.% <63 µm abundances, respectively. Note that most EFU samples have a markedly high ultra-fine-ash content (≥7 ϕ or <10 µm) of 4–27 wt.% (cf. Wilson 1981: 2.6 – 6.5 wt.%). The fines content is also compared to a reference sample of the Y6 ignimbrite at Exposure D sieved for this study, which contained 8.3 wt.% ultra-fine-ash, and the Y6 data obtained by Corna (2022) at a location 17 km from the vent with a total of 4.85 wt.% ultra-fine-ash.

When normalized to total 100 % of the ≤2 mm size fraction within the given EFU types, the extremely fine- and ultra-fine-ash contents of both Type 1 and Type 2 samples converge on a linear trend where increasing ultra-fine-ash content increases with extremely fine-ash content (*Figure 5.6*). The Type 2 samples still typically have higher ash contents compared to the Type 1 samples on this trend with ultra-fine-ash content at 14–40 wt.% normalised compared to 6–24 wt.%, respectively.

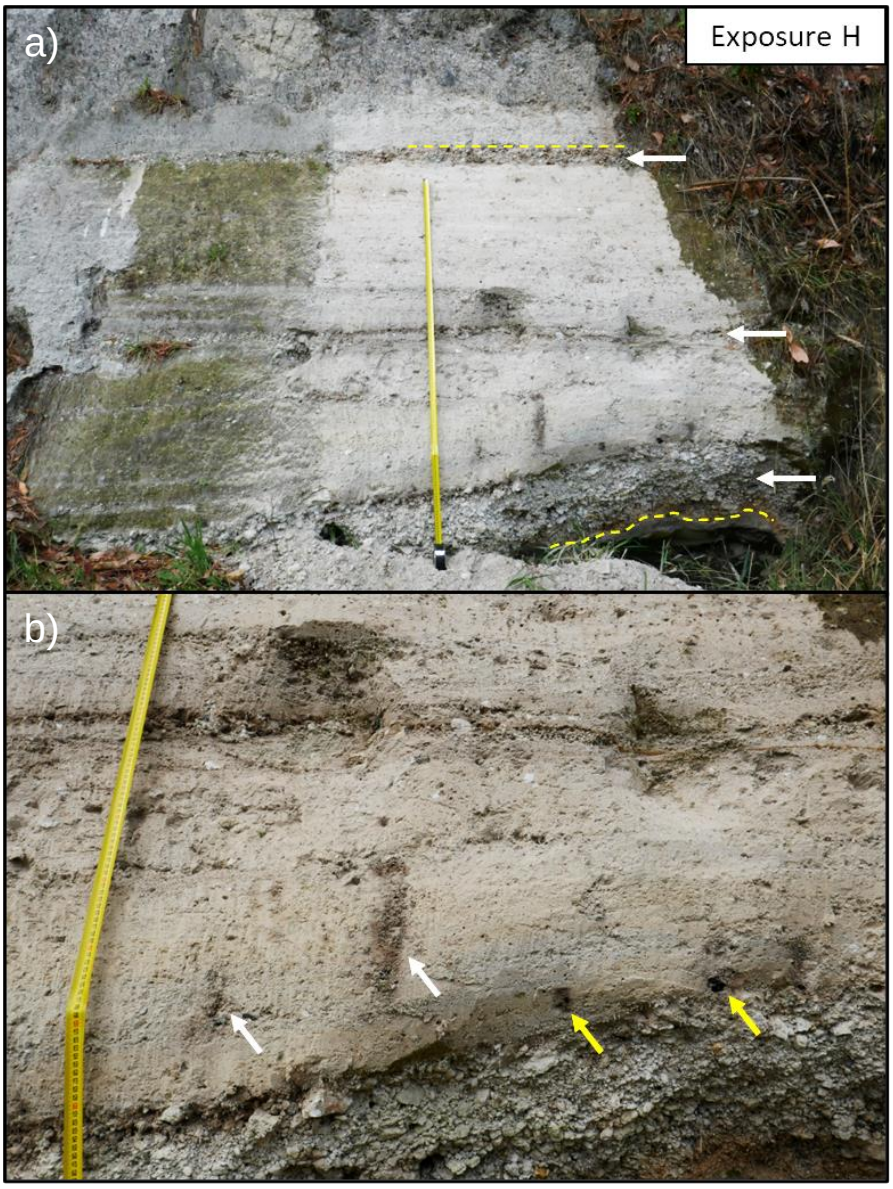

Figure 5.4 The interbedded plinian fall and ignimbrite at Exposure H. a) The yellow dotted lines indicate the basal contact with unit Y4 and upper contact with unit Y6. The white arrows mark the Y5 fall. b) White arrows show degassing pipe features, and the yellow arrows indicate fragments of carbonized vegetation.

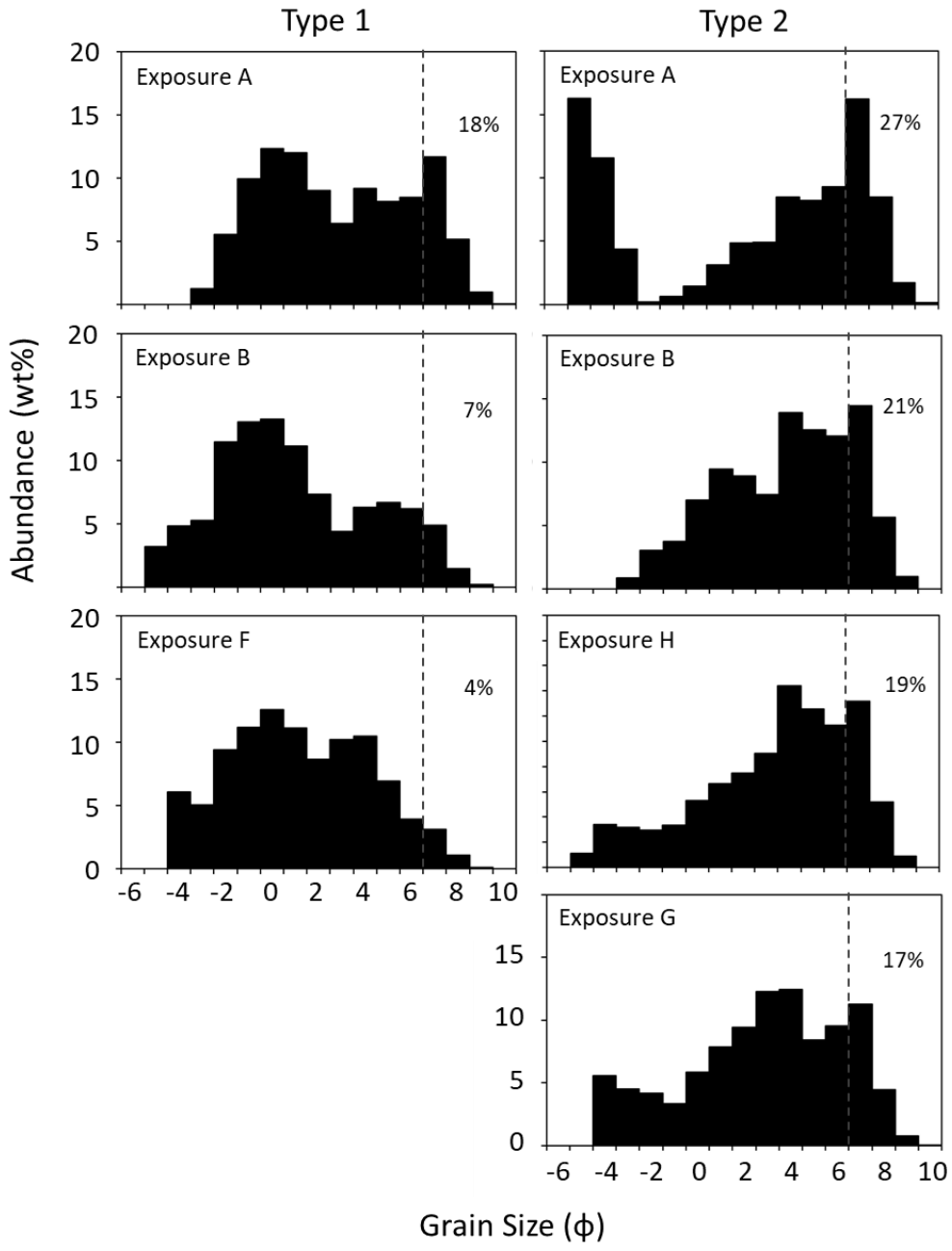

Figure 5.5 Grain size distribution examples of Type 1 (left) and Type 2 (right) EFU deposits at the denoted exposures (wt.% of full ϕ grain sizes). The total abundance of ash <10 µm in wt.% is noted in each graph. The distribution from Exposure G represents the lower of the two ash rich beds.

The distal ash-rich beds at Exposure G are markedly different in their grain size distributions with the lower bed being very fine skewed and polymodal (*Figure 5.5*) while the upper bed is coarse skewed and polymodal. The lower bed has Md_ϕ = 2.7 ϕ while the upper has an Md_ϕ of -2.7 ϕ and the proportion of coarse material is attributed to the distal nature of fine ash deposition and incorporation of plinian pumices during PDC emplacement and subsequent

fall deposition. When investigating the extremely fine- and ultra-fine-ash content within the ≤2 mm size fraction, the lower bed contains 42 wt.% and 20 wt.%, respectively, while the upper contains 39 wt.% and 26 wt.%, respectively. These values lie along the linear trend identified above within the EFU samples (*Figure 5.6*).

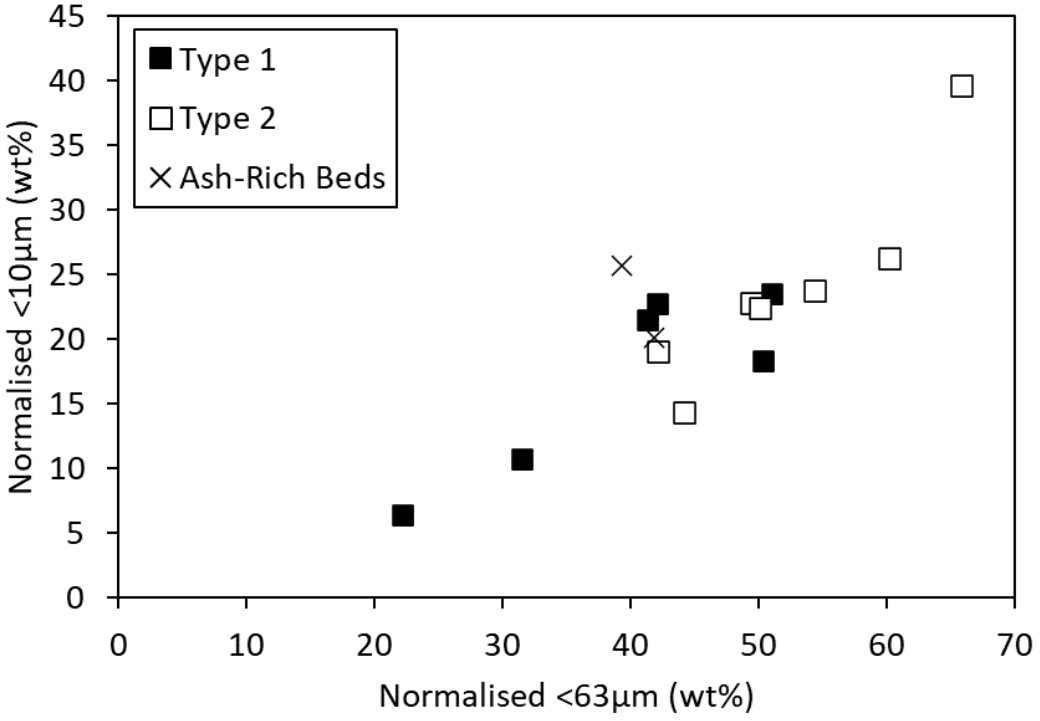

Figure 5.6 Abundance of ash <10 µm versus <63 µm normalised within the ≤2 mm size fraction for the Type 1 and 2 EFU deposits from all exposures and distal ash beds of Exposure G

5.2.3 Pumice density

To define any possible trends that might permit correlation of individual EFU within the overall Taupō eruption deposits, or their temporal relationship with the Y5 fall deposit, clast density and vesicularity measurements of Y5 fall pumices in exposures D (see also *Chapter 4, Section 4.2.6*), G, and H were obtained as per methods outlined in Houghton & Wilson (1989) and Shea et al. (2010). Samples from exposure G were selected where the lower 5 samples and then every second sample from 9 to 21 (inclusive) was analysed (due to time restrictions). In the lower samples and the distal ash beds there was a relatively small number of pumices within the 8–32 mm size fraction, therefore measurements were obtained for use

as comparative averages, rather than for density distributions. Where there was a lack of suitably sized pumices available, layers were excluded from this analysis. As shown in *Chapter 4*, there is a clear distinction in averaged density measurements between the lower samples of exposure D at 625–645 ± 115 kg m^{-3} and the upper samples at 550–590 ± 90 kg m^{-3} (*Figure 5.7*). The lower samples of exposure G have average pumice densities similar to those in D (*Figure 5.7*), of 610-650 ± 120 kg m^{-3}, while the upper Y5 fall samples are 575–590 ± 95 kg m^{-3}. There is no significant variation in pumice densities within exposure H, with all averaged measurements within 560–600 ± 100 kg m^{-3}, similar to the upper fall samples of Exposures D and G (*Figure 5.7*).

5.2.4 Componentry

Componentry was undertaken through samples from the EFU deposits in order to see if there were systematic variations that could be used to assess the relative timing of EFU emplacement in relation to the Y5 plinian fall and behaviour of the buoyant plume. To obtain componentry data, relative point counts (num%) were conducted on the 1 ϕ size fraction of box samples from each location according to the methods outlined in *Chapter 2*. All samples were measured with the exception that only every second sample from G-9 to G-21 (inclusive) was examined, due to time restrictions. Four main component groups were defined: 1) pumice, 2) wall-rock lithic (henceforth, lithic), 3) obsidian and 4) crystal. Lithic clasts (F, for 'foreign') were further defined according to their relative stratigraphic depth below surface (as in *Chapters 3 and 4*): F1, shallow seated lithics (0–400 m); F2, post-Oruanui sediments and volcaniclastics (400–3000 m); and F3 plutonic intrusive rocks (>4000 m).

In general, the EFU deposits contain the highest proportion of pumice (54–86 num%) compared to Y5 fall deposits (6–68 num% with one anomalous sample at 84 num%), with Type 2 deposits having a narrower range within this distribution of 72–84 num%. Within the 1 ϕ size fraction, the EFU deposits have a distinct lack of lithic (5–26 num%) and crystal (3–19 num%) content when compared to the Y5 fall deposits (4–60 num% and 0.5–59 num%, respectively).

The additional categorization of the composite pumice (CP; *Figure 5.8*) component type within Exposure D (see *Chapter 4, Section 4.2.4* for more details) was conducted by determining the relative abundance of CP in each full ϕ size class coarser than 2 ϕ. The total

relative abundance of this component in each sampled interval (inclusive of the Y4-G units below the Y5 deposit for comparison: see *Chapter 3*) was calculated by normalizing the weighted percent (wt.%) of components in each grain size to the measured weight of that grain size and then collated. It shows that CP is a relatively sparse component, with abundances <5 wt.% in the whole deposit, however there is a clear trend in the data (*Figure 5.9*). There has been no CP clasts identified within either the Y4-G units or in the lower portion of the Y5 deposit. The abundance of this component is initially very low (0.55 wt.%), then increases upwards to a peak of ~4 wt.%, followed by a gradual waning (*Figure 5.9*).

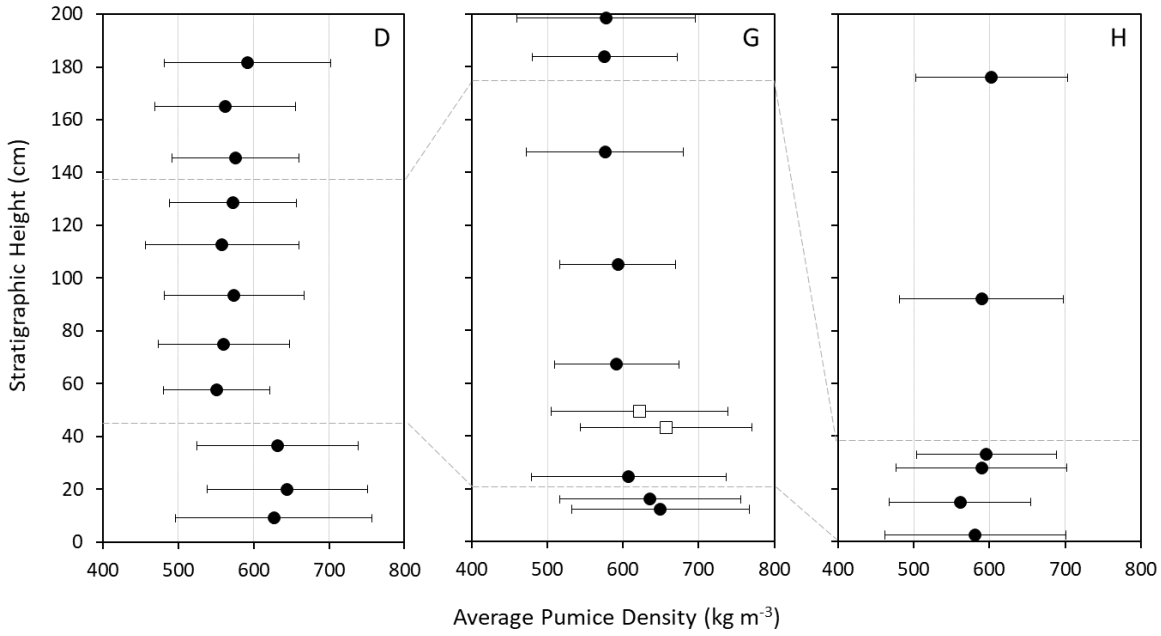

Figure 5.7 Density distributions of pumices from exposures D, G, and H with stratigraphic height in cm. The boundaries between the three eruption stages of the Y5 (see Chapter 4) are shown by dotted grey lines. Note that Exposure H does not include stage 1 of the Y5 phase. The white squares in the Exposure G distribution represent pumices within the ash-rich beds.

In conjunction with granulometry and pumice density, comparison of the component ratios of Y5 fall layers in exposures that contain EFUs against those in the detailed stratigraphic profile of Exposure D, allows relative correlations to be made regarding the timing of flows based on the three temporal Y5 eruption stages determined in *Chapter 4*. These stages are (following the initial clearing of the vent): 1) the continuous excavation of the conduit at relatively low MDR; 2) increasing MDR with decreased conduit erosion, coinciding with

deepening fragmentation, and increased viscous shear; and 3) the acceleration of conduit erosion, promotion the potential early onset of collapse that led to the Y6 ignimbrite-producing blast event. It is expected that with greater distance from source, pumice fall deposits at any given time will decrease in thickness (Sparks et al. 1997). This is, however, dependent on the degree of erosion caused by PDC emplacement, whether that depositing the EFUs or Y6 ignimbrite.

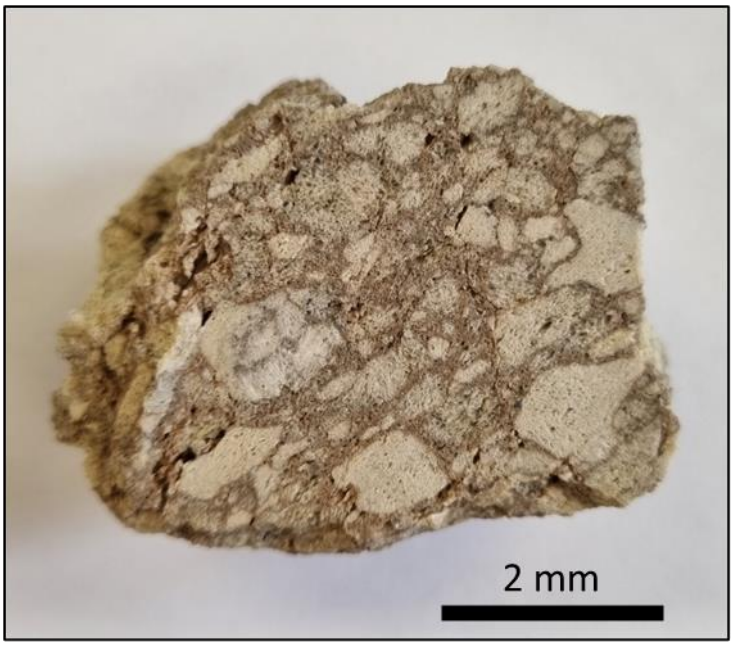

Figure 5.8 Example of a composite pumice (CP) fragment (face has been cut for thin section preparation).

With particular focus on the F:J (where F refers to foreign lithics and J refers to pumice; *Figure 5.10*) and F2:F1 (*Figure 5.11*) ratios, trends are noted in proximal Exposures A and B that align with those identified in the lower portions of Exposures C, E and G, where lithic abundances are high relative to pumice and the F2:F1 ratio is initially high. F2:F1 ratios then decrease somewhat with stratigraphic height. These trends are also noted in stage 1 of the Y5 eruption at Exposure D (*Figure 5.10*, *Figure 5.11*; *Chapter 4*) and align with finer grain sizes and moderately denser pumices (*Figure 5.7*). Note that these features are not identified in the lower pumice fall portion of Exposure H. The upper fall beds of Exposure B, as well as those identified in mid to upper zones of Exposures E and G show a general decrease in the F:J ratio (*Figure 5.10*), while F2:F1 subtly decreases (*Figure 5.11*). This correlates with

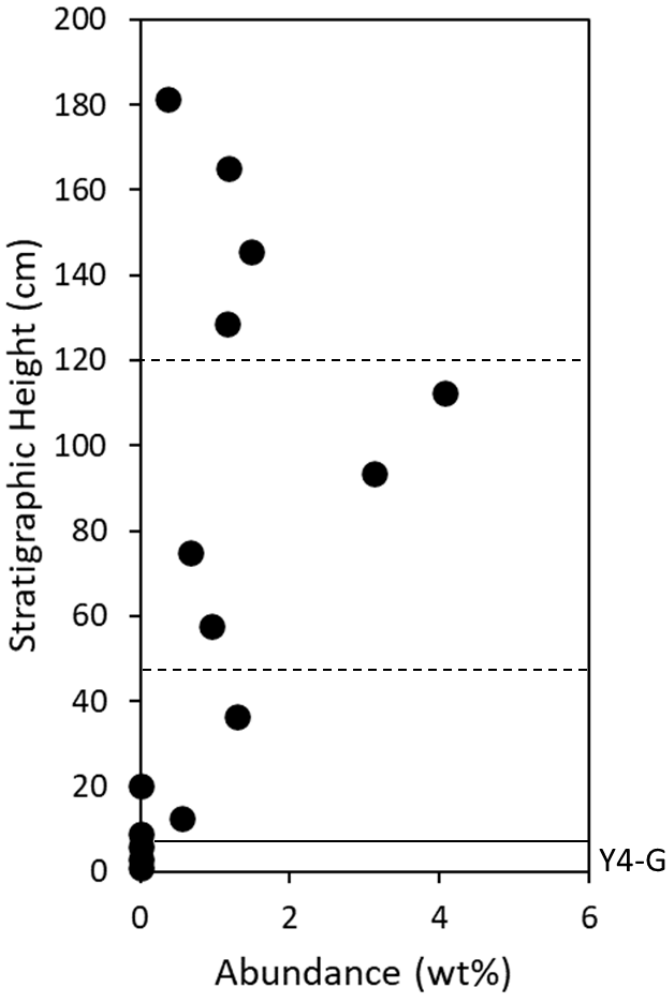

Figure 5.9 The total abundance (in wt.%) of composite pumices (CP) in Unit Y5 at Exposure D with stratigraphic height in cm. The contact between units Y4-G and Y5 is defined by a solid line. The dotted lines define the boundaries between the three eruptive stages of the Y5 phase.

increasing grain sizes, decreasing abundances of extremely fine ash, and a shift to less dense pumice that collectively align with the trends identified in stage two of the Y5 phase at Exposure D (*Figure 5.7*; see also *Chapter 4*, *Figure 4.3*, *Figure 4.4*). The lowermost Y5 fall deposit at Exposure H begins with low density (560–600 ± 100 kg m^{-3}; *Figure 5.7*), coarse pumice (Md_ϕ -2 to -3 ϕ) and has similar trends in F:J and F2:F1 ratios (decreasing with stratigraphic height) as those at Exposure D inferred to represent stage 2 of the Y5 phase (*Chapter 4*). Upper fall deposits at Exposures F, G and H then correlate with a relative increase in both F:J and F2:F1 ratios seen in stage three at Exposure D, which also aligns with a moderate increase in pumice density (*Figure 5.7*) and ash content, as well as decreasing overall grain size. Therefore, given the general correlations made and relative

stratigraphic heights, the timing of the EFU deposits can be inferred in relation to Y5 fall deposition within the three eruption stages (*Figure 5.12*). PDCs occur at all stages during the Y5 phase of the eruption; however, runout distances and the frequency of PDCs increase with relative stratigraphic height.

The relative stratigraphic timing of EFUs was also assessed by normalising the stratigraphic height of Exposure D to 100 % and estimating the relative stratigraphic height within Exposure D for each flow unit based on *Figure 5.12*. Trends seen in the ratios of F2:J, F1:J and F2:F1 (*Figure 5.13, Figure 5.14*) show that at given inferred relative heights, the EFU component ratios behave similarly to those of the Y5 fall at the reference Exposure D. The F2:J ratio (*Figure 5.13*) in both the EFUs and fall increases subtly with relative height, then begins to decrease at 40 – 50 % relative height. This decrease in ratio continues to approximately 70 – 75 % relative height and then increases again in both the EFUs and fall deposits. Similarities in the F2:F1 and F1:J trends between the EFUs and fall are also noted (*Figure 5.14*).

5.3 Discussion

5.3.1 The relative timing of the Early Flow Units

As discussed in *Chapters 3 and 4*, the location of the Y5 vent is most likely to have been at the originally proposed location in proximity to the younger Horomatangi Reefs (Walker 1980). Initial investigations (Wilson 1981) determined that the EFU erupted coevally with the Y5 plinian plume, most likely from the same vent location. The presence of composite pumices (Taddeuchi & Wohletz 2001; Kuehn 2002; Giachetti et al. 2021) within the Y5 fall deposits enable new insights into this interpretation and to suggest a new formation mechanism for such clasts. Giachetti et al. (2021) proposed that composite pumices form during low energy collisions just above the fragmentation zone, where the unfragmented magma sits directly below the fully fluidized gas-pyroclast mixture and individual pyroclasts can sinter together. However, for this to occur during Plinian style fragmentation, the foam post-fragmentation must be brought back together under a uniform ‘hydrostatic’ stress to sinter without inducing eutaxitic fabrics (pers. comm. C.J.N. Wilson, 2022), which has not been observed in the Y5 CP clasts. Therefore, as previously mentioned (*Chapter 4*), it is more likely that the formation of these clasts during the Y5 phase occurred due to recycling

of welded or trapped EFU material from the vent area during the eruption. This is supported by the minor inclusions of lithic fragments and the sintering of pumice fragments within a light orange-red pumiceous matrix, similar in colour to proximal products of the EFUs (Wilson & Walker 1985). Individual pumice fragments retain their original vesicle orientations, with directions appearing random between each fragment during amalgamation, while the pumiceous matrix material shows evidence of flow direction around the pumice fragments. There is no evidence of CP clasts in the upper Y4 (Y4-G), nor in the base of the Y5 deposit (*Figure 5.9*). Minor amounts of CP clasts are noted in the lower Y5; however, intensified incorporation and increasing abundance of these clasts occurs later and increases upward (*Figure 5.9*). This is consistent with field observations, where at all observed exposures, the presence of Y5 fall material at the base of the deposit show that the first flows to reach locations outside of the present Lake Taupō did not occur at the onset of phase Y5, and instead began after the onset of sedimentation and deposition from the buoyant plume. Ultimately, the presence of recycled EFU CP material in the Y5 fall deposit implies that the PDCs were likely generated from the same vent as the coeval Plinian plume. It would be expected that had the EFU generation began at or prior to the onset of the Y5 phase, CP clasts would also be evident in the initial Y5 fall beds, as they occur at all other intervals inferred to be equivalent to EFU generation (*Figure 5.9*, *Figure 5.12*). It cannot be ruled out, however, that the initial opening of the Y5 phase was simply not accompanied by large enough PDCs to reach the perimeter of the lake that insufficiently welded in the vent area. For example, the first flows noted at Exposures A and B show that initial PDCs were smaller volume with relatively short runout lengths compared to their later counterparts, hence even lower-volume flows may have occurred at Y5 onset. Determining the amount of PDC material that flowed into the contemporaneous Lake Taupō, however, is beyond the scope of this study. In conjunction with the initial fall material, the thin bands of Y5 Fall that succeed EFU deposition, immediately prior to the Y6 ignimbrite at Exposures A, I, F and H (*Figure 5.2*, *Figure 5.4*), suggest that the EFU package is entirely contained within Y5 airfall activity.

There are several aspects of the EFU types discussed in this chapter that suggest contrasts to the proximal and distal EFU concepts (Wilson 1981; Wilson & Walker 1985) in, for example, different sectors of distribution, flow unit thicknesses and grain size characteristics. As shown in *Figure 5.1*, I predominantly use the original dispersal maps (Wilson 1981;

Wilson & Walker 1985) to define the runout extents of Type 1 and Type 2 based on similarities in deposit characteristics to the proximal and distal EFUs, respectively. The proximal EFUs were noted to have large pumice clasts and are relatively massive, topographically constrained deposits, while the distal EFUs were finer grained, typically stratified deposits that were sedimented from flows that mantled topography (Wilson 1981; Wilson & Walker 1985). Type 1 EFUs have been defined here as those that are massive, coarser grained, pink-orange to cream coloured deposits while the Type 2 are massive to moderately stratified, finer grained and white to grey coloured. The total ash content in the Type 1 deposits is also typically lower than those of the Type 2 (<1 mm at ~40–70 wt.% versus 65–95 wt.%, respectively). By predominantly using grain size and componentry comparisons between the Type 1 and Type 2 deposits, I have noted that the sectors of distribution for a select few flows deviated from what was original defined as simply proximal or distal EFUs, discussed below. The Type 1 deposits incorporate the PDC identified at Exposure F at ~16 km runout length, as this deposit shows features such as oxidization colouring, a massive, poorly sorted structure, and lower abundance of fine-ash, that align with those identified in Type 1 deposits as opposed to distal EFU features (*Figure 5.1b*, *Figure 5.3*). The earliest EFUs identified in exposures A and B (*Figure 5.3*), distal extents of which only reached proximal to medial distances from source during stage one of the Y5 phase, have been defined on the map as additional Type 2 deposits of shorter runout flows (*Figure 5.1b*). The distal ash-rich beds in Exposure G align with EFU type deposits based on grain size characteristics, componentry, and general field observations (*Figure 5.3*,*Figure 5.5*, *Figure 5.7*). Therefore, the occurrence of these fine-ash bands and those observed in additional exposures have been added to the map as the deposits of time equivalent weak gravity current outflows of very distal PDC ash (like those described from Y2 by Talbot et al. 1994), likely to have occurred within stage two of phase Y5. Also note that the general confinement of the fine-ash bands to topographical lows (*Figure 5.1b*) suggesting a directional outflow of the gravity currents.

The relative timings of the EFUs within the stages of Y5, as determined through relative stratigraphic heights, field mapping, componentry, granulometry and pumice density profiles compared with reference Exposure D (*Figure 5.12*; *Chapter 4*), show that the EFUs became increasingly energetic and voluminous (based predominantly on runout distance) toward the later stages of the Y5 phase as eruption intensity increased. The inference that

the eruption intensified is based on the increase in grain size with stratigraphic height at Exposure D and other observed Y5 deposit localities. The shorter runout and least energetic PDCs are noted to have occurred early in stage 1 of the eruption following the onset of the buoyant Plinian plume (*Chapter 4*) and are relatively sparse (*Figure 5.1b*, *Figure 5.3*, *Figure 5.12*). At Exposure H (*Figure 5.4*), the onset of pumice fall deposition occurs as lithic-poor, medium- to coarse-grained lapilli that contains pumices with densities like those identified in stage 2 of phase Y5 in exposures proximal to the general axis of deposition (i.e., exposures D and G; *Figure 5.1b*, *Figure 5.7*, *Figure 5.12*). EFU correlations indicate that PDCs deposited at Exposure H have likely been generated following the climax of the Y5 phase (*Figure 5.12*; *Chapter 4*). The trends identified at Exposure H also suggest that the onset of Y5 deposition occurred at a later stage to the north of the vent, as the buoyant plume increased in height (i.e., the umbrella cloud expanded in width) and developed to more climactic conditions. This is compared to the initial deposits in the main dispersal direction, which originated from a relatively lower plume height.

When comparing the extremely fine- and ultra-fine-ash contents of the Type 1 and Type 2 samples (*Figure 5.6*), it is noted that both PDC types converge on a linear trend. The linear convergence suggests that the two deposit types may be mechanically associated, with the Type 2 being the distal, topography-climbing reaches of Type 1 PDCs. This is seen particularly in samples A-6 and B-10, which show features of Type 2 deposits yet are in medial to proximal deposition regions, suggesting that they are simply distal extents of shorter runout, lower energy (or lower volume) PDCs. Additionally, *Figure 5.13* and *Figure 5.14* show that there is no significant deviation in the time-variant trends between the EFU types and the Y5 fall deposit, which would be expected if the PDCs do have varying generation mechanisms. For example, mass partitioning to feed PDCs is expected to be seen in the deposited mixture as enrichment of denser components where partial column collapse is involved. The material leaving the vent that rises with the buoyant plume, however, appears to be the same as that being fed into the intraplinian PDCs with similar time variance despite the contrasting deposition style (Type 1 versus Type 2). Therefore, it can be inferred that the EFUs are a product of one generation mechanism and the deposit types simply represent the relative runout distance and/or topographical constraints on runout (i.e., valley ponding versus topography climbing) for individual flows.

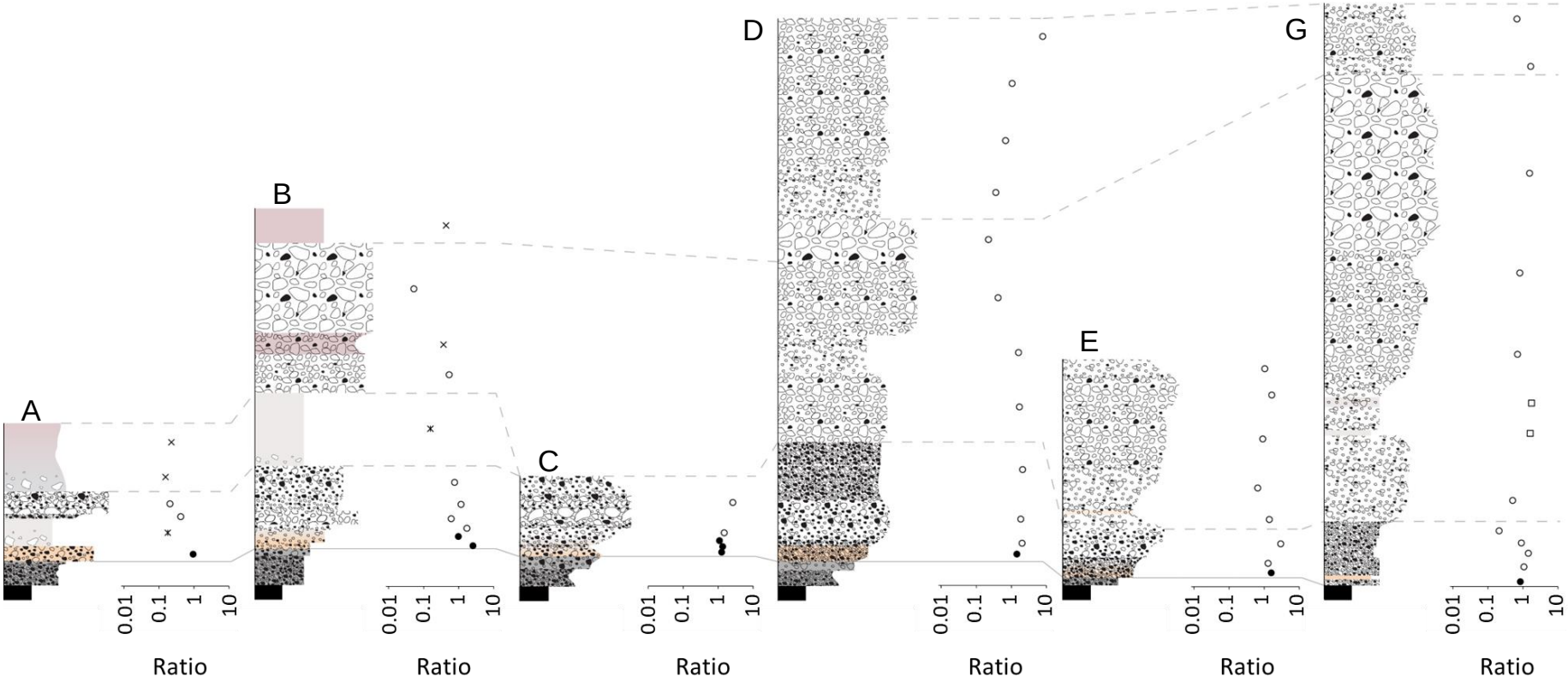

Figure 5.10 Examples of deposit characteristics, in this case the ratio of F:J clasts with height, used to define the three eruptive stages of phase Y5. This figure shows the stratigraphic columns of various exposures (noted by letters above) where solid black and dark grey indicate the Y4-G, light orange indicates the ash-rich base of the Y5, solid light grey represents Type 2 EFUs while pink represents Type 1. Patterned fill represents fall deposition. The solid black correlation line marks the contact between Y4-G and Y5, while the dotted correlation lines indicate the boundaries between the three Y5 stages. Black dots show F:J ratios of samples from the base of the Y5, white dots represent ash-poor fall and crosses represent the PDC deposits.

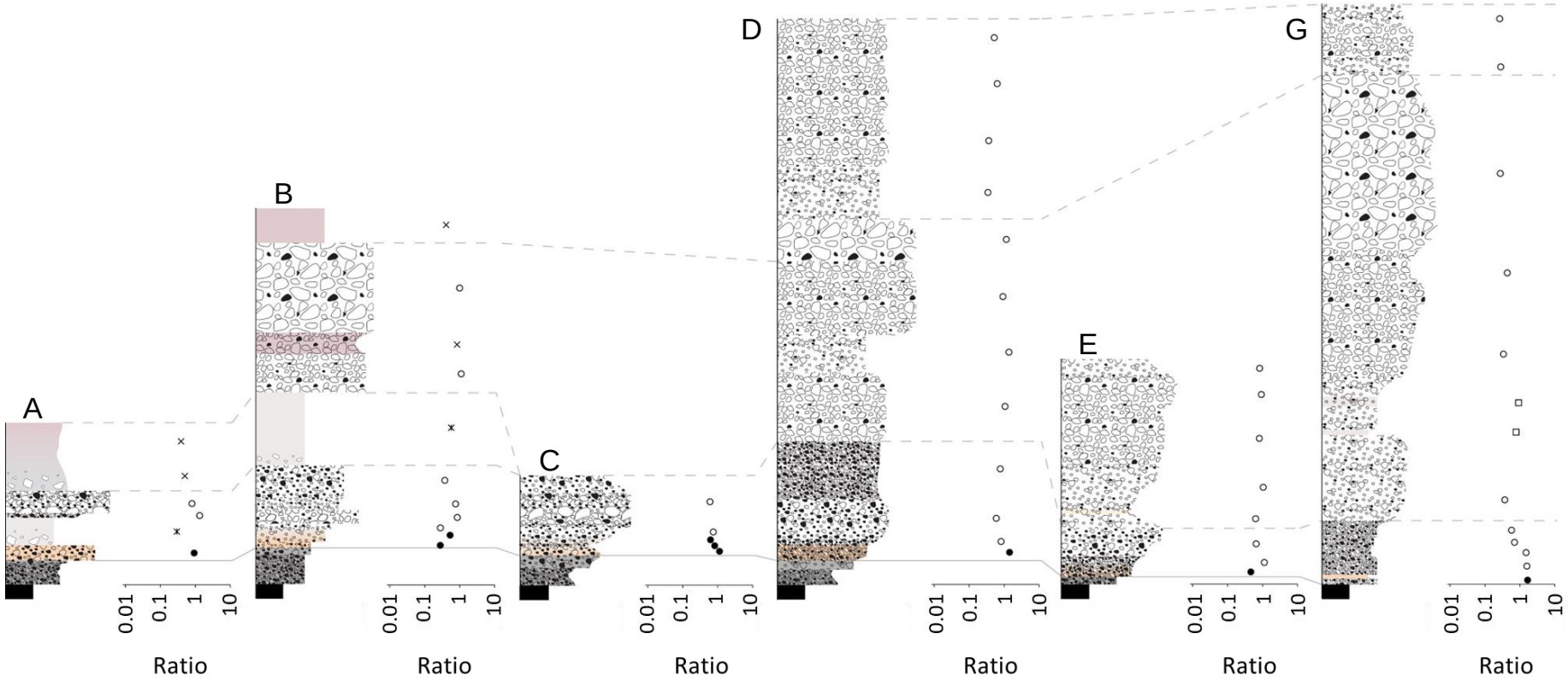

Figure 5.11 Stratigraphic columns showing the ratio of F2:F1 with height in the three eruptive stages of phase Y5. Details as in Figure 5.10.

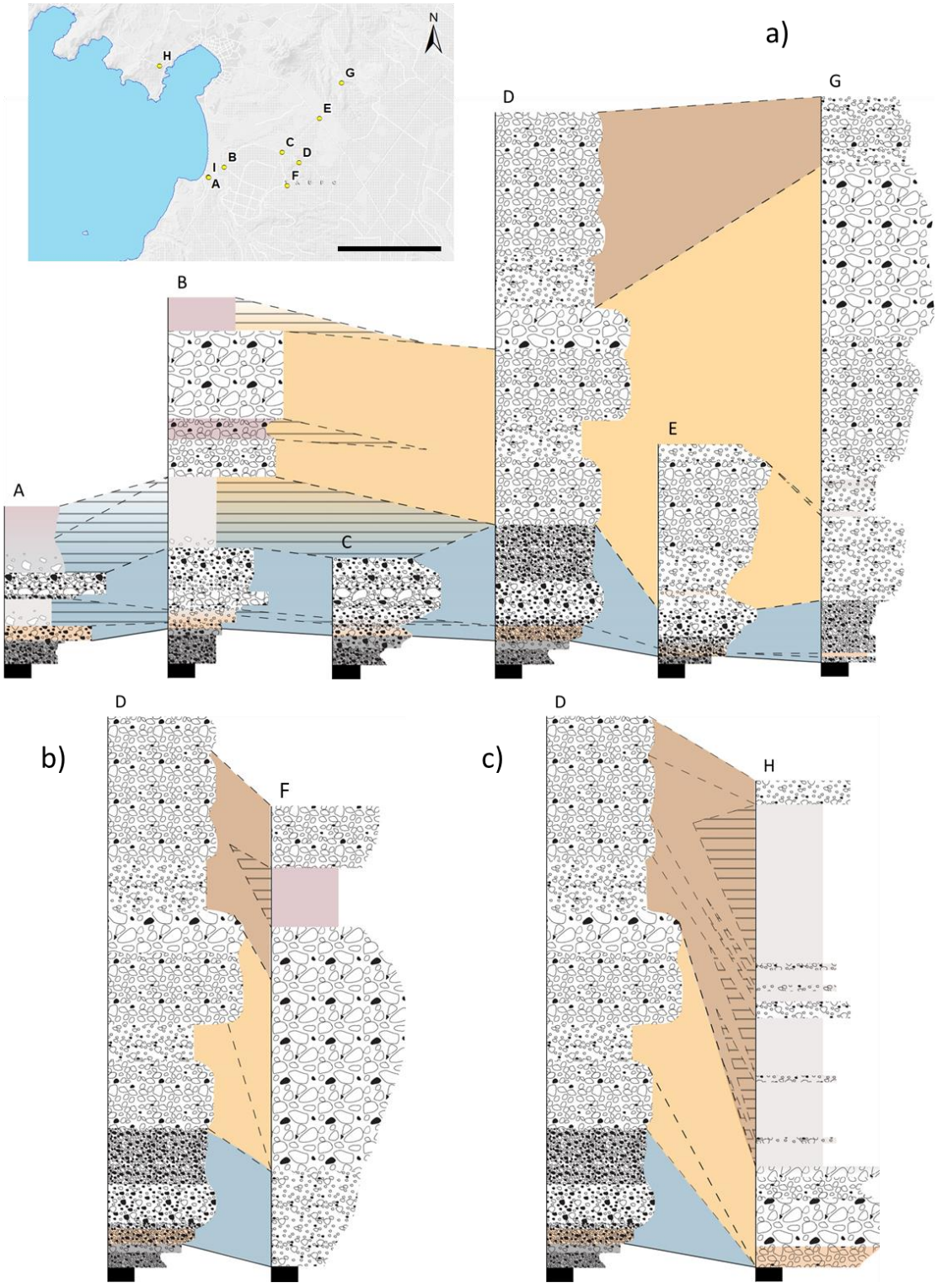

Figure 5.12 The three stages of phase Y5, correlated between the stratigraphic columns of each of the exposure locations (indicated by the inset) in relation to the reference Exposure D. a) shows the transect from A to G (excluding Exposure F), b) shows the correlation of exposures F to D, and c) shows the correlation of exposures H to D. Stage 1 of phase Y5 is defined by blue, stage 2 by yellow and stage 3 by brown. Note that Stage 1 deposits are absent at Exposure H. Rough correlation of the EFU deposits are depicted by horizontal fill lines. The contact between units Y4-G and Y5 is defined by a solid line.

5.3.2 Transport regime of the Early Flow Units

The grain size, grading, bedding and high temperature emplacement (indicated by incipient welding of Type 1 PDCs (Wilson & Walker 1985) to be at least 600 ºC, based on estimates for the onset of sintering in such rhyolitic compositions (e.g., Boyd 1961; Grunder et al. 2005; Quane & Russell 2005) of the EFU deposits, and the variation of deposit thickness with terrain indicate the PDCs were emplaced by the dominant transport mechanism of a dense concentrated underflow with a vertically stratified more dilute flow proportion above. The runout lengths of the EFUs are typical for medium-sized, pumice-rich ignimbrites documented in historical eruptions (e.g., Mt St Helens 1980, Mount Pinatubo 1991); however, linking the dominant transport mechanisms of PDCs quantitatively to deposit characteristics for modelling purposes is underexplored (e.g., Sulpizio et al. 2010; Lube et al. 2020). In analogy to fluid-particle transport in aeolian and aqueous environments, there are typically two endmembers of PDC and PDC deposit (dense and dilute transport regimes). The dichotomy of PDC transport and deposition is controlled by the occurrence and abundance of mesoscale particle clustering in an intermediate PDC transport regime (Wilson & Houghton 2000; Breard et al. 2016, 2018; Breard & Lube 2017).

The generation of two different basal regions in PDCs (a thin, immobile bedload region and thick, highly mobile granular-fluid avalanches or underflows) is controlled by the sedimentation rate of particles into the basal flow region relative to the escape velocity of the gas in the basal flow. Breard et al. (2018) showed that these two conditions can be described using the non-dimensional ratio of timescales, $T_{av/ma}$, which expresses the ratio of gas escape and formation rate of a concentrated region of particles:

$$T_{av/ma} = \frac{C_{ac} V_s}{C_{bed} V_g}$$

Where V_g and C_{bed} are the vertical upward gas velocity and the particle volumetric concentration within the aggrading dense flow region, respectively. C_{ac} is the particle volumetric concentration of the basal portion of an ash-cloud surge, and V_s is the settling velocity of particles directly above the dense flow region.

Breard et al. (2018) also derived an empirical PDC transport parameter $T_{de\text{-}di}$ and showed that this allows discrimination between deposits of dominantly dilute PDCs (flows that are unable to generate an underflow with elevated gas pore pressure) and concentrated transport

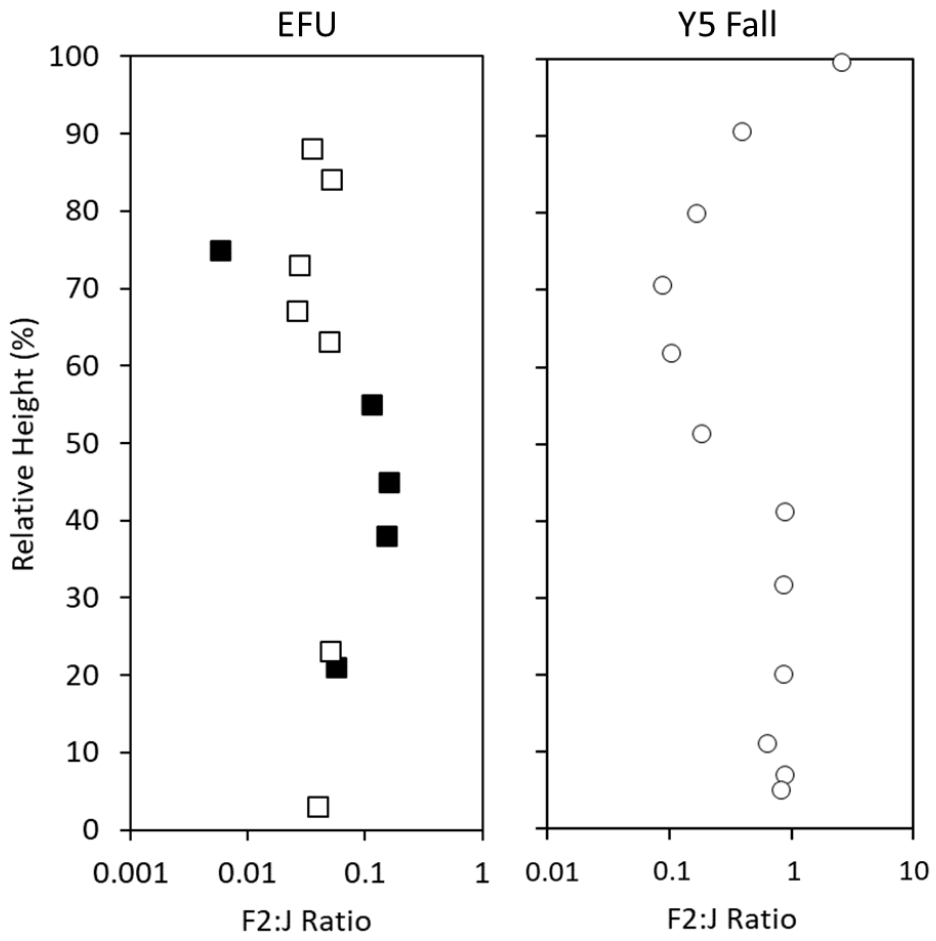

Figure 5.13 The F2:J ratio of EFU ignimbrite and Y5 fall material with relative height, normalised to 100%. The relative height of the Type 1 (solid black squares) and Type 2 (white squares) EFUs was determined based on their rough height correlation in association with unit Y5 at Exposure D (cf. Fig. 5.12). Note the similarity in the relative trends between the overall EFU and the fall.

regimes (deposits of flows that can generate mobile underflows). The non-dimensional ratio $T_{de\text{-}di}$ assesses the flow mobility from a PDC deposit by assessing its runout length, flow inundation area and the effect of the hydraulic permeability, which controls the gas pore pressure of PDCs and, hence, the friction on the PDC at its lower flow boundary:

$$T_{de-di} = \frac{A^3 d_{s,1/2}}{(V^{5/3} L^2)},$$

where $d_{s,1/2}$ is the Sauter mean diameter of the deposit at the half runout distance, A is the inundation area, V is the volume of the deposit and L is the runout distance. The Sauter mean (*D32*, equivalent to $d_{s,1/2}$) is used to characterise the significance of drag forces on particle

motion and is calculated from the sorting and geometric mean of a grain size distribution (Breard et al. 2018):

$$D_{32}(mm) = 2^{-\left[\mu_\varphi + \frac{ln2}{2}\sigma_\varphi{}^2\right]},$$

where μ_ϕ and σ_ϕ are the geometric mean and standard deviation, respectively, in ϕ units.

When applied to estimated deposit volume, runout, inundation, and grain-size data collected here for the ignimbrites formed in phase Y5, the EFU fall into the dense flow regime of Breard et al. (2018) with ratios of $T_{de\text{-}di}$ ranging from 1.5×10^{-4} to 1.3×10^{-3} (*Figure 5.15*). As discussed above, this interpretation of the dominant PDC transport regime of EFUs agrees with the general geometric, bedding and grading characteristics of their deposits (see above). The reason for the formation of dominantly dense PDCs in the Y5 eruption phase is probably related to both the high mass eruption rate resulting in high PDC mass fluxes and the high fragmentation efficiency resulting in the formation of large quantities of very fine ash, which promote mesoscale particle clustering and rapid sedimentation.

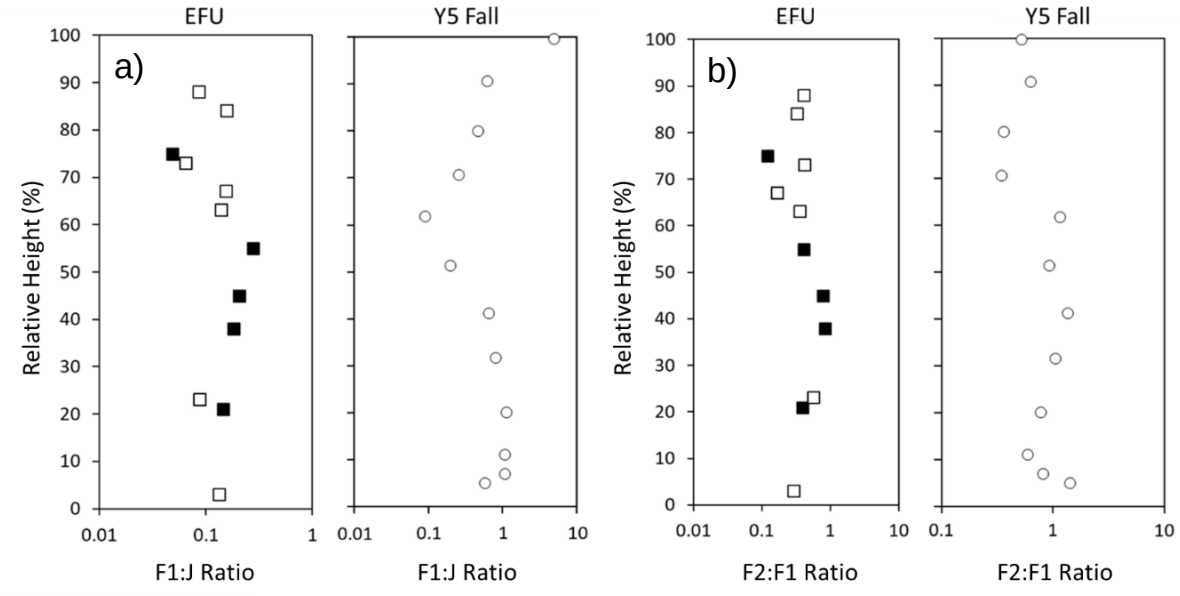

Figure 5.14 The F1:J ratio (a) and F2:F1 ratio (b) of EFU and Y5 fall with relative height, normalised to 100%. The relative height of the Type 1 (solid black squares) and Type 2 (white squares) EFUs was determined based on their rough height correlation in association with unit Y5 at Exposure D (cf. Fig. 5.12). Note the similarity in the relative trends between the overall EFU and the fall.

5.3.3 The nature and generation of the Early Flow Units

In the case of large-scale Plinian eruptions, the two widely accepted interpretations for the generation and dynamical controls of PDCs are regimes of total- or partial column collapse (e.g., Sparks & Wilson 1976; Wilson et al. 1978; Sparks et al. 1997). Partial column collapse is considered a representation of the transitional regime of column unsteadiness between a sustained Plinian column and total collapse conditions. In such cases, changes in physical properties of the erupting mixture, variations in conduit geometry, mass discharge rate and/ or fragmentation style are inferred to result in the buoyancy of the erupting mixture not being achieved, thereby inducing collapse conditions (Turner 1969, 1986; Woods 1995, 2010; Neri et al. 2002; Kaminski et al. 2005; Carey & Bursik 2015; Cioni et al. 2015; Lherm & Jellinek 2019). Features representing these interpretations, such as loss of fine ash, enrichment in dense components, and stratification and cross bedding have been identified in numerous deposits with coeval deposition of Plinian fall and PDCs, such as Fogo A 4.6 ka (Walker & Crosdale 1971), and Vesuvius 79 CE (Shea et al. 2011). This is, however, not the case for all Plinian eruptions involving coeval fall-flow deposits, such as Novarupta 1912 (further discussed in *Chapter 6, Section 6.3.2*; Fierstein & Hildreth 1992; Houghton et al. 2004) and is also not identified in the Y5 eruption phase. Generalised steady versus unsteady column regimes may oversimplify the interpretation of both ignimbrite and plinian air fall deposits in natural eruption scenarios, whereby deposit features in intraplinian ignimbrite deposits deviate from what is expected based on modelled scenarios. For example, partitioning of the erupted mass between the buoyant umbrella cloud and the collapsing mixture will result in a deposit that is enriched in dense components and lack large quantities of fine ash (Neri & Dobran 1994; Neri et al. 2002; Kaminski et al. 2011; Gilchrist & Jellinek 2021). In contrast, the EFU show no loss of ultra-fine material (e.g., *Figure 5.5*, *Figure 5.6*) and no enrichment in dense clasts such as crystals and lithics compared to their fall counterparts (e.g., *Figure 5.13, Figure 5.14*), suggesting that the material had not been winnowed and therefore not seen a high part of the column in the sense of collapse. The high ultra-fine-ash content in the EFU is likely to be a result of high fragmentation efficiency, as typically secondary generation of fine material by abrasion is controlled by the bubble size distribution which produces ash sizes generally between 30 and 63 µm, sometimes as fine as 10 µm (Dufek & Manga 2008; Heap et al. 2014; Buckland et al. 2018). The EFU deposits were also inferred to be deposited from flows in the dense flow regime, as explained in *Section 5.3.2*. This

contradicts the interpretation that these flows are generated by collapsing sediment waves, which are expected to emplace relatively dilute PDCs (Gilchrist & Jellinek 2021).

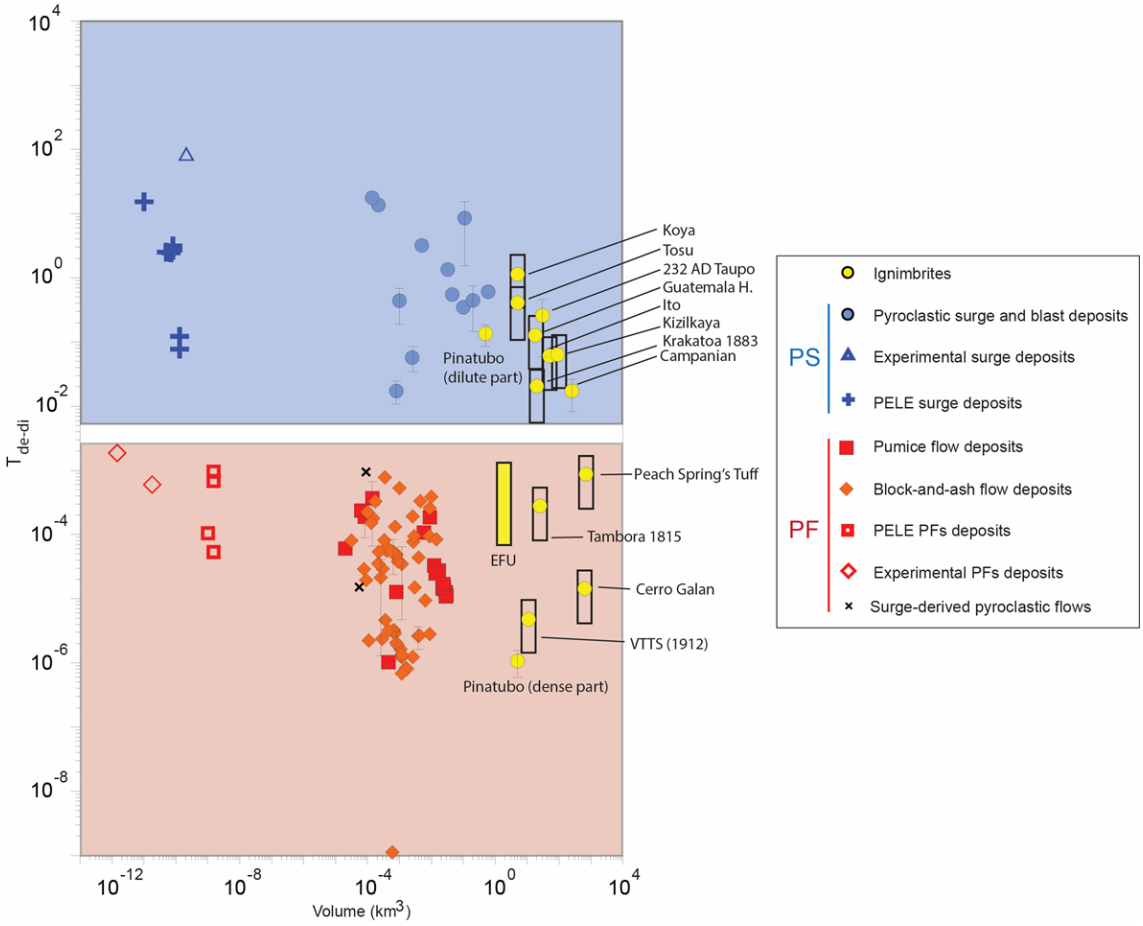

Figure 5.15 Classification of PDC deposits with the transport factor 'T_{de-di}" in relation to their volume, from Breard et al. (2018). The plot highlights the distinction between dilute (blue) and dense (red) transport regimes for a range of experimental and natural PDCs. In addition to the original points plotted by Breard et al. (2018), I have plotted the range of T_{de-di} calculated in this study for the EFU. Note the similarity to the PDCs of Tambora 1815.

The likely scenario to explain the observations regarding the EFU deposits is the 'gargling eruption' process in which large, debris filled vent structures, or subsidence causing large portions of PDCs to become trapped within developing basins, result in an eruption needing to penetrate its own deposits. This results in overloaded annular zones within the jet region which fail to rise with the buoyant plume and has been previously recognized in deposits of the Novarupta 1912 eruption (see *Chapter 6, Section 6.3.2*), which may provide a direct analogue to the complexities of the Y5 eruption (Wilson & Walker 1985; Fierstein &

Hildreth 1992; Wilson & Hildreth 1997; Houghton et al. 2004; Hildreth & Fierstein 2012; Fierstein & Wilson 2005; Valentine & Cole 2021). Gargling dynamics occur when preexisting deposits interact with a juvenile erupting mixture and form a dense sheath along the margins of the erupting jet (Houghton et al. 2004; Hildreth & Fierstein 2012; Valentine & Cole 2021). Numerical models by Valentine & Cole (2021) shows that air entrainment into the jet is highly affected by the dense sheath as its bulk mixture is typically denser than that of the jet core. Therefore, the highest density region occurs on the outer edge of the jet, producing fluidized PDCs (Valentine & Cole 2021). Collapse of material can occur at all heights along the sheath while the core remains similar to the contents coming from the vent. Simulations by Valentine & Cole (2021) are 2D axisymmetric; however, natural cases may be more complex due to external factors such as surface winds or vent geometry and sheath collapse may only occur on one side of the erupting jet producing lobate, directional PDCs. It is also noted by Valentine & Cole (2021) that thicker preexisting deposits or basin infill may result in a more dynamic behaviour at vent, where time variant oscillation in jet height occurs during the eruption.

In the case of the Y5 eruption and its intraplinian EFU, the following explanations can be used to infer PDC generation through what is termed the gargle dynamics model.

1. The anomalously high proportions of ultra-fine ash (<10 μm at 4 – 27 wt.%) in EFU deposits and lack of evidence for enrichment of dense clasts (this thesis and Wilson & Walker 1985), indicates that there has been minimal to no mass partitioning between the buoyant umbrella cloud and collapsing mass that would be expected in the case of a partial column collapse regime (Neri & Dobran 1994; Neri et al. 2002; Kaminski et al. 2011; Gilchrist & Jellinek 2021). It can also be noted that typically during transport, the size of secondary fine material produced by abrasion is restricted to the pumice vesicle wall thickness (generally between 30 and 63 μm, sometimes as fine as 10 μm; Dufek & Manga 2008; Heap et al. 2014; Buckland et al. 2018) and hence ultra-fine ash at these proportions is inferred to predominantly be a direct product of highly efficient fragmentation during the Y5 phase of the eruption (Walker 1980; Wilson 1985).

2. Incipient welding of sections of the Type 1 deposits (Wilson & Walker 1985) indicates that the EFU were emplaced at high temperatures of at least 600 ºC, based

on estimates for the onset of sintering in such rhyolitic compositions (e.g., Boyd 1961; Grunder et al. 2005; Quane & Russell 2005). The high temperature emplacement also indicates that the mass collapsing or being diverted to form the PDCs is likely to have originated from lower heights in the dense sheath where entrained air had limited capacity to cool the mixture (Valentine & Cole 2021).

3. The Y5 phase is inferred to have occurred from the same vent location as the earlier Y2 phase (see *Chapter 3*). Any preexisting Y2 deposits within the vent region may have contributed to the dynamics of gargling during phase Y5. However, note that flows that reached sites outside Lake Taupō did not begin immediately during phase Y5 (i.e., *Figure 5.9*, *Figure 5.12*; *Section 5.3.1*) and therefore the infill of Y2 material may not have been sufficient in itself to cause gargling during powerful activity. Further infill leading to gargling may have been produced by a build-up of early stage Y5 material as the vent developed and erupted material was able to accumulate within the vent area. Additionally, the first flows to reach onshore were relatively short runout flows (*Figure 5.1b*) in comparison to later, more widely distributed EFU. The presence and gradual increase of CP clasts within the Exposure D (*Figure 5.9*) toward the climax of the Y5 phase, as inferred from grain size characteristics of the Y5 fall deposit, suggest that vent infill was increased as portions of PDCs became trapped within the basin. As the EFUs increased in frequency and size, the amount of EFU infill increased and is reflected in higher portions of CP clasts being recycled into the buoyant plume.

4. In the case of the Y5 phase, the transition from jet to buoyant plume is different to standard eruption models due to the extreme mass eruption rate (Wilson and Walker 1987). This may allow for the dense sheath to be significantly larger and denser without effecting the buoyancy of the plume. It is recognized, however, that the Valentine & Cole (2021) simulations are 2D axisymmetric and may not entirely represent natural cases in which asymmetry in the development of the dense sheath occurs due to spatial variability in vent fill because of vent geometry or other external factors (Houghton et al. 2004; Hildreth & Fierstein 2012; Valentine & Cole 2021). Any possible EFU deposits west of the vent, however, would be beneath modern Lake Taupō and therefore there is an inability to confirm whether PDCs occurred axisymmetrically or preferentially to one side of the erupting jet.

5. The increased mobility and runout distance of EFUs during the later, more powerful stages of the Y5 phase may be explained by both an increase in collapse height of the dense sheath due to higher MDR and an increased amount of infill material interacting with the primary jet. If the vent fill is thicker and coarser, interaction with the juvenile jet is minimized and the juvenile component of PDCs will be reduced (Valentine & Cole 2021). The fine grained, pumice dominated nature of the EFU and the similar trends identified in components of the EFU and Y5 fall deposits at time relative intervals (*Figure 5.13, Figure 5.14*) suggests that the vent fill may be relatively fine grained compared to the juvenile jet and therefore more complex interactions between the dense sheath and jet core occurred.

6. A lack of time correlative bedding has been identified in the Y5 plinian deposit (see *Chapter 4*) yet, in the partial collapse regime, oscillation and temporary reduction of the column height is expected to result in correlatable variations in grain size across an associated fall deposit (Walker 1971, 1980; Carazzo et al. 2015; Cioni et al. 2015; Houghton & Carey 2015). Where gargle dynamics are concerned, the dense sheath on one side of an eruptive jet can produce PDCs simultaneous with a jet core that entrains air on the unaffected side to become buoyant (Fierstein & Hildreth 1992; Houghton et al. 2004; Valentine & Cole 2021). This results in a sustained plinian column seemingly without interruption, regardless of the development of coeval PDCs, consistent with observations of the Y5 plinian deposit.

5.4 Conclusions

This study has shown the value of detailed quantitative investigation into time-variant physical properties, such as granulometry, componentry and pumice density, of intraplinian PDC deposits and their plinian fall counterparts. Previously, the oversimplification of generation mechanisms and dynamical controls that results from the basic categorization of fall and flow deposits has led to the generalized interpretation that the EFUs were a product of partial column collapse. The physical properties of the PDC deposits, however, deviate from the traditional expectation of relatively dilute flows enriched in dense components that results from partial mass partitioning between a buoyant umbrella cloud and collapsing sediment waves. The unusually high ultra-fine-ash content, relative lack of lithics and

crystals and the dense transport regime of the EFU, in combination with the lack of time correlative bedding identified in the Y5 plinian deposit, indicate that the intraplinian PDCs of the Y5 eruption were instead likely a product of gargling dynamics, as similarly described by Wilson & Walker (1985). In this case, the synchronous emplacement of plinian fall and PDCs could occur with little to no interaction with the coexisting Plinian column, which simultaneously undergoes no diminution. Originally proposed by Wilson & Hildreth (1997), computational modelling of gargle dynamics has only recently been initiated (Valentine & Cole 2021). Therefore, the quantitative investigation of the intraplinian EFUs expands opportunities for the amalgamation of field studies and computational based eruption modelling and plays an important role in furthering the understanding of the behaviour and consequent sedimentation dynamics of large-scale Plinian eruptions.

6 Discussion

Through detailed quantitative analysis of deposit characteristics at selected proximal to medial localities, this study provides new interpretations of eruption behaviour and sedimentation dynamics of the Y5 phase of the Taupō 232 ± 10 CE eruption. In this chapter, I summarise the key findings of this research and discuss their implications for understanding the Taupō eruption, improving our knowledge regarding other global case studies, and opening opportunities for further research surrounding the amalgamation of field studies and computational modelling for hazard mitigation and management purposes. This chapter will revisit and discuss the following aspects:

1. A review of the source location for the Y5 phase and the implications for the configuration of vents during the Taupō eruption;

2. The use of deposit features, particularly lithic lithologies and bedform correlations in relation to: granulometry, componentry and pumice density, in deciphering the complexities in the vertical stratigraphy, and providing new opportunities for the interpretation of plinian deposits;

3. The generation and dynamical controls of intraplinian PDCs in terms of the relationships between the Early Flow Unit (EFU) and Y5 fall deposits, the resulting implications for other case studies and implications for understanding Plinian eruption dynamics;

4. A new spatiotemporal model for the Y5 phase based on the above discussion points; and,

5. Implications for eruption plume computational modelling and future research opportunities resulting from this study.

6.1 A review of the vent location for the Y5 phase: Implications for the vent configuration of the Taupō 232 CE eruption

In this this review section, I have outlined three vent foci for the various phases of the Taupō 232 ± 10 CE eruption (*Figure 6.1*). These vent sites are the same as those defined by Walker (1980, 1981a) and Smith & Houghton (1995a) but are differently assigned to the eruption phases, as discussed below. The location of the Y5 eruptive vent was originally inferred to be in the vicinity of the (younger) Horomatangi Reefs area within Lake Taupō (*Figure 6.2*) based on isopachs and isopleths (Walker 1980). Walker considered the Y5 deposit as a single eruptive unit purely from the perspective of the widespread fall deposit. He did not consider the presence and relevance of the intraplinian EFU deposits, which were shown by Wilson & Walker (1985) to be coeval with the Y5 fall deposit. Bedding characteristics in the Y5 deposit were briefly considered by Walker (1980) but were considered in extreme detail by Houghton et al. (2014). Houghton et al (2014) used their observations to propose the presence of 26 subunits within the Y5 fall deposit (despite a maximum observed thickness of only 2.1 m: Houghton & Wilson 1989). They also proposed an alternative vent location in proximity to Motutaiko Island (*Figure 6.1*) ~6 km SW of the Walker (1980) location. This new Y5 source is effectively the same source proposed for phases Y1, Y2 and Y3 of the Taupō eruption (Smith & Houghton 1995a; Houghton et al. 2010, 2014). The newly proposed Y5 vent location was based on observed internal variations within the vertical stratigraphy of the Y5 deposit, where isopach measurements based on qualitative correlations of sub-units resulted in changes in dispersal directions from that originally determined by Walker (1980). However, no actual data on isopach thicknesses were presented in Houghton et al. (2014) and the quantitative basis for the presented dispersal directions is missing. In addition, several factors suggest that their proposed vent location for the Y5 phase is not viable:

1. Motutaiko Island is a ~7000-year-old rhyolite dome (Wilson 1993) at the southern margin of the caldera collapse area proposed to have accompanied the Taupō 232 ± 10 CE eruption (Davy & Caldwell 1998). It is unlikely that the rhyolite dome would remain following the Plinian Y5 eruption phase. If the island dome was only partially destroyed during the Y5 phase, it would be expected that there would be an influx in rhyolite lava lithics in the base of the Y5 deposit. This is, however,

contradictory to the trends seen in my data where such lithics gradually decrease in abundance from the upper Y4 to lower Y5 deposits.

2. An event of this magnitude would be unlikely to occur on the rim of the subsequent caldera collapse area.

3. The distribution of the low-energy EFU ignimbrite is centered about an area well north of the Houghton et al. (2014) proposed vent (Wilson & Walker 1985; this thesis *Chapter 5*) but is consistent with the original Walker (1980) vent site.

4. Deposit dispersal axes produced by Houghton et al. (2014) for the proximal to medial regions of the Y5 fall deposit do not align at any stage with the overall deposit dispersal axis presented by Walker (1980), that is, the wind influence shifting from E to NE, versus an overall E dispersal, respectively: *Figure 6.2*).

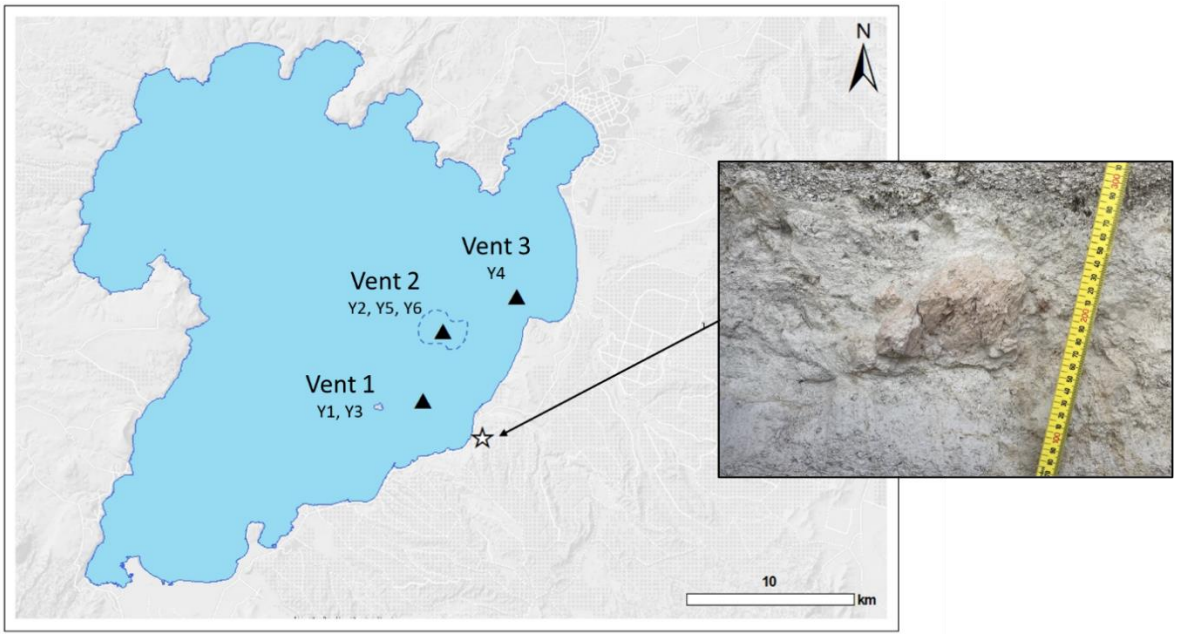

Figure 6.1 The location of the three vents proposed for the various eruptive phases of the Taupō 232 ± 10 CE eruption as revised in this study. Here, Vent 1 is interpreted to produce the Y1 and Y3 phases (cf. Y2 vent location: Smith & Houghton 1995a; Y5 and Y6 vent locations: Houghton et al. 2014). Vent 2 likely produced the Y2, Y5, and Y6 phases, and Vent 3 produced the Y4 phase. The white star shows the location that ballistic pumices (photo inset) were found within Y1 deposits. The dashed blue line represents the Horomatangi Reefs.

Based on these lines of evidence, I infer that the vent location proposed by Houghton et al. (2014) was not the source of the Y5 eruption phase. In support of this, I found that there is a significant influx of intermediate depth F2-type lithics at the boundary between units Y4 and Y5, which suggests that new pre-Oruanui-aged material has been excavated. When comparing the F2-type lithics in the upper Y4 (Y4-G) and lower Y5 deposits (*Chapter 3*), it was determined that there was a distinct change in clast type across the boundary zone, with a lack of brecciated volcaniclastics identified in Y4-G. Similarities have also been observed between the F2 lithics in the Y5 and those of Y2 (see Walters 2020), which may be linked to similar regions of country-rock excavation and are consistent with similar or coincident vent locations (*Chapter 3*).

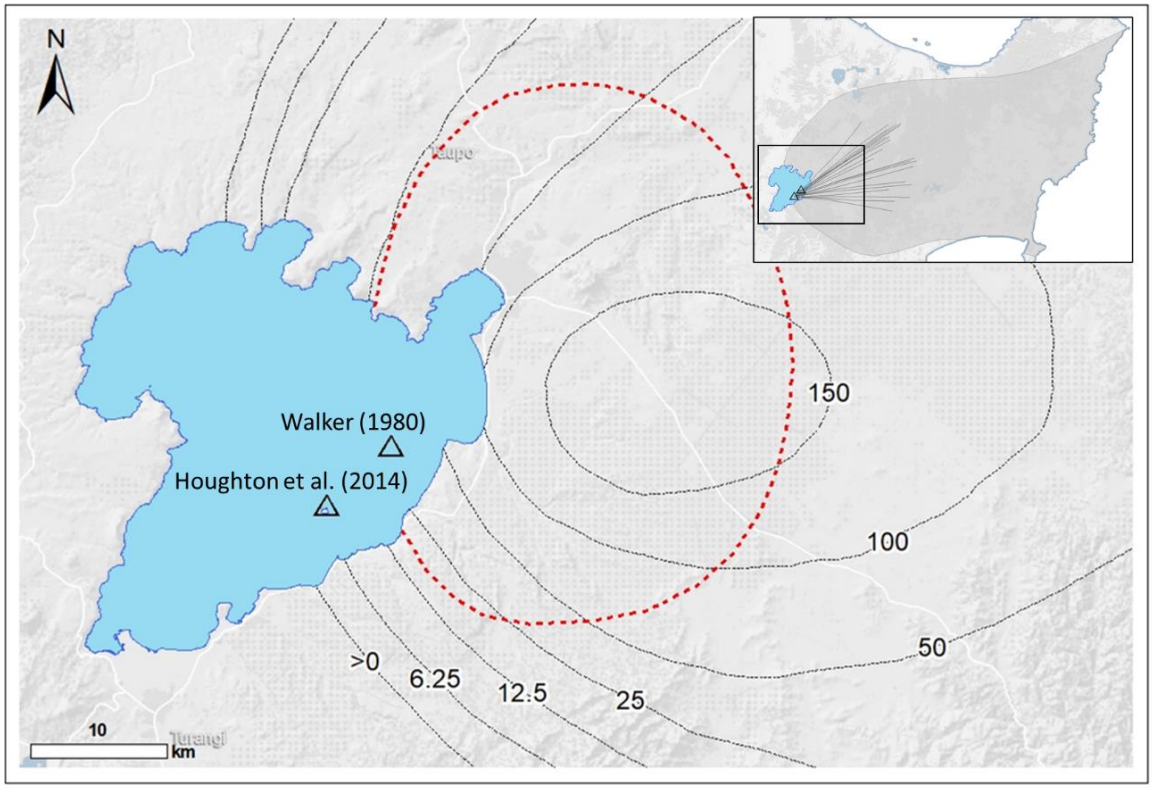

Figure 6.2 Map showing the locations of the original Y5 vent location determined by Walker (1980) and the location revised by Houghton et al. (2014). The isopach measurements of the Y5 deposit from Walker (1980) are marked by black lines with thicknesses in cm, and the 64 mm maximum lithic isopleth is defined by the red dotted line. The inset shows the deposit extent in grey, with dark grey lines showing the various dispersal axes of the Houghton et al. (2014) subunits.

Detailed mapping by Walker (1981a) placed the Y2 vent at a location coincident with that proposed by Walker (1980) for Y5, in proximity to the (younger) Horomatangi Reefs area (vent 2; *Figure 6.1*). Smith & Houghton (1995a) revised the Y2 vent location to one comparable with that for the Y1 and Y3 phases (vent 1; *Figure 6.1*), whilst leaving the Y5 vent location unchanged. This revision, however, was solely based on detailed analysis of the deposit characteristics of phase Y3 and its revised isopachs and isopleths (Smith & Houghton 1995a; Smith 1998). The assumption was that the Y2 material was discharged from the same vent as the vesiculated magma of the Y1 and Y3 phases, in contrast to the gas-poor magma of phase Y4 eruption, during successive, uninterrupted eruptive events. The three main pieces of evidence used to explain this were:

1. Similar wall-rock lithic and juvenile proportions between the Y2 and Y3 deposits;

2. The juvenile clasts of the Y3 phase had a slightly lower average water-quenched clast vesicularity than the Y2 deposits (Houghton & Wilson 1989) but were otherwise similar; and,

3. The contact between the two units was observed to be transitional.

It is noted here, however, that several discrepancies arise from this assumption.

1. The detailed isopleth and isopach data gathered by Walker (1981a) do not align with a vent site located as far SW as that proposed by Smith & Houghton (1995a).

2. The proportions of wall-rock lithics to juvenile material in the assessment by Smith & Houghton (1995) was based on lithic material as a whole and did not consider the various lithic component types and their inferred source depths. Such information, as I have demonstrated in *Chapters 3* through *5*, is important for interpreting the nature and position of vents. Bulk lithic data in relation to juvenile material is important for understanding general conduit dynamics (e.g., vent widening or erosion) but may not provide enough detail when it comes to understanding transitional and dynamic vents, source locations or fragmentation depths.

3. Field observations by Walters (2020) define a relatively sharp contact between the Y2 plinian and Y3 phreatoplinian deposits at numerous exposure locations.

4. Walker (1981a) noted a lack of ballistic clasts in the Y2 deposit, suggesting a vent location at least a few kilometres from the shoreline of Lake Taupō. Ballistic pumice clasts were identified within the Y1 ash beds during field work for this study (white star, *Figure 6.1*) and, given the size discrepancy between the two eruptions (Wilson & Walker 1985), it is most unlikely for the Y2 phase to have occurred from a similar vent location without the occurrence of ballistically emplaced material on land. Such material is, however, missing in unit Y2 from the location (Te Heu Heu Road) where the ballistic pumice clasts occur in unit Y1.

Therefore, based on the existing data for the Y2 eruption, I concur with Walker's (1981a) source location at vent 2 (*Figure 6.1*). Consequently, in agreement with the Y2 vent location and, based on the lithic similarities documented here and in Walters (2020), I infer that the Y5 source is similarly located at vent 2 (*Figure 6.1*). Additionally, ballistic clasts have not been identified in the proximal deposits of the Y5 eruption phase (Walker 1980) and therefore similarly counts strongly against the possibility of the proposed south-westerly vent location.

In addition to the Y5 deposit, my investigations into the final stages of the Y4 phase (Y4-G), originally defined by Smith & Houghton (1995a) and Smith (1998; layer Rn-G), provide insight into the transition between the Y4 and Y5 events. Detailed work by Smith & Houghton (1995a) and Smith (1998) determined that Y4 was vented from a separate source to the other stages of the Taupō eruption at vent 3 (*Figure 6.1*). The Y4 phase involved a complex sequence of PDC and fall deposits which are divided into subunits with various dispersal geometries (bilobate, concentric, elliptical and trilobate). Although complex, the isopach and isopleth maps of the individual subunits convincingly converge on the vent 3 source location (Smith & Houghton 1995a; Smith 1998). The presence of the separate vent 3 is also strongly supported by the poorly vesicular, degassed nature of the Y4 juvenile clasts (Houghton & Wilson 1989; Dunbar & Kyle 1992; Smith 1998). It was inferred that the Y4 magma resided for some time at shallow levels and was passively degassed within a separate conduit that restricted magma rise prior to or during the earlier phases of the Taupō eruption (Smith 1998). By investigating the components in the Y4-G and lower Y5 deposits, I suggest the presence of a transitional vent location between vents 2 and 3 that produced the Y4-G material. The coarser grain sizes and somewhat more vesiculated pumice compared to the bulk of the Y4 material indicates that less degassed magma erupted from this possible source

with lesser amounts of water-induced fragmentation. The lithic lithologies show, however, that there is a distinct variance between the Y4-G and Y5 F2 lithics, indicating that the vents for the successive units were independent of each other. In addition, the sharp contrast between the deposits implies that Y4 activity ceased prior to the onset of Y5. The isopachs measured in this study (*Figure 6.3*; *Chapter 3*) show that the azimuth of dispersal for the Y4-G is on a similar orientation to the azimuth between the Y4 and Y5 vent sites. Therefore, Y4-G may have erupted from any location between the Y4 and Y5 vents. Constraining the vent site further is, however, beyond the scope of this study.

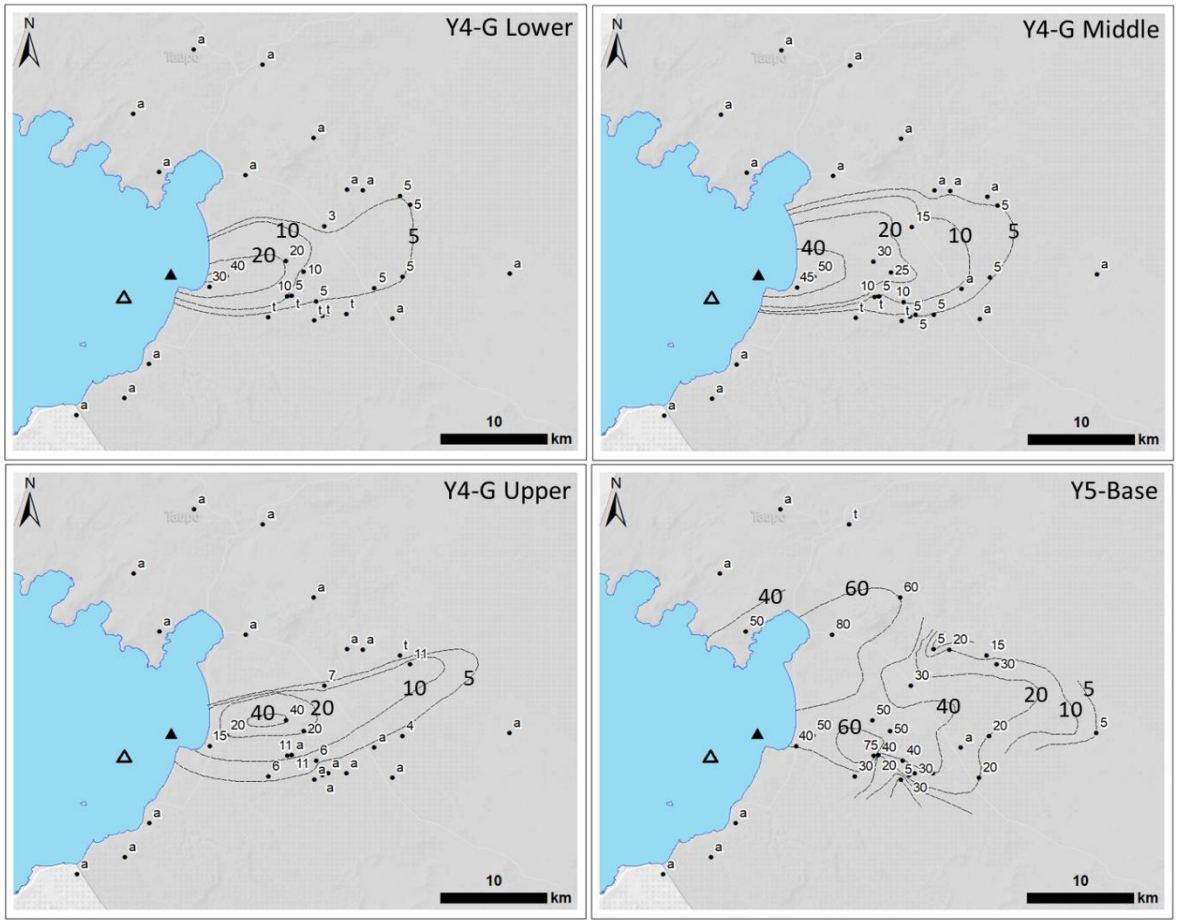

Figure 6.3 (Fig 3.2 repeated here for convenience) Isopachs defined for the Y4-G Lower, Middle and Upper, and Y5-Base units. Black dots show field locations with thicknesses in mm. a is absent and t is trace deposit. Thicknesses of isopachs are in mm. Scale bars are 10 km. Black triangle is the Smith & Houghton (1995a) Y4 vent and the Walker (1980) vent is an open triangle. Inset below:

Based on the information described above, I suggest an updated vent configuration for the Taupō eruption sequence (cf. Smith & Houghton 1995a; Houghton et al. 2010). The eruption involved a minimum of three vents, as described by Smith & Houghton (1995a) and Houghton et al. (2014); however, the phases produced by each of the source vents have been modified. The eruption began with Y1 phreatomagmatic activity at the southernmost vent (vent 1; *Figure 6.1*) and followed with a new, dry vent opening for the Plinian Y2 phase at vent 2 (cf. Smith & Houghton 1995a). Data for Y1 and Y3 imply a common vent source (Smith & Houghton 1995a) which suggests activity migrated to vent 1 following the Y2 phase. Toward the end of Y3 activity, the northernmost vent (vent 3; *Figure 6.1*) opened and the eruption of degassed Y4 material began. The interbedding of Y3 and Y4 deposits during this transition of activity suggests that both vents 1 and 3 were simultaneously active for a short period of time, as documented by Smith & Houghton (1995a) and Smith (1998). Following Y4, activity moved to vent 2 with a dramatic increase in mass discharge rate (MDR) to produce the plinian Y5 deposit (cf. Houghton et al. 2010, 2014). Field data shows that the vent locations for the Y4 and Y5 eruption phases were discernibly different. The coarser Y4-G phase of the Y4 eruption with its moderately more vesicular juvenile clasts may, however, have occurred from a transitional vent location between vents 2 and 3, erupting slightly less degassed magma from a source with lesser amounts of water-induced fragmentation. Drastic changes in eruption conditions at vent 2 resulted in the powerful Y5 Plinian phase, then the immensely destructive outburst that formed the Y6 Taupo ignimbrite. It is possible that, based on the multi-vent lineation and the abundance of young rhyolite lava lithics in units Y2 and Y5, vent 2 was topographically elevated compared to vents 1 and 3, inhibiting water inundation and producing dry eruptions.

6.2 The interpretation of plinian deposits

6.2.1 Introduction

Through detailed analysis of granulometry, componentry and the textural characteristics of juvenile clasts at selected exposures, I have demonstrated (*Chapter 4*) that quantitative investigations into the in-depth stratigraphical variations in deposit characteristics of single, compositionally uniform plinian deposits provide the opportunity to further understand source conditions, particle transport and sedimentation. Quantitative investigations improve

on interpretations (Cioni et al. 2015; Houghton & Carey 2015) regarding the temporal evolution of eruptions with relatively complex observable deposit features (i.e., internal bedding structures). In the case of the Y5 plinian deposit, the temporal evolution of the eruption is less complex than its observable deposit features suggest, with three successive stages distinguished within the relatively steady, continuous eruption following the initial clearing of the vent. These stages are 1) the continuous excavation of the conduit at relatively low MDR; 2) increasing MDR with decreased conduit erosion, coinciding with deepening fragmentation, and increased viscous shear; and 3) the acceleration of conduit erosion, promoting the potential early onset of vent area collapse that led to the Y6 ignimbrite producing blast event. This is contrary to the interpretation of Houghton et al. (2014), who proposed complex correlations between 26 subtly variable stratigraphical sub-units within the Y5 deposit. These correlations were based predominantly on granulometric features and wall-rock clast abundances. They proposed that the total extent of the Y5 fall deposit, defined originally by Baumgart & Healy (1956) and Healy (1964) and refined by Walker (1980), had been exaggerated by a shift in wind direction. In their model, the fluctuation of eruptive pulses feeding plumes between ~35 and 40 km high produced the variably layered deposit (Houghton et al. 2014).

In contrast to this interpretation, there are several issues that arise:

1. Quantitative data on isopach thicknesses were not presented in Houghton et al. (2014) and the quantitative basis for the presented dispersal directions is missing. There are noticeably subtle differences in individual sub-unit dispersal directions that are unsupported by data (*Figure 6.1*).

2. The total deposit extent, determined through a more widespread field investigation of the entire Y5 deposit (Walker 1980), does not reflect a more north-easterly directed dispersal. Although the Walker (1980) investigation treated the Y5 unit as a single eruptive unit and disregarded the intraplinian nature of the EFU, as well as bedform characteristics and alternating coarse-fine material, the isopachs determined are still a reliable indicator of the total deposit extent.

3. When comparing the consequent calculations of column heights for each sub-unit (35–40 km; Houghton et al. 2014) to that of the similarly vented 3500 BP Waimihia Plinian eruption (42 km high: Wilson & Walker 1987), discrepancies arise. The

Waimihia fall deposit is observably less coarse grained than the Y5 deposit at any given distance from the vent along their respective dispersal axes. This conflicts with the Houghton et al. (2014) column height calculations, as the more powerful of the two events would be assumed to possess the coarser grain size when observed at similar distances downwind.

4. The coevally emplaced EFU deposits, which have been identified at varying stratigraphic heights in proximal to medial Y5 exposures (Wilson & Walker 1985), have been disregarded in the Houghton et al. (2014) study. The Proximal EFU ignimbrite is distributed about an area consistent with the original Walker (1980) vent site, well north of the Houghton et al. (2014) proposed vent (Wilson & Walker 1985; this thesis *Chapter 5*).

Here, I discuss how a quantitative understanding of deposit characteristics in the vertical stratigraphy and the lateral correlation of bedform features allows us to further the understanding of eruption behaviour and sedimentation dynamics in large Plinian eruptions.

6.2.2 The use of lithic lithologies in understanding time-variant progressions during an eruption

By investigating the time-variance in relative lithic abundances and their relationship to other deposit characteristics such as grain size, juvenile-clast types and abundances and pumice densities, I show that lithic types play an important role in informing vent location, the evolution of the conduit, and the nature of erupted facies (i.e., PDC and fall). In this thesis, three dominant groups of lithic components were subdivided by their inferred stratigraphic depth of origin based on previous investigations of the TVZ (i.e., Chernet 1987; Brown et al. 1998; Cole et al. 1998; Cattell et al. 2016; Rosenberg et al. 2009, 2020). To recap, these are defined as: F1) pre-232 ± 10 CE volcanic material at inferred depths of ~0 – 400 m (Chernet 1987; Wilson 1993; Cole et al. 1998, Cattell et al. 2016; Rosenberg et al. 2009, 2020); F2) predominantly Huka Group sediments, minor Whakamaru ignimbrite and hydrothermally altered material from depths of ~400 – 3000 m (Wilson et al. 1986; Chernet 1987; Cole et al. 1998, Cattell et al. 2016; Rosenberg et al. 2009, 2020) and F3) plutonic microdiorites and granitoids from depths of >4000 m (Chernet 1987; Brown et al. 1998).

The analysis of lithic types in the stratigraphy of the Y5 deposit shows the following results.

1. The variation in F2-type lithologies between the Y4 and Y5 deposits, in conjunction with large disparities in obsidian abundance and average pumice densities (1343 ± 21 kg m^{-3} versus 636 ± 11 kg m^{-3}, respectively), suggests a distinct shift in vent locations in the transition at the cessation of the Y4 and onset of Y5 (*Chapter 3*).

2. Similarities in F2-type lithics identified in the Y5 and Y2 deposits (Walters 2020) can be attributed to analogous regions of crustal excavation and used to infer similar vent locations (*Chapter 3*).

3. High abundances of shallower seated lithics (types F1 and F2) at the onset of the Y5 phase represent the clearing of the vent as the fragmentation front is inferred to have developed at, or shallower than, the depth of pre-Oruanui material. Succeeding conduit flaring, growth and excavation is indicated by a rapid increase in F1-type lithic abundance with height (*Chapter 4*).

4. A decrease in the abundance of shallow-seated lithics relative to deeper material indicates that the fragmentation level deepened, and the rates of erosion of the shallower conduit decreased relative to deeper levels as the Y5 phase progressed to climactic conditions (*Chapter 4*).

5. Following climactic conditions, episodes of conduit instability and accelerated conduit widening are indicated by increases in F1-type lithics in conjunction with increasing overall abundances of lithics in later stages of Y5 deposition. MDR is likely to decrease with conduit instability (Taddeucci & Wohletz 2001), which is shown in the Y5 deposits through the simultaneous decrease in bulk pumice vesicularity, diminishing grain size and smaller maximum pumice (MP) sizes toward the end of the eruption (*Chapter 4*).

6. The relatively continuous nature of variations in lithic abundances with height, as well as maximum pumice sizes and pumice densities (*Chapter 4*), suggest the Y5 phase was a relatively unitary, continuous event. A lack of marker horizons and no significant variation in lithic abundances counts against the hypothesis that

fluctuations in plume height acted to produce numerous wind dependent dispersal axes.

7. The composite pumice (CP) component identified in the Y5 fall deposits was likely formed due to the recycling of welded or trapped EFU material from the vent area during the eruption, consistent with the previous inference that the EFUs were generated from the same vent location as the Y5 Plinian plume (*Chapters 4 and 5*).

8. Trends in lithic proportions in the Y5 fall deposits coevally deposited with the EFU allow for the time-relative correlation of flows throughout the eruption based on the three successive stages distinguished in the eruption progression (*Chapter 5; Figure 6.8*).

9. There are no significant disparities in the time-variant trends between the EFU types (Type 1 and Type 2) and the Y5 fall deposit (e.g., *Figure 6.4*) when comparing the proportions of lithic types and juveniles between the reference Y5 fall Exposure D and temporally linked EFUs. The material leaving the vent that rises with the buoyant plume is indistinguishable from that being fed into the intraplinian PDCs, with similar time variance. The lack of variation between Type 1 and Type 2 with relative height suggest the EFU are a product of one generation mechanism and the deposit types simply represent the contrasts in relative volume, runout distance, and/or the topographical constraints on runout (i.e., valley ponding versus topography climbing) of individual flows (*Chapter 5*).

10. Grain size affects the interpretation of the relationship between lithic types with stratigraphic height. As relative grain size increases, lithic fragments are diluted by pumice abundance. Similarly, durable lithics (e.g., F1 type) are more likely to dominate larger grain sizes while more friable sediments or crystalline components (types F2 and F3) are relatively reduced as grain size increases. Therefore, selecting a representative grain size to account for this is important in order to understand the relationships between lithic abundances, lithic lithologies and the associated conduit dynamics (*Chapters 3 – 5*).

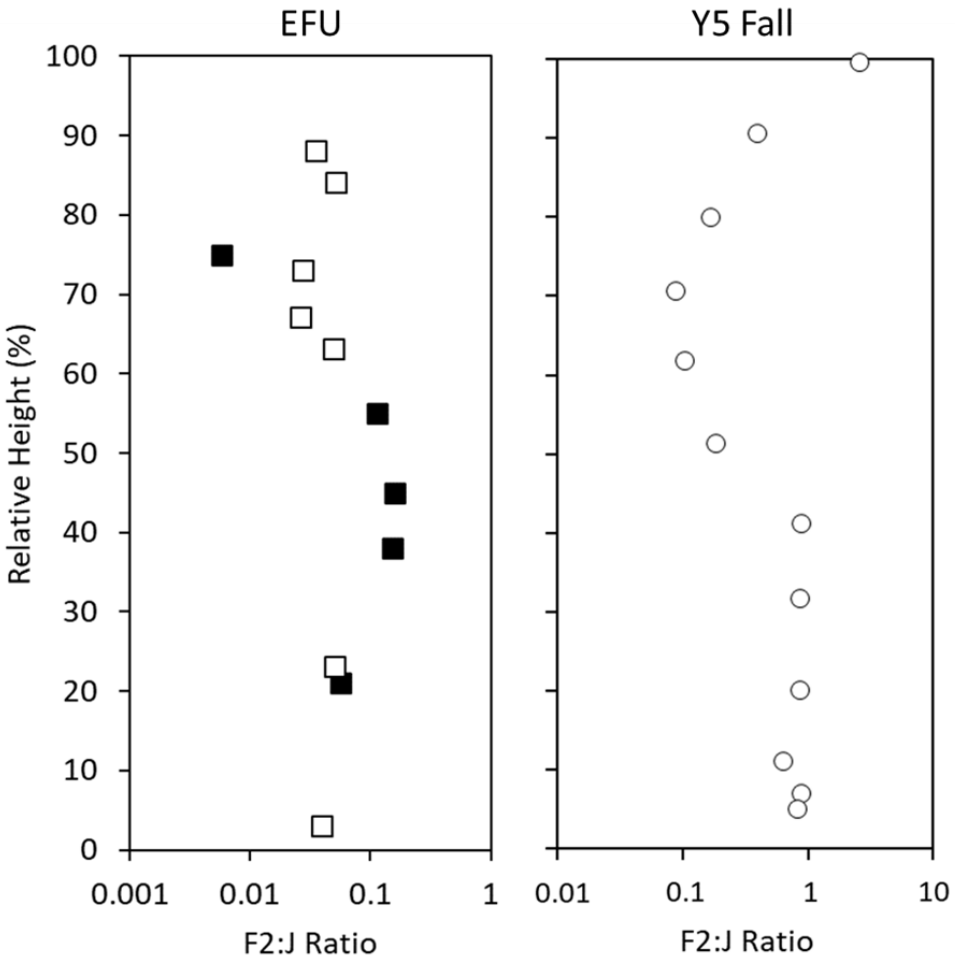

Figure 6.4 (Fig 5.13 repeated here for convenience) The F2:J ratio of EFU and Y5 fall with relative height, normalised to 100%. The relative height of the Type 1 (solid black squares) and Type 2 (white squares) EFUs was determined based on their rough height correlation in association with the Y5 fall deposit at Exposure D (cf. Fig. 5.12). Note the similarity in the relative trends between the overall EFU and the fall.

I have shown in this study that detailed analysis of lithic types based on relative source depth, in conjunction with granulometry, juvenile textural characteristics and other physical deposit features, is crucial for more accurate interpretation and deepening understanding of the following:

1. The dynamical relationship between vents and determining likely source locations of a multi-phase, multi-source eruption (*Chapter 3*);

2. The source conditions, fragmentation depths and temporal evolution of a Plinian eruption, allowing for the identification and time-relative correlation of transient

eruption stages in the case of a compositionally uniform, large plinian deposit (*Chapter 4*);

3. The time-relative correlation of intraplinian PDCs, where partial mass partitioning is not a factor in plume development and dispersal (*Chapter 5*);

4. The generation and emplacement mechanisms of intraplinian PDCs with observably variant deposit characteristics (*Chapter 5*).

6.2.3 Complexities in the vertical stratigraphy of plinian deposits

As discussed in *Sections 6.2.1* and *6.2.2* above, phase Y5 constitutes a relatively steady, continuous eruption with three successive stages. Nevertheless, complexities in the Y5 deposit stratigraphy in proximal to medial areas furnish points of contention in field observations and interpretations around whether 1), that the eruption occurred as a singular, steady, high magnitude event (Walker 1980) or 2) that it involved multiple pulses dispersed by changing wind directions, producing multiple subunits (Houghton et al. 2014).

Through observations made of bedform features in a 4000 m-long sequence of exposures (*Figure 6.5*) in the Wairakei Estates (24 km NE of vent), I established several uncertainties in lateral correlatability. At closely spaced sections, the seemingly discontinuous nature of bedform features over lateral distances of 2 to 3000 metres makes the identification of sub-unit layering across the dispersal fan of the Y5 deposit unreliable (cf. Houghton et al. 2014). This lack of correlatability also precludes the possibility that the coarse-fine fluctuations were caused by partial column collapse, temporarily reducing plume height, and producing intraplinian PDCs (Walker 1980; Woods & Wohletz 1991; Cioni et al. 2015; Houghton & Carey 2015; Trolese et al. 2019). It can moreover be noted that, for an eruption of this magnitude, unnaturally powerful wind conditions would be required to alter plume deposition to the degree outlined by Houghton et al. (2014) and draws an unlikely scenario for the layering observed in the Y5 deposit (Dr. M.K. Butwin National Weather Service Alaska Aviation Weather Unit/ Anchorage Volcanic Ash Advisory Centre, pers. comm., 2022). To explain the origin of such bedform structures, I consider the influence of highly turbulent gas-particle transport (e.g., Carazzo & Jellinek 2013; Bonadonna et al. 2015a; Manzella et al. 2015; Lherm & Jellinek 2019) and introduce the concept of deposition by ‘tephra swathes’ in *Chapter 4*.

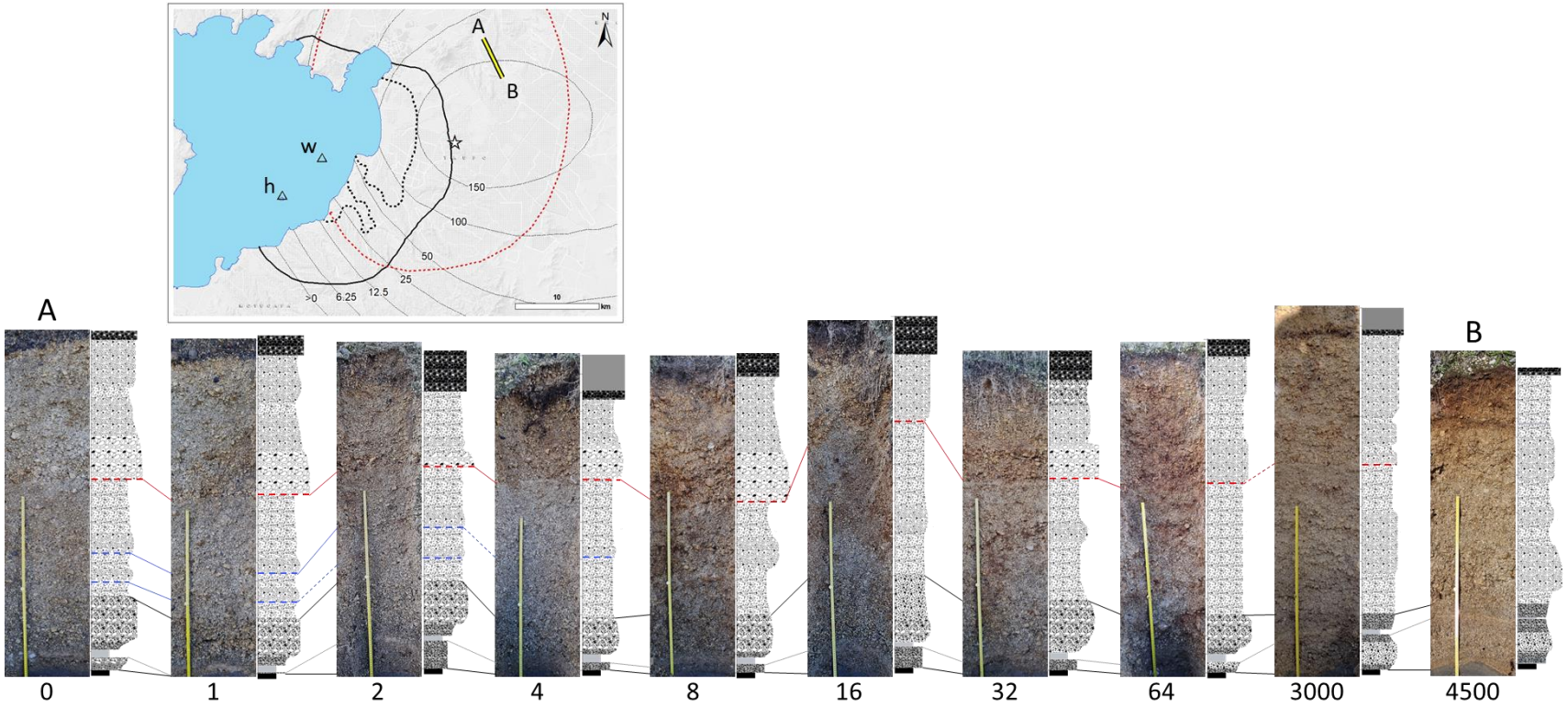

Figure 6.5 (Fig 4.13 repeated here for convenience) Photographs and associated stratigraphic columns of exposures taken at logarithmic distances (indicated at base in meters, starting point 0m) from cross sectional point A to B in the inset (based on Fig. 2). Solid lines between images shows the correlation possible for the distinct change in grain size, indicated by red dashed lines on the stratigraphic columns, uncertainty is suggested between 64 m and 3000 m by dashed red lines between images. Blue solid lines indicate correlations made between outcrops for features showing transient changes in grain size, indicated by blue dashed lines on the stratigraphic columns, uncertainty is suggested between 1 and 4 m by dashed blue lines between the images. Light grey solid lines show correlations made between outcrops for ash beds (solid light grey in stratigraphic column) with uncertainty shown between 3000 and 4500 m by dashed light grey lines. Black solid lines show the correlations made in all exposures of the upper and lower contacts of the lithic rich zone at the base of the deposit. The black solid base in the stratigraphic column is unit Y4, while the black and solid dark grey upper portion indicates the onset of the Y6 ignimbrite.

Turbulent gas-particle transport and gravitational instability modelling has solely focused on the preferential sedimentation of fine ash portions of relatively small eruptive plumes (e.g., Carazzo & Jellinek 2013; Bondadonna et al. 2015; Manzella et al. 2015; Lherm & Jellinek 2019). Complexities observed in the large-scale Y5 plinian deposit, however, shows that there may be dynamical intricacies in the proximal to medial regions of deposition during such powerful events and preferential sedimentation may not, in fact, be restricted to finer grain sizes. When crudely comparing coarse material fall out to other natural examples, such as hail storms, I find that the lengths and widths of hail swaths produced during ordinary cell storms (Atlas 1963; Charlton & List 1972; Nelson & Young 1979; Schmid et al. 1997; Basara et al. 2007; Kunz & Puskeiler 2010; Barrett & Dixon 2012; Gallo et al. 2012; Tuovinen et al. 2015; Knight et al. 2019; Nisi et al. 2018) are comparable to the fade-out distances of bedforms observed in the Wairakei Estates exposures and sections correlated at greater distances. Deposit thicknesses are also comparably similar between the hail precipitation and pumice sedimentation features, with most bedform structures having observed thicknesses of <20 cm. Given the comparable dimensions between hailstorm swathes and the Y5 deposit bedform features, and the similarities observed between precipitation and tephra sedimentation behaviour during smaller explosive eruptions, it is suggested that the centimetre to decimetre-thickness, coarse-fine fluctuations identified in the Y5 deposits (e.g., *Figure 6.5*) result from gravitational instabilities in the umbrella cloud inducing sedimentation of pyroclasts as tephra swathes. These results have implications for the reconstruction of the temporal evolution of plinian eruptions worldwide, where correlation of this behaviour to the parent eruption cloud by means of computational modelling may provide improved opportunities for the amalgamation of quantitative field studies and computational based eruption modelling.

6.3 Generation and dynamical controls of intraplinian PDCs

6.3.1 Introduction

Detailed analysis of the properties of the Taupō EFU deposits and their stratigraphical relationship with the Y5 fall deposit has shed new light on their generation mechanisms and dynamical controls. This new information has implications for the amalgamation of field

studies and computational based eruption modelling for other Plinian eruptions globally. The EFU deposits are differentiated into two main types: Type 1 centimetre to metre thick, massive, pink-orange to cream coloured, coarser grained deposits, and Type 2 decimetre to centimetre thick, massive to moderately stratified, white-grey, finer grained deposits. In this study, I have determined that the Type 1 and Type 2 EFUs are mechanically similar and have likely been generated through the same mechanism, with the variation in distribution simply representing the relative runout distance and/or topographical constraints on the runout for individual flows. The generation mechanism for the EFU PDCs strongly aligns with the modelling of gargle dynamics (*Figure 6.6*; cf. Wilson & Walker 1985; Valentine & Cole 2021), as opposed to the partial collapse regime (*Figure 6.7*; Gilchrist & Jellinek 2021 for an overview), the reasoning for which is outlined below.

1. The anomalously high proportion of ash <10 μm (4 – 27 wt.% of the total grain size) in the EFU deposits, is inferred to predominantly be a direct result of highly efficient fragmentation (*Chapter 5*). This, in conjunction with a lack of evidence for enrichment of dense clasts such as lithics and crystals (see also Wilson 1981), indicates that there has been minimal to no mass partitioning between the buoyant umbrella cloud and collapsing mass that would be expected in the case of partial column collapse (Neri & Dobran 1994; Neri et al. 2002; Kaminski et al. 2011; Gilchrist & Jellinek 2021). Instead, material has been more directly diverted from the erupting mixture at vent.

2. When calculating the empirical PDC transport parameter $T_{de\text{-}di}$ (Breard et al. 2018) based on deposit volume, runout, inundation, and grain-size data collected, I determined the EFUs represent the products of concentrated flows that propagated within the dense flow regime (*Chapter 5*). This is consistent with the conclusions of Wilson (1981) and Wilson & Walker (1985) and in contrast to the interpretation that PDCs produced by partial column collapse are relatively dilute due to mass partitioning based on analogue and numerical modelling (Turner 1969, 1986; Woods 1995, 2010; Neri et al. 2002; Kaminski et al. 2005; Carey & Bursik 2015; Cioni et al. 2015; Lherm & Jellinek 2019; Gilchrist & Jellinek 2021).

3. The high temperature of emplacement of the EFU deposits, reflected by incipient welding, indicates that the materials that propagated to form the EFU PDCs is likely

to have originated from lower heights (maximum a few hundred meters) around the jet where entrained air has limited capacity to cool the mixture (Valentine & Cole 2021; *Chapter 5*).

4. The variation of lithic and juvenile ratios with stratigraphic height is similar in the EFU and Y5 deposits (*Figure 6.4*). It is therefore determined that the material leaving the vent that rose into the buoyant plume to generate the widespread Y5 fall deposit was the same as that which was fed into the intraplinian PDCs, with both batches of material showing a similar temporal variance (*Chapter 5*).

5. A lack of time-correlative bedding has been identified in the Y5 plinian deposit (*Figure 6.5*) yet, in the partial collapse regime, oscillation and temporary reduction of the column height is expected to result in correlatable variations in grain size across an associated fall deposit (Walker 1971; Sparks 1976; Carazzo et al. 2015; Cioni et al. 2015; Houghton & Carey 2015). Where gargle dynamics are concerned, a dense sheath on one side of an eruptive jet can produce PDCs simultaneous with a juvenile jet core that entrains air on the unaffected side to become buoyant (Fierstein & Hildreth 1992; Houghton et al. 2004; Valentine & Cole 2021). This situation results in a sustained plinian column seemingly without interruption, regardless of the development of coeval PDCs, consistent with observations of deposits of the Y5 eruption phase (*Chapters 4 and 5*).

6. Flows forming the EFU deposits began after the onset of fall deposition, with the first flows to reach onshore localities in the initial stages of the Y5 phase identified as relatively short runout flows in comparison to later, more voluminous and/or higher velocity EFUs in conjunction with increasing mass eruption rates (*Figure 6.8*). This sequence suggests that increased eruption rates, further development of the buoyant plume, and accumulation of fall within the vent area was required to initiate gargle dynamics and the entrainment of the dense sheath on the jet. The presence of recycled CP clasts toward the climax of the Y5 phase implies that vent infill was increasing as increasing proportions of material became trapped within a basin-like vent structure. As the EFUs increase in frequency and size, the amount of EFU infill increased, reflected in higher portions of CP clasts being recycled into the buoyant plume (*Chapters 4 and 5*).

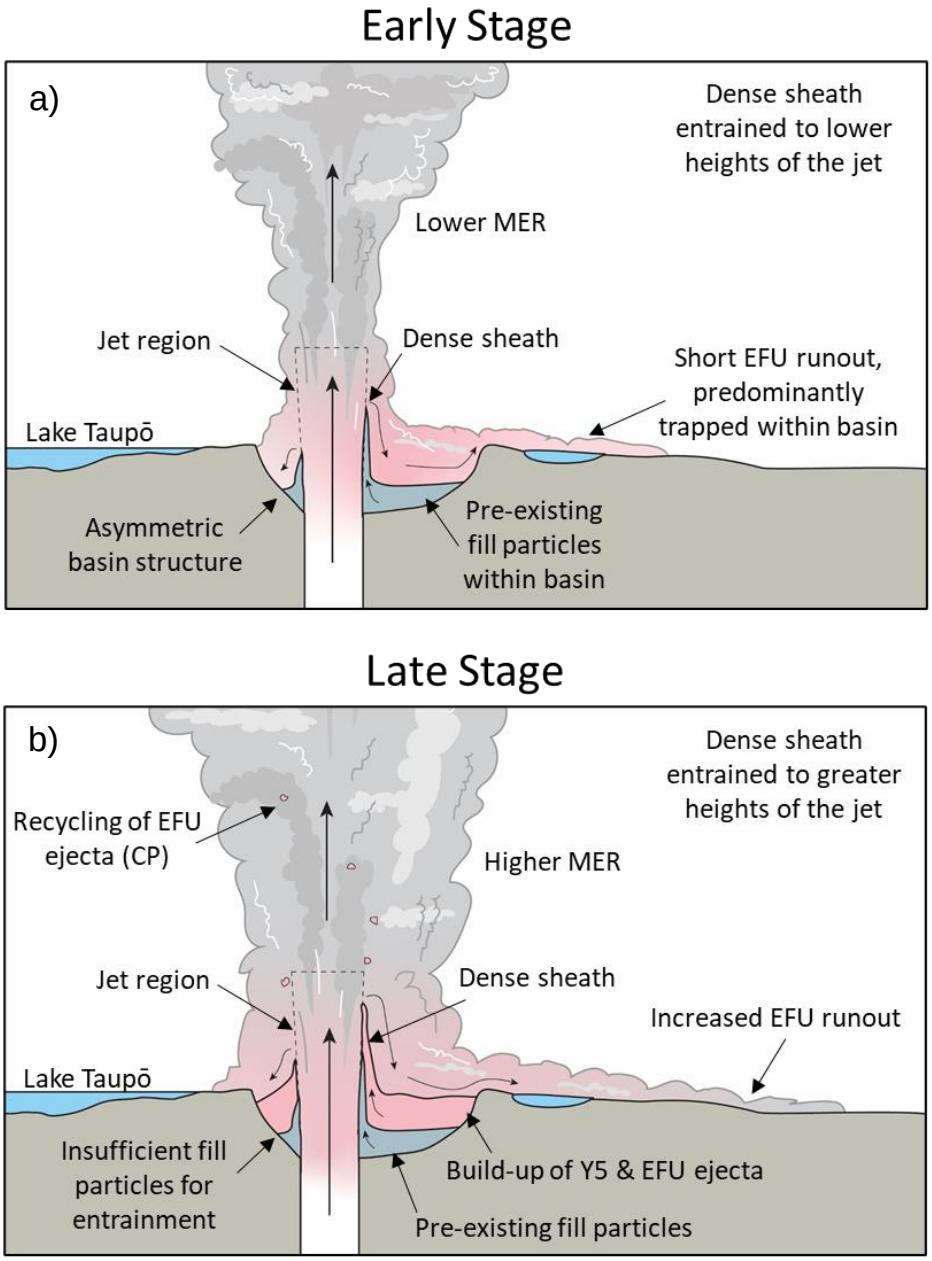

Figure 6.6 Schematic of the EFU generation by gargle dynamics in early (a) and late (b) stages of the eruption.

PDCs that are assumed have occurred as a result of partial column collapse during the transition to total collapse, such as those produced during Waimihia eruption (discussed below; Wilson 1993), Vesuvius 79 CE (e.g., Shea et al. 2011) and Mt. Pelee 79 ± 21 cal CE (e.g., Carazzo et al. 2020), exhibit features expected to be seen in PDC deposits that occur as a result of partial column collapse, such as loss of fine ash and enrichment in dense components. As I have shown for the Y5 phase, however, this is not always the case for Plinian eruptions with intraplinian PDCs and illustrates the complexities in interpreting

natural cases of coeval PDC-fall deposition. Thorough field investigations of other well-exposed intraplinian PDC deposits, such as those of the Novarupta, 1912 eruption (Fierstein & Hildreth 1992; Wilson & Hildreth 1997; Houghton et al. 2004; Fierstein & Wilson 2005), the Bishop Tuff (Wilson & Hildreth 1997), and Mt St Helens (Criswell 1987, 2021), show that characteristics that represent gargle dynamics are not unique to the Y5 deposit and possibly provide direct analogues to the complexities of the Y5 eruption, discussed below.

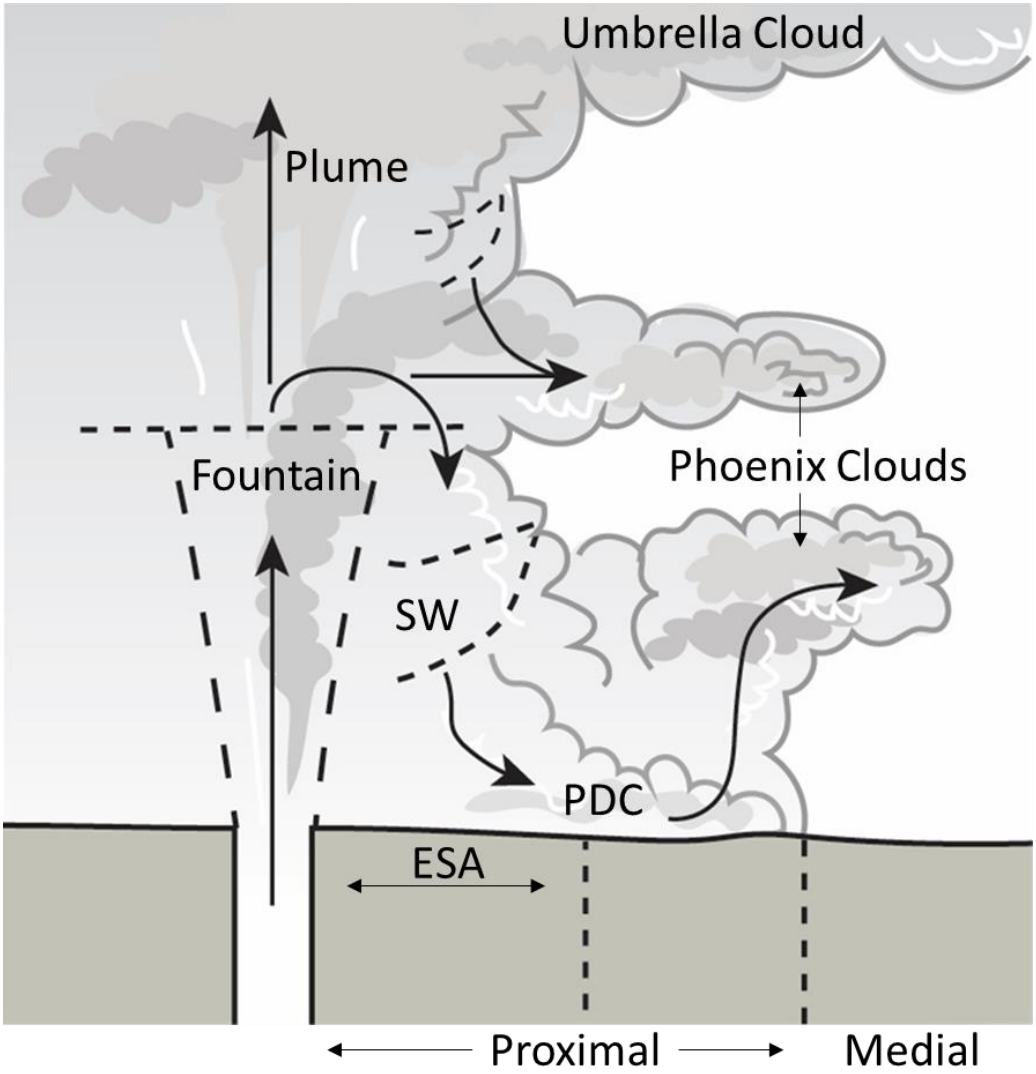

Figure 6.7 Schematic of the partial column collapse model modified from Gilchrist & Jellinek (2021). ESA refers to the enhanced settling annulus and SW refers to sediment waves. Material collapses by sediment waves from the fountain/plume transition zone to produce typically dilute PDCs due to partial mass partitioning of fines into the umbrella cloud. Phoenix clouds are produced as fine ash from sediment waves become buoyant.

6.3.2 Intraplinian PDC case studies and implications for interpretations of eruption dynamics

Detailed field investigations of numerous plinian deposits with intraplinian PDCs have shown that the simple eruption models that define 'stable' versus 'unstable' plume and column dynamics (Sparks & Wilson 1976; Wilson et al. 1980; Neri & Dobran 1994; Woods 1995; Neri et al. 2002; Kaminski et al. 2011; Gilchrist & Jellinek 2021) may be too simple for explaining complexities identified in the natural eruption deposits. Similarities to the Y5 sequence of events have been identified in deposits of the Novarupta 1912 (Fierstein & Hildreth 1992; Wilson & Hildreth 1997; Houghton et al. 2004) and Bishop Tuff (Wilson & Hildreth 1997) eruptions, while eyewitness accounts describe the coeval occurrence of a Plinian plume and PDCs during Mt St Helens (although evidence of this is not preserved in the deposits; e.g., Criswell 1987, 2021). In these cases, the eruption phases generated synchronous high plinian columns and substantial ignimbrite volumes from the same vent sources. Both the Bishop and Novarupta examples show that plinian fall deposition was initiated first, similar to the Y5 eruption, and coeval fall-flow activity was sustained from early on in each eruption progression.

The Bishop Tuff fall deposit in its proximal dispersal area is noted to have reverse grading, where pumices increase in size with height in the stratigraphical profile (Wilson & Hildreth 1997, and references therein). In that example, with increasing inferred plume height and eruption rate into the buoyant plume, the coeval PDCs became more widespread and hence voluminous. It is also noted that this eruption involved the deposition of coeval plinian fall, thick non-welded to densely welded ignimbrite (emplacement temperatures up to 630 – 650 ºC; Riehle 1973; Cas & Wright 1987; Riehle et al. 1995) and more distal, less- to non-welded ignimbrite (Wilson & Hildreth 1997, 2003). As discussed by Wilson & Hildreth (1997), field evidence of the coeval nature of the fall deposits and ignimbrite in the Bishop Tuff indicate that gargle dynamics is a likely generation mechanism for PDCs in this eruption. Further comparison to the Y5 can be drawn in that subtle grain size fluctuations in the Bishop Tuff normal-fall units (cf. Wilson & Hildreth 1998) may be interpreted to represent preferential sedimentation of material from the umbrella cloud of a relatively steady plume, rather than large-scale changes in the nature of the plume (i.e., fluctuations in height due to mass partitioning of material into PDCs).

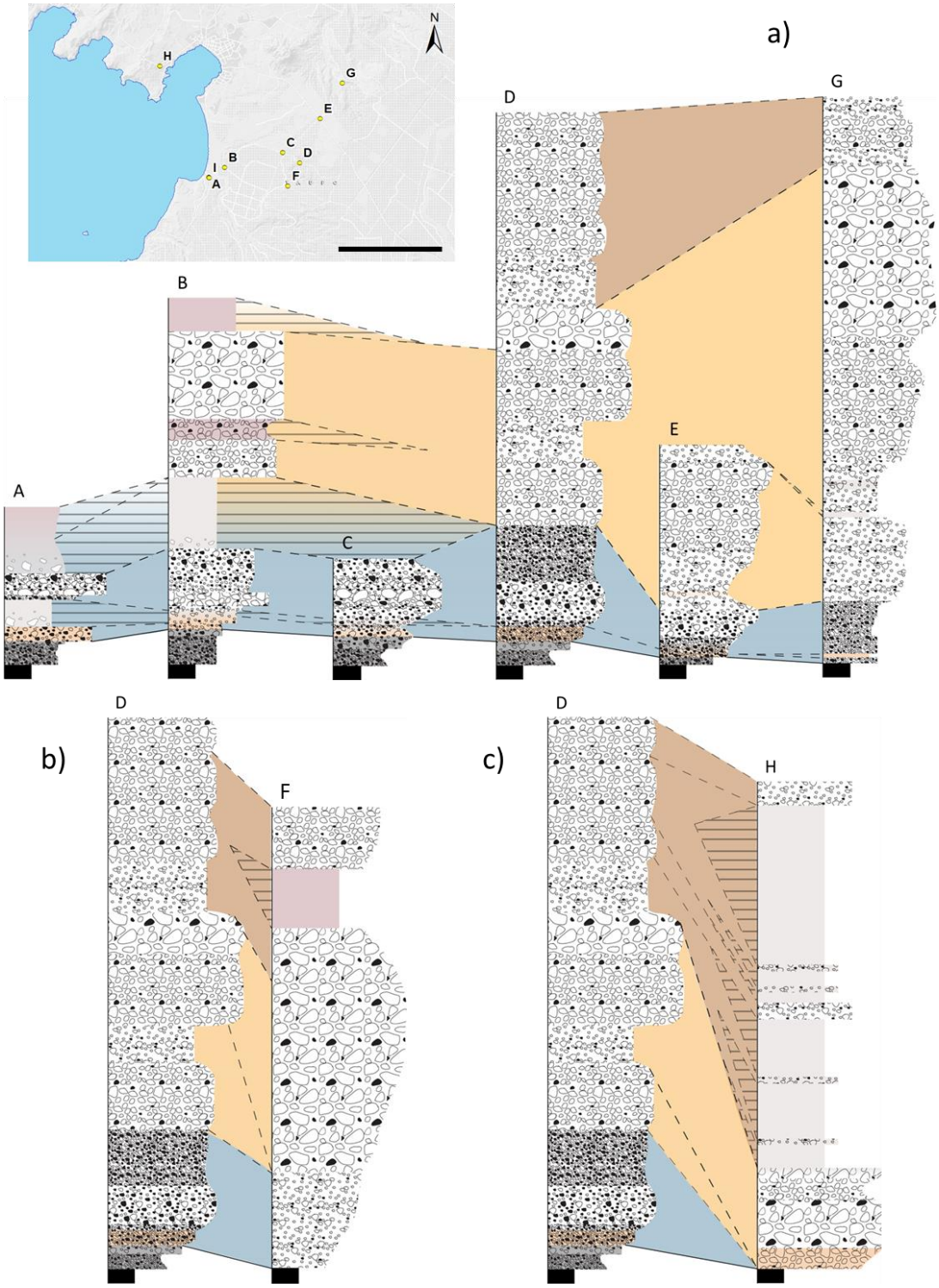

Figure 6.8 (Fig 5.12 repeated here for convenience) The three stages of phase Y5, correlated between the stratigraphic columns of each of the exposure locations (indicated by the inset) in relation to the reference Exposure D. a) shows the transect from A to G (excluding Exposure F), b) shows the correlation of exposures F to D, and c) shows the correlation of exposures H to D. Stage 1 of phase Y5 is defined by blue, stage 2 by yellow and stage 3 by brown. Note that Stage 1 deposits are absent at Exposure H. Rough correlation of the EFU deposits are depicted by horizontal fill lines. The contact between units Y4-G and Y5 is defined by a solid line.

Similarly, the VTTS ignimbrite, emplaced during the first 16-hour phase of three in the Novarupta, 1912 eruption, involved coeval fall and flow activity. Nine compositionally distinct packages of ignimbrite with contemporaneous fall deposits were identified based predominantly on systematic changes in the proportions of rhyolite, dacite and andesite juvenile clasts (Fierstein & Hildreth 1992; Fierstein & Wilson 2005). It was determined that during the middle to late stages of the first phase of the Novarupta eruption, the Plinian column was sustained throughout the generation of voluminous flows but was never fully interrupted. The distribution of the flow packages and the low energy emplacement of most of them suggest that the flows underwent little to no ascent with the coexisting Plinian column and were instead generated by gargle dynamics (Fierstein & Hildreth 1992; Fierstein & Wilson 2005; Valentine & Cole 2021). The VTTS ignimbrite provides a possible analogue for the EFU deposits and Y5 vent structure, with the advantage that the vent geometry is still intact at Novarupta and hence so are the most proximal flow and fall packages (Fierstein & Hildreth 1992; Fierstein & Wilson 2005). The vent that produced the EFU is submerged beneath Lake Taupō, at closest ~4 km from the lake's edge, and therefore the vent geometry and most proximal EFU deposits are neither preserved nor accessible. Nevertheless, Type 1 facies have topographically limited run out distances and show similar traits to the fines rich, poorly sorted valley-ponded ignimbrites (VPI or valley-filling ignimbrite as defined by Fierstein & Hildreth 1992) defined in the VTTS ignimbrite sequence. Therefore, near-vent equivalents in the VTTS ignimbrite may provide insight as to the nature of the most proximal EFU units that are confined within the current Lake Taupō. Additionally, assumptions can be made regarding the geometry of the Y5 vent based on that of Novarupta, suggesting a basin-like structure (Fierstein & Hildreth 1992).

In contrast, the Waimihia (eruption S; Wilson 1993) generated a large-scale plinian fall deposit and late-stage ignimbrite that was erupted from a vent location in the vicinity of the subsequent Y5 eruption (Walker 1981a; Wilson 1993). The Waimihia is subdivided into two compositionally distinct fall units with similar volume (est. 8.2 km^3 and 7.9 km^3: Blake et al 1992) and deposit dispersal, although along slightly divergent dispersal axes (Walker 1981a). The lower fall unit, S1, contains overwhelmingly rhyolitic pumice while the upper unit, S2, is still dominantly rhyolitic but contains distinct quantities of rhyodacite pumice and minor andesitic scoria (Walker 1981a; Blake et al. 1992; Wilson 1993). The lack of evidence for interbedded flow deposits throughout the bulk of the fall stratigraphy shows

that the Plinian plume was steadily maintained throughout the progression of the eruption and flow activity began as S2 activity waned (Wilson 1993), supported by the proportions of rhyodacite and andesite in the ignimbrite, S3. This is also shown in more medial to distal regions where the PDC deposits are time-equivalent to the upper, finer-grained and partly bedded parts of the fall deposit (C.J.N. Wilson pers. comm. 2022). The stratigraphic relationships and deposit features seen in the S1 to S3 phases of the Waimihia eruption (Walker 1981a; Wilson 1993) contrast with those of the Taupō EFUs. In the Waimihia event, the transition from S2 to S3 represents a relatively short-lived phase of coeval Plinian plume and PDC generation (compared to the Y5) prior to the cessation (or weakening) of the eruptive column and onset of substantial PDCs.

The case that multiple methods for the generation of intraplinian PDCs (i.e., partial collapse regimes versus gargle dynamics) can occur at the same volcano and, particularly, the same vent site, highlights the importance for quantitative investigation into Plinian eruptions and their deposits for use in the amalgamation of field studies and computational based eruption modelling. Other local examples of coeval plinian fall and ignimbrite deposition include units I and L of the Mangaone Subgroup, Okataina Volcanic Centre (Jurado-Chichay & Walker 2000). In Unit I, the pumice fall was dispersed to the east while ignimbrites were emplaced mostly to the north and northeast, therefore both facies are only seen coexisting at the same locality over a limited area. Unit L has alternating ash and plinian fall beds, with the fall showing similar granulometric and componentry properties with height, suggesting that fall deposition was interrupted. Jurado-Chichay & Walker (2000) discusses the possibility that the ash beds were the product of temporary plinian column cessation during an unstable eruption, or the interaction of water producing alternating wet and dry episodes. Further research opportunity is presented here to investigate an alternative interpretation for coeval fall and flow deposition and understand the dynamics of intraplinian PDC generation. To understand the complex thresholds and dynamical controls of large-scale eruptions and the generation of PDCs is crucial for improving our knowledge base for use in hazard planning and mitigation at volcanoes globally.

6.4 Reestablishing the beast: A spatiotemporal model of the Y5 eruption

This study has established that detailed quantitative investigation into the physical properties of pyroclasts and the host deposits is necessary for improving the interpretation of the dynamics and sedimentation of large-scale Plinian eruptions. Through this, a new spatiotemporal model of the Y5 phase of the Taupō eruption is defined (*Figure 6.9*).

Initial vent clearing: The change in eruptive style between the phreatoplinian Y4 and plinian Y5 phases of the Taupō 232 ± 10 CE eruption was concurrent with a distinct shift in vent location from vent 3 to vent 2 (*Figure 6.1*). The Y4 eruption shows evidence of sudden termination, where plinian-like pulses of magma-water interaction driven fragmentation marked the final stages of this event, immediately prior to the opening of a new vent and the rapid discharge of actively vesiculating Y5 magma. Fine ash identified in the basal layer of the Y5 deposit (Y5-Base, *Chapter 3*) may be related to weak, dilute PDCs (like those documented by Talbot et al. 1994), formed during the cessation of the Y4 eruption; however, further investigation is required to confirm this.

Stage 1: Following the initial clearing of the vent, the conduit was continuously excavated at relatively low mass eruption rate, as exhibited by higher lithic:pumice ratios, finer overall grain size and higher-density pumices in the fall deposit when compared to later stages of the Y5. During vent development, the earliest-stage Y5 material accumulated within the basin-like vent area. This provided sufficient infill to allow for gargle dynamics to initiate and the formation of a dense sheath on the eruptive jet produced PDCs simultaneous with a buoyant, sustained plinian column, seemingly without interruption. Subsequently, the sporadic PDCs produced occurred as short runout flows, the distal reaches of which extended to ~10 km from source (*Figure 6.6*; early stage).

Stage 2: The buoyant plume increased in height and developed to more climactic conditions, defined by an increasing mass eruption rate with relatively continuous rates of conduit erosion, coinciding with deepening fragmentation, and increased viscous shear in the conduit. As the plume intensified, fall deposition extended to greater areas from source compared to Stage 1, shown through deposition initiated at Exposure H (e.g., *Figure 6.8*). During this time, vent infill was increased as portions of PDCs became trapped within the vent surrounds. With increasing mass eruption rate, PDCs increased in frequency and size,

consequently trapping more fill material which is reflected in higher portions of composite pumice clasts being recycled into the buoyant plume (*Figure 6.7*; late stage). As the intensity of the buoyant plume steadily increased, gravitational instabilities in the umbrella cloud led to deposition of tephra swathes, creating variations in bedform characteristics within the bulk of the proximal to medial Y5 plinian fall deposit.

Stage 3: The mass eruption rate was still relatively high during this stage but, however, slowly began to wane as rates of conduit erosion increased again. This conduit erosion possibly acted to promote the potential early onset of conduit collapse that led to or accompanied the Y6 ignimbrite-producing blast event. As EFU infill increased in the vent area, the fine-grained nature of the material promoted more complex interactions between the dense sheath and primary jet. This allowed for the dense sheath to rise to greater heights in the jet region and produce more voluminous PDCs with farther runout distances than the preceding flows (*Figure 6.6*; late stage). Gravitational instabilities continued to deposit tephra swathes from the umbrella cloud with a sustained plinian column continuing, seemingly without interruption. Prior to the Y6-ignimbrite-producing blast event, EFU deposition ceased in many locations (e.g., Exposures I and H) while Y5 fall deposition continued.

Interpretations from this study indicate that the Y5 phase of the Taupō 232 ± 10 CE eruption was, in agreement with Walker (1980), a large and extremely powerful eruption beyond the general depiction of a 'standard' Plinian event. It would therefore be pertinent to revisit estimates and calculations regarding eruption rates, mass volume, and plume height, inclusive of the erupted material incorporated into the intraplinian EFU. Further analysis of the Y5 eruption is required to reestablish a realistic estimation of the eruption dynamics and its spatiotemporal evolution for use in hazard modelling and mitigation at large Plinian producing volcanoes globally.

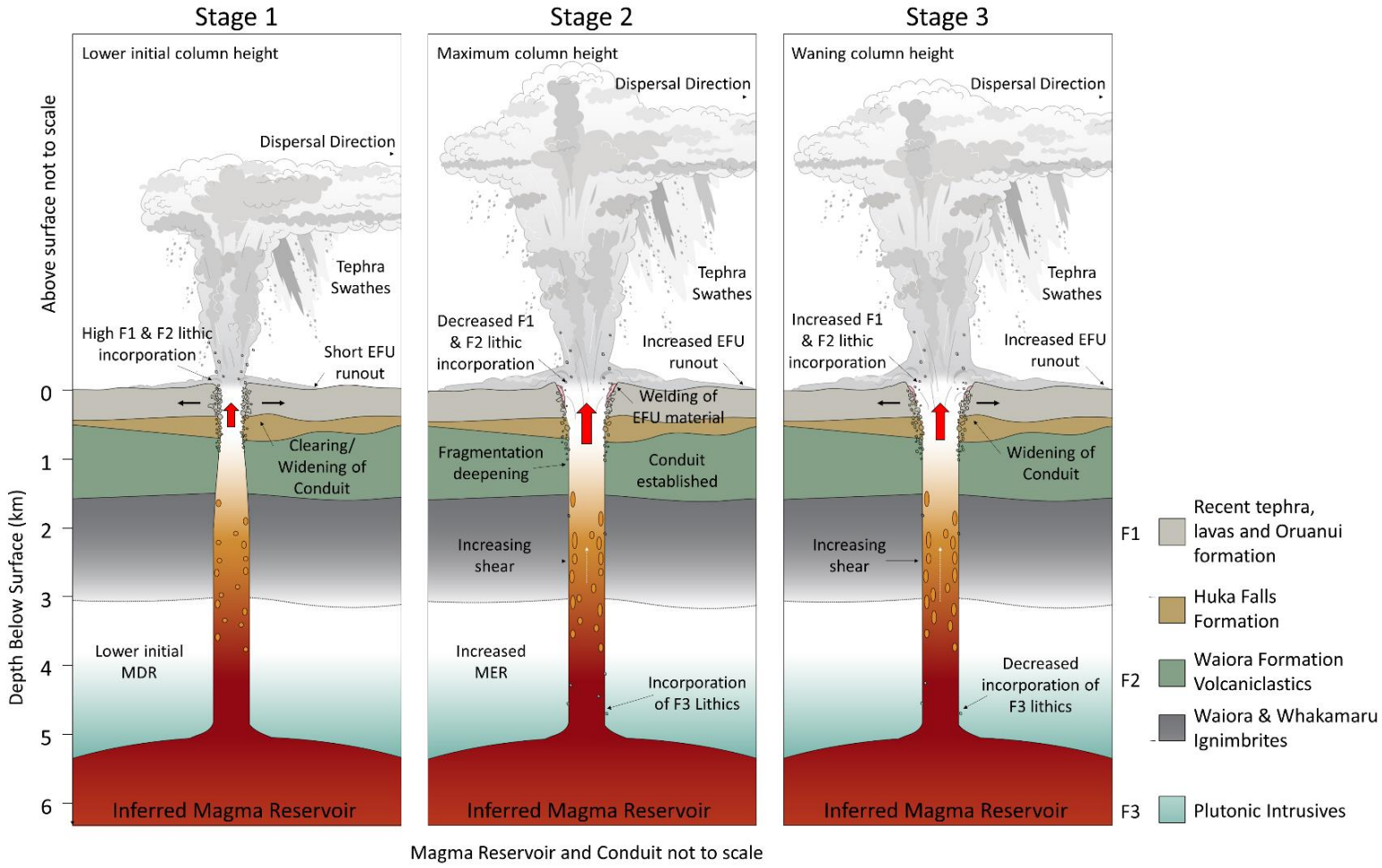

Figure 6.9 Schematic diagram of the three transient stages of phase Y5. Following initial establishment of the vent, the phase steadily reaches climax at stage 2 after which it gradually wanes. Colours of the surrounding crust match the lithic types in the legend. Red arrows indicate changes in MDR and black arrows indicate episodes of accelerated conduit widening. Relative thickness of crustal stratigraphy is to scale; however, for ease of display of features, the conduit, magma reservoir and eruption column are not to scale.

6.5 Modelling of Plinian eruptions: Uses and limitations

Partial column collapse has been widely considered to represent the transitional regime of column unsteadiness between a sustained Plinian column and total collapse conditions through years of analogue and numerical modelling (Turner 1969, 1986; Woods 1995, 2010; Neri et al 2002; Kaminski et al. 2005; Carey & Bursik 2015; Cioni et al. 2015; Lherm & Jellinek 2019). Reviews of existing partial column collapse models by Gilchrist & Jellinek (2021) revisited the characterisation of transitional regimes through analogue experiments. They proposed that Plinian eruptions commonly occur in the partial column collapse regime, during which large-volume annular sediment waves descend periodically around the jet column from the fountain-plume transition height. As a general observation, however, this is not often seen in natural eruption scenarios or deposits. Water-based analogue models are limited by the lack of consideration for non-linearities of gas-particle mixtures (especially with regard to compressibility and phase behaviour), where there is a fundamental contrast between gas-solid and liquid-solid fluid-particle behaviours (e.g., Zenz & Othmer 1960; Davidson & Harrison 1963, 1971; Batchelor 1993; Harris & Crighton 1994; Wilson & Houghton 2000). The use of liquid-particle analogue experimental setups confines models of the partial column collapse regime to one where the erupted mixture partitions between the buoyant umbrella cloud and collapsing sediment waves producing PDCs that spread as relatively dilute flows (Gilchrist & Jellinek 2021). This behaviour is not always the case, even in observed events like 1980 Mount St. Helens (e.g. Rowley et al. 1985), and is not inferred to occur in many intraplinian flow deposits, although possibly present in the later stages of the Novarupta 1912 eruption (Houghton et al. 2004). The use of interpretations from liquid-particle analogue models to solely explain the generation of PDCs when associated with Plinian eruptions restricts consideration of real-world scenarios such as the Y5 (this study), the Novarupta 1912 eruption (Hildreth & Fierstein 2012, for overview), and the Bishop Tuff (Wilson & Hildreth 1997).

Field studies in the above examples outlined the complexities in PDC generation, showing that PDCs, both dilute and concentrated, could undergo little to no ascent with the coexisting Plinian column which, contrary to partial collapse models, could also never be fully interrupted (*Chapter 5*; Fierstein & Hildreth 1992; Wilson & Hildreth 1997; Houghton et al.

2004; Fierstein & Wilson 2005). This behaviour, termed gargling by Wilson & Hildreth (1997), has recently been modelled as ' gargle dynamics ' by Valentine & Cole (2021). These models showed that debris filled vent structures cause large portions of the venting material to become trapped, resulting in an eruption jet needing to penetrate its own earlier ejecta. This interaction results in the formation of a dense sheath along the margins of the erupting jet which fails to rise with the buoyant plume due to overloaded annular zones, producing concentrated, highly fluidal PDCs (Fierstein & Wilson 2005; Valentine & Cole 2021). These field observations and models show that generalised steady versus unsteady column regimes can oversimplify the interpretation of both ignimbrite and plinian fall deposits in natural eruption scenarios, and often disregard field data altogether. The amalgamation of quantitative field data and numerical models will help to improve the understanding of the dynamics of intraplinian PDC events and reduce the reliance on numerical models as the primary justification for the generation of PDCs simultaneous with fall deposition.

Modelling of the partial collapse regime has also influenced the interpretation of plinian fall deposits, whereby coarser-finer grain size fluctuations in vertical stratigraphy of a unitary deposit are often interpreted as partial collapse of the column with mass partitioning temporarily reducing the plume height (Walker 1980; Woods & Wohletz 1991; Cioni et al. 2015; Houghton & Carey 2015; Trolese et al. 2019). In this case, fluctuations are expected to correlate across the dispersal fan at any given stratigraphical height, which I have shown is not the case for the Y5 fall deposit. Instead, I infer that the influence of highly turbulent gas-particle transport on gravitational instabilities results in the preferential sedimentation of particles as curtains of material from the umbrella cloud producing internal complexities within plinian fall deposits (c.f. Carazzo & Jellinek 2013; Bonadonna et al. 2015a; Manzella et al. 2015; Lherm & Jellinek 2019). Although gravitational instabilities have been observed in eruptive clouds from explosive eruptions of many sizes, deposit features are yet to be linked or attributed to this sedimentation mechanism. Previous turbulent gas-particle transport and gravitational instability modelling has solely focused on the preferential sedimentation of fine ash fractions of relatively small eruptive plumes, while individual particle settling is expected to represent sedimentation in the coarser fraction (Carazzo & Jellinek 2013; Bondadonna et al. 2015; Manzella et al. 2015; Lherm & Jellinek 2019; Fries et al. 2021). My investigation into the Y5 deposit has shown that there is a seemingly discontinuous nature of bedform features over distances greater than tens to hundreds of

metres, making the identification of sub-unit layering across the dispersal fan unreliable and precluding the possibility of influence solely from plume height fluctuations or changes in wind direction. The focus on finer grain sizes during smaller eruptions in modelling scenarios limits the capability to correlate sedimentation behaviour with the parent eruption cloud by means of analogue experimental or numerical computational modelling for large-scale events. Such correlations, as presented here, may provide a new opportunity for the understanding of the behaviour of pyroclastic fall out and the associated hazards.

6.6 Implications for hazard management and mitigation

Constituting one of the most powerful natural phenomena on Earth, Plinian eruptions have the potential to cause widespread havoc on communities in terms of health issues, impacts of critical infrastructure, and agriculture. Tephra fall has the potential to damage or hinder critical infrastructure, here defined based on Wilson et al. (2014) as energy sector infrastructure, water supply and wastewater networks, transportation routes, communications, and urban areas. Tephra accumulation on agricultural land can also cause severe damage by covering the land and constricting water supplies as well as having direct health implications on livestock and communities (Rose & Durant 2009; Wilson et al. 2011; Biass et al. 2017; Geshi 2020). Although the destruction caused by large-scale pumice fall events can be significant, PDCs are known to be one of the most destructive and hazardous phenomena of explosive volcanism, with the potential to rapidly transport hot debris for many kilometres. Human exposure to even small-scale PDCs can cause fatalities by heat and dynamic pressure damage (Spence et al. 2004; Geshi 2020) and their destructive potential is even more hazardous to critical infrastructure and agriculture than that of tephra fall. It is therefore pertinent to hazard management and mitigation that we further our understanding of PDC generation, timescales, and dynamics during large Plinian eruptions.

In the case of Taupō volcano, Plinian eruptions have been identified to generate PDCs once a column model height of ~30 km (estimated using the methods of Carey & Sparks 1986) is exceeded (e.g., unit Y5, Waimihia (eruption S) and Opepe (eruption E: Wilson 1993). This relationship suggests that there is a size or intensity (Carey & Sigurdsson 1989) control in Plinian eruptions at this volcano on the production of PDCs. Understanding the threshold of

PDC generation, their timescales and runout distances based on the size of the eruption would allow for relatively reliable hazard planning for communities living around Taupō volcano and for estimates at other volcanoes globally.

7 Conclusions

7.1 Specific findings of this study

This study has shown that through the detailed, quantitative characterisation of deposit features in plinian eruption deposits involving coeval fall and PDCs, we can identify the temporal changes in eruptive behaviour, conditions at source and the nature of sedimentation. Through this research, I have reconstructed the spatiotemporal evolution of the large Plinian Y5 phase of the Taupō 232 ± 10 CE eruption, which may constitute the basis for the amalgamation of field studies and computational eruption modelling at similar volcanoes around the globe. I present here a summary of the specific findings presented in this Ph.D. thesis.

1. The change in eruptive style between the phreatoplinian Y4 and plinian Y5 phases of the Taupō eruption was concurrent with a distinct shift in vent location as shown through sharp contrasts in lithic and pumice types, and the abundance of obsidian at the boundary of the Y4 and Y5 deposits.

2. The vent location of the Y5 phase is comparable to that of the plinian Y2 phase determined by Walker (1981a), primarily shown through similarities in lithic lithologies in the Y5 deposit versus the Y2 (Walters 2020) which suggests similar regions of crustal excavation.

3. There are three transient stages within the relatively steady, continuous eruption of the Y5 following the initial clearing of the vent: 1) the continuous excavation of the conduit at relatively low mass discharge rate; 2) increasing mass discharge rate with decreased conduit erosion, coinciding with deepening fragmentation, and increased viscous shear, and 3) a moderate decline in mass discharge rate following its peak at the end of stage 2 and the acceleration of conduit erosion, promoting the potential early onset of caldera collapse that led to the Y6 ignimbrite-producing blast event.

4. Variations in bedform features observed in vertical sections of Y5 fall are not caused by either relatively steady source conditions with shifting wind directions, or mass partitioning of material due to partial column collapse. Instead, I infer that such

features reflect the preferential sedimentation from the eruption umbrella cloud due to gravitational instabilities leading to deposition of tephra swathes.

5. The composite pumice (CP) component identified in the Y5 fall deposits were likely formed due to the recycling of welded or trapped EFU material from the vent area during the Y5 phase, implying that the EFUs were generated from the same vent location as the Y5 Plinian plume (cf. Wilson & Walker 1985).

6. Unusually high ultra-fine-ash content, low content of high-density pyroclasts (in comparison to ignimbrites formed by partial- or total column collapse), the high concentration of the EFU and high temperature emplacement (as shown through incipient welding and carbonized vegetation), in combination with the lack of time correlative bedding identified in the Y5 plinian deposit, indicate that the intraplinian PDCs of the Y5 eruption phase were likely a product of gargling dynamics, as similarly described by Wilson & Walker (1985). In the case of gargle dynamics, PDC material is generated from a dense sheath that forms at relatively low heights on the outer regions of the eruptive jet, and not from material collapsing from the buoyancy-driven region of the plume.

7. Type 1 and Type 2 EFU deposits are likely a product of one generation mechanism and the deposit types simply represent the contrasts in relative volume, runout distance, and/or the topographical constraints on runout (i.e., valley ponding versus topography climbing) of individual flow pulses or units.

8. Investigating the time-variance in relative lithic abundances and their relationship to other deposit characteristics such as grain size, juvenile-clast types and abundances, and pumice densities, shows that lithic lithologies play an important role in informing vent location, the evolution of the conduit and fragmentation depths, source conditions, and the temporal evolution of a Plinian eruption. This allows for the identification and time-relative correlation of transient eruption stages in the case of a compositionally uniform, large plinian deposit with interbedded PDCs.

9. Current computational modelling of Plinian eruptions regarding generalized steady versus unsteady column regimes can place restrictions on the interpretation of both ignimbrite and plinian fall deposits in natural eruption scenarios, often disregarding

field data. The amalgamation of quantitative field data and numerical models will help to improve the understanding of the dynamics of intraplinian PDC events and reduce the reliance on numerical models to explain the generation mechanisms of PDCs simultaneous with fall deposition.

7.2 Opportunities for future research

This study has shown that detailed, quantitative investigation into plinian deposit characteristics can help to inform the spatiotemporal evolution of large-Plinian eruptions in terms of transitional vent dynamics in multiphase sequences, fragmentation behaviour in the conduit, source conditions, eruptive behaviour, and the nature of pyroclastic deposition. It has presented potential opportunities for further research regarding the dynamics and sedimentation of large-Plinian eruptions, and below, I outline several possibilities.

7.2.1 Further investigation into transitional vent dynamics

Detailed mapping of the Y4-G units, in addition to further investigation into the lithic lithologies of the earlier beds in the Y4 deposit versus the late-stage Y4-G, may provide further insight into the transitional nature between the Y4 and Y5 vents. Did the Y4-G occur from an interim vent location between the two, and is it possible to constrain the location of this site?

An in-depth investigation into the lithic lithologies across the transition of the Y2 and Y3 deposits may also provide further insight into the transitional nature between these vents and improve the understanding regarding the distinctly different vent locations as described in *Chapter 6* (*Section 6.1*).

7.2.2 Further investigation into the Y5 fall, EFU and other intraplinian PDC deposits

Following the establishment of the three successive, continuous stages of the Y5 phase through quantitative investigations of deposit characteristic (e.g., variation in pumice densities and relative proportions of lithic and juvenile components with stratigraphic height), the possibility to systematically map the lateral dispersion of the Y5 plume with time-variance using additional medial to distal sections arises. The variation of eruptive

plume height and mass discharge rate may also be characterised and calculated. This will be important to inform input conditions for future numerical modelling of the Y5 phase.

Further study of the EFU deposits, and additional grain sizes for componentry analysis, as well as additional locations and extensive field mapping may allow for a finer-scaled resolution of the relative timing of EFU emplacement. There is also potential for mapping and analysis of individual flow packages with distance from source to further constrain the generation mechanism of Type 1 deposits and their Type 2 counterparts.

The opportunity to conduct similar work on additional intraplinian PDC deposits and their fall counterparts (for example in the older Waimihia eruption deposits, also from Taupō) will help to constrain the formation mechanisms of such PDCs. This will allow for the amalgamation of field studies and computational modelling to provide better understanding and an in-depth database of large Plinian eruptions worldwide.

7.2.3 Are the features of the Y5 phase seen in other Plinian eruptions globally?

One major question that arises from this study is whether the debated, discontinuous stratification features seen in the Y5 fall deposit are also identified in other large Plinian fall deposits globally. If so, are the interpretations of these structures causing assessments to downgrade possibly larger scale events: i.e., have bedforms been assumed to result from alternations in plume height when, in fact, they are simply a result of sedimentation instabilities in an otherwise stable plume? Recognising and analysing such structures in other deposits globally will further the ability to correlate deposit features with the parent umbrella cloud for modelling purposes.

7.2.4 Implications for modelling of Plinian eruptions

Numerous implications for modelling arise from the results of this study.

1. Can quantitative field data be used to inform computational eruption modelling? The common input conditions used in plume modelling are estimates of mass eruption rate, vent geometry, vent overpressure, magma temperature, particle size and density distributions, and water content. Detailed field studies on Plinian deposits may be used to constrain temporal variation in these parameters to inform systematic

numerical studies of the effects of time-variant/ evolving eruption conditions on resulting dynamics. This could also include simulations of Plinian eruptions through a granular substrate as a possible mechanism to generate gargling dynamics.

2. Does the size of an eruption effect the potential for gargle dynamics, and can we recreate the deposits of the Y5 and coeval EFUs using the gargle dynamics scenario?

3. Can we reconstruct the temporal evolution of large Plinian eruptions and correlate tephra swathe deposition with gravitational instabilities in the parent eruption cloud? Do models show that coarser grain sizes have the potential to behave in this manner with the same time and length scales that the deposits indicate?

References

Atlas, D., (1963). Radar analysis of severe storms. In: Severe Local Storms, Meteorological Monographs 5: 177-223.

Austin-Erickson, A., Büttner, R., Dellino, P., Ort, M., & Zimanowski, B., (2008). Phreatomagmatic explosions of rhyolitic magma: experimental and field evidence. Journal of Geophysical Research, 113: B11201.

Baines, P. & Sparks, R. S. J., (2005). Dynamics of giant volcanic ash clouds from supervolcanic eruptions. Geophysical Research Letters, 32: L24808.

Barberi, F., Cioni, R., Rosi, M., Santacroce, R., Sbrana, A., & Vecci, R., (1989). Magmatic and phreatomagmatic phases in explosive eruptions of Vesuvius as deduced by grain-size and component analysis of the pyroclastic deposits. Journal of Volcanology and Geothermal Research, 38: 287-307.

Barker, S. J., Wilson, C. J. N., Allan, A. S. R., & Schipper, C. I., (2015). Fine-scale temporal recovery, reconstruction and evolution of a post-supereruption magmatic system. Contributions to Mineralogy and Petrology, 170: 5.

Barker, S. J., Wilson, C. J. N., Morgan, D. J., & Rowland, J. V., (2016). Rapid priming, accumulation and recharge of magma driving recent eruptions at a hyperactive caldera volcano. Geology, 44: 323-326.

Barker, S. J., Wilson, C. J. N., Illsley-Kemp, F., Leonard, G. S., Mestel, E. R. H., Mauriohooho, K., & Charlier, B. L. A., (2021). Taupo: an overview of New Zealand's youngest supervolcano. New Zealand Journal of Geology and Geophysics, 64: 320-346.

Barrett, K. & Dixon, R., (2012). NDVI analysis of hail swaths associated with the 5 May 1995 Parker County and Tarrant County, Texas, hailstorm. National Weather Digest, 36(1): Special section, 10p.

Basara, J. B., Cheresnick, D. R., Mitchell, D., & Illston, B. G., (2007). An analysis of severe hail swaths in the southern plains of the United States. Transactions in GIS, 11: 531-554.

Batchelor, G. K., (1993). Secondary instability of a gas-fluidized bed. Journal of Fluid Mechanics, 257: 359-371.

Baumgart, I. L., (1954). Some ash showers of the central North Island. New Zealand Journal of Science and Technology B35: 456-467.

Baumgart, I. L. & Healy, J., (1956). Recent volcanicity at Taupo, New Zealand. Proceedings of the 8th Pacific Science Congress: 113-125.

Belousov, A., Voight, B., & Belousova, M., (2007). Directed blasts and blast-generated pyroclastic density currents: a comparison of the Bezymianny 1956, Mount St Helens

1980, and Soufrière Hills, Montserrat 1997 eruptions and deposits. Bulletin of Volcanology, 69: 701-740.

Bercovici, D. & Michaut, C., (2010). Two-phase dynamics of volcanic eruptions: compaction, compression and the conditions for choking. Geophysical Journal International, 182: 843-864.

Biass, S., Todde, A., Cioni, R., Pistolesi, M., Geshi, N. & Bonadonna, C., (2017). Potential impacts of tephra fallout from a large-scale explosive eruption at Sakurajima volcano. Japan. Bulletin of Volcanology, 79: 1-24.

Bibby, H. M., Caldwell, T. G., Davey, F. J., & Webb, T. H., (1995). Geophysical evidence on the structure of the Taupo Volcanic Zone and its hydrothermal circulation. Journal of Volcanology and Geothermal Research, 68: 29-58.

Blake, S., Wilson, C. J. N., Smith, I. E. M. & Walker, G. P. L. (1992). Petrology and dynamics of the Waimihia mixed magma eruption, Taupo Volcano, New Zealand. Journal of the Geological Society, London, 149: 193-207.

Blott, S. J. & Pye, K., (2001). GRADISTAT: a grain size distribution and statistics package for the analysis of unconsolidated sediments. Earth Surface Processes and Landforms, 26: 1237-1248.

Boggs, S., (2006). Principles of Sedimentology and Stratigraphy. Pearson Education Inc, New Jersey, USA.

Bokulich, A. & Oreskes, N., (2017) Models in the Geosciences. In: Springer Handbook of Model-Based Science (eds Magnani, L. & Bertolotti, T.). Springer, Switzerland:891-911

Bonadonna, C., Ernst, G., & Sparks, R. S. J. (1998). Thickness variations and volume estimates of tephra fall deposits: the importance of particle Reynolds number. Journal of Volcanology and Geothermal Research, 81: 173-187.

Bonadonna, C., Mayberry, G., Calder, E., Sparks, R. S. J., Choux, C., Jackson, P., Lejeune, A., Loughlin, S., Norton, G., & Rose, W. I., (2002). Tephra fallout in the eruption of Soufrière Hills Volcano, Montserrat. In: The Eruption of Soufrière Hills Volcano, Montserrat from 1995 to 1999 (eds Druitt, T. H., Kokelaar, B. P.). Geological Society of London Memoirs 21: 483-516.

Bonadonna, C. & Houghton, B. F., (2005). Total grain-size distribution and volume of tephra-fall deposits. Bulletin of Volcanology, 67: 441-456.

Bonadonna, C., Costa, A., Folch, A., & Koyaguchi, T., (2015a). Tephra Dispersal and Sedimentation. In: The Encyclopedia of Volcanoes (2nd Edition) (eds Sigurdsson, H., Houghton, B. F., McNutt, S., Rymer, H. and Stix, J.) Elsevier, Oxford: 587-597.

Bonadonna, C., Biass, S., & Costa, A., (2015b). Physical characterization of explosive volcanic eruptions based on tephra deposits: propagation of uncertainties and sensitivity analysis. Journal of Volcanology and Geothermal Research, 296: 80-100.

Bond, A., & Sparks, R. S. J., (1976). The Minoan eruption of Santorini, Greece. Journal of the Geological Society, London, 132: 1-16.

Boyd, F. R., (1961). Welded tuffs and flows in the rhyolite plateau of Yellowstone Park, Wyoming. Geological Society of America Bulletin, 72: 387-426.

Branney, M. J. & Kokelaar, P., (2002) Pyroclastic Density Currents and the Sedimentation of Ignimbrites. Geological Society of London Memoirs, 27.

Breard, E. C. & Lube, G., (2017). Inside pyroclastic density currents–uncovering the enigmatic flow structure and transport behaviour in large-scale experiments. Earth and Planetary Science Letters, 458: 22-36.

Breard, E. C., Lube, G., Jones, J. R., Dufek, J., Cronin, S. J., Valentine, G. A., & Moebis, A., (2016). Coupling of turbulent and non-turbulent flow regimes within pyroclastic density currents. Nature Geoscience, 9: 767-771.

Breard, E. C., Dufek, J., & Lube, G., (2018). Enhanced mobility in concentrated pyroclastic density currents: An examination of a self-fluidization mechanism. Geophysical Research Letters, 45: 654-664.

Brown, S., Burt, R., Cole, J., Krippner, S., Price, R., & Cartwright, I., (1998). Plutonic lithics in ignimbrites of Taupo Volcanic Zone, New Zealand; sources and conditions of crystallisation. Chemical Geology, 148: 21-41.

Buckland, H. M., Eychenne, J., Rust, A. C., & Cashman, K. V., (2018). Relating the physical properties of volcanic rocks to the characteristics of ash generated by experimental abrasion. Journal of Volcanology and Geothermal Research, 349: 335-350.

Burgisser, A., & Bergantz, G. W., (2002). Reconciling pyroclastic flow and surge: the multiphase physics of pyroclastic density current. Earth and Planetary Science Letters, 202: 405-418.

Burgisser, A., Bergantz, G. W., & Breidenthal, R. E., (2005). Addressing complexity in laboratory experiments: the scaling of dilute multiphase flows in magmatic systems. Journal of Volcanology and Geothermal Research, 141: 245-265.

Bursik, M. I., Sparks, R. S. J., Gilbert, J. S., & Carey, S. N., (1992). Sedimentation of tephra by volcanic plumes: I. Theory and its comparison with a study of the Fogo A plinian deposit, Sao Miguel (Azores). Bulletin of Volcanology, 54: 329-344.

Carazzo, G., & Jellinek, A. M., (2012). A new view of the dynamics, stability and longevity of volcanic clouds. Earth and Planetary Science Letters, 325: 39-51.

Carazzo, G. & Jellinek, A. M., (2013). Particle sedimentation and diffusive convection in volcanic ash-clouds. Journal of Geophysical Research: Solid Earth, 118: 1420-1437.

Carazzo, G., Kaminski, E., & Tait, S., (2006). The route to self-similarity in turbulent jets and plumes. Journal of Fluid Mechanics, 547: 137-148.

Carazzo, G., Kaminski, E., & Tait, S., (2008). On the rise of turbulent plumes: Quantitative effects of variable entrainment for submarine hydrothermal vents, terrestrial and extra-terrestrial explosive volcanism. Journal of Geophysical Research: Solid Earth, 113: B09201.

Carazzo, G., Kaminski, E., & Tait, S., (2015). The timing and intensity of column collapse during explosive volcanic eruptions. Earth and Planetary Science Letters, 411: 208-217.

Carazzo, G., Tait, S., Michaud-Dubuy, A., Fries, A., & Kaminski, E. (2020). Transition from stable column to partial collapse during the 79 cal CE P3 Plinian eruption of Mt. Pelée volcano (Lesser Antilles). Journal of Volcanology and Geothermal Research, 392: 106764.

Carey, S. N. & Bursik, M. I., (2015). Volcanic plumes. In: The Encyclopedia of Volcanoes (2nd Edition) (eds Sigurdsson, H., Houghton, B. F., McNutt, S., Rymer, H. and Stix, J.) Elsevier, Amsterdam: 571-585.

Carey, S. N. & Sigurdsson, H., (1989). The intensity of plinian eruptions. Bulletin of Volcanology, 51: 28-40.

Carey, S. N. & Sparks, R. S. J., (1986). Quantitative models of the fallout and dispersal of tephra from volcanic eruption columns. Bulletin of Volcanology, 48: 109-125.

Carrigan, C. R. & Sigurdsson, H., (2000). Plumbing systems. In: The Encyclopedia of Volcanoes (eds Sigurdsson, H., Houghton, B. F., McNutt, S., Rymer, H. and Stix, J.) Academic Press, San Diego: 219-235.

Cashman, K. V., (2004). Volatile controls on magma ascent and eruption. Washington DC American Geophysical Union Geophysical Monograph Series, 150: 109-124.

Cashman, K. V. & Mangan, M. T., (1994). Physical aspects of magmatic degassing; II, Constraints on vesiculation processes from textural studies of eruptive products. Reviews in Mineralogy and Geochemistry, 30: 447-478.

Cashman, K. V. & Rust, A., (2016). Volcanic Ash: Generation and Spatial Variations. In: Volcanic Ash: Hazard Observation (eds Mackie, S., Cashman, C., Ricketts, H., Rust, A. and Watson, M.) Elsevier, Amsterdam: 5-22.

Cashman, K. V. & Scheu, B., (2015). Magmatic Fragmentation. In: The Encyclopedia of Volcanoes (2nd Edition) (eds Sigurdsson, H., Houghton, B. F., McNutt, S., Rymer, H. and Stix, J.) Elsevier, Oxford: 459-471.

Cashman, K. V., Sturtevant, B., Papale, P., & Navon, O., (2000). Magmatic fragmentation. In: The Encyclopedia of Volcanoes (eds Sigurdsson, H., Houghton, B. F. McNutt, S., Rymer, H. and Stix, J.) Academic Press, San Diego: 421-430.

Cas, R. A. F. & Wright J. V., (1987) Volcanic successions Modern and Ancient: A geological approach to processes, products and successions. Allen and Unwin, London: 1–518.

Cattell, H., Cole, J., & Oze, C., (2016). Volcanic and sedimentary facies of the Huka Group arc-basin sequence, Wairakei–Tauhara geothermal field, New Zealand. New Zealand Journal of Geology and Geophysics, 59: 236-256.

Chambefort, I., Lewis, B., Wilson, C. J. N., Rae, A. J., Coutts, C., Bignall, G., & Ireland, T. R. (2014). Stratigraphy and structure of the Ngatamariki geothermal system from new zircon U-Pb geochronology: implications for Taupo Volcanic Zone evolution. Journal of Volcanology and Geothermal Research, 274: 51-70.

Charlton, R. B. & List, R., (1972). Hail size distributions and accumulation zones. Journal of the Atmospheric Sciences, 29: 1182-1193.

Chernet, T., (1987). Lithic inclusions in the Taupo Pumice Formation. Victoria University of Wellington, MSc Thesis.

Cioni, R., Civetta, L., Marianelli, P., Metrich, N., Santacroce, R., & Sbrana, A., (1995). Compositional layering and syn-eruptive mixing of a periodically refilled shallow magma chamber: the AD 79 Plinian eruption of Vesuvius. Journal of Petrology, 36: 739-776.

Cioni, R., Pistolesi, M., & Rosi, M., (2015). Plinian and Subplinian Eruptions. The Encyclopedia of Volcanoes (2nd Edition) (eds Sigurdsson, H., Houghton, B. F., McNutt, S., Rymer, H. & Stix, J.) Elsevier, Oxford: 519-535.

Clarke, A. B., Voight, B., Neri, A., & Macedonio, G. (2002). Transient dynamics of vulcanian explosions and column collapse. Nature, 415: 897–901.

Cole, J., W., (1990). Structural control and origin of volcanism in the Taupo volcanic zone, New Zealand. Bulletin of Volcanology, 52: 445-459.

Cole, J. W. & Lewis, K. B., (1981). Evolution of the Taupo-Hikurangi subduction system. Tectonophysics, 72: 1-21.

Cole, J., W., Brown, S. J. A., Burt, R. M., Beresford, S. W., & Wilson, C. J. N., (1998). Lithic types in ignimbrites as a guide to the evolution of a caldera complex, Taupō Volcanic Centre, New Zealand. Journal of Volcanology and Geothermal Research, 80: 217-237.

Collins Dictionary (2023). Retrieved April 9, 2023, from https://www.collinsdictionary.com/dictionary/english/buoyancy

Constantinescu, R., Hopulele-Gligor, A., Connor, C. B., Bonadonna, C., Connor, L. J., Lindsay, J. M., & Volentik, A. C., (2021). The radius of the umbrella cloud helps characterize large explosive volcanic eruptions. Communications Earth & Environment, 2.

Costa, A., Melnik, O., & Vedeneeva, E., (2007). Thermal effects during magma ascent in conduits. Journal of Geophysical Research: Solid Earth, 112: B12205.

Costa, A., Folch, A., & Macedonio, G., (2013). Density-driven transport in the umbrella region of volcanic clouds: Implications for tephra dispersion models. Geophysical Research Letters, 40: 4823-4827.

Corna, L., (2022) The Interactions of Pyroclastic Density Currents with Obstacles – a Large-scale Experimental Study. Massey University, New Zealand. PhD Thesis

Criswell, C. W., (1987). Chronology and pyroclastic stratigraphy of the May 18, 1980, eruption of Mount St. Helens, Washington. Journal of Geophysical Research: Solid Earth, 92: 10237-10266.

Criswell, C. W., (2021). A revised narrative of the May 18, 1980 Plinian eruption of Mount St. Helens: Changes in the conduit and magma supply. Journal of Volcanology and Geothermal Research, 419: 107388.

Crowe, C., Troutt, T., Chung, J., Davis, R., & Moore, E., (1995). A turbulent flow without particle mixing. Aerosol Science Technology, 22: 135-138.

Dartevelle, S., Ernst, G. G. J., Stix, J., & Bernard, A., (2002). Origin of the Mount Pinatubo climactic eruption cloud: Implications for volcanic hazards and atmospheric impacts. Geology, 30: 663-666.

Davidson, J. F., & Harrison, D., (1963) Fluidized Particles. Cambridge University Press, Cambridge, UK.

Davidson, J., F., & Harrison, D., (1971). Fluidization. Academic Press, London.

Davy, B. W., & Caldwell, T. G., (1998). Gravity, magnetic and seismic surveys of the caldera complex, Lake Taupo, North Island, New Zealand. Journal of Volcanology and Geothermal Research, 81: 69-89.

Di Muro, A., Neri, A., & Rosi, M., (2004). Contemporaneous convective and collapsing eruptive dynamics: the transitional regime of explosive eruptions. Geophysical Research Letters, 31: L10607.

Dingwell, D. B., Lavallée, Y., Hess, K. U., Flaws, A., Marti, J., Nichols, A. R. L., Gilg, H. A., & Schillinger, B., (2016). Eruptive shearing of tube pumice: pure and simple. Solid Earth, 7: 1383-1393.

Doyle, E. E., Johnston, D. M., Smith, R., & Paton, D., (2019). Communicating model uncertainty for natural hazards: a qualitative systematic thematic review. International Journal of Disaster Risk Reduction, 33: 449-476.

Dufek, J., (2016). The fluid mechanics of pyroclastic density currents. Annual Review of Fluid Mechanics, 48: 459-485.

Dufek, J., & Manga, M., (2008). In situ production of ash in pyroclastic flows. Journal of Geophysical Research, 113: B09207.

Duffield, W. A., Bacon, C. R., & Roquemore, G. R., (1979). Origin of reverse-graded bedding in air-fall pumice, Coso Range, California. Journal of Volcanology and Geothermal Research, 5: 35-48.

Dunbar, N. W., & Kyle, P. R., (1992). Volatile contents of obsidian clasts in tephra from the Taupo Volcanic Zone, New Zealand: Implications to eruptive processes. Journal of Volcanology and Geothermal Research, 49: 127-145.

Dunbar, N. W., & Kyle, P. R., (1993). Lack of volatile gradient in the Taupo plinian-ignimbrite transition: evidence from melt inclusion analysis. American Mineralogist, 78: 612-618.

Durant, A. J., Rose, W. I., Sarna-Wojcicki, A., Carey, S. N., & Volentik, A., (2009). Hydrometeor-enhanced tephra sedimentation: Constraints from the 18 May 1980 eruption of Mount St. Helens. Journal of Geophysical Research, 114: B03204.

Eastwood, A. A., Gravley, D. M., Wilson, C. J. N., Chambefort, I., Oze, C., Cole, J. W., & Ireland, T. R., (2013). U-Pb dating of subsurface pyroclastic deposits (Tahorakuri Formation) at Ngatamariki and Rotokawa geothermal fields. Paper presented at the 35th New Zealand Geothermal Workshop, Rotorua, New Zealand.

Eychenne, J., Le Pennec, J. L., Troncoso, L., Gouhier, M., & Nedelec, J. M., (2012). Causes and consequences of bimodal grain-size distribution of tephra fall deposited during the August 2006 Tungurahua eruption (Ecuador). Bulletin of Volcanology, 74: 187-205.

Fierstein, J., & Hildreth, W., (1992). The plinian eruptions of 1912 at Novarupta, Katmai National Park, Alaska. Bulletin of Volcanology, 54: 646-684.

Fierstein, J., & Nathenson, M., (1992). Another look at the calculation of fallout tephra volumes. Bulletin of Volcanology, 54: 156-167.

Fierstein, J. & Wilson, C. J. N., (2005). Assembling an ignimbrite: Compositionally defined eruptive packages in the 1912 Valley of Ten Thousand Smokes ignimbrite, Alaska. Geological Society of America Bulletin, 117: 1094-1107.

Fierstein, J., Houghton, B. F., Wilson, C. J. N., & Hildreth, W., (1997). Complexities of plinian fall deposition at vent: an example from the 1912 Novarupta eruption (Alaska). Journal of Volcanology and Geothermal Research, 76: 215-227.

Fisher, R. V., (1966). Rocks composed of volcanic fragments and their classification. Earth-Science Reviews, 1:287-298

Fisher, R. V., & Schmincke, H. U., (1984). Pyroclastic Rocks. Springer, Heidelberg.

Folk, R. L., & Ward, W. C., (1957). Brazos River bar: a study in the significance of grain size parameters. Journal of Sedimentary Petrology, 27: 3-26.

Freundt, A., Wilson, C. J. N., & Carey, S. N., (2000). Ignimbrites and block-and-ash flow deposits. In: The Encyclopedia of Volcanoes (eds. Sigurdsson, H., Houghton, B. F., McNutt, S., Rymer, H. & Stix, J.) Academic Press, San Diego: 581-600.

Fries, A., Lemus, J., Jarvis, P. A., Clarke, A. B., Phillips, J. C., Manzella, I., & Bonadonna, C., (2021). The influence of particle concentration on the formation of settling-driven gravitational instabilities at the base of volcanic clouds. Frontiers in Earth Science, 9: 640090.

Froggatt, P. C., (1981). Stratigraphy and nature of Taupo Pumice Formation. New Zealand Journal of Geology and Geophysics, 24: 231-248.

Froggatt, P. C., Wilson, C. J. N., & Walker, G. P. L., (1981). Orientation of logs in the Taupo Ignimbrite as an indicator of flow direction and vent position. Geology, 9: 109-111.

Gallo, K., Smith, T., Jungbluth, K., & Schumacher, P., (2012). Hail swaths observed from satellite data and their relation to radar and surface-based observations: A case study from Iowa in 2009. Weather and Forecasting, 27: 796-802.

Geshi, N., (2020). Volcanological challenges to understanding explosive large-scale eruptions. Earth, Planets and Space, 72: 1-10.

Giachetti, T., Trafton, K. R., Wiejaczka, J., Gardner, J. E., Watkins, J. M., Shea, T., & Wright, H. M., (2021). The products of primary magma fragmentation finally revealed by pumice agglomerates. Geology, 49: 1307-1311.

Gilchrist, J. T., & Jellinek, A., M., (2021). Sediment waves and the gravitational stability of volcanic jets. Bulletin of Volcanology, 83: 64.

Girault, F., Carazzo, G., Tait, S., Ferrucci, F., & Kaminski, E., (2014). The effect of total grain-size distribution on the dynamics of turbulent volcanic plumes. Earth and Planetary Science Letters, 394: 124-134.

Gravley, D. M., Wilson, C. J. N., Leonard, G. S., & Cole, J. W., (2007). Double trouble: paired ignimbrite eruptions and collateral subsidence in the Taupo Volcanic Zone, New Zealand. Geological Society of America Bulletin, 119: 18-30.

Grunder, A. L., Laporte, D., & Druitt, T. H. (2005). Experimental and textural investigation of welding: effects of compaction, sintering, and vapor-phase crystallization in the rhyolitic Rattlesnake Tuff. Journal of Volcanology and Geothermal Research, 142: 89-104.

Hanson, J., Rust, A., Phillips, J., Sulpizio, R., Engwell, S., & Costa, A., (2016). Conduit evolution during the Avellinio Plinian eruption (Vesuvius): Insights from fieldwork, lithic grain size distributions and modelling. In EGU General Assembly Conference Abstracts, EPSC2016-17736.

Harris, S. E., & Crighton, D. G., (1994). Solitons, solitary waves, and voidage disturbances in gas- fluidized beds. Journal of Fluid Mechanics, 266: 243-276.

Healy, J., (1964). Stratigraphy and chronology of late Quaternary volcanic ash in Taupo, Rotorua, and Gisborne districts. New Zealand Geological Survey Bulletin, 73: 1-42.

Heap, M. J., Xu, T., & Chen, C. F., (2014). The influence of porosity and vesicle size on the brittle strength of volcanic rocks and magma. Bulletin of Volcanology, 76: 856.

Hildreth, W. & Mahood, G. A., (1985). Correlation of ash-flow tuffs. Geological Society of America Bulletin, 96: 968-974.

Hildreth, W. & Fierstein, J. (2012). The Novarupta-Katmai eruption of 1912–largest eruption of the twentieth century: centennial perspectives: U.S. Geological Survey Professional Paper 1791, p. 259

Hochstein, M. P. & Browne, P. R. L., (2000). Surface manifestations of geothermal systems with volcanic heat sources. In: The Encyclopedia of Volcanoes (eds. Sigurdsson, H., Houghton, B. F., McNutt, S., Rymer, H. & Stix, J.), Academic Press, San Diego: 835-855.

Hogg, A. G., Lowe, D. J., Palmer, J., Boswijk, G., & Bronk Ramsey, C. (2012). Revised calendar date for the Taupo eruption derived by ^{14}C wiggle-matching using a New Zealand kauri ^{14}C calibration data set. The Holocene, 22: 439-449.

Hogg, A. G., Wilson, C. J. N., Lowe, D. J., Turney, C. S. M., White, P., Lorrey, A. M., Manning, S. W., Palmer, J. G., Bury, S., Brown, J., Southon, J., & Petchey, F. (2019). Wiggle-match radiocarbon dating of the Taupo eruption. Nature Communications, 10: 4669.

Horwell, C., J. & Baxter, P., J., (2006). The respiratory health hazards of volcanic ash: a review for volcanic risk mitigation. Bulletin of Volcanology, 69: 1-24.

Houghton, B. F. & Carey, R. J. (2015). Pyroclastic fall deposits. In: The Encyclopedia of Volcanoes (2nd Edition) (eds Sigurdsson, H., Houghton, B. F., McNutt, S., Rymer, H. & Stix, J.), Elsevier, Oxford: 599-616.

Houghton, B. F. & Wilson, C. J. N., (1989). A vesicularity index for pyroclastic deposits. Bulletin of Volcanology, 51: 451-462.

Houghton, B. F., White, J. D., & Van Eaton, A. R., (2015). Phreatomagmatic and related eruption style. In: The Encyclopedia of Volcanoes (2nd Edition) (eds Sigurdsson, H., Houghton, B. F., McNutt, S., Rymer, H. & Stix, J.), Elsevier, Oxford: 537-552.

Houghton, B. F., Wilson, C. J. N., McWilliams, M. O., Lanphere, M. A., Weaver, S. D., Briggs, R. M., & Pringle, M. S., (1995). Chronology and dynamics of a large silicic magmatic system: Central Taupo Volcanic Zone, New Zealand. Geology, 23: 13-16.

Houghton, B. F., Wilson, C. J. N., Smith, R. T., & Gilbert, J. S., (2000a). Phreatoplinian eruptions. In: The Encyclopedia of Volcanoes (eds Sigurdsson, H., Houghton, B. F., McNutt, S., Rymer, H. & Stix, J.), Academic Press, San Diego: 513-525.

Houghton, B. F., Wilson, C. J. N., & Pyle, D. M., (2000b). Pyroclastic fall deposits. In: The Encyclopedia of Volcanoes (eds. Sigurdsson, H., Houghton, B. F., McNutt, S., Rymer, H. & Stix, J.), Academic Press, San Diego: 555-570.

Houghton, B. F., Wilson, C. J. N., Fierstein, J., & Hildreth, W., (2004). Complex proximal deposition during the Plinian eruptions of 1912 at Novarupta, Alaska. Bulletin of Volcanology, 66: 95-133.

Houghton, B. F., Carey, R. J., Cashman, K. V., Wilson, C. J. N., Hobden, B. J., & Hammer, J. E., (2010). Diverse patterns of ascent, degassing, and eruption of rhyolite magma during the 1.8 ka Taupo eruption, New Zealand: evidence from clast vesicularity. Journal of Volcanology and Geothermal Research, 195: 31-47.

Houghton, B. F., Carey, R. J., & Rosenberg, M. D., (2014). The 1800a Taupo eruption: "III wind" blows the ultraplinian type event down to Plinian. Geology, 42: 459-461.

Illsley-Kemp, F., Barker, S. J., Wilson, C. J. N., Chamberlain, C. J., Hreinsdóttir, S., Ellis, S. and Wadsworth, F. B., (2021). Volcanic unrest at Taupō volcano in 2019: Causes, mechanisms and implications. Geochemistry, Geophysics, Geosystems, 22, e2021GC009803.

Inman, D. L., (1952). Measures for describing the size distribution of sediments. Journal of Sedimentary Research, 22: 125-145.

Jessop, D. & Jellinek, A. M., (2014). Effects of particle mixtures and nozzle geometry on entrainment into volcanic jets. Geophysical Research Letters, 41: 3858-3863.

Jurado-Chichay, Z., & Walker, G. P. L., (2000). Stratigraphy and dispersal of the Mangaone Subgroup pyroclastic deposits, Okataina volcanic centre, New Zealand. Journal of Volcanology and Geothermal Research, 104: 319-380.

Kaminski, E. & Jaupart, C., (2001). Marginal stability of atmospheric eruption columns and pyroclastic flow generation. Journal of Geophysical Research: Solid Earth, 106: 21785-21798.

Kaminski, E., Tait, S., & Carazzo, G., (2005). Turbulent entrainment in jets with arbitrary buoyancy. Journal of Fluid Mechanics, 526: 361-376.

Kaminski, E., Tait, S., Ferrucci, F., Martet, M., Hirn, B., & Husson, P. (2011). Estimation of ash injection in the atmosphere by basaltic volcanic plumes: The case of the Eyjafjallajökull 2010 eruption. Journal of Geophysical Research: Solid Earth, 116.

Klug, C. & Cashman, K. V., (1996). Permeability development in vesiculating magmas: implications for fragmentation. Bulletin of Volcanology, 58: 87-100.

Klug, C., Cashman, K. V., & Bacon, C. R., (2002). Structure and physical characteristics of pumice from the climactic eruption of Mount Mazama (Crater Lake), Oregon. Bulletin of Volcanology, 64: 486-501.

Knight, C., Knight, N., Brooks, H., & Skripnikova, K., (2019). Hail and Hailstorms. Elsevier, Amsterdam.

Komac, B. & Zorn, M., (2013). Geohazards. Springer, Dordrecht, Netherlands, 387 pp.

Komorowski, J. C., Jenkins, S., Baxter, P. J., Picquout, A., Lavigne, F., Charbonnier, S., & Budi-Santoso, A., (2013). Paroxysmal dome explosion during the Merapi 2010 eruption: Processes and facies relationships of associated high-energy pyroclastic density currents. Journal of Volcanology and Geothermal Research, 261: 260-294.

Krumbein, W., (1934). Size frequency distributions of sediments. Journal of Sedimentary Petrology, 4: 65-77.

Krumbein, W., (1938). Size frequency distributions of sediments and the normal phi curve. Journal of Sedimentary Petrology, 8: 84-90.

Kuehn, S. C., (2002). Stratigraphy, distribution, and geochemistry of the Newberry Volcano tephras. Washington State University. PhD Thesis.

Kunz, M. & Puskeiler, M., (2010). High-resolution assessment of the hail hazard over complex terrain from radar and insurance data. Meteorologische Zeitschrift, 19: 427-439.

Lherm, V. & Jellinek, A. M., (2019). Experimental constraints on the distinct effects of ash, lapilli, and larger pyroclasts on entrainment and mixing in volcanic plumes. Bulletin of Volcanology, 81: 73.

Lirer, L., Pescatore, T., Booth, B., & Walker, G. P. L., (1973). Two plinian pumice-fall deposits from Somma-Vesuvius, Italy. Geological Society of America Bulletin, 84: 759-772.

Lowe, D. J. & Pittari, A., (2021). The Taupō eruption sequence of AD 232±10 in Aotearoa New Zealand: A retrospection. Journal of Geography. (Chigaku Zasshi), 130: 117-141.

Lube, G., Breard, E. C., Esposti-Ongaro, T., Dufek, J., & Brand, B., (2020). Multiphase flow behaviour and hazard prediction of pyroclastic density currents. Nature Reviews Earth and Environment, 1: 348-365.

Macedonio, G., Dobran, F., & Neri, A., (1994). Erosion processes in volcanic conduits and application to the AD 79 eruption of Vesuvius. Earth and Planetary Science Letters, 121: 137-152.

Manville, V., Segschneider, B., Newton, E., White, J. D. L., Houghton, B. F., & Wilson, C. J. N. (2009). Environmental impact of the 1.8 ka Taupo eruption, New Zealand: landscape responses to a large-scale explosive rhyolite eruption. Sedimentary Geology, 220: 318-336.

Manzella, I., Bonadonna, C., Phillips, J. C., & Monnard, H., (2015). The role of gravitational instabilities in deposition of volcanic ash. Geology, 43: 211-214.

Marti, J., Soriano, C., & Dingwell, D., (1999). Tube pumices as strain markers of the ductile–brittle transition during magma fragmentation. Nature, 402: 650-653.

Mastin, L. G., (2005). The controlling effect of viscous dissipation on magma flow in silicic conduits. Journal of Volcanology and Geothermal Research, 143: 17-28.

Mastin, L. G., Guffanti, M., Servranckx, R., Webley, P., Barsotti, S., Dean, K., Durant, A., Ewert, J. W., Neri, A., & Rose, W. I., (2009). A multidisciplinary effort to assign realistic source parameters to models of volcanic ash-cloud transport and dispersion during eruptions. Journal of Volcanology and Geothermal Research, 186: 10-21.

McGraw-Hill Dictionary of Scientific and Technical Terms (2003) Retrieved February 1, 2020, from https://encyclopedia2.thefreedictionary.com/gravitational+instability

Mele, D., Sulpizio, R., Dellino, P., & La Volpe, L., (2011). Stratigraphy and eruptive dynamics of a pulsating Plinian eruption of Somma-Vesuvius: The Pomici di Mercato (8900 years BP). Bulletin of Volcanology, 73: 257-278.

Milicich, S. D., Chambefort, I., Wilson, C. J. N., Alcaraz, S., Ireland, T. R., Bardsley, C., & Simpson, M. P., (2020). A zircon U-Pb geochronology for the Rotokawa geothermal system, New Zealand, with implications for Taupō Volcanic Zone evolution. Journal of Volcanology and Geothermal Research, 389: 106729.

Mitchell, S., Biass, S., Houghton, B. F., Anderson, A., Bonny, E., Walker, B., Mintz, B., Turner, N., Frank, D., & Carey, R. J., (2018). The interplay among clast size, vesicularity, post fragmentation expansion, and clast breakage: an example from the 1.8 ka Taupo eruption. Geological Society of America Special Papers, 538: 375-383.

Mullet, B. & Segall, P., (2021). Stress-driven failure of cylindrical volcanic conduits. Journal of Geophysical Research: Solid Earth, 126: e2021JB022278.

Nakada, S., (2000). Hazards from pyroclastic flows and surges. In: The Encyclopedia of Volcanoes (eds Sigurdsson, H., Houghton, B. F., McNutt, S., Rymer, H. & Stix, J.), Academic Press, San Diego: 945-955.

Nelson, S. P. & Young, S. K., (1979). Characteristics of Oklahoma hailfalls and hailstorms. Journal of Applied Meteorology, 18: 339-347.

Neri, A. & Dobran, F., (1994). Influence of eruption parameters on the thermofluid dynamics of collapsing volcanic columns. Journal of Geophysical Research: Solid Earth, 99: 11833-11857.

Neri, A., Di Muro, A., & Rosi, M. (2002). Mass partition during collapsing and transitional columns by using numerical simulations. Journal of Volcanology and Geothermal Research, 115: 1-18.

Nisbet, E. E., (2019) Stratigraphy, grain-size characteristics and componentry of Y1 – the initial phase of the AD232 Taupō eruption, New Zealand. Massey University, New Zealand. Honours Thesis.

Nisi, L., Hering, A., Germann, U., & Martius, O., (2018). A 15-year hail streak climatology for the Alpine region. Quarterly Journal of the Royal Meteorological Society, 144: 1429-1449.

Ohashi, M., Ichihara, M., Takeda, S., Hirota, K., Sato, S., Kuwano, O., & Kameda, M., (2020). Formation of tube-pumice structure under pure shear: Insights from extension tests of solidifying foam. Journal of Volcanology and Geothermal Research, 392: 106772.

Palladino, D. M. & Taddeucci, J., (1998). The basal ash deposit of the Sovana Eruption (Vulsini Volcanoes, central Italy): the product of a dilute pyroclastic density current. Journal of Volcanology and Geothermal Research, 87: 233-254.

Palladino, D. M., Simei, S., & Kyriakopoulos, K., (2008). On magma fragmentation by conduit shear stress: evidence from the Kos Plateau Tuff, Aegean Volcanic Arc. Journal of Volcanology and Geothermal Research, 178: 807-817.

Pfeiffer, T., (2001). Vent development during the Minoan eruption (1640 BC) of Santorini, Greece, as suggested by ballistic blocks. Journal of Volcanology and Geothermal Research, 106: 229-242.

Pittari, A., Cas, R. A. F., Wolff, J. A., Nichols, H. J., Larson, P., & Martí, J., (2008). The use of lithic clast distributions in pyroclastic deposits to understand pre-and syn-caldera collapse processes: a case study of the Abrigo Ignimbrite, Tenerife, Canary Islands. Developments in Volcanology, 10: 97-142.

Polacci, M., Papale, P., & Rosi, M., (2001). Textural heterogeneities in pumices from the climactic eruption of Mount Pinatubo, 15 June 1991, and implications for magma ascent dynamics. Bulletin of Volcanology, 63: 83-97.

Polacci, M., Pioli, L., & Rosi, M., (2003). The Plinian phase of the Campanian Ignimbrite eruption (Phlegrean Fields, Italy): evidence from density measurements and textural characterization of pumice. Bulletin of Volcanology, 65: 418-432.

Pyle, D. M., (1989). The thickness, volume and grainsize of tephra fall deposits. Bulletin of Volcanology, 51: 1-15.

Pyle, D. M., (2015). Sizes of volcanic eruptions. In: The Encyclopedia of Volcanoes (2nd Edition) (eds Sigurdsson, H., Houghton, B. F., McNutt, S., Rymer, H. & Stix, J.), Elsevier, Oxford: 257-264.

Quane, S. L. & Russell, J. K., (2005). Welding: insights from high-temperature analogue experiments. Journal of Volcanology and Geothermal Research, 142: 67-87.

Rampino, M. R. & Self, S., (1982). Historic eruptions of Tambora (1815), Krakatau (1883), and Agung (1963), their stratospheric aerosols, and climatic impact. Quaternary Research, 18: 127-143.

Rampino, M. R. & Self, S., (1984). Sulphur-rich volcanic eruptions and stratospheric aerosols. Nature, 310: 677-679.

Rampino, M. R., Self, S., & Stothers, R., B., (1988). Volcanic winters. Annual Review of Earth and Planetary Sciences, 16: 73-99.

Riehle, J. R., (1973). Calculated compaction profiles of rhyolitic ash-flow tuffs. Geological Society of America Bulletin, 84: 2193-2216.

Riehle, J. R., Miller, T. F., & Bailey, R. A., (1995). Cooling, degassing and compaction of rhyolitic ash flow tuffs: a computational model. Bulletin of Volcanology, 57: 319-336.

Rose, W. I. & Durant, A. J., (2009). Fine ash content of explosive eruptions. Journal of Volcanology and Geothermal Research, 186: 32-39.

Rose, W. I., Self, S., Murrow, P. J., Bonadonna, C., Durant, A. J., & Ernst, G. G. J., (2008). Nature and significance of small volume fall deposits at composite volcanoes: Insights from the October 14, 1974, Fuego eruption, Guatemala. Bulletin of Volcanology, 70: 1043-1067.

Rosenberg, M. D., Bignall, G., & Rae, A. J., (2009). The geological framework of the Wairakei-Tauhara geothermal system, New Zealand. Geothermics, 38: 72-84.

Rosenberg, M. D., Wilson, C. J. N., Bignall, G., Ireland, T. R., Sepulveda, F., & Charlier, B. L. A., (2020). Structure and evolution of the Wairakei-Tauhara geothermal system (Taupo Volcanic Zone, New Zealand) revisited with a new zircon geochronology. Journal of Volcanology and Geothermal Research, 390: 106705.

Rosi, M., Vezzoli, L., Castelmenzano, A., & Grieco, G., (1999). Plinian pumice fall deposit of the Campanian Ignimbrite eruption (Phlegraean Fields, Italy). Journal of Volcanology and Geothermal Research, 91: 179-198.

Rosi, M., Paladio-Melosantos, M., Di Muro, A., Leoni, R., & Bacolcol, T., (2001). Fall vs flow activity during the 1991 climactic eruption of Pinatubo Volcano (Philippines). Bulletin of Volcanology, 62: 549-566.

Rowell, C. R., Jellinek, A. M., Hajimirza, S., & Aubry, T. J., (2022). External surface water influence on explosive eruption dynamics, with implications for stratospheric sulfur delivery and volcano-climate feedback. Frontiers in Earth Science, 10, 788294.

Rowley, P. D., MacLeod, N. S., Kuntz, M. A., & Kaplan, A. M., (1985). Proximal bedded deposits related to pyroclastic flows of May 18, 1980, Mount St. Helens, Washington. Geological Society of America Bulletin, 96: 1373-1383.

Rust, A., Manga, M., & Cashman, K. V., (2003). Determining flow type, shear rate and shear stress in magmas from bubble shapes and orientations. Journal of Volcanology and Geothermal Research, 122: 111-132.

Scasso, R. A., Corbella, H., & Tiberi, P., (1994). Sedimentological analysis of the tephra from the 12–15 August 1991 eruption of Hudson volcano. Bulletin of Volcanology, 56: 121-132.

Schmid, W., Schiesser, H., & Bauer-Messmer, B., (1997). Supercell storms in Switzerland: Case studies and implications for nowcasting severe winds with Doppler radar. Meteorological Applications, 4: 49-67.

Scollo, S., Tarantola, S., Bonadonna, C., Coltelli, M., & Saltelli, A., (2008). Sensitivity analysis and uncertainty estimation for tephra dispersal models. Journal of Geophysical Research: Solid Earth, 113: B06202.

Self, S., (1983). Large-scale phreatomagmatic silicic volcanism: A case study from New Zealand. Journal of Volcanology and Geothermal Research, 17: 433-469.

Self, S., (2006). The effects and consequences of very large explosive volcanic eruptions. Philosophical Transactions of the Royal Society A: Mathematical, Physical and Engineering Sciences, 364: 2073-2097.

Self, S., (2015). Explosive super-eruptions and potential global impacts. In: Volcanic Hazards, Risks and Disasters (eds Shroder, J.F. & Papale, P.). Elsevier: 399-418.

Self, S. & Rampino, M. R., (1981). The 1883 eruption of Krakatau. Nature, 294: 699-704.

Self, S. & Sparks, R. S. J., (1978). Characteristics of widespread pyroclastic deposits formed by the interaction of silicic magma and water. Bulletin of Volcanology, 41: 196-212.

Self, S., Gertisser, R., Thordarson, T., Rampino, M., R., & Wolff, J., A., (2004). Magma volume, volatile emissions, and stratospheric aerosols from the 1815 eruption of Tambora. Geophysical Research Letters, 31, L20608.

Shea, T., Houghton, B. F., Gurioli, L., Cashman, K. V., Hammer, J. E., & Hobden, B. J., (2010). Textural studies of vesicles in volcanic rocks: an integrated methodology. Journal of Volcanology and Geothermal Research, 190: 271-289.

Shea, T., Gurioli, L., Houghton, B. F., Cioni, R., & Cashman, K. V., (2011). Column collapse and generation of pyroclastic density currents during the AD 79 eruption of Vesuvius: the role of pyroclast density. Geology, 39: 695-698.

Sigurdsson, H., (2003). Volcanology. Elsevier, Amsterdam.

Sigurdsson, H. & Carey, S. N., (1989). Plinian and co-ignimbrite tephra fall from the 1815 eruption of Tambora volcano. Bulletin of Volcanology, 51: 243-270.

Smith, R. T., (1998). Eruptive and depositional models for units 3 and 4 of the 1.85 ka Taupo eruption: Implications for the nature of large-scale 'wet' eruptions. University of Canterbury, PhD Thesis.

Smith, R. T. & Houghton, B. F., (1995a). Vent migration and changing eruptive style during the 1800a Taupo eruption: new evidence from the Hatepe and Rotongaio phreatoplinian ashes. Bulletin of Volcanology, 57: 432-439.

Smith, R. T. & Houghton, B. F., (1995b). Delayed deposition of plinian pumice during phreatoplinian volcanism: the 1800-yr-BP Taupo eruption, New Zealand. Journal of Volcanology and Geothermal Research, 67: 221-226.

Sparks, R. S. J., (1976). Grain size variations in ignimbrites and implications for the transport of pyroclastic flows. Sedimentology, 23: 147-188.

Sparks, R. S. J., (1978). The dynamics of bubble formation and growth in magmas: a review and analysis. Journal of Volcanology and Geothermal Research, 3: 1-37.

Sparks, R. S. J., (1986). The dimensions and dynamics of volcanic eruption columns. Bulletin of Volcanology, 48: 3-15.

Sparks, R. S. J., Self, S., Grattan, J. P., Oppenheimer, C., Pyle, D. M., & Rymer, H., (2005). Super-eruptions: Global Effects and Future Threats. Report of a Geological Society of London working group.

Sparks, R. S. J., & Wilson, L., (1976). A model for the formation of ignimbrite by gravitational column collapse. Journal of the Geological Society, 132: 441-451.

Sparks, R. S. J. & Wilson, C. J. N. (1990). The Minoan deposits: a review of their characteristics and interpretation. In: Thera and the Aegean World III, D. Hardy (Editor), Third International Congress, Santorini, Greece.

Sparks, R. S. J., Wilson, L., & Sigurdsson, H., (1981). The pyroclastic deposits of the 1875 eruption of Askja, Iceland. Philosophical Transactions of the Royal Society of London. Series A, Mathematical and Physical Sciences, 299: 241-273.

Sparks, R. S. J., Bursik, M. I., Carey, S. N., Gilbert, J. S., Glaze, L. S., Sigurdsson, H., & Woods, A. W., (1997). Volcanic Plumes, J. Wiley and Sons, Chichester, UK.

Spence, R. J., Baxter, P. J., & Zuccaro, G., (2004). Building vulnerability and human casualty estimation for a pyroclastic flow: a model and its application to Vesuvius. Journal of Volcanology and Geothermal Research, 133: 321-343.

Spinks, K. D., Acocella, V., Cole, J. W., & Bassett, K. N., (2005). Structural control of volcanism and caldera development in the transtensional Taupo Volcanic Zone, New Zealand. Journal of Volcanology and Geothermal Research, 144: 7-22.

Sulpizio, R., Bonasia, R., Dellino, P., Mele, D., Di Vito, M., & La Volpe, L., (2010). The Pomici di Avellino eruption of Somma–Vesuvius (3.9 ka BP). Part II: sedimentology and physical volcanology of pyroclastic density current deposits. Bulletin of Volcanology, 72: 559-577.

Sutton, A. N., Blake, S., & Wilson, C. J. N., (1995). An outline geochemistry of rhyolite eruptives from Taupo volcanic centre, New Zealand. Journal of Volcanology and Geothermal Research, 68: 153-175.

Sutton, A. N., Blake, S., Wilson, C. J. N., & Charlier, B. L. A., (2000). Late Quaternary evolution of a hyperactive rhyolite magmatic system: Taupo volcanic centre, New Zealand. Journal of the Geological Society, 157: 537-552.

Suzuki-Kamata, K., Kamata, H., & Bacon, C. R., (1993). Evolution of the caldera-forming eruption at Crater Lake, Oregon, indicated by component analysis of lithic fragments. Journal of Geophysical Research, 98: 14059-14074.

Taddeucci, J. & Wohletz, K. H., (2001). Temporal evolution of the Minoan eruption (Santorini, Greece), as recorded by its Plinian fall deposit and interlayered ash flow beds. Journal of Volcanology and Geothermal Research, 109: 299-317.

Talbot, J. P., Self, S., & Wilson, C. J. N., (1994). Dilute gravity current and rain-flushed ash deposits in the 1.8 ka Hatepe Plinian deposit, Taupo, New Zealand. Bulletin of Volcanology, 56: 538-551.

Tanner, W. F., (1969). The particle size scale. Journal of Sedimentary Research, 39: 810-812.

Thorarinsson, S., (1967). The eruptions of Hekla in historical times: a tephrochronological study. In: Einarsson, T., Kjartansson, G., Thorarinsson, S. (eds) The eruption of Hekla 1947–1948. Societas Scientiarum Islandica, Reykjavík, pp. 1–177.

Trolese, M., Cerminara, M., Esposti Ongaro, T., & Giordano, G., (2019). The footprint of column collapse regimes on pyroclastic flow temperatures and plume heights. Nature Communications, 10: 2476.

Tuovinen, J. P., Punkka, A. J., Rauhala, J., Hohti, H., & Schultz, D. M., (2009). Climatology of severe hail in Finland: 1930–2006. Monthly Weather Review, 137: 2238-2249.

Turner, J. S., (1969). Buoyant plumes and thermals. Annual Review of Fluid Mechanics, 1: 29-44.

Turner, J. S., (1986). Turbulent entrainment: the development of the entrainment assumption, and its application to geophysical flows. Journal of Fluid Mechanics, 173: 431-471.

USGS Volcano Hazards Program Glossary (2016). Retrieved April 9, 2023, from https://volcanoes.usgs.gov/vsc/glossary/

Valentine, G. A. & Cole, M. A., (2021). Explosive caldera-forming eruptions and debris-filled vents: Gargle dynamics. Geology, 49: 1240-1244.

Vallance, J. W., (2000). Lahars. In: The Encyclopedia of Volcanoes (eds. Sigurdsson, H., Houghton, B. F., McNutt, S., Rymer, H. & Stix, J.). Academic Press, San Diego: 601-616.

Vandergoes, M. J., Hogg, A. G., Lowe, D. J., Newnham, R. M., Denton, G. H., Southon, J., Barrell, D. J. A., Wilson, C. J. N., McGlone, M. S., Allan, A. S. R., Almond, P. C., Petchey, F., Dabell, K., Dieffenbacher-Krall, A. C., & Blaauw, M., (2013). A revised age for the Kawakawa/Oruanui tephra, a key marker for the Last Glacial Maximum in New Zealand. Quaternary Science Reviews, 74: 195-201.

Van Eaton, A. R. & Wilson, C. J. N., (2013). The nature, origins and distribution of ash aggregates in a large-scale wet eruption deposit: Oruanui, New Zealand. Journal of Volcanology and Geothermal Research, 250: 129-154.

Varekamp, J. C., (1993). Some remarks on volcanic vent evolution during plinian eruptions. Journal of Volcanology and Geothermal Research, 54: 309-318.

Veitch, G. & Woods, A. W., (2002). Particle recycling in volcanic plumes. Bulletin of Volcanology, 64: 31-39.

Villamor, P. & Berryman, K., (2001). A late Quaternary extension rate in the Taupo Volcanic Zone, New Zealand, derived from fault slip data. New Zealand Journal of Geology and Geophysics, 44: 243-269.

Villamor, P., Berryman, K. R., Ellis, S. M., Schreurs, G., Wallace, L. M., Leonard, G. S., & Ries, W. F., (2017). Rapid evolution of subduction-related continental intra arc rifts: the Taupo Rift, New Zealand. Tectonics, 36: 2250-2272.

Walker, G. P. L., (1971). Grain-size characteristics of pyroclastic deposits. The Journal of Geology, 79: 696-714.

Walker, G. P. L. (1973). Explosive volcanic eruptions—a new classification scheme. Geologische Rundschau, 62: 431-446.

Walker, G. P. L., (1980). The Taupo pumice: product of the most powerful known (ultraplinian) eruption? Journal of Volcanology and Geothermal Research, 8: 69-94.

Walker, G. P. L., (1981a). Characteristics of two phreatoplinian ashes, and their water-flushed origin. Journal of Volcanology and Geothermal Research, 9: 395-407.

Walker, G. P. L., (1981b). The Waimihia and Hatepe plinian deposits from the rhyolitic Taupo Volcanic Centre. New Zealand Journal of Geology and Geophysics, 24: 305-324.

Walker, G. P. L. and Croasdale, R., (1971). Two Plinian-type eruptions in the Azores. Journal of the Geological Society, London, 127: 17-55.

Walker, G. P. L., Heming, R. F., & Wilson, C. J. N., (1980a). Low-aspect ratio ignimbrites. Nature, 283: 286-287.

Walker, G. P. L., Wilson, C. J. N., & Froggatt, P. C., (1980b). Fines-depleted ignimbrite in New Zealand—The product of a turbulent pyroclastic flow. Geology, 8 (5): 245-249.

Walker, G. P. L., Self, S., & Froggatt, P. C., (1981). The ground layer of the Taupo ignimbrite: a striking example of sedimentation from a pyroclastic flow. Journal of Volcanology and Geothermal Research, 10: 1-11.

Walters, H., (2020). Vertical and lateral variations of grainsize and pyroclast componentry in the Taupo 232 CE Y2 fall deposit: implications for spatiotemporal deposition and conduit conditions in large Plinian eruptions. Massey University, New Zealand, MSc Thesis.

White, J. D. L., (1996). Impure coolants and interaction dynamics of phreatomagmatic eruptions. Journal of Volcanology and Geothermal Research, 74: 155-170.

White, J. D. L. & Houghton, B. F. (2006). Primary volcaniclastic rocks. Geology, 34: 677-680.

Wilson, C. J. N., (1981). Studies on the origins and emplacement of pyroclastic flows, University of London, PhD Thesis.

Wilson, C. J. N., (1985). The Taupo eruption, New Zealand. II. The Taupo ignimbrite. Philosophical Transactions of the Royal Society of London. Series A, Mathematical and Physical Sciences, 314: 229-310.

Wilson, C. J. N., (1986). Pyroclastic flows and ignimbrites. Science Progress: 171-207.

Wilson, C. J. N., (1991). Ignimbrite morphology and the effects of erosion: a New Zealand case study. Bulletin of Volcanology, 53: 635-644.

Wilson, C. J. N., (1993). Stratigraphy, chronology, styles and dynamics of late Quaternary eruptions from Taupo volcano, New Zealand. Philosophical Transactions of the Royal Society of London. Series A: Physical and Engineering Sciences, 343: 205-306.

Wilson, C. J. N., (2001). The 26.5 ka Oruanui eruption, New Zealand: an introduction and overview. Journal of Volcanology and Geothermal Research, 112: 133-174.

Wilson, C. J. N. & Hildreth, W., (1997). The Bishop Tuff: new insights from eruptive stratigraphy. The Journal of Geology, 105: 407-440.

Wilson, C.J.N. & Hildreth, W., (1998). Hybrid fall deposits in the Bishop Tuff, California: a novel intermediate pyroclastic depositional mechanism. Geology, 26: 7-10

Wilson, C. J. N. & Hildreth, W. (2003). Assembling an ignimbrite: Mechanical and thermal building blocks in the Bishop Tuff, California. The Journal of Geology, 111: 653-670.

Wilson, C. J. N. & Houghton, B. F., (1990). Eruptive mechanisms in the Minoan eruption: evidence from pumice vesicularity. In: *Thera and the Aegean World III*, Volume 2 (Earth Sciences) (eds Hardy, D. A., Keller, J., Galanopoulos, V. P., Flemming, N. C. and Druitt, T. H.). The Thera Foundation, London: pp. 122-128.

Wilson, C. J. N. & Houghton, B. F., (2000). Pyroclast transport and deposition. In: The Encyclopedia of Volcanoes (eds Sigurdsson, H., Houghton, B. F., McNutt, S., Rymer, H. and Stix, J.). Academic Press, San Diego: 545-554.

Wilson, C. J. N. & Rowland, J. V., (2016). The volcanic, magmatic and tectonic setting of the Taupo Volcanic Zone, New Zealand, reviewed from a geothermal perspective. Geothermics, 59: 167-186.

Wilson, C. J. N. & Walker, G. P. L. (1981). Violence in pyroclastic flow eruptions. In: Tephra Studies (eds. Self, S. and Sparks, R. S. J.), D. Reidel, Dordrecht, Netherlands: 441-448.

Wilson, C. J. N. & Walker, G. P. L., (1982). Ignimbrite depositional facies: the anatomy of a pyroclastic flow. Journal of the Geological Society, London, 139: 581-592.

Wilson, C. J. N. & Walker, G. P. L., (1985). The Taupo eruption, New Zealand I. General aspects. Philosophical Transactions of the Royal Society of London. Series A, Mathematical and Physical Sciences, 314: 199-228.

Wilson, C. J. N., Rogan, A. M., Smith, I. E. M., Northey, D. J., Nairn, I. A., & Houghton, B. F., (1984). Caldera volcanoes of the Taupo volcanic zone, New Zealand. Journal of Geophysical Research, 89: 8463-8484.

Wilson, C. J. N., Houghton, B. F., & Lloyd, E. F., (1986). Volcanic history and evolution of the Maroa-Taupo area, central North Island. In: Late Cenozoic Volcanism in New Zealand (ed Smith, I. E. M.). Royal Society of New Zealand Bulletin, 23: 194-223.

Wilson, C. J. N., Houghton, B. F., McWilliams, M. O., Lanphere, M. A., Weaver, S. D., & Briggs, R. M., (1995). Volcanic and structural evolution of Taupo Volcanic Zone, New Zealand: a review. Journal of Volcanology and Geothermal Research, 68: 1-28.

Wilson, C. J. N., Gravley, D., Leonard, G., & Rowland, J., (2009). Volcanism in the central Taupo Volcanic Zone, New Zealand: tempo, styles and controls. In: Studies in volcanology: the legacy of George Walker (eds Thordarson, T., Larsen, G., Self, S., Rowland, S. and Hoskuldsson, A). Special Publications of IAVCEI, 2: 225-247.

Wilson, G., Wilson, T. M., Deligne, N. I., & Cole, J. W., (2014). Volcanic hazard impacts to critical infrastructure: A review. Journal of Volcanology and Geothermal Research, 286: 148-182.

Wilson, L., (1976). Explosive volcanic eruptions—III. Plinian eruption columns. Geophysical Journal International, 45: 543-556.

Wilson, L., Sparks, R. S. J., Huang, T. C., & Watkins, N. D., (1978). The control of volcanic column heights by eruption energetics and dynamics. Journal of Geophysical Research: Solid Earth, 83: 1829-1836.

Wilson, L., & Walker, G. P. L. (1987). Explosive volcanic eruptions-VI. Ejecta dispersal in plinian eruptions: the control of eruption conditions and atmospheric properties. Geophysical Journal of the Royal Astronomical Society, 89: 657-679.

Wilson, L., Sparks, R. S. J., & Walker, G. P. L., (1980). Explosive volcanic eruptions—IV. The control of magma properties and conduit geometry on eruption column behaviour. Geophysical Journal of the Royal Astronomical Society, 63: 117-148.

Wilson, T. M., Cole, J. W., Stewart, C., Cronin, S. J., & Johnston, D. M. (2011). Ash storms: impacts of wind-remobilised volcanic ash on rural communities and agriculture following the 1991 Hudson eruption, southern Patagonia, Chile. Bulletin of Volcanology, 73: 223-239.

Woodhouse, M. J., Hogg, A. J., Phillips, J. C., & Sparks, R. S. J., (2013). Interaction between volcanic plumes and wind during the 2010 Eyjafjallajökull eruption, Iceland. Journal of Geophysical Research: Solid Earth, 118: 92-109.

Woods, A. W., (1995). The dynamics of explosive volcanic eruptions. Reviews of Geophysics, 33: 495-530.

Woods, A. W., (2010). Turbulent plumes in nature. Annual Review of Fluid Mechanics, 42: 391-412.

Woods, A. W. & Bursik, M. I., (1991). Particle fallout, thermal disequilibrium, and volcanic plumes. Bulletin of Volcanology, 53: 559-570.

Woods, A. W. & Wohletz, K. H., (1991). Dimensions and dynamics of co-ignimbrite eruption columns. Nature, 350: 225-227.

Wright, H. M., Cashman, K. V., Gottesfeld, E. H., & Roberts, J. J., (2009). Pore structure of volcanic clasts: measurements of permeability and electrical conductivity. Earth and Planetary Science Letters, 280: 93-104.

Zenz, F. A. & Othmer, D. F., (1960). Fluidization and Fluid-Particle Systems.: Reinhold, New York.

Zhou, X., Luo, K. H., & Williams, J. J., (2001). Large-eddy simulation of a turbulent forced plume. European Journal of Mechanics-B/Fluids, 20: 233-254.

Appendix A: Exposure Locations

Locations of the 8 studied exposures in WSG84 UTM coordinates, their measured thickness from the base of the Y4-G to top of Y5, number of samples taken and the permits required for access.

Exposure	UTM	East	North	Thickness	# Samples	Permits Required
A	60S	419917	5704781	79cm	10	n/a
B	60S	421445	5705812	180cm	14	Timberlands
C	60S	426988	5707485	35cm	9	Timberlands
D	60S	428674	5706559	199cm	16	Timberlands
E	60S	430455	5710938	82cm	9	n/a
F	60S	427643.9	5704256	120cm	4	Timberlands
G	60S	432428	5714449	206cm	22	Wairakei
H	60S	414727	5715310	192cm	15	n/a
I	60S	419978.3	5704724	n/a	1	n/a

Appendix B: Samples

Samples taken from each exposure with their mid-point cumulative thickness from the base of the Y4-G. The type of deposits refer to those identified throughout this thesis.

Exposure A			Exposure B			Exposure C			Exposure D		
Samples	**Mid Point**	**Deposit Type**	**Samples**	**Mid Point**	**Deposit Type**	**Samples**	**Mid Point**	**Deposit Type**	**Samples**	**Mid Point**	**Deposit Type**
A-1	1.5	Y4-G	B-1	2	Y4-G	C-1	1	Y4-G	D-1	1	Y4-G
A-2	3.75	Y4-G	B-2	6.5	Y4-G	C-2	2.5	Y4-G	D-2	3	Y4-G
A-3	6	Y4-G	B-3	10	Y4-G	C-3	4	Y4-G	D-3	5.75	Y4-G
A-4	8.5	Y4-G	B-4	12	Y5-Base	C-4	6.75	Y4-G	D-4	9.5	Y5-Base
A-5	10.75	Y5-Base	B-5	16.5	Y5-Base	C-5	9.75	Y5-Base	D-5	13	Y5 Fall
A-6	16.5	Type 2 EFU	B-6	20.5	Y5 Fall	C-6	11.5	Y5-Base	D-6	20.5	Y5 Fall
A-7	22.5	Y5 Fall	B-7	24	Y5 Fall	C-7	13	Y5-Base	D-7	37	Y5 Fall
A-8	29	Y5 Fall	B-8	28.5	Y5 Fall	C-8	15.75	Y5 Fall	D-8	58	Y5 Fall
A-9	39	Type 1 EFU	B-9	36	Y5 Fall	C-9	25	Y5 Fall	D-9	75.5	Y5 Fall
A-10	59	Type 1 EFU	B-10	54.5	Type 2 EFU				D-10	94	Y5 Fall
			B-11	75.5	Y5 Fall				D-11	113	Y5 Fall
			B-12	87	Type 1 EFU				D-12	129	Y5 Fall
			B-13	106.5	Y5 Fall				D-13	146	Y5 Fall
			B-14	143	Type 1 EFU				D-14	165.5	Y5 Fall

									D-15	182	Y5 Fall
									D (Y6)	210	Y6 Ig

Exposure E			Exposure G			Exposure H		
Samples	**Mid Point**	**Deposit Type**	**Samples**	**Mid Point**	**Deposit Type**	**Samples**	**Mid Point**	**Deposit Type**
E-1	1.5	Y4-G	G-1	0.5	Y5-Base	H-1	2.5	Y5-Base
E-2	3.75	Y5-Base	G-2	3	Y5 Fall	H-2	15	Y5 Fall
E-3	7.25	Y5 Fall	G-3	6.25	Y5 Fall	H-3	28	Y5 Fall
E-4	13	Y5 Fall	G-4	9.25	Y5 Fall	H-4	33	Y5 Fall
E-5	19	Y5 Fall	G-5	12.25	Y5 Fall	H-5	38.5	Type 2 EFU
E-6	31	Y5 Fall	G-6	16	Y5 Fall	H-6	43.5	Hybrid
E-7	50.75	Y5 Fall	G-7	24.5	Y5 Fall	H-7	55	Type 2 EFU
E-8	66.5	Y5 Fall	G-8	36.5	Y5 Fall	H-8	66.5	Hybrid
E-9	74.25	Y5 Fall	G-9	43.25	Distal Ash	H-9	78	Type 2 EFU
			G-10	46.15	Y5 Fall	H-10	92	Y5 Fall
Exposure F			G-11	49.3	Distal Ash	H-11	102.5	Hybrid
Samples	**Mid Point**	**Deposit Type**	G-12	54.05	Y5 Fall	H-12	111	Hybrid
F (Y4-G)	1	Y4-G	G-13	67.175	Y5 Fall	H-13	124	Type 2 EFU
F-1	85	Y5 Fall	G-14	85.925	Y5 Fall	H-14	160	Type 2 EFU
F-2	100	Type 1 EFU	G-15	105.05	Y5 Fall	H-15	176	Y5 Fall
F-3	115	Y5 Fall	G-16	125.8	Y5 Fall			
			G-17	147.8	Y5 Fall	**Exposure I**		

			G-18	169.8	Y5 Fall	**Samples**	**Mid Point**	**Deposit Type**
			G-19	183.8	Y5 Fall	I-1	n/a	Type 1 EFU
			G-20	191.55	Y5 Fall			
			G-21	198.55	Y5 Fall			
			G-22	202.05	Y5 Fall			

Appendix C: Grain Size Distributions

Grain size distributions of each sample in full phi with mean, sorting, mode, and median measurements included.

Phi	Microns	A-1	A-2	A-3	A-4	A-5	A-6	A-7	A-8	A-9	A-10
-6	**63000**	0.00	0.00	0.00	0.00	0.00	0.00	0.00	0.00	0.00	0.00
-5	**31500**	0.00	0.00	0.00	0.00	0.00	16.30	0.00	3.50	0.00	0.00
-4	**16000**	0.00	0.00	0.00	4.48	11.80	11.55	1.01	42.19	13.75	0.00
-3	**8000**	0.00	0.00	0.00	22.29	16.86	4.35	20.00	32.76	4.23	1.22
-2	**4000**	1.41	0.83	2.55	32.93	18.07	0.21	43.00	13.68	1.62	5.54
-1	**2000**	9.11	6.83	9.68	20.81	10.41	0.62	27.70	3.55	2.93	9.93
0	**1000**	27.59	27.68	27.97	10.85	5.89	1.48	4.78	0.86	4.98	12.32
1	**500**	48.52	47.51	38.40	4.20	4.21	3.15	0.71	0.32	6.85	12.00
2	**250**	8.59	11.06	15.64	1.48	1.96	4.86	0.37	0.27	7.05	8.98
3	**125**	0.00	0.00	0.59	0.17	0.95	4.93	0.36	0.40	7.09	6.40
4	**62.5**	0.00	0.02	0.21	0.33	2.32	8.50	0.51	0.63	11.95	9.17
5	**31.25**	0.18	0.20	0.13	0.44	3.74	8.20	0.42	0.52	11.08	8.11
6	**15.625**	0.89	0.89	0.41	0.54	5.90	9.31	0.37	0.42	10.25	8.44
7	**7.813**	2.19	2.76	2.14	0.89	10.82	16.21	0.50	0.57	12.20	11.69
8	**3.906**	1.24	1.82	1.87	0.46	5.71	8.46	0.24	0.28	5.05	5.16
9	**1.953**	0.26	0.37	0.37	0.10	1.19	1.72	0.05	0.06	0.96	0.97
10	**0.977**	0.03	0.04	0.03	0.01	0.15	0.16	0.00	0.00	0.02	0.05
	Mean	0.40	0.62	0.62	-1.90	0.49	1.68	-2.14	-3.35	2.02	2.37
	Sorting	0.84	1.55	1.29	1.39	4.12	4.24	0.99	1.02	4.07	3.19
	Mode	0.75	0.75	0.75	-2.24	-2.24	6.74	-2.24	-4.24	1.75	-0.24

	Median	0.62	0.65	0.62	-2.14	-1.33	3.32	-2.16	-3.42	3.13	2.00

Phi	Microns	B-1	B-2	B-3	B-4	B-5	B-6	B-7
-6	**63000**	0.00	0.00	0.00	0.00	0.00	0.00	0.00
-5	**31500**	0.00	0.00	0.00	0.00	0.00	0.00	6.30
-4	**16000**	0.00	0.00	0.00	4.57	4.68	0.90	53.26
-3	**8000**	0.00	0.52	1.66	14.13	12.25	24.23	22.90
-2	**4000**	1.73	3.06	16.65	27.92	20.97	34.08	11.06
-1	**2000**	9.99	11.25	31.18	20.74	16.37	25.83	3.64
0	**1000**	33.52	30.38	30.01	15.45	11.41	10.75	1.36
1	**500**	46.88	40.94	15.33	8.57	6.30	2.04	0.39
2	**250**	5.13	10.20	3.92	2.13	2.04	0.26	0.12
3	**125**	0.00	0.12	0.18	0.35	0.60	0.11	0.06
4	**62.5**	0.02	0.06	0.17	0.69	1.58	0.22	0.12
5	**31.25**	0.08	0.05	0.15	0.93	2.77	0.29	0.16
6	**15.625**	0.26	0.19	0.16	1.33	5.30	0.40	0.19
7	**7.813**	1.15	1.40	0.32	2.06	9.94	0.58	0.28
8	**3.906**	1.00	1.50	0.20	0.93	4.81	0.25	0.13
9	**1.953**	0.21	0.30	0.05	0.18	0.90	0.05	0.03
10	**0.977**	0.02	0.03	0.00	0.02	0.08	0.00	0.00
	Mean	0.34	0.35	-0.63	-1.31	0.59	-2.11	-3.63
	Sorting	0.80	0.87	1.27	2.16	3.90	1.05	0.90
	Mode	0.75	0.75	-1.24	-2.24	-0.24	-2.24	-4.24
	Median	0.55	0.55	-0.48	-1.41	-1.13	-2.13	-4.09

Phi	Microns	B-8	B-9	B-10	B-11	B-12	B-13	B-14
-6	**63000**	0.00	0.00	0.00	0.00	0.00	0.00	0.00
-5	**31500**	0.00	0.00	0.00	6.48	7.14	21.44	3.23
-4	**16000**	5.03	30.60	0.00	28.05	35.06	43.39	4.84
-3	**8000**	22.44	26.93	0.86	32.93	7.89	19.16	5.28
-2	**4000**	33.47	22.32	3.04	19.54	3.28	9.06	11.47
-1	**2000**	25.51	11.30	3.76	6.91	1.91	3.26	13.08
0	**1000**	10.60	4.75	7.02	2.80	2.03	1.39	13.28
1	**500**	1.50	1.28	9.47	0.91	3.14	0.58	11.17
2	**250**	0.21	0.33	8.88	0.50	4.47	0.39	7.33
3	**125**	0.14	0.31	7.44	0.38	4.51	0.36	4.41
4	**62.5**	0.22	0.48	13.87	0.51	8.02	0.37	6.35
5	**31.25**	0.22	0.46	12.53	0.40	8.22	0.26	6.71
6	**15.625**	0.21	0.43	12.05	0.24	6.15	0.14	6.22
7	**7.813**	0.29	0.54	14.47	0.23	5.56	0.13	4.92
8	**3.906**	0.13	0.23	5.64	0.10	2.16	0.06	1.48
9	**1.953**	0.03	0.04	0.96	0.02	0.46	0.01	0.24
10	**0.977**	0.00	0.00	0.00	0.00	0.00	0.00	0.00
	Mean	-2.15	-2.89	3.69	-3.22	-0.82	-3.46	0.79
	Sorting	1.14	1.38	2.87	1.10	3.87	0.31	3.45
	Mode	-2.24	-4.24	6.74	-3.24	4.76	-4.24	5.74
	Median	-2.16	-3.14	3.83	-3.26	-3.01	-4.17	-0.04

Phi	Microns	C-1	C-2	C-3	C-4	C-5	C-6	C-7	C-8	C-9
-6	**63000**	0.00	0.00	0.00	0.00	0.00	0.00	0.00	0.00	0.00
-5	**31500**	0.00	0.00	0.00	0.00	0.00	0.00	0.00	26.22	11.59
-4	**16000**	0.00	0.00	0.00	0.00	0.00	2.49	7.95	4.03	23.17

-3	**8000**	0.00	0.00	0.00	3.89	7.60	8.26	10.49	15.25	19.36
-2	**4000**	0.00	0.15	1.54	10.49	14.41	23.19	20.50	19.93	19.66
-1	**2000**	2.30	1.93	5.72	24.56	16.14	23.45	18.10	17.03	13.49
0	**1000**	20.60	14.13	19.75	32.08	14.62	17.95	15.22	10.47	7.87
1	**500**	58.13	51.42	38.80	21.47	9.83	6.91	6.17	2.60	2.24
2	**250**	12.84	24.33	25.86	5.51	4.02	1.94	1.64	0.49	0.29
3	**125**	0.24	0.04	0.37	0.39	0.75	0.62	0.73	0.24	0.10
4	**62.5**	0.40	0.06	0.10	0.33	2.29	1.12	1.23	0.44	0.34
5	**31.25**	0.48	0.18	0.14	0.30	4.56	1.84	1.96	0.51	0.40
6	**15.625**	0.84	0.97	0.81	0.26	8.18	3.58	4.18	0.73	0.42
7	**7.813**	2.31	3.77	3.79	0.42	11.75	5.72	7.66	1.27	0.66
8	**3.906**	1.52	2.52	2.64	0.25	4.83	2.42	3.48	0.64	0.34
9	**1.953**	0.31	0.46	0.44	0.06	0.93	0.44	0.63	0.13	0.07
10	**0.977**	0.03	0.05	0.04	0.01	0.10	0.04	0.06	0.01	0.01
	Mean	0.73	0.88	0.79	-0.32	1.27	-0.53	0.24	-1.95	-2.87
	Sorting	1.27	1.51	1.71	1.19	3.63	2.59	3.71	0.94	1.14
	Mode	0.75	0.75	0.75	-0.24	-1.24	-1.24	-2.24	-2.24	-4.24
	Median	0.73	0.83	0.79	-0.32	-0.09	-1.15	-1.19	-2.38	-3.10

Phi	Microns	D-1	D-2	D-3	D-4	D-5	D-6	D-7
-6	**63000**	0.00	0.00	0.00	0.00	0.00	0.00	0.00
-5	**31500**	0.00	0.00	0.00	0.00	0.00	4.16	2.82
-4	**16000**	0.00	0.00	0.00	3.36	0.00	13.17	9.85
-3	**8000**	0.00	0.00	1.51	8.59	3.70	26.04	20.19
-2	**4000**	0.53	0.25	9.74	20.63	20.22	29.39	23.18
-1	**2000**	0.61	2.21	30.24	20.84	40.50	16.12	21.54
0	**1000**	10.97	8.35	37.19	15.45	27.81	7.46	14.53

1	**500**	53.96	21.47	15.60	5.60	5.48	1.80	5.17
2	**250**	25.38	50.80	3.03	2.28	0.31	0.17	0.56
3	**125**	0.31	1.22	0.46	0.84	0.12	0.07	0.01
4	**62.5**	0.42	0.31	0.16	1.53	0.23	0.18	0.21
5	**31.25**	0.78	0.40	0.13	2.55	0.29	0.25	0.42
6	**15.625**	1.06	1.69	0.19	4.78	0.35	0.31	0.46
7	**7.813**	2.26	6.90	0.64	8.57	0.60	0.52	0.67
8	**3.906**	2.09	5.18	0.69	4.12	0.32	0.27	0.33
9	**1.953**	1.28	1.08	0.35	0.80	0.07	0.06	0.07
10	**0.977**	0.36	0.13	0.07	0.08	0.01	0.01	0.01
	Mean	1.08	1.61	-0.37	0.70	-1.17	-2.52	-1.93
	Sorting	1.36	1.61	1.11	3.56	1.00	1.39	1.56
	Mode	0.75	1.75	-0.24	-1.24	-1.24	-2.24	-2.24
	Median	0.85	1.67	-0.37	-1.08	-1.17	-2.38	-2.13

Phi	Microns	D-8	D-9	D-10	D-11	D-12	D-13	D-14	D-15
-6	**63000**	0.00	0.00	0.00	0.00	0.00	0.00	0.00	0.00
-5	**31500**	6.46	0.79	7.15	23.66	5.86	10.63	6.17	3.24
-4	**16000**	21.22	17.16	29.66	35.71	27.17	28.97	15.14	12.78
-3	**8000**	28.48	29.74	32.45	18.21	37.33	25.56	28.74	15.43
-2	**4000**	23.33	25.88	16.08	12.69	20.33	16.38	22.03	19.38
-1	**2000**	11.89	14.71	7.26	5.31	4.97	9.05	13.19	18.89
0	**1000**	5.31	8.02	4.87	2.55	2.31	5.36	8.65	17.19
1	**500**	1.35	1.88	1.10	0.58	0.63	1.77	3.80	9.45
2	**250**	0.22	0.24	0.16	0.13	0.13	0.25	0.46	2.20
3	**125**	0.14	0.14	0.12	0.12	0.13	0.17	0.21	0.12
4	**62.5**	0.31	0.31	0.26	0.24	0.28	0.37	0.36	0.27

5	**31.25**	0.36	0.37	0.29	0.27	0.31	0.44	0.40	0.32
6	**15.625**	0.33	0.30	0.24	0.21	0.23	0.40	0.34	0.27
7	**7.813**	0.39	0.31	0.25	0.21	0.22	0.45	0.35	0.30
8	**3.906**	0.17	0.13	0.10	0.08	0.09	0.18	0.13	0.12
9	**1.953**	0.03	0.02	0.02	0.02	0.02	0.03	0.02	0.02
10	**0.977**	0.00	0.00	0.00	0.00	0.00	0.00	0.00	0.00
	Mean	-2.89	-2.55	-3.22	-3.25	-3.24	-3.01	-2.74	-2.03
	Sorting	1.30	1.38	1.07	0.29	1.02	1.10	1.49	1.79
	Mode	-3.24	-3.24	-3.24	-4.24	-3.24	-4.24	-3.24	-2.24
	Median	-3.11	-2.44	-3.29	-4.13	-3.26	-3.29	-3.00	-2.02

Phi	Microns	F (Y4-G)	F-1	F-2	F-3
-6	**63000**	0.00	0.00	0.00	0.00
-5	**31500**	0.00	6.98	0.00	14.29
-4	**16000**	0.00	22.96	6.06	28.64
-3	**8000**	0.00	23.40	5.07	27.26
-2	**4000**	0.00	19.95	9.42	15.26
-1	**2000**	0.63	11.14	11.19	7.92
0	**1000**	2.33	6.59	12.57	4.09
1	**500**	20.93	2.90	11.14	0.88
2	**250**	61.31	1.48	8.67	0.30
3	**125**	2.22	1.05	10.22	0.31
4	**62.5**	1.01	1.36	10.46	0.38
5	**31.25**	1.33	1.01	6.92	0.27
6	**15.625**	2.39	0.55	3.92	0.16
7	**7.813**	4.66	0.44	3.11	0.15
8	**3.906**	2.56	0.17	1.11	0.06

9	**1.953**	0.57	0.03	0.13	0.01
10	**0.977**	0.06	0.00	0.00	0.00
	Mean	1.50	-2.79	0.81	-3.29
	Sorting	1.21	1.64	3.03	0.82
	Mode	1.75	-3.24	-0.24	-4.24
	Median	1.71	-3.07	0.75	-3.36

Phi	Microns	E-1	E-2	E-3	E-4	E-5	E-6	E-7	E-8	E-9
-6	**63000**	0.00	0.00	0.00	0.00	0.00	0.00	0.00	0.00	0.00
-5	**31500**	0.00	0.00	0.00	0.00	0.00	0.00	0.00	0.00	0.00
-4	**16000**	0.00	0.00	0.00	0.00	0.00	0.00	0.00	0.00	0.00
-3	**8000**	1.50	2.51	10.33	40.20	15.34	33.15	42.67	70.59	48.72
-2	**4000**	2.03	11.04	15.69	25.58	17.54	20.68	26.28	15.69	28.82
-1	**2000**	8.81	16.72	24.95	18.99	23.09	19.13	16.76	7.71	10.78
0	**1000**	25.10	19.72	25.00	9.70	22.69	15.17	9.64	3.82	5.30
1	**500**	34.62	14.52	13.77	3.32	12.74	8.62	3.41	1.44	2.41
2	**250**	18.78	5.72	3.51	0.32	1.68	1.89	0.38	0.14	0.72
3	**125**	0.58	0.54	0.24	0.17	0.20	0.22	0.16	0.09	0.62
4	**62.5**	0.38	1.87	0.49	0.30	0.65	0.24	0.20	0.16	0.87
5	**31.25**	0.43	3.82	0.67	0.27	0.99	0.21	0.19	0.14	0.72
6	**15.625**	1.04	6.03	1.15	0.29	1.35	0.20	0.11	0.09	0.44
7	**7.813**	3.54	10.51	2.52	0.52	2.31	0.30	0.12	0.08	0.40
8	**3.906**	2.60	5.60	1.39	0.27	1.16	0.15	0.05	0.03	0.17
9	**1.953**	0.55	1.25	0.26	0.05	0.23	0.03	0.01	0.01	0.03
10	**0.977**	0.06	0.17	0.02	0.01	0.02	0.00	0.00	0.00	0.00
	Mean	0.69	1.73	-0.85	-2.20	-0.96	-1.82	-2.23	-2.86	-2.33

	Sorting	1.76	3.33	2.09	1.17	2.07	1.43	1.08	0.80	1.17
	Mode	0.75	-0.24	-0.24	-3.24	-1.24	-3.24	-3.24	-3.24	-3.24
	Median	0.68	0.49	-1.02	-2.30	-1.13	-2.09	-2.35	-3.14	-2.46

Phi	**Microns**	**G-1**	**G-2**	**G-3**	**G-4**	**G-5**	**G-6**	**G-7**	**G-8**	**G-9**	**G-10**	**G-11**
-6	**63000**	0.00	0.00	0.00	0.00	0.00	0.00	0.00	0.00	0.00	0.00	0.00
-5	**31500**	0.00	0.00	0.00	0.00	0.00	0.00	8.52	4.84	0.00	0.00	0.00
-4	**16000**	0.00	0.00	0.00	0.00	0.00	3.14	20.48	16.89	5.57	5.92	4.15
-3	**8000**	0.00	0.06	0.46	10.13	3.37	26.64	34.28	22.65	4.51	19.42	11.40
-2	**4000**	0.53	1.89	12.99	40.75	23.12	31.91	18.76	20.78	4.19	21.90	14.71
-1	**2000**	9.28	33.19	49.30	29.64	37.03	17.10	8.47	15.04	3.34	15.52	11.83
0	**1000**	38.51	47.70	21.63	7.00	19.79	7.62	4.39	9.85	5.85	16.23	13.22
1	**500**	17.61	9.27	6.00	3.02	8.06	3.26	2.04	4.92	7.88	12.71	12.15
2	**250**	3.71	2.10	2.20	1.31	2.12	1.33	0.53	1.26	9.44	3.78	6.25
3	**125**	2.00	0.33	0.31	0.55	1.09	1.86	0.56	0.90	12.29	0.60	1.74
4	**62.5**	2.77	0.55	0.59	0.99	1.32	2.29	0.62	0.92	12.45	0.78	1.79
5	**31.25**	3.04	0.68	0.85	1.15	0.60	1.19	0.37	0.57	8.41	0.50	2.62
6	**15.625**	6.49	0.96	1.35	1.43	0.90	1.22	0.35	0.52	9.52	0.74	5.24
7	**7.813**	10.32	1.94	2.61	2.45	1.57	1.52	0.41	0.57	11.28	1.19	9.50
8	**3.906**	4.69	1.09	1.40	1.28	0.84	0.73	0.19	0.24	4.46	0.59	4.54
9	**1.953**	0.94	0.22	0.28	0.27	0.18	0.17	0.04	0.05	0.77	0.12	0.80
10	**0.977**	0.13	0.02	0.03	0.03	0.02	0.02	0.00	0.00	0.04	0.01	0.07
	Mean	1.74	-0.68	-1.07	-1.81	-1.20	-2.06	-3.31	-2.56	2.45	-1.62	0.82
	Sorting	2.97	1.22	1.69	1.87	1.54	1.94	1.51	1.82	3.54	1.83	3.85
	Mode	-0.24	-0.74	-1.24	-2.24	-1.74	-3.24	-3.74	-3.24	2.74	-3.24	-2.74
	Median	0.07	-0.76	-1.25	-2.02	-1.37	-2.38	-3.46	-2.73	2.78	-1.83	-0.39

Phi	Microns	G-12	G-13	G-14	G-15	G-16	G-17	G-18	G-19	G-20	G-21	G-22
-6	**63000**	0.00	0.00	0.00	0.00	0.00	4.59	0.00	0.00	0.00	0.00	0.00
-5	**31500**	0.00	18.34	10.30	17.36	13.28	20.18	8.87	0.00	17.76	1.30	0.00
-4	**16000**	2.85	28.29	30.05	29.67	25.10	19.21	19.72	14.72	16.98	11.44	5.99
-3	**8000**	19.94	21.90	25.84	25.06	25.02	17.68	23.06	18.67	17.73	17.35	11.49
-2	**4000**	20.22	14.59	17.55	14.92	17.83	16.01	20.93	23.46	15.81	18.68	14.64
-1	**2000**	19.69	8.38	8.57	6.70	8.98	11.12	14.34	20.77	12.95	18.42	17.03
0	**1000**	18.83	5.07	4.61	3.48	5.62	7.07	8.28	14.43	10.42	16.92	20.04
1	**500**	11.49	2.00	1.98	1.82	2.86	3.28	3.91	6.46	6.01	10.60	14.68
2	**250**	3.84	0.38	0.32	0.40	0.59	0.39	0.44	0.84	1.17	3.09	8.33
3	**125**	1.02	0.23	0.18	0.17	0.19	0.12	0.10	0.16	0.28	0.77	2.79
4	**62.5**	0.52	0.26	0.22	0.21	0.25	0.15	0.16	0.21	0.26	0.54	1.53
5	**31.25**	0.34	0.22	0.18	0.12	0.15	0.12	0.13	0.15	0.26	0.38	1.23
6	**15.625**	0.46	0.17	0.11	0.05	0.07	0.03	0.03	0.07	0.19	0.28	1.10
7	**7.813**	0.54	0.12	0.07	0.02	0.04	0.01	0.01	0.04	0.12	0.18	0.85
8	**3.906**	0.22	0.04	0.02	0.01	0.01	0.01	0.01	0.02	0.03	0.05	0.26
9	**1.953**	0.05	0.01	0.00	0.00	0.00	0.00	0.00	0.00	0.01	0.01	0.04
10	**0.977**	0.00	0.00	0.00	0.00	0.00	0.00	0.00	0.00	0.00	0.00	0.00
	Mean	-1.59	-3.62	-3.50	-3.74	-3.39	-3.57	-2.99	-2.27	-2.99	-1.91	-1.03
	Sorting	1.68	1.60	1.46	1.49	1.59	1.90	1.68	1.58	1.96	1.82	2.13
	Mode	-2.24	-4.74	-4.74	-4.74	-4.74	-4.74	-3.74	-2.24	-5.24	-2.24	-0.74
	Median	-1.64	-3.86	-3.67	-3.89	-3.55	-3.68	-3.07	-2.27	-3.15	-1.93	-0.96

Phi	Microns	H-1	H-2	H-3	H-4	H-5	H-6	H-7	H-8	H-9
-6	**63000**	0.00	0.00	0.00	0.00		0.00	0.00	0.00	0.00
-5	**31500**	1.39	16.21	1.03	21.12	0.00	0.00	0.00	0.00	1.11
-4	**16000**	6.20	21.31	14.47	21.35	0.00	0.00	0.10	0.00	3.42

-3	**8000**	11.16	26.28	23.50	13.19	0.64	0.84	0.95	6.43	3.15
-2	**4000**	16.65	18.78	24.46	10.98	1.96	4.46	2.52	19.80	2.98
-1	**2000**	13.94	7.93	16.84	7.35	3.14	15.51	5.52	16.88	3.35
0	**1000**	10.61	4.47	9.41	6.94	5.97	18.72	9.70	14.17	5.31
1	**500**	5.81	2.06	4.37	5.30	8.02	14.04	10.82	8.66	6.65
2	**250**	4.17	0.74	1.82	4.05	9.31	13.51	10.30	9.16	7.48
3	**125**	3.04	0.32	0.79	2.64	11.69	10.50	7.78	7.16	9.02
4	**62.5**	4.85	0.45	0.81	2.89	17.65	8.07	13.97	6.82	14.41
5	**31.25**	5.03	0.40	0.56	1.71	15.71	5.35	11.56	4.18	12.54
6	**15.625**	5.41	0.34	0.57	0.92	12.35	3.48	9.43	2.74	11.29
7	**7.813**	7.47	0.45	0.89	0.98	9.92	3.75	11.55	2.70	13.17
8	**3.906**	3.46	0.21	0.41	0.46	3.17	1.54	4.90	1.10	5.20
9	**1.953**	0.73	0.04	0.07	0.09	0.47	0.22	0.89	0.19	0.91
10	**0.977**	0.08	0.00	0.00	0.00	0.00	0.00	0.00	0.00	0.00
	Mean	0.56	-3.20	-2.01	-2.07	3.36	1.16	3.04	0.24	3.15
	Sorting	3.77	1.19	1.72	1.88	2.46	2.46	2.83	2.69	3.22
	Mode	-0.24	-3.24	-2.24	-2.24	1.75	-0.24	0.75	-1.24	3.73
	Median	-0.46	-3.25	-2.27	-3.21	3.53	0.87	3.17	-0.25	3.53

Phi	**Microns**	**H-10**	**H-11**	**H-12**	**H-13**	**H-14**	**H-15**		**Phi**	**Microns**	**I-1**
-6	**63000**	0.00	0.00	0.00	0.00	0.00	0.00		**-6**	**63000**	0.00
-5	**31500**	2.28	0.00	0.00	0.00	0.00	3.35		**-5**	**31500**	0.00
-4	**16000**	17.21	0.00	0.74	0.77	1.16	17.88		**-4**	**16000**	3.61
-3	**8000**	16.08	1.10	1.97	1.45	0.48	27.63		**-3**	**8000**	6.89
-2	**4000**	16.75	5.37	0.12	1.60	0.39	20.11		**-2**	**4000**	8.77
-1	**2000**	10.61	12.80	24.40	2.66	0.91	9.25		**-1**	**2000**	9.19
0	**1000**	8.36	16.12	17.99	3.90	2.25	4.66		**0**	**1000**	10.02

1	**500**	6.04	13.59	12.53	5.33	4.63	2.50		**1**	**500**	9.37
2	**250**	6.41	13.11	13.42	6.41	7.20	3.40		**2**	**250**	7.78
3	**125**	4.05	8.29	10.49	9.26	8.24	2.66		**3**	**125**	5.61
4	**62.5**	4.36	10.25	7.02	17.75	16.31	2.83		**4**	**62.5**	8.65
5	**31.25**	2.82	6.91	4.51	16.05	17.05	1.90		**5**	**31.25**	7.01
6	**15.625**	1.86	5.18	2.70	12.53	15.82	1.40		**6**	**15.625**	6.87
7	**7.813**	2.09	5.11	2.78	14.72	17.47	1.62		**7**	**7.813**	10.38
8	**3.906**	0.92	1.87	1.15	6.35	6.81	0.70		**8**	**3.906**	4.89
9	**1.953**	0.17	0.30	0.17	1.21	1.27	0.13		**9**	**1.953**	0.91
10	**0.977**	0.00	0.00	0.00	0.00	0.00	0.00		**10**	**0.977**	0.05
	Mean	-1.37	1.61	0.92	3.98	4.30	-1.96			**Mean**	1.99
	Sorting	2.97	2.68	2.20	2.51	2.25	2.55			**Sorting**	3.82
	Mode	-2.24	-0.24	-1.24	3.73	5.74	-3.24			**Mode**	6.74
	Median	-2.07	1.52	0.69	4.04	4.46	-2.46			**Median**	1.27

Appendix D: Exposure D Full Componentry

Weighted percent measurements of the components in each sample from Exposure D with the total wt.% in the whole sample grain size and the wt.% in each full phi grain size from -4 to 2 ϕ.

Total wt.% of Components in Whole Sample: Exposure D										
Sample	**J1**	**J2**	**J3**	**J4**	**G**	**F1**	**F2**	**F3**	**C**	**CP**
D-15	10.73152	12.30211	7.621009	0.18785	0.739249	42.74946	12.81944	2.712012	9.761365	0.375979
D-14	38.92777	29.02749	11.24828	0.131929	0.245715	8.607581	3.494109	0.394045	6.741677	1.181397
D-13	32.66199	23.98617	16.83217	0.289474	0.023429	18.0521	2.521453	1.033682	3.110202	1.489327
D-12	41.46064	30.49671	17.61879	0.139263	0.010933	5.014505	1.596582	0.531011	1.975821	1.155755
D-11	39.67197	34.60066	3.631808	0.008903	0.036118	14.46517	1.15726	0.39635	1.955003	4.07676
D-10	41.57528	27.18887	10.27435	0.045678	0.035984	11.28738	2.545041	0.256145	3.672335	3.11893
D-9	43.1288	22.987	13.47651	0.240876	0.185071	10.92111	4.796287	0.326951	3.275631	0.661757
D-8	49.78486	18.56906	6.165676	0.295207	0.122149	15.03506	4.785541	1.294442	2.995807	0.952193
D-7	33.93402	22.32031	5.401128	0.230108	0.713133	24.3003	5.283128	1.134605	5.390643	1.292619
D-6	36.953	20.75867	2.030452	0.184412	0.336421	26.10751	10.6945	0.447385	2.487649	0
D-5	11.78846	12.42634	1.466601	0.10555	0.774469	44.44154	18.36948	1.029752	9.046775	0.551029
D-4	20.23086	13.01622	2.518958	0	2.369709	32.42958	23.59337	1.197933	4.643366	0
D-3	6.314334	17.6408	0.428589	0	34.23638	33.65412	4.804575	0.562179	2.359025	0
D-2	0.525647	16.04371	0.552511	0.023854	29.6361	42.17588	5.574115	0.659149	4.80904	0
D-1	2.369462	10.61953	0	0	26.82356	51.32628	4.85533	0.761375	3.244467	0
wt.% of Components in -4 phi: Exposure D										
Sample	**J1**	**J2**	**J3**	**J4**	**G**	**F1**	**F2**	**F3**	**C**	**CP**
D-15	22.67307	20.09607	21.56541	1.141565	0	25.5948	8.929076	0	0	0

D-14	67.02886	21.06282	7.944747	0.571881	0	0	3.391695	0	0	0
D-13	45.83798	22.8134	20.44055	0	0	10.90808	0	0	0	0
D-12	44.29308	43.50347	11.18264	0	0	0	0	0	0	1.020807
D-11	37.49605	48.07284	0	0	0	4.296611	0	0	0	10.13449
D-10	53.66986	27.11449	8.856186	0	0	4.937099	0	0	0	5.42237
D-9	59.67734	24.60648	9.861227	0	0	0	4.516256	0	0	1.338695
D-8	52.68728	31.9778	5.973048	0	0	7.340468	0	0	0	2.021403
D-7	63.99405	12.94485	6.245569	0	0	11.08748	0	0	0	5.728059
D-6	76.19481	23.80519	0	0	0	0	0	0	0	0
D-5	0	0	0	0	0	0	0	0	0	0
D-4	71.64948	28.35052	0	0	0	0	0	0	0	0
D-3	0	0	0	0	0	0	0	0	0	0
D-2	0	0	0	0	0	0	0	0	0	0
D-1	0	0	0	0	0	0	0	0	0	0
wt.% of Components in -3 phi: Exposure D										
Sample	**J1**	**J2**	**J3**	**J4**	**G**	**F1**	**F2**	**F3**	**C**	**CP**
D-15	27.49274	11.19745	5.519146	0.084262	0.402584	42.17302	13.13079	0	0	0
D-14	52.59126	34.10627	4.826089	0	0	7.185874	0.44246	0.319554	0	0.528494
D-13	41.03119	28.73881	7.382751	0.186399	0	18.92621	2.496422	0.242985	0	0.99524
D-12	42.2741	33.1033	20.15851	0	0	0.749407	0.927324	0.620013	0	2.16735
D-11	32.11042	50.25921	5.0689	0	0	10.45239	1.231778	0	0	0.87731
D-10	42.7396	33.51413	10.46656	0	0	10.09883	0.914732	0	0	2.266146
D-9	66.28698	19.00016	8.938459	0	0	4.350577	0.437694	0	0	0.986131
D-8	94.57152	1.923403	1.185171	0.056085	0	1.761235	0.157385	0.026955	0	0.318248
D-7	54.75352	22.21417	3.048191	0	0	14.5747	2.223143	0.845761	0	2.340514
D-6	49.37834	16.37913	3.388609	0	0	25.00459	5.341801	0.507522	0	0
D-5	8.379888	0	0	0	0	91.62011	0	0	0	0
D-4	60.364	9.571958	0	0	0	14.69498	15.36906	0	0	0

D-3	48.9726	0	0	0	0	51.0274	0	0	0	0
D-2	0	0	0	0	0	0	0	0	0	0
D-1	0	0	0	0	0	0	0	0	0	0
wt.% of Components in -2 phi: Exposure D										
Sample	**J1**	**J2**	**J3**	**J4**	**G**	**F1**	**F2**	**F3**	**C**	**CP**
D-15	9.372129	9.862175	10.38285	0.122511	0	55.13017	14.11945	0	0	1.01072
D-14	29.62612	28.91623	24.1363	0	0	7.288216	6.720303	0.425935	0	2.886891
D-13	20.92511	24.20154	17.95154	1.349119	0	26.18392	3.854626	4.129956	0	1.404185
D-12	29.8691	24.43475	28.48076	0.634669	0	11.78104	3.887346	0.753669	0	0.158667
D-11	30.10427	28.65792	16.17894	0	0	21.56071	1.547259	0.739993	0	1.210898
D-10	27.21207	30.75138	13.60603	0	0	17.60952	6.034233	0.870322	0	3.916449
D-9	30.79594	26.30876	24.25214	0.026709	0	11.24466	6.169872	0.801282	0	0.400641
D-8	28.41996	20.22239	14.35221	1.137833	0	22.05844	8.223429	4.344453	0	1.241272
D-7	30.95698	28.17786	8.047366	0.241663	0.77332	26.63122	4.180764	0.362494	0	0.628323
D-6	24.2755	28.41551	2.371095	0.451637	0	27.43696	17.0493	0	0	0
D-5	14.69388	16.53061	4.693878	0.306122	0.510204	41.12245	22.14286	0	0	0
D-4	19.64234	16.87338	5.422556	0	2.394001	35.59273	18.97894	1.096048	0	0
D-3	13.02056	16.76331	0	0	28.62414	37.79652	2.95203	0.843437	0	0
D-2	0	16.94915	0	0	47.45763	35.59322	0	0	0	0
D-1	0	53.84615	0	0	0	46.15385	0	0	0	0
wt.% of Components in -1 phi: Exposure D										
Sample	**J1**	**J2**	**J3**	**J4**	**G**	**F1**	**F2**	**F3**	**C**	**CP**
D-15	6.407792	9.996155	4.741766	0.012816	0.025631	55.23517	11.40587	11.53403	0.384468	0.256312
D-14	29.19255	26.86335	16.92547	0.15528	0.15528	19.25466	2.484472	0.310559	2.329193	2.329193
D-13	10.76159	33.27815	12.91391	0	0.165563	34.10596	6.622517	1.15894	0.827815	0.165563
D-12	21.22241	17.14771	19.35484	0.169779	0.169779	32.93718	5.602716	2.207131	0.848896	0.339559
D-11	20.03311	32.28477	10.09934	0.165563	0.496689	22.18543	8.940397	0.165563	3.807947	1.821192

D-10	19.66874	28.36439	7.867495	0.621118	0.207039	29.39959	9.937888	0.207039	2.277433	1.449275
D-9	19.53255	25.04174	11.5192	1.502504	0.166945	32.55426	8.180301	0.166945	1.168614	0.166945
D-8	15.67944	13.70499	8.478513	0	0.929152	40.65041	16.60859	1.277584	1.858304	0.813008
D-7	21.72897	31.54206	6.308411	0.46729	0.700935	31.54206	5.607477	1.869159	0	0.233645
D-6	11.40684	23.70089	1.774398	0.253485	1.013942	46.38783	14.32193	1.013942	0.126743	0
D-5	18.87179	15.79487	0.410256	0.102564	0.205128	45.64103	16.20513	1.435897	0	1.333333
D-4	14.84018	9.589041	2.739726	0	1.826484	43.15068	25.11416	2.625571	0.114155	0
D-3	8.66426	22.92419	0.180505	0	37.54513	27.43682	3.068592	0.180505	0	0
D-2	1.308411	29.34579	0.747664	0	40.93458	26.16822	1.308411	0.186916	0	0
D-1	6.666667	66.66667	0	0	0	20	6.666667	0	0	0
wt.% of Components in 0 phi: Exposure D										
Sample	**J1**	**J2**	**J3**	**J4**	**G**	**F1**	**F2**	**F3**	**C**	**CP**
D-15	2.221753	3.971007	4.825527	0	0.88468	45.27651	18.09271	1.736184	22.25774	0.733882
D-14	7.936371	12.82162	8.911114	0.259547	2.001396	19.3922	7.472647	1.667445	38.79363	0.744035
D-13	5.575895	9.268903	3.80216	0.27743	0.063673	35.6116	8.833655	2.510972	34.05571	0
D-12	3.907301	2.918875	1.600973	0	0.102091	23.9603	5.98903	1.245974	60.04344	0.232025
D-11	3.146057	5.324342	1.220095	0	0.277875	20.99139	8.580591	10.96595	49.4937	0
D-10	2.804921	3.71215	2.189003	0	0.391191	27.52817	8.795133	1.702096	52.87733	0
D-9	20.03889	17.50925	11.23235	0.103828	1.680133	18.76746	9.074605	0.440799	21.15268	0
D-8	2.21343	3.628885	0.921471	0.161495	0.104497	46.21746	9.174809	1.740345	35.28663	0.550983
D-7	6.859408	17.26284	5.153024	0.457294	1.266026	37.51503	10.48854	2.363108	18.41455	0.220179
D-6	3.15272	9.577281	1.425474	0.103238	1.854308	41.35543	20.31202	1.337722	20.88181	0
D-5	1.811922	7.640273	0.905961	0	1.63073	43.47205	21.97963	1.380081	21.17936	0
D-4	3.451068	12.03872	0.889839	0	3.620561	34.062	35.57755	0.426087	9.93418	0
D-3	2.596231	16.13844	0.396035	0	33.38357	37.80156	6.836008	0.119911	2.728243	0
D-2	1.936553	20.48828	0.715847	0.233592	30.28031	39.6692	5.240751	0.546304	0.889157	0
D-1	19.37984	10.80078	0	0	32.56006	30.59515	5.443669	1.008906	0.211591	0

wt.% of Components in 1 phi: Exposure D										
Sample	**J1**	**J2**	**J3**	**J4**	**G**	**F1**	**F2**	**F3**	**C**	**CP**
D-15	0.133076	0.931532	1.264223	0	4.890545	31.87171	14.04285	1.620201	45.24586	0
D-14	1.557401	1.965292	1.779887	0	1.223673	13.80896	8.157817	0.385642	71.12133	0
D-13	2.373214	5.417118	2.321622	0	0.257958	21.93675	5.329412	1.90373	60.41376	0.046432
D-12	3.864379	3.174311	3.174311	0	0	12.71565	3.37213	0.092009	73.60721	0
D-11	3.62688	4.890175	3.91214	0	0	7.062227	4.47451	1.581157	74.45291	0
D-10	2.223143	3.692679	2.223143	0	0.113041	8.349976	6.202193	1.269829	75.926	0
D-9	0.978043	1.515967	1.418162	0.044012	1.173652	12.9933	11.92234	2.714069	67.24045	0
D-8	1.529465	2.294197	1.979307	0	0	19.56815	15.57355	0.350877	58.70445	0
D-7	3.115019	3.864201	1.498364	0.039431	3.351603	22.12058	18.42987	1.880841	45.70009	0
D-6	3.398567	5.211136	1.246141	0	1.501034	27.58503	13.67923	2.347843	45.03101	0
D-5	2.276647	4.415316	1.103829	0	2.035185	22.70783	14.63263	0.70714	52.12142	0
D-4	3.534996	9.342491	0.656499	0	3.888496	24.99243	28.40117	1.055449	28.12847	0
D-3	2.473564	14.28483	1.113104	0	37.24569	31.27821	5.114093	2.244759	6.245749	0
D-2	0	15.27967	1.546157	0	30.19554	45.12051	4.674852	0	3.183265	0
D-1	0	12.40594	0	0	28.13369	52.69473	3.64721	1.084672	2.03376	0
wt.% of Components in 2 phi: Exposure D										
Sample	**J1**	**J2**	**J3**	**J4**	**G**	**F1**	**F2**	**F3**	**C**	**CP**
D-15	0.568485	0.550719	2.025227	0	2.185113	19.86143	6.271096	1.936401	66.60153	0
D-14	5.522209	7.643057	14.40576	0	0.240096	8.123249	5.602241	0.280112	58.18327	0
D-13	7.975142	25.94511	11.70378	0	0	5.126877	14.44847	0.31072	34.4899	0
D-12	7.490145	17.87122	18.06833	0	0	4.336399	1.379763	0.459921	50.39422	0
D-11	12.31471	30.67275	20.29647	0	2.052452	0.114025	2.736602	0	31.813	0
D-10	8.962494	23.67267	8.962494	0	0.146128	1.607404	18.65563	0.730638	37.26254	0
D-9	8.5195	13.47974	5.831125	0	0.302916	2.271867	28.13328	1.514578	39.94699	0
D-8	5.584364	15.15756	9.812525	0	1.954527	7.219785	32.18987	0.678101	27.20383	0.199442
D-7	1.186094	7.93456	0.654397	0	1.840491	32.10634	11.90184	2.167689	42.20859	0

D-6	3.984064	16.49402	1.2749	0	1.115538	19.04382	24.42231	1.23506	32.43028	0
D-5	0	24.15699	3.233831	0	2.62576	11.08347	16.0586	1.713654	41.12769	0
D-4	2.28025	15.55719	3.052593	0	7.429202	27.47334	24.1633	0.919456	19.12468	0
D-3	5.376838	11.67279	1.470588	0	30.97426	35.20221	3.860294	0.505515	10.9375	0
D-2	0.483304	15.02636	0.087873	0	28.69069	42.06942	6.239016	0.988576	6.414763	0
D-1	0	4.491609	0	0	22.7542	58.24284	7.230997	0	7.280355	0

Appendix E: 1 phi Componentry

Point counted number percent of components in each sample from the 8 studied exposures in the 1 phi grain size.

num% of Components in 1 phi: Exposure A							
Sample	**J**	**G**	**F1**	**F2**	**F3**	**C**	**CP**
A-1	24.89627	10.78838	55.60166	1.244813	6.639004	0.829876	0
A-2	30.17456	19.70075	41.64589	3.491272	2.244389	2.743142	0
A-3	32.09169	17.19198	40.68768	5.730659	2.005731	2.292264	0
A-4	26.57534	14.24658	40.27397	12.60274	0.821918	5.479452	0
A-5	45.54295	2.269044	21.88006	20.25932	0.810373	9.23825	0
A-6	80.36072	2.004008	10.82164	3.206413	0.400802	3.206413	0
A-7	58.06988	0.831947	9.983361	13.31115	0.998336	16.80532	0
A-8	66.00567	1.133144	7.082153	5.665722	0.849858	19.26346	0
A-9	78.00338	1.184433	7.106599	3.553299	1.353638	8.460237	0.338409
A-10	73.5119	1.190476	10.71429	4.166667	1.785714	8.630952	0
num% of Components in 1 phi: Exposure B							
Sample	**J**	**G**	**F1**	**F2**	**F3**	**C**	**CP**
B-1	23.7721	17.68173	53.43811	1.375246	2.1611	1.571709	0
B-2	25.44529	18.82952	47.83715	3.307888	1.017812	3.562341	0
B-3	28.79377	26.45914	33.85214	6.614786	0.77821	3.501946	0
B-4	23.49869	15.4047	46.73629	13.05483	0.522193	0.78329	0
B-5	42.85714	1.930502	27.41313	14.67181	0	13.12741	0
B-6	28.49162	1.675978	37.05773	10.42831	1.489758	20.85661	0
B-7	44.55446	1.320132	13.53135	11.55116	2.310231	26.73267	0
B-8	32.04633	0.3861	18.14672	13.89961	5.405405	30.11583	0
B-9	35.49784	0	17.31602	6.493506	3.463203	37.22944	0
B-10	76.37475	0.610998	6.720978	3.869654	1.425662	10.7943	0.203666
B-11	54.25791	0.729927	13.13869	14.59854	1.459854	15.32847	0.486618
B-12	68.68557	1.159794	12.5	10.56701	2.448454	4.639175	0
B-13	84.4098	0.222717	2.227171	2.227171	0	10.91314	0
B-14	54.06562	3.281027	14.9786	6.134094	2.56776	18.9729	0
num% of Components in 1 phi: Exposure C							
Sample	**J**	**G**	**F1**	**F2**	**F3**	**C**	**CP**
C-1	15.16966	20.95808	55.28942	4.391218	1.197605	2.994012	0
C-2	25.41353	26.76692	42.55639	2.857143	0.601504	1.804511	0
C-3	17.5644	24.82436	49.8829	3.981265	1.639344	2.107728	0
C-4	28.34821	27.45536	33.03571	3.571429	1.785714	5.803571	0
C-5	35.01326	5.570292	19.3634	21.75066	2.65252	15.64987	0
C-6	35.66265	0.963855	25.06024	20.48193	2.168675	15.66265	0

C-7	34.93282	0.383877	22.26488	13.81958	1.919386	26.67946	0
C-8	28.09735	0.663717	22.34513	16.59292	2.654867	29.64602	0
C-9	19.39587	3.338633	28.93482	17.32909	4.292528	26.70906	0
num% of Components in 1 phi: Exposure D							
Sample	**J**	**G**	**F1**	**F2**	**F3**	**C**	**CP**
D-1	12.10046	28.53881	51.82648	4.3379	1.369863	1.826484	0
D-2	24.93075	32.68698	36.28809	4.155125	0	1.939058	0
D-3	26.19048	28.57143	29.59184	6.122449	2.380952	7.142857	0
D-4	32.78302	3.537736	19.10377	27.35849	0.471698	16.74528	0
D-5	19.13747	2.425876	20.75472	16.98113	0.808625	39.89218	0
D-6	23.81853	1.512287	25.70888	15.31191	3.024575	30.62382	0
D-7	19.8044	3.178484	22.00489	17.11491	2.200489	35.69682	0
D-8	21.4876	0	17.35537	18.4573	0.550964	42.14876	0
D-9	19.09722	1.041667	12.15278	16.66667	1.736111	49.30556	0
D-10	36.43617	0.265957	7.180851	6.648936	1.329787	48.1383	0
D-11	48.84793	0	4.37788	5.069124	1.382488	40.32258	0
D-12	37.31343	0	9.552239	3.283582	0.597015	49.25373	0
D-13	33.00654	0.326797	15.35948	5.555556	1.633987	43.79085	0.326797
D-14	20.28986	1.207729	12.56039	7.971014	0.724638	57.24638	0
D-15	6.079665	5.24109	30.18868	15.72327	1.677149	41.09015	0
num% of Components in 1 phi: Exposure E							
Sample	**J**	**G**	**F1**	**F2**	**F3**	**C**	**CP**
E-1	30.92784	21.99313	37.1134	3.092784	1.37457	5.498282	0
E-2	32.88591	4.026846	34.22819	15.77181	2.348993	10.73826	0
E-3	32.48408	2.123142	18.89597	21.23142	1.910828	22.92994	0.424628
E-4	16.59836	1.02459	29.09836	19.05738	1.02459	33.19672	0
E-5	31.55963	3.119266	26.42202	16.69725	1.284404	20.91743	0
E-6	44.84848	1.212121	13.33333	13.93939	2.121212	24.54545	0
E-7	29.90431	0.478469	13.8756	11.24402	2.15311	41.86603	0.478469
E-8	15.17241	0.45977	11.95402	11.03448	2.068966	59.08046	0.229885
E-9	21.42857	1.691729	11.84211	9.774436	0.75188	54.32331	0.18797
num% of Components in 1 phi: Exposure F							
Sample	**J**	**G**	**F1**	**F2**	**F3**	**C**	**CP**
F (Y4-G)	24.7191	27.24719	42.41573	2.808989	1.123596	1.685393	0
F-1	59.44206	0.429185	7.51073	4.077253	0.643777	27.897	0
F-2	86.05042	0	4.201681	0.504202	0.168067	9.07563	0
F-3	42.32365	1.037344	11.82573	7.676349	1.86722	35.26971	0
num% of Components in 1 phi: Exposure G							
Sample	**J**	**G**	**F1**	**F2**	**F3**	**C**	**CP**
G-1	33.22684	2.875399	29.71246	23.00319	0.638978	10.54313	0
G-2	31.06796	1.618123	27.83172	25.56634	0.970874	12.94498	0

G-3	44.16244	2.538071	13.70558	22.84264	0.507614	16.24365	0
G-4	40.67278	0.611621	16.20795	25.68807	1.529052	15.29052	0
G-5	30.99174	2.066116	17.35537	26.03306	0.826446	22.72727	0
G-7	42.7451	0.784314	22.35294	15.68627	0.392157	18.03922	0
G-9	71.65775	3.475936	8.823529	5.080214	1.069519	9.893048	0
G-11	56.47383	3.856749	20.11019	7.438017	1.101928	10.7438	0.275482
G-13	37.00306	1.529052	17.12538	5.810398	1.529052	37.00306	0
G-15	35.30752	0	19.36219	8.428246	0.911162	35.07973	0.911162
G-17	18.5336	1.01833	20.77393	5.702648	2.03666	51.93483	0
G-19	17.07746	1.584507	20.59859	5.809859	1.93662	52.99296	0
G-21	56.61157	4.958678	28.09917	7.438017	2.479339	0.413223	0

Appendix F: Pycnometry

The bulk density measurements using pycnometry for pumices 4 – 8 mm from the J1, J2 and J3 pumice types.

J1 (4-8mm)		J2 (4-8mm)		J3 (4-8mm)	
Clast #	Density	Clast #	Density	Clast #	Density
1	0.4491	1	0.6476	1	0.686
2	0.3034	2	0.7967	2	0.8191
3	0.5377	3	0.2691	3	0.6026
4	0.3874	4	0.916	4	0.6393
5	0.3651	5	0.4446	5	0.493
6	0.3837	6	0.6243	6	0.6916
7	0.6972	7	0.5672	7	0.583
8	0.98847	8	0.8002	8	0.644
9	0.4954	9	0.4191	9	0.8499
10	0.3354	10	0.6046	10	0.8683
11	0.6507	11	0.6932	11	0.7664
12	0.5593	12	0.8134	12	1.0078
13	0.5102	13	0.7639	13	0.5019
14	0.5988	14	0.7644	14	0.6444
15	0.508	15	0.5745	15	0.6551
16	0.5347	16	0.6474	16	0.8344
17	0.7605	17	0.7161	17	0.5598
18	0.6873	18	1.0141	18	0.589
19	0.5779	19	0.045	19	0.4277
20	0.6802	20	0.6197	20	0.5634
21	0.4961	21	0.4699	21	0.5684
22	0.7883	22	0.6114	22	0.7205
23	0.691	23	0.49	23	0.5244
24	0.5657	24	0.6237	24	0.5573
25	0.6808	25	0.6391	25	0.4164
26	0.6068	26	0.8568	26	1.3523
27	0.5302	27	0.4743	27	0.5923
28	0.4163	28	0.6643	28	0.7802
29	0.4728	29	0.6395	29	0.6447
30	0.4468	30	0.708	30	0.9182
31	0.54	31	0.5995	31	0.433
32	0.9037	32	0.6923	32	0.6727
33	0.6279	33	0.437	33	0.6222
34	0.5925	34	0.5006	34	0.9251
35	0.3538	35	0.5351	35	0.6336
36	0.4341	36	0.6185	36	0.9752

37	0.7181	37	0.6042	37	0.4823
38	0.65	38	0.6125	38	0.9991
39	0.7209	39	0.6665	39	0.648
40	0.5991	40	0.695	40	0.6972
41	0.6102	41	0.4964	41	0.6625
42	0.6542	42	0.8158	42	0.7989
43	0.6798	43	0.6533	43	0.6947
44	0.4892	44	0.7029	44	0.7052
45	0.5721	45	0.548	45	0.7174
46	0.4588	46	0.7237	46	0.8116
47	0.4396	47	0.1353	47	0.4308
48	0.5106	48	0.5859	48	0.8028
49	0.3749	49	0.5473	49	0.5191
50	0.4809	50	0.7128	50	0.5384
51	0.3578	51	0.5591	51	0.8551
52	0.6467	52	0.8125	52	1.0805
53	0.6529	53	0.4219	53	0.4369
54	0.6576	54	0.9596	54	0.7125
55	0.5137	55	0.4923	55	0.6674
56	0.5099	56	0.7386	56	0.6904
57	0.4182	57	0.395	57	0.5494
58	0.6666	58	0.575	58	0.5951
59	1.1723	59	0.6049	59	0.6117
60	0.6286	60	0.7177	60	0.6223
61	0.4151	61	0.6301	61	0.5291
62	0.6647	62	0.9272	62	0.6313
63	0.6633	63	0.4467	63	0.4864
64	0.4436	64	0.6056	64	0.9081
65	0.5914	65	0.7141	65	0.5273
66	0.5561	66	0.7394	66	0.6366
67	0.4857	67	0.515	67	0.5378
68	0.6615	68	0.6936	68	0.6851
69	0.6238	69	0.6843	69	0.6842
70	0.5185	70	0.7204	70	0.7463
71	0.5021	71	0.5882	71	0.619
72	0.9414	72	0.7056	72	0.9621
73	0.4608	73	0.424	73	0.7175
74	0.5865	74	0.4509	74	0.7625
75	0.7024	75	0.5319	75	0.6564
76	0.7531	76	0.6808	76	0.6621
77	0.6922	77	0.485	77	0.5586
78	0.6023	78	0.7995	78	0.7041
79	0.5244	79	0.452	79	0.5454
80	0.5047	80	0.7956	80	0.6257
81	0.5823	81	0.6971	81	0.5544
82	0.5377	82	0.7772	82	0.6626

83	0.4364	83	0.5038	83	0.6504
84	0.7056	84	0.5939	84	0.8243
85	0.4785	85	0.5832	85	0.5558
86	0.4957	86	0.5936	86	0.7298
87	0.8017	87	0.5416	87	0.7109
88	0.6034	88	0.5699	88	0.7173
89	0.6699	89	0.55	89	0.5839
90	0.5458	90	0.6189	90	0.5954
91	0.5562	91	0.4581	91	0.555
92	0.609	92	0.6325	92	0.6489
93	0.8531	93	0.4476	93	0.5472
94	0.7352	94	0.6621	94	0.7542
95	0.6447	95	0.5284	95	0.7442
96	0.744	96	0.5697	96	0.6045
97	0.9593	97	0.5926	97	0.5187
98	0.5282	98	0.6655	98	0.6625
99	0.6774	99	0.5625	99	0.5608
100	0.6467	100	0.5875	100	0.6278
101	0.7556	101	0.5294	101	0.625
102	0.616	102	0.7171	102	0.5017
103	0.7029	103	0.5367	103	0.6026
104	0.5823	104	0.5813	104	0.5886
105	0.5571	105	0.531	105	0.6473
106	0.4833			106	0.5455
107	0.7307			107	0.6819
108	0.5018			108	0.6347
109	0.4517			109	0.6275
110	0.6422			110	0.683
111	0.6166			111	0.6765
112	0.7346			112	0.5879
113	0.4838			113	0.5632
114	0.6022			114	0.7732
115	0.6806			115	0.4874
116	0.4866			116	0.6164
117	0.4145			117	0.642
118	0.9898			118	0.5439
119	0.5887			119	0.6216
120	0.4937			120	0.4791
121	0.606			121	0.4146
122	0.757			122	0.6041
123	0.6607				
124	0.7381				
125	0.644				
126	0.8205				
127	0.7273				
128	0.5518				

129	0.7823				
130	0.6234				
131	0.6037				
132	0.7375				
133	0.7333				
134	0.7488				
135	0.5353				
136	0.691				
137	0.6407				
138	0.3311				
139	0.5314				
140	0.6218				
141	0.6036				
142	0.7311				
143	0.5407				
144	0.661				
145	0.7481				
146	0.7024				
147	0.5068				
148	0.9738				
149	0.6272				
150	0.5503				
151	0.8463				
152	0.9845				
153	0.8976				
154	0.6802				
155	0.4207				
156	0.618				
157	0.7237				
158	0.5579				
159	0.7109				
160	0.8849				
161	0.4683				
162	0.5248				
163	0.5305				
164	0.4516				
165	0.5131				
166	0.5357				
167	0.6289				
168	0.6403				
169	0.5175				
170	0.7013				

Appendix G: Porosity

Measurements of connected porosity (ϕ_{conn}), bulk porosity (ϕ_{bulk}), and isolated porosity (ϕ_{iso}) for mean density bin of each pumice type (J1, J2, J3) and the ±0.5 standard deviation densities. The porosity measurements presented are the averag, the minimum measurement, maximum measurement, standard deviation, and error in measurement for each density bin.

J1 Porosity							
Average	**-1.5**	**-1**	**-0.5**	**0**	**0.5**	**1**	**1.5**
ϕ_{conn}	77.70115	64.86878	67.71379	65.86433	55.3907	55.94744	57.01459
ϕ_{bulk}	84.06235	81.18569	78.48001	75.9988	71.55769	73.17828	66.04877
ϕ_{iso}	6.361205	16.3169	10.76622	10.13447	16.16699	17.23084	9.034179
Minimum	**-1.5**	**-1**	**-0.5**	**0**	**0.5**	**1**	**1.5**
ϕ_{conn}	76.91218	64.32774	67.13698	65.76445	54.5045	55.43933	56.71326
ϕ_{bulk}	83.54419	80.88267	78.03382	75.89856	70.98151	72.70635	65.80064
ϕ_{iso}	6.632007	16.55492	10.89685	10.13411	16.47701	17.26702	9.087382
Maximum	**-1.5**	**-1**	**-0.5**	**0**	**0.5**	**1**	**1.5**
ϕ_{conn}	78.44982	65.39451	68.27864	65.96364	56.25611	56.44719	57.31214
ϕ_{bulk}	84.57546	81.48785	78.92178	76.09888	72.12859	73.64611	66.29653
ϕ_{iso}	6.125644	16.09334	10.64314	10.13524	15.87248	17.19892	8.984388
Std Dev	**-1.5**	**-1**	**-0.5**	**0**	**0.5**	**1**	**1.5**
ϕ_{conn}	0.768908	0.533402	0.570842	0.099594	0.875823	0.503934	0.299445
ϕ_{bulk}	0.51564	0.302593	0.443982	0.100158	0.573543	0.469882	0.247946
ϕ_{iso}	0.253386	0.230829	0.12687	0.000577	0.302295	0.03407	0.051506
Error	**-1.5**	**-1**	**-0.5**	**0**	**0.5**	**1**	**1.5**
ϕ_{conn}	0.443929	0.30796	0.329576	0.057501	0.505657	0.290947	0.172885
ϕ_{bulk}	0.297705	0.174702	0.256333	0.057826	0.331135	0.271287	0.143152
ϕ_{iso}	0.146292	0.133269	0.073249	0.000333	0.17453	0.01967	0.029737

J2 Porosity							
Average	**-1.5**	**-1**	**-0.5**	**0**	**0.5**	**1**	**1.5**
ϕ_{conn}	75.88076	75.77566	73.02418	70.84233	59.81867	60.19937	60.92293
ϕ_{bulk}	85.70646	81.99135	78.07116	75.1559	71.33459	69.36728	65.35344
ϕ_{iso}	9.825698	6.215698	5.046974	4.313568	11.51592	9.167916	4.430517
Minimum	**-1.5**	**-1**	**-0.5**	**0**	**0.5**	**1**	**1.5**
ϕ_{conn}	73.62832	75.5716	72.64568	70.65217	58.6159	59.6556	59.63074
ϕ_{bulk}	84.2994	81.69977	77.72125	74.96176	70.54918	68.98358	64.3357

ϕ_{iso}	10.67108	6.128168	5.075564	4.309582	11.93328	9.327985	4.704963
Maximum	**-1.5**	**-1**	**-0.5**	**0**	**0.5**	**1**	**1.5**
ϕ_{conn}	77.79449	75.97633	73.39235	71.03004	60.95775	60.73059	62.17391
ϕ_{bulk}	87.07532	82.28064	78.41997	75.34966	72.12	69.75041	66.3569
ϕ_{iso}	9.280829	6.30431	5.027616	4.319613	11.16225	9.019814	4.18299
Std Dev	**-1.5**	**-1**	**-0.5**	**0**	**0.5**	**1**	**1.5**
ϕ_{conn}	2.085377	0.202368	0.373346	0.188936	1.171066	0.537511	1.271643
ϕ_{bulk}	1.388002	0.290437	0.349361	0.19395	0.78541	0.383413	1.01061
ϕ_{iso}	0.700518	0.088072	0.024121	0.005051	0.38595	0.154124	0.261102
Error	**-1.5**	**-1**	**-0.5**	**0**	**0.5**	**1**	**1.5**
ϕ_{conn}	1.203993	0.116837	0.215552	0.109082	0.676115	0.310332	0.734183
ϕ_{bulk}	0.801363	0.167684	0.201704	0.111977	0.453457	0.221364	0.583476
ϕ_{iso}	0.404444	0.050848	0.013926	0.002916	0.222828	0.088984	0.150747

J3 Porosity							
Average	**-1.5**	**-1**	**-0.5**	**0**	**0.5**	**1**	**1.5**
ϕ_{conn}	77.11161	75.68948	68.44784	66.56543	59.58068	61.81818	45.97701
ϕ_{bulk}	83.53884	80.47765	76.08658	73.47998	68.48109	71.07232	62.0584
ϕ_{iso}	6.427229	4.788173	7.638739	6.914557	8.900415	9.254139	16.08139
Minimum	**-1.5**	**-1**	**-0.5**	**0**	**0.5**	**1**	**1.5**
ϕ_{conn}	76.65519	74.85994	66.59021	66.00051	59.42492	60.78431	44.75309
ϕ_{bulk}	83.21484	79.86667	74.77901	73.10225	68.31744	69.66796	61.04003
ϕ_{iso}	6.559654	5.006723	8.1888	7.101734	8.892525	8.883647	16.28694
Maximum	**-1.5**	**-1**	**-0.5**	**0**	**0.5**	**1**	**1.5**
ϕ_{conn}	77.55481	76.47449	70.13167	67.11678	59.73545	62.8091	47.15302
ϕ_{bulk}	83.8605	81.08458	77.37914	73.85639	68.64436	72.44343	63.06819
ϕ_{iso}	6.305684	4.610098	7.247474	6.739611	8.908911	9.634332	15.91517
Std Dev	**-1.5**	**-1**	**-0.5**	**0**	**0.5**	**1**	**1.5**
ϕ_{conn}	0.44983	0.807374	1.771439	0.558147	0.155265	1.012469	1.200049
ϕ_{bulk}	0.322829	0.60896	1.300072	0.377072	0.163458	1.387769	1.014084
ϕ_{iso}	0.127024	0.198656	0.47289	0.181096	0.008195	0.375353	0.186234
Error	**-1.5**	**-1**	**-0.5**	**0**	**0.5**	**1**	**1.5**
ϕ_{conn}	0.259709	0.466137	1.022741	0.322246	0.089642	0.584549	0.692849
ϕ_{bulk}	0.186385	0.351583	0.750597	0.217703	0.094373	0.801229	0.585482
ϕ_{iso}	0.073337	0.114694	0.273023	0.104556	0.004732	0.21671	0.107522

Appendix H: Pumice Type Density

Bulk clast density and vesicularity for the 8 – 32 mm pumices of the J1, J2, and J3 pumice types taken from a representative mid-height sample at Exposure D. Measurements followed methods by Houghton & Wilson (1989) and Shea et al. (2010).

J1 (8-32mm)			J2 (8-32mm)			J3 (8-32mm)		
Clast #	Density	Vesicularity	Clast #	Density	Vesicularity	Clast #	Density	Vesicularity
1	0.51	80%	1	0.55	79%	1	0.67	74%
2	0.85	67%	2	0.47	81%	2	0.68	73%
3	0.44	83%	3	0.43	83%	3	0.69	73%
4	0.80	68%	4	0.60	76%	4	0.50	80%
5	0.44	83%	5	0.70	73%	5	0.40	84%
6	0.60	77%	6	0.54	79%	6	0.55	78%
7	0.61	76%	7	0.56	78%	7	0.59	77%
8	0.54	79%	8	0.72	72%	8	0.68	73%
9	0.62	75%	9	0.38	85%	9	0.48	81%
10	0.66	74%	10	0.50	80%	10	0.62	76%
11	0.63	75%	11	0.70	72%	11	0.60	77%
12	0.58	77%	12	0.38	85%	12	0.67	74%
13	0.42	83%	13	0.38	85%	13	0.53	79%
14	0.69	73%	14	0.39	85%	14	0.52	80%
15	0.51	80%	15	0.73	71%	15	0.56	78%
16	0.65	75%	16	0.55	78%	16	0.57	77%
17	0.69	73%	17	0.30	88%	17	0.49	81%
18	0.58	77%	18	0.53	79%	18	0.58	77%
19	0.66	74%	19	0.49	81%	19	0.39	85%
20	0.56	78%	20	0.52	80%	20	0.57	78%
21	0.63	75%	21	0.59	77%	21	0.46	82%
22	0.50	80%	22	0.55	78%	22	0.67	73%
23	0.45	82%	23	0.52	80%	23	0.71	72%
24	0.53	79%	24	0.50	80%	24	0.54	79%
25	0.54	79%	25	0.65	75%	25	0.49	81%
26	0.66	74%	26	0.89	65%	26	0.64	75%
27	0.63	75%	27	0.54	79%	27	0.59	77%
28	0.59	77%	28	0.37	86%	28	0.58	77%
29	0.58	77%	29	0.42	84%	29	0.63	75%
30	0.62	76%	30	0.60	76%	30	0.74	71%
31	0.56	78%	31	0.53	79%	31	0.58	77%
32	0.54	79%	32	0.50	80%	32	0.56	78%
33	0.60	76%	33	0.54	79%	33	0.73	71%
34	0.57	78%	34	0.58	77%	34	0.59	77%

35	0.54	79%	35	0.52	80%	35	0.57	77%
36	0.47	82%	36	0.59	77%	36	0.60	76%
37	0.46	82%	37	0.58	77%	37	0.57	78%
38	0.64	75%	38	0.33	87%	38	0.44	83%
39	0.62	76%	39	0.52	80%	39	0.48	81%
40	0.62	75%	40	0.63	75%	40	0.56	78%
41	0.50	80%	41	0.46	82%	41	0.65	75%
42	0.60	76%	42	0.50	80%	42	0.55	78%
43	0.31	88%	43	0.58	77%	43	0.43	83%
44	0.55	78%	44	0.46	82%	44	0.55	78%
45	0.66	74%	45	0.57	77%	45	0.60	76%
46	0.66	74%	46	0.62	75%	46	0.69	73%
47	0.50	80%	47	0.42	83%	47	0.66	74%
48	0.55	78%	48	0.49	81%	48	0.47	82%
49	0.77	70%	49	0.60	77%	49	0.70	72%
50	0.56	78%	50	0.61	76%	50	0.62	76%
51	0.57	77%	51	0.54	79%	51	0.52	79%
52	0.62	76%	52	0.64	75%	52	0.53	79%
53	0.66	74%	53	0.59	77%	53	0.51	80%
54	0.64	75%	54	0.51	80%	54	0.45	82%
55	0.40	84%	55	0.51	80%	55	0.50	80%
56	0.51	80%	56	0.58	77%	56	0.62	76%
57	0.60	76%	57	0.67	74%	57	0.48	81%
58	0.60	76%	58	0.52	80%	58	0.45	82%
59	0.55	78%	59	0.50	80%	59	0.54	79%
60	0.66	74%	60	0.55	79%	60	0.58	77%
61	0.53	79%	61	0.52	80%	61	0.56	78%
62	0.67	74%	62	0.71	72%	62	0.52	80%
63	0.71	72%	63	0.46	82%	63	0.52	80%
64	0.66	74%	64	0.54	79%	64	0.62	76%
65	0.49	81%	65	0.50	80%	65	0.65	74%
66	0.62	76%	66	0.67	74%			
67	0.36	86%	67	0.59	77%			
68	0.48	81%	68	0.55	78%			
69	0.61	76%	69	0.67	74%			
70	0.65	74%	70	0.55	78%			
71	0.64	75%	71	0.61	76%			
72	0.45	82%	72	0.58	77%			
73	0.54	79%	73	0.53	79%			
74	0.60	76%	74	0.60	76%			
75	0.53	79%	75	0.64	75%			
76	0.62	75%	76	0.50	80%			
77	0.53	79%	77	0.59	77%			
78	0.60	76%	78	0.45	82%			
79	0.58	77%	79	0.52	79%			
80	0.56	78%	80	0.58	77%			

81	0.54	79%	81	0.60	76%			
82	0.67	74%	82	0.64	75%			
83	0.46	82%	83	0.64	75%			
84	0.62	75%	84	0.62	76%			
85	0.39	85%	85	0.48	81%			
86	0.52	79%	86	0.92	64%			
87	0.45	82%	87	0.44	83%			
88	0.41	84%	88	0.58	77%			
89	0.58	77%	89	0.72	72%			
90	0.52	80%	90	0.51	80%			
91	0.61	76%	91	0.58	77%			
92	0.49	81%	92	0.54	79%			
93	0.57	78%	93	0.76	70%			
94	0.60	77%	94	0.68	73%			
95	0.54	79%	95	0.48	81%			
96	0.52	80%	96	0.59	77%			
97	0.47	82%	97	0.67	74%			
98	0.16	94%	98	0.58	77%			
99	0.75	71%	99	0.69	73%			
100	0.52	80%	100	0.53	79%			

Appendix I: Density Suites

Bulk clast density and vesicularity for the 8 – 32 mm pumices from the Y5 fall samples at Exposures D, G and H. Measurements followed methods by Houghton & Wilson (1989) and Shea et al. (2010). Where possible, 100 clasts were measured; however, some samples had very low numbers of large pumices and therefore measurements were taken for averaged comparison.

D-3			D-4			D-6			D-7		
Clast #	Density	Vesicularity	Clast #	Density	Vesicularity	Clast #	Density	Vesicularity	Clast #	Density	Vesicularity
1	1.50	41%	1	0.51	80%	1	0.55	78%	1	0.59	77%
2	1.26	50%	2	0.59	77%	2	0.64	75%	2	0.70	72%
3	1.06	58%	3	0.33	87%	3	0.59	77%	3	0.65	74%
4	1.92	24%	4	0.73	71%	4	0.54	79%	4	0.55	78%
5	1.60	37%	5	0.51	80%	5	0.47	82%	5	0.77	70%
6	1.49	41%	6	0.63	75%	6	0.65	74%	6	0.70	72%
7	1.00	61%	7	0.75	70%	7	0.66	74%	7	0.69	73%
8	1.26	50%	8	0.68	73%	8	0.56	78%	8	0.55	78%
9	1.28	50%	9	0.75	71%	9	0.87	66%	9	0.66	74%
10	1.36	47%	10	0.55	78%	10	0.72	72%	10	0.68	73%
11	1.04	59%	11	0.53	79%	11	0.56	78%	11	0.60	76%
12	1.42	44%	12	0.59	77%	12	0.83	67%	12	0.67	73%
13	1.40	45%	13	0.81	68%	13	0.78	69%	13	0.67	73%
14	1.24	51%	14	0.73	71%	14	0.73	71%	14	0.67	74%
15	1.47	42%	15	0.61	76%	15	0.78	69%	15	0.60	76%
16	1.27	50%	16	1.11	56%	16	0.69	73%	16	0.74	71%
17	1.35	47%	17	0.60	76%	17	0.76	70%	17	0.76	70%

18	1.30	49%	18	0.58	77%	18	0.49	81%	18	0.71	72%
19	1.29	49%	19	0.65	74%	19	0.78	69%	19	0.52	79%
20	1.25	51%	20	1.17	54%	20	0.67	74%	20	0.64	75%
21	1.48	42%	21	0.59	77%	21	0.40	84%	21	0.61	76%
22	1.63	36%	22	0.71	72%	22	0.41	84%	22	0.78	69%
23	1.04	59%	23	0.61	76%	23	0.62	75%	23	0.53	79%
24	1.89	26%	24	0.55	78%	24	0.74	71%	24	0.44	83%
25	1.85	27%	25	0.74	71%	25	0.64	75%	25	0.67	74%
26	1.60	37%	26	0.55	78%	26	0.73	71%	26	0.71	72%
27	1.90	25%	27	0.67	74%	27	0.62	75%	27	1.17	54%
28	1.17	54%	28	0.82	68%	28	0.64	75%	28	0.71	72%
29	1.30	49%	29	0.68	73%	29	0.69	73%	29	0.69	73%
30	1.72	32%	30	0.58	77%	30	0.84	67%	30	0.64	75%
31	2.29	10%	31	0.63	75%	31	0.75	71%	31	0.67	74%
			32	0.51	80%	32	0.76	70%	32	0.58	77%
			33	0.74	71%	33	0.58	77%	33	0.61	76%
			34	0.42	83%	34	0.66	74%	34	0.60	76%
			35	0.68	73%	35	0.57	78%	35	0.69	73%
			36	1.01	60%	36	0.71	72%	36	0.60	77%
			37	0.65	75%	37	0.51	80%	37	0.83	67%
			38	0.99	61%	38	0.55	78%	38	0.74	71%
			39	0.59	77%	39	0.57	78%	39	0.67	74%
			40	0.59	77%	40	0.63	75%	40	0.49	81%
			41	0.72	72%	41	0.61	76%	41	0.69	73%
			42	0.71	72%	42	0.57	78%	42	0.60	76%
			43	0.76	70%	43	0.63	75%	43	0.71	72%
			44	0.39	84%	44	0.59	77%	44	0.53	79%
			45	0.52	80%	45	0.74	71%	45	0.70	72%
			46	0.65	75%	46	0.73	71%	46	0.61	76%

			47	0.53	79%	47	0.48	81%	47	0.47	81%
			48	0.70	72%	48	0.61	76%	48	0.49	81%
			49	0.66	74%	49	0.70	72%	49	0.69	73%
			50	0.63	75%	50	0.50	80%	50	0.40	84%
			51	0.60	76%	51	0.36	86%	51	0.69	73%
			52	0.67	73%	52	0.52	80%	52	0.71	72%
			53	0.70	73%	53	0.64	75%	53	0.48	81%
			54	0.62	76%	54	0.71	72%	54	0.69	73%
			55	0.56	78%	55	0.67	74%	55	0.71	72%
			56	0.70	72%	56	0.64	75%	56	0.86	66%
			57	0.60	76%	57	0.47	82%	57	0.44	83%
			58	0.60	76%	58	0.61	76%	58	0.61	76%
			59	0.69	73%	59	0.74	71%	59	0.65	74%
			60	0.60	76%	60	0.83	67%	60	0.74	71%
			61	0.72	72%	61	0.65	74%	61	0.69	73%
			62	0.50	80%	62	0.79	69%	62	0.67	74%
			63	0.54	79%	63	0.65	74%	63	0.47	82%
			64	0.74	71%	64	0.42	83%	64	0.59	77%
			65	0.70	72%	65	0.82	68%	65	0.69	73%
			66	0.73	71%	66	0.81	68%	66	0.55	78%
			67	0.58	77%	67	0.59	77%	67	0.67	74%
			68	0.74	71%	68	0.63	75%	68	0.55	78%
			69	0.62	75%	69	0.64	75%	69	0.60	76%
			70	0.60	76%	70	0.69	73%	70	0.51	80%
			71	0.69	73%	71	0.66	74%	71	0.54	79%
			72	0.63	75%	72	0.72	72%	72	0.60	76%
			73	0.69	73%	73	0.72	72%	73	0.69	73%
			74	0.63	75%	74	0.72	72%	74	0.46	82%
			75	0.50	80%	75	0.71	72%	75	0.68	73%

			76	0.43	83%	76	0.81	68%	76	0.64	75%
			77	0.58	77%	77	0.65	74%	77	0.52	80%
			78	0.64	75%	78	0.58	77%	78	0.71	72%
			79	0.49	81%	79	0.62	76%	79	0.64	75%
			80	0.68	73%	80	0.53	79%	80	0.65	74%
			81	0.58	77%	81	0.71	72%	81	0.67	74%
			82	0.69	73%	82	0.78	69%	82	0.61	76%
			83	0.64	75%	83	0.68	73%	83	0.62	75%
			84	0.51	80%	84	0.76	70%	84	0.48	81%
			85	0.75	71%	85	0.69	73%	85	0.62	76%
			86	0.73	71%	86	0.56	78%	86	0.70	72%
			87	0.38	85%	87	0.82	68%	87	0.61	76%
			88	0.63	75%	88	0.72	72%	88	0.76	70%
			89	0.54	79%	89	0.64	75%	89	0.71	72%
			90	0.46	82%	90	0.77	70%	90	0.68	73%
			91	0.61	76%	91	0.52	79%	91	0.66	74%
			92	0.68	73%	92	0.63	75%	92	0.76	70%
			93	0.66	74%	93	0.72	71%	93	0.59	77%
			94	0.68	73%	94	0.66	74%	94	0.52	79%
			95	0.80	69%	95	0.77	70%	95	0.55	78%
			96	0.61	76%	96	0.61	76%	96	0.66	74%
			97	0.50	80%	97	0.81	68%	97	0.59	77%
			98	0.59	77%	98	0.67	74%	98	0.92	64%
			99	0.50	80%	99	0.63	75%	99	0.53	79%
			100	0.56	78%	100	0.55	78%	100	0.62	75%

D-8			D-9			D-10			D-11		
Clast #	**Density**	**Vesicularity**	**Clast #**	**Density**	**Vesicularity**	**Clast #**	**Density**	**Vesicularity**	**Clast #**	**Density**	**Vesicularity**
1	0.59	77%	1	0.61	76%	1	0.51	80%	1	0.63	75%
2	0.47	81%	2	0.60	77%	2	0.56	78%	2	0.49	81%
3	0.49	81%	3	0.54	79%	3	0.60	76%	3	0.77	70%
4	0.59	77%	4	0.59	77%	4	0.60	76%	4	0.68	73%
5	0.62	76%	5	0.65	74%	5	0.62	76%	5	0.61	76%
6	0.50	80%	6	0.47	81%	6	0.59	77%	6	0.55	78%
7	0.59	77%	7	0.57	78%	7	0.67	73%	7	0.50	80%
8	0.62	76%	8	0.62	76%	8	0.57	77%	8	0.59	77%
9	0.52	79%	9	0.46	82%	9	0.59	77%	9	0.74	71%
10	0.69	73%	10	0.55	79%	10	0.65	75%	10	0.63	75%
11	0.58	77%	11	0.60	76%	11	0.54	79%	11	0.45	82%
12	0.52	79%	12	0.65	74%	12	0.67	74%	12	0.36	86%
13	0.44	83%	13	0.45	82%	13	0.69	73%	13	0.53	79%
14	0.67	74%	14	0.51	80%	14	0.60	76%	14	0.74	71%
15	0.47	81%	15	0.54	79%	15	0.40	84%	15	0.55	78%
16	0.72	71%	16	0.50	80%	16	0.65	75%	16	0.60	76%
17	0.51	80%	17	0.76	70%	17	0.47	82%	17	0.72	72%
18	0.48	81%	18	0.57	78%	18	0.52	79%	18	0.59	77%
19	0.56	78%	19	0.46	82%	19	0.56	78%	19	0.64	75%
20	0.61	76%	20	0.59	77%	20	0.45	82%	20	0.62	75%
21	0.62	76%	21	0.55	78%	21	1.00	61%	21	0.45	82%
22	0.59	77%	22	0.79	69%	22	0.58	77%	22	0.58	77%
23	0.63	75%	23	0.53	79%	23	0.76	70%	23	0.50	80%
24	0.60	76%	24	0.66	74%	24	0.44	83%	24	0.67	74%
25	0.46	82%	25	0.67	74%	25	0.63	75%	25	0.64	75%
26	0.61	76%	26	0.58	77%	26	0.48	81%	26	0.65	74%

27	0.53	79%	27	0.67	74%	27	0.56	78%	27	0.60	76%
28	0.47	81%	28	0.62	75%	28	0.56	78%	28	0.60	76%
29	0.51	80%	29	0.51	80%	29	0.52	80%	29	0.48	81%
30	0.60	76%	30	0.46	82%	30	0.82	68%	30	0.71	72%
31	0.58	77%	31	0.75	71%	31	0.62	76%	31	0.54	79%
32	0.56	78%	32	0.54	79%	32	0.59	77%	32	0.49	81%
33	0.47	81%	33	0.56	78%	33	0.57	77%	33	0.52	80%
34	0.54	79%	34	0.70	73%	34	0.56	78%	34	0.61	76%
35	0.63	75%	35	0.57	78%	35	0.41	84%	35	0.49	81%
36	0.60	76%	36	0.66	74%	36	0.44	83%	36	0.65	74%
37	0.56	78%	37	0.51	80%	37	0.54	79%	37	0.60	76%
38	0.53	79%	38	0.55	78%	38	0.72	72%	38	0.58	77%
39	0.63	75%	39	0.62	76%	39	0.50	80%	39	0.54	79%
40	0.44	83%	40	0.76	70%	40	0.59	77%	40	0.62	75%
41	0.43	83%	41	0.54	79%	41	0.60	76%	41	0.55	79%
42	0.54	79%	42	0.68	73%	42	0.60	76%	42	0.63	75%
43	0.61	76%	43	0.54	79%	43	0.59	77%	43	0.57	78%
44	0.48	81%	44	0.66	74%	44	0.50	80%	44	0.62	76%
45	0.56	78%	45	0.65	74%	45	0.66	74%	45	0.56	78%
46	0.64	75%	46	0.52	79%	46	0.28	89%	46	0.59	77%
47	0.62	76%	47	0.60	76%	47	0.66	74%	47	0.50	80%
48	0.41	84%	48	0.51	80%	48	0.61	76%	48	0.55	78%
49	0.58	77%	49	0.60	76%	49	0.67	74%	49	0.50	80%
50	0.52	79%	50	0.56	78%	50	0.51	80%	50	0.58	77%
51	0.52	80%	51	0.42	84%	51	0.51	80%	51	0.52	80%
52	0.68	73%	52	0.54	79%	52	0.75	71%	52	0.73	71%
53	0.55	79%	53	0.41	84%	53	0.63	75%	53	0.48	81%
54	0.52	79%	54	0.55	78%	54	0.48	81%	54	0.77	70%
55	0.58	77%	55	0.56	78%	55	0.69	73%	55	0.54	79%

56	0.52	80%	56	0.61	76%	56	0.65	74%	56	0.39	85%
57	0.63	75%	57	0.47	81%	57	0.50	80%	57	0.61	76%
58	0.56	78%	58	0.57	78%	58	0.53	79%	58	0.59	77%
59	0.54	79%	59	0.61	76%	59	0.61	76%	59	0.63	75%
60	0.56	78%	60	0.67	74%	60	0.60	77%	60	0.49	81%
61	0.55	78%	61	0.49	81%	61	0.55	78%	61	0.52	80%
62	0.62	76%	62	0.48	81%	62	0.59	77%	62	0.48	81%
63	0.67	74%	63	0.44	83%	63	0.58	77%	63	0.54	79%
64	0.53	79%	64	0.35	86%	64	0.62	76%	64	0.40	84%
65	0.61	76%	65	0.55	78%	65	0.59	77%	65	0.65	75%
66	0.52	79%	66	0.56	78%	66	0.45	82%	66	0.75	70%
67	0.50	80%	67	0.65	74%	67	0.63	75%	67	0.44	83%
68	0.35	86%	68	0.61	76%	68	0.51	80%	68	0.59	77%
69	0.52	79%	69	0.38	85%	69	0.55	78%	69	0.54	79%
70	0.47	82%	70	0.57	78%	70	0.60	76%	70	0.10	96%
71	0.49	81%	71	0.59	77%	71	0.65	74%	71	0.52	79%
72	0.57	78%	72	0.69	73%	72	0.59	77%	72	0.66	74%
73	0.57	77%	73	0.53	79%	73	0.54	79%	73	0.53	79%
74	0.53	79%	74	0.60	76%	74	0.72	71%	74	0.63	75%
75	0.46	82%	75	0.63	75%	75	0.54	79%	75	0.61	76%
76	0.62	76%	76	0.43	83%	76	0.58	77%	76	0.54	79%
77	0.58	77%	77	0.47	81%	77	0.60	77%	77	0.63	75%
78	0.59	77%	78	0.62	76%	78	0.53	79%	78	0.44	83%
79	0.60	76%	79	0.39	84%	79	0.60	76%	79	0.44	83%
80	0.64	75%	80	0.47	81%	80	0.53	79%	80	0.69	73%
81	0.62	75%	81	0.64	75%	81	0.44	83%	81	0.57	78%
82	0.48	81%	82	0.62	76%	82	0.71	72%	82	0.81	68%
83	0.57	77%	83	0.60	76%	83	0.55	78%	83	0.54	79%
84	0.52	80%	84	0.78	69%	84	0.41	84%	84	0.61	76%

85	0.59	77%	85	0.52	80%	85	0.57	78%	85	0.67	74%
86	0.61	76%	86	0.68	73%	86	0.62	76%	86	0.63	75%
87	0.69	73%	87	0.54	79%	87	0.54	79%	87	0.59	77%
88	0.60	76%	88	0.57	78%	88	0.67	74%	88	0.64	75%
89	0.58	77%	89	0.49	81%	89	0.57	77%	89	0.53	79%
90	0.57	78%	90	0.59	77%	90	0.61	76%	90	0.37	85%
91	0.50	80%	91	0.57	78%	91	0.62	76%	91	0.57	77%
92	0.41	84%	92	0.58	77%	92	0.61	76%	92	0.64	75%
93	0.56	78%	93	0.59	77%	93	0.46	82%	93	0.49	81%
94	0.55	78%	94	0.36	86%	94	0.51	80%	94	0.51	80%
95	0.59	77%	95	0.62	76%	95	0.69	73%	95	0.67	74%
96	0.58	77%	96	0.50	80%	96	0.56	78%	96	0.58	77%
97	0.61	76%	97	0.60	77%	97	0.66	74%	97	0.43	83%
98	0.57	78%	98	0.54	79%	98	0.57	78%	98	0.58	77%
99	0.46	82%	99	0.51	80%	99	0.58	77%	99	0.55	79%
100	0.37	85%	100	0.56	78%	100	0.59	77%	100	0.45	82%

D-12			**D-13**			**D-14**			**D-15**		
Clast #	**Density**	**Vesicularity**	**Clast #**	**Density**	**Vesicularity**	**Clast #**	**Density**	**Vesicularity**	**Clast #**	**Density**	**Vesicularity**
1	0.30	88%	1	0.68	73%	1	0.55	78%	1	0.37	86%
2	0.70	72%	2	0.66	74%	2	0.42	83%	2	0.60	76%
3	0.55	78%	3	0.51	80%	3	0.48	81%	3	0.54	79%
4	0.62	76%	4	0.50	80%	4	0.67	74%	4	0.69	73%
5	0.63	75%	5	0.56	78%	5	0.70	72%	5	0.66	74%
6	0.42	84%	6	0.57	78%	6	0.53	79%	6	0.66	74%
7	0.37	85%	7	0.92	64%	7	0.62	76%	7	0.59	77%
8	0.74	71%	8	0.57	77%	8	0.49	81%	8	0.46	82%

9	0.54	79%	9	0.58	77%	9	0.67	74%	9	0.60	76%
10	0.43	83%	10	0.60	76%	10	0.54	79%	10	0.72	71%
11	0.58	77%	11	0.42	84%	11	0.59	77%	11	0.78	69%
12	0.48	81%	12	0.63	75%	12	0.57	78%	12	0.59	77%
13	0.64	75%	13	0.61	76%	13	0.64	75%	13	0.58	77%
14	0.74	71%	14	0.44	83%	14	0.41	84%	14	0.52	79%
15	0.56	78%	15	0.53	79%	15	0.66	74%	15	0.60	76%
16	0.60	76%	16	0.50	80%	16	0.55	78%	16	0.61	76%
17	0.66	74%	17	0.61	76%	17	0.42	83%	17	0.73	71%
18	0.47	82%	18	0.57	77%	18	0.64	75%	18	0.36	86%
19	0.67	73%	19	0.64	75%	19	0.62	76%	19	0.75	71%
20	0.63	75%	20	0.64	75%	20	0.71	72%	20	0.66	74%
21	0.53	79%	21	0.50	80%	21	0.68	73%	21	0.46	82%
22	0.63	75%	22	0.60	76%	22	0.53	79%	22	0.71	72%
23	0.57	78%	23	0.45	82%	23	0.57	78%	23	0.62	76%
24	0.57	77%	24	0.60	76%	24	0.62	76%	24	0.66	74%
25	0.68	73%	25	0.55	78%	25	0.65	74%	25	0.80	68%
26	0.59	77%	26	0.56	78%	26	0.47	81%	26	0.40	84%
27	0.56	78%	27	0.55	78%	27	0.56	78%	27	0.77	70%
28	0.65	74%	28	0.64	75%	28	0.56	78%	28	0.70	73%
29	0.68	73%	29	0.61	76%	29	0.51	80%	29	0.55	78%
30	0.50	80%	30	0.68	73%	30	0.51	80%	30	0.65	74%
31	0.51	80%	31	0.75	71%	31	0.47	82%	31	0.73	71%
32	0.58	77%	32	0.52	80%	32	0.63	75%	32	0.77	70%
33	0.68	73%	33	0.56	78%	33	0.66	74%	33	0.60	76%
34	0.63	75%	34	0.56	78%	34	0.48	81%	34	0.51	80%
35	0.67	74%	35	0.65	74%	35	0.49	81%	35	0.56	78%
36	0.56	78%	36	0.44	83%	36	0.59	77%	36	0.58	77%
37	0.66	74%	37	0.58	77%	37	0.66	74%	37	0.45	82%

38	0.44	83%	38	0.53	79%	38	0.75	71%	38	0.71	72%
39	0.57	77%	39	0.67	74%	39	0.48	81%	39	0.87	66%
40	0.66	74%	40	0.38	85%	40	0.57	77%	40	0.48	81%
41	0.68	73%	41	0.65	75%	41	0.79	69%	41	0.60	76%
42	0.59	77%	42	0.73	71%	42	0.53	79%	42	0.55	78%
43	0.67	74%	43	0.56	78%	43	0.45	82%	43	0.67	74%
44	0.63	75%	44	0.72	71%	44	0.65	75%	44	0.57	77%
45	0.63	75%	45	0.50	80%	45	0.46	82%	45	0.51	80%
46	0.64	75%	46	0.55	78%	46	0.53	79%	46	0.65	74%
47	0.44	83%	47	0.60	76%	47	0.59	77%	47	0.51	80%
48	0.64	75%	48	0.69	73%	48	0.58	77%	48	0.56	78%
49	0.61	76%	49	0.57	78%	49	0.47	81%	49	0.62	75%
50	0.54	79%	50	0.57	77%	50	0.50	80%	50	0.62	75%
51	0.68	73%	51	0.69	73%	51	0.64	75%	51	0.63	75%
52	0.48	81%	52	0.55	78%	52	0.65	75%	52	0.76	70%
53	0.57	78%	53	0.42	83%	53	0.73	71%	53	0.73	71%
54	0.56	78%	54	0.62	75%	54	0.48	81%	54	0.56	78%
55	0.58	77%	55	0.82	68%	55	0.42	83%	55	0.66	74%
56	0.61	76%	56	0.60	76%	56	0.47	81%	56	0.48	81%
57	0.57	78%	57	0.55	78%	57	0.61	76%	57	0.59	77%
58	0.56	78%	58	0.47	81%	58	0.45	82%	58	0.68	73%
59	0.74	71%	59	0.56	78%	59	0.69	73%	59	0.69	73%
60	0.61	76%	60	0.58	77%	60	0.69	73%	60	0.73	71%
61	0.67	73%	61	0.56	78%	61	0.50	80%	61	0.49	81%
62	0.41	84%	62	0.56	78%	62	0.64	75%	62	0.52	79%
63	0.59	77%	63	0.45	82%	63	0.47	82%	63	0.49	81%
64	0.61	76%	64	0.55	78%	64	0.47	82%	64	0.52	80%
65	0.42	84%	65	0.77	70%	65	0.50	80%	65	0.68	73%
66	0.65	74%	66	0.53	79%	66	0.55	78%	66	0.75	71%

67	0.62	76%	67	0.53	79%	67	0.47	82%	67	0.74	71%
68	0.52	79%	68	0.58	77%	68	0.62	75%	68	0.42	83%
69	0.57	77%	69	0.56	78%	69	0.51	80%	69	0.56	78%
70	0.47	81%	70	0.57	77%	70	0.46	82%	70	0.58	77%
71	0.57	78%	71	0.68	73%	71	0.75	71%	71	0.73	71%
72	0.70	72%	72	0.50	80%	72	0.73	71%	72	0.68	73%
73	0.57	78%	73	0.49	81%	73	0.63	75%	73	0.57	78%
74	0.56	78%	74	0.61	76%	74	0.43	83%	74	0.44	83%
75	0.54	79%	75	0.59	77%	75	0.70	72%	75	0.33	87%
76	0.45	82%	76	0.59	77%	76	0.48	81%	76	0.66	74%
77	0.67	74%	77	0.64	75%	77	0.52	80%	77	0.68	73%
78	0.46	82%	78	0.55	78%	78	0.53	79%	78	0.63	75%
79	0.46	82%	79	0.55	78%	79	0.54	79%	79	0.46	82%
80	0.66	74%	80	0.54	79%	80	0.71	72%	80	0.48	81%
81	0.46	82%	81	0.53	79%	81	0.54	79%	81	0.70	73%
82	0.62	76%	82	0.48	81%	82	0.61	76%	82	0.56	78%
83	0.57	77%	83	0.52	80%	83	0.50	80%	83	0.38	85%
84	0.65	75%	84	0.53	79%	84	0.77	70%	84	0.49	81%
85	0.56	78%	85	0.54	79%	85	0.73	71%	85	0.61	76%
86	0.52	80%	86	0.54	79%	86	0.51	80%	86	0.72	72%
87	0.71	72%	87	0.65	74%	87	0.65	75%	87	0.45	82%
88	0.58	77%	88	0.55	78%	88	0.55	78%	88	0.64	75%
89	0.53	79%	89	0.57	78%	89	0.44	83%	89	0.68	73%
90	0.61	76%	90	0.70	72%	90	0.48	81%	90	0.51	80%
91	0.47	81%	91	0.66	74%	91	0.58	77%	91	0.64	75%
92	0.60	76%	92	0.47	82%	92	0.60	76%	92	0.39	85%
93	0.61	76%	93	0.59	77%	93	0.64	75%	93	0.72	72%
94	0.54	79%	94	0.66	74%	94	0.63	75%	94	0.46	82%
95	0.53	79%	95	0.58	77%	95	0.68	73%	95	0.68	73%

96	0.58	77%	96	0.64	75%	96	0.43	83%	96	0.60	76%
97	0.63	75%	97	0.67	74%	97	0.47	81%	97	0.57	78%
98	0.57	77%	98	0.63	75%	98	0.51	80%	98	0.69	73%
99	0.57	77%	99	0.61	76%	99	0.59	77%	99	0.64	75%
100	0.57	77%	100	0.55	78%				100	0.70	73%

G-4			**G-7**			**G-9**			**G-11**		
Clast #	**Density**	**Vesicularity**	**Clast #**	**Density**	**Vesicularity**	**Clast #**	**Density**	**Vesicularity**	**Clast #**	**Density**	**Vesicularity**
1	0.80	68%	1	0.43	83%	1	0.69	73%	1	0.47	82%
			2	0.64	75%	2	0.72	72%	2	0.73	71%
G-5			3	0.64	75%	3	0.57	78%	3	0.32	87%
Clast #	**Density**	**Vesicularity**	4	0.46	82%	4	0.66	74%	4	0.68	73%
1	0.68	73%	5	0.47	82%	5	0.80	68%	5	0.63	75%
2	0.68	73%	6	0.63	75%	6	0.66	74%	6	0.89	65%
3	0.63	75%	7	0.60	76%	7	0.52	80%	7	0.50	80%
4	0.87	66%	8	1.00	61%	8	0.73	71%	8	0.78	69%
5	0.55	78%	9	0.58	77%	9	0.68	73%	9	0.37	85%
6	0.50	80%	10	0.65	74%	10	0.52	79%	10	0.76	70%
7	0.66	74%	11	0.47	81%	11	0.49	81%	11	0.66	74%
8	0.74	71%	12	0.63	75%	12	0.59	77%	12	0.41	84%
9	0.68	73%	13	0.68	73%	13	0.93	63%	13	0.52	80%
10	0.50	80%	14	0.62	75%	14	0.62	76%	14	0.69	73%
11	0.65	74%	15	0.89	65%	15	0.78	69%	15	0.75	71%
12	0.57	77%	16	0.60	77%	16	0.79	69%	16	0.73	71%
13	0.67	74%	17	0.47	81%	17	0.58	77%	17	0.62	75%
14	0.92	64%	18	0.63	75%	18	0.50	80%	18	0.48	81%
15	0.59	77%	19	0.53	79%	19	0.88	65%	19	0.52	79%

16	0.76	70%	20	0.60	76%	20	0.91	64%	20	0.69	73%
17	0.64	75%	21	0.59	77%	21	0.55	78%	21	0.56	78%
18	0.61	76%	22	0.65	74%	22	0.77	70%	22	0.69	73%
19	0.52	80%	23	0.84	67%	23	0.58	77%	23	0.82	68%
20	0.64	75%	24	0.62	76%	24	0.66	74%	24	0.54	79%
21	0.64	75%	25	0.54	79%	25	0.64	75%	25	0.74	71%
22	0.70	73%	26	0.62	76%	26	0.51	80%	26	0.71	72%
23	0.68	73%	27	0.64	75%	27	0.67	74%	27	0.62	76%
24	0.60	76%	28	0.65	74%	28	0.49	81%	28	0.41	84%
25	0.85	67%	29	0.75	71%	29	0.65	74%	29	0.55	78%
26	0.67	74%	30	0.71	72%	30	0.64	75%	30	0.69	73%
27	0.55	78%	31	0.68	73%	31	0.76	70%	31	0.54	79%
28	0.63	75%	32	0.67	74%	32	0.68	73%	32	0.76	70%
29	0.66	74%	33	0.02	99%	33	0.78	69%	33	0.69	73%
30	0.39	84%	34	0.70	73%	34	0.71	72%	34	0.75	70%
31	0.65	74%	35	0.87	66%	35	0.70	73%	35	0.72	72%
32	0.93	63%	36	0.53	79%	36	0.75	71%	36	0.50	80%
33	0.67	74%	37	0.64	75%	37	0.63	75%	37	0.47	82%
34	0.56	78%	38	0.67	74%	38	0.56	78%	38	0.69	73%
35	0.62	76%	39	0.76	70%				39	0.51	80%
36	0.66	74%	40	0.85	67%				40	0.54	79%
37	0.50	80%	41	0.56	78%				41	0.66	74%
38	0.60	76%	42	0.73	71%				42	0.63	75%
39	1.00	61%	43	0.72	72%				43	0.76	70%
40	0.62	75%	44	0.65	74%				44	0.82	68%
41	0.67	74%	45	0.58	77%				45	0.72	72%
42	0.63	75%	46	0.45	82%				46	0.59	77%
43	0.76	70%	47	0.75	70%				47	0.74	71%
			48	0.63	75%				48	0.69	73%

G-6			49	0.73	71%				49	0.60	77%
Clast #	**Density**	**Vesicularity**	50	0.67	74%				50	0.56	78%
1	0.57	77%	51	0.56	78%				51	0.56	78%
2	0.50	80%	52	0.46	82%				52	0.56	78%
3	0.79	69%	53	0.61	76%				53	0.49	81%
4	0.63	75%	54	0.56	78%				54	0.58	77%
5	0.83	67%	55	0.64	75%				55	0.77	70%
6	0.52	80%	56	0.61	76%				56	0.51	80%
7	0.74	71%	57	0.55	79%				57	0.77	70%
8	0.56	78%	58	0.55	78%				58	0.62	76%
9	0.75	70%	59	0.62	75%				59	0.84	67%
10	0.59	77%	60	0.52	79%				60	0.53	79%
11	0.82	68%	61	0.75	71%				61	0.52	80%
12	0.47	81%	62	0.67	74%				62	0.74	71%
13	0.64	75%	63	0.56	78%				63	0.63	75%
			64	0.93	63%				64	0.75	71%
			65	0.47	82%				65	0.74	71%
			66	0.64	75%				66	0.60	76%
			67	0.75	71%				67	0.77	70%
			68	0.50	80%				68	0.62	76%
			69	0.61	76%				69	0.55	78%
			70	0.57	78%				70	0.76	70%
			71	0.65	74%				71	0.47	82%
			72	0.65	74%				72	0.67	74%
			73	0.65	74%				73	0.61	76%
			74	0.60	76%				74	0.67	74%
			75	0.37	85%				75	0.72	72%
			76	0.85	66%				76	0.61	76%

			77	0.54	79%				77	0.65	74%
			78	0.59	77%						
			79	0.77	70%						
			80	0.38	85%						
			81	0.65	75%						
			82	0.60	76%						
			83	0.70	72%						
			84	0.76	70%						
			85	0.67	74%						
			86	0.60	76%						
			87	0.76	70%						
			88	0.57	77%						
			89	0.62	75%						
			90	0.73	71%						
			91	0.84	67%						
			92	0.55	78%						
			93	0.72	72%						
			94	0.60	76%						
			95	0.60	76%						
			96	0.65	74%						
			97	0.69	73%						
			98	0.65	74%						
			99	0.78	69%						
			100	0.78	69%						

G-13			G-15			G-17			G-19			G-21		
Clast #	**Density**	**Vesicularity**	**Clast #**	**Density**	**Vesicularity**	**Clast #**	**Density**	**Vesicularity**	**Clast #**	**Density**	**Vesicularity**	**Clast #**	**Density**	**Vesicularity**
1	0.66	74%	1	0.67	73%	1	0.62	75%	1	0.40	84%	1	0.63	75%
2	0.46	82%	2	0.74	71%	2	0.56	78%	2	0.55	78%	2	0.56	78%
3	0.64	75%	3	0.63	75%	3	0.70	72%	3	0.54	79%	3	0.56	78%
4	0.61	76%	4	0.56	78%	4	0.66	74%	4	0.65	74%	4	0.49	81%
5	0.67	73%	5	0.71	72%	5	0.46	82%	5	0.68	73%	5	0.56	78%
6	0.67	74%	6	0.64	75%	6	0.60	77%	6	0.74	71%	6	0.70	72%
7	0.51	80%	7	0.63	75%	7	0.48	81%	7	0.63	75%	7	0.63	75%
8	0.46	82%	8	0.63	75%	8	0.57	78%	8	0.49	81%	8	0.51	80%
9	0.64	75%	9	0.49	81%	9	0.41	84%	9	0.43	83%	9	0.68	73%
10	0.54	79%	10	0.62	76%	10	0.63	75%	10	0.66	74%	10	1.08	57%
11	0.69	73%	11	0.62	76%	11	0.61	76%	11	0.71	72%	11	0.52	80%
12	0.51	80%	12	0.63	75%	12	0.51	80%	12	0.47	82%	12	0.60	76%
13	0.57	78%	13	0.54	79%	13	0.55	78%	13	0.60	76%	13	0.50	80%
14	0.71	72%	14	0.53	79%	14	0.60	76%	14	0.64	75%	14	0.62	75%
15	0.54	79%	15	0.65	74%	15	0.62	76%	15	0.64	75%	15	0.63	75%
16	0.82	68%	16	0.65	74%	16	0.56	78%	16	0.38	85%	16	0.69	73%
17	0.56	78%	17	0.65	74%	17	0.56	78%	17	0.58	77%	17	0.62	76%
18	0.56	78%	18	0.52	80%	18	0.59	77%	18	0.69	73%	18	0.49	81%
19	0.63	75%	19	0.59	77%	19	0.65	74%	19	0.44	83%	19	0.77	70%
20	0.69	73%	20	0.62	76%	20	0.49	81%	20	0.68	73%	20	0.68	73%
21	0.71	72%	21	0.56	78%	21	0.59	77%	21	0.59	77%	21	0.57	78%
22	0.72	72%	22	0.58	77%	22	0.63	75%	22	0.52	80%	22	0.53	79%
23	0.52	80%	23	0.58	77%	23	0.56	78%	23	0.63	75%	23	0.42	83%
24	0.59	77%	24	0.56	78%	24	0.47	81%	24	0.65	75%	24	0.37	85%
25	0.61	76%	25	0.68	73%	25	0.60	77%	25	0.67	74%	25	0.46	82%
26	0.69	73%	26	0.65	75%	26	0.84	67%	26	0.62	76%	26	0.52	80%

27	0.57	78%	27	0.60	76%	27	0.67	73%	27	0.64	75%	27	0.73	71%
28	0.57	77%	28	0.52	80%	28	0.46	82%	28	0.70	72%	28	0.46	82%
29	0.55	78%	29	0.56	78%	29	0.62	76%	29	0.66	74%	29	0.65	75%
30	0.50	80%	30	0.65	75%	30	0.58	77%	30	0.62	76%	30	0.92	64%
31	0.54	79%	31	0.53	79%	31	0.71	72%	31	0.63	75%	31	0.60	76%
32	0.66	74%	32	0.61	76%	32	0.50	80%	32	0.51	80%	32	0.74	71%
33	0.47	82%	33	0.64	75%	33	0.37	85%	33	0.52	80%	33	0.50	81%
34	0.71	72%	34	0.71	72%	34	0.67	74%	34	0.55	78%	34	0.52	80%
35	0.60	76%	35	0.52	79%	35	0.59	77%	35	0.40	84%	35	0.68	73%
36	0.45	82%	36	0.66	74%	36	0.85	66%	36	0.59	77%	36	0.58	77%
37	0.57	78%	37	0.61	76%	37	0.63	75%	37	0.71	72%	37	0.52	80%
38	0.52	80%	38	0.58	77%	38	0.72	72%	38	0.57	77%	38	0.61	76%
39	0.62	76%	39	0.49	81%	39	0.59	77%	39	0.52	80%	39	0.51	80%
40	0.70	72%	40	0.73	71%	40	0.66	74%	40	0.64	75%	40	0.62	76%
41	0.69	73%	41	0.62	75%	41	0.49	81%	41	0.60	76%	41	0.66	74%
42	0.61	76%	42	0.53	79%	42	0.59	77%	42	0.56	78%	42	0.55	78%
43	0.62	75%	43	0.56	78%	43	0.50	80%	43	0.57	77%	43	0.71	72%
44	0.59	77%	44	0.56	78%	44	0.50	80%	44	0.54	79%	44	0.53	79%
45	0.68	73%	45	0.64	75%	45	0.62	76%	45	0.68	73%	45	0.69	73%
46	0.61	76%	46	0.55	78%	46	0.74	71%	46	0.59	77%	46	0.50	80%
47	0.70	72%	47	0.59	77%	47	0.58	77%	47	0.54	79%	47	0.67	73%
48	0.58	77%	48	0.53	79%	48	0.51	80%	48	0.46	82%	48	0.64	75%
49	0.68	73%	49	0.67	73%	49	0.49	81%	49	0.53	79%	49	0.36	86%
50	0.57	78%	50	0.52	80%	50	0.63	75%	50	0.72	72%	50	0.60	76%
51	0.76	70%	51	0.63	75%	51	0.49	81%	51	0.56	78%	51	0.55	78%
52	0.60	76%	52	0.64	75%	52	0.54	79%	52	0.51	80%	52	0.83	67%
53	0.62	76%	53	0.69	73%	53	0.65	74%	53	0.52	80%	53	0.56	78%
54	0.70	73%	54	0.61	76%	54	0.52	79%	54	0.65	74%	54	0.50	81%
55	0.46	82%	55	0.62	76%	55	0.45	82%	55	0.55	79%	55	0.96	62%

56	0.61	76%	56	0.67	74%	56	0.59	77%	56	0.53	79%	56	0.63	75%
57	0.65	75%	57	0.73	71%	57	0.60	76%	57	0.50	80%	57	0.48	81%
58	0.65	74%	58	0.48	81%	58	0.40	84%	58	0.67	74%	58	0.67	74%
59	0.63	75%	59	0.69	73%	59	0.59	77%	59	0.64	75%	59	0.44	83%
60	0.45	82%	60	0.53	79%	60	0.57	78%	60	0.47	81%	60	0.46	82%
61	0.66	74%	61	0.68	73%	61	0.55	78%	61	0.93	63%	61	0.49	81%
62	0.63	75%	62	0.62	76%	62	0.91	64%	62	0.41	84%	62	0.67	73%
63	0.55	78%	63	0.67	74%	63	0.55	78%	63	0.63	75%	63	0.47	82%
64	0.67	74%	64	0.54	79%	64	0.40	84%	64	0.60	76%	64	0.52	79%
65	0.48	81%	65	0.66	74%	65	0.36	86%	65	0.51	80%	65	0.66	74%
66	0.66	74%	66	0.85	67%	66	0.71	72%	66	0.51	80%	66	0.59	77%
67	0.57	77%	67	0.67	74%	67	0.55	78%	67	0.60	76%	67	0.55	78%
68	0.61	76%	68	0.44	83%	68	0.57	77%	68	0.66	74%	68	0.58	77%
69	0.46	82%	69	0.47	82%	69	0.49	81%	69	0.76	70%	69	0.64	75%
70	0.71	72%	70	0.55	78%	70	0.51	80%	70	0.42	84%	70	0.54	79%
71	0.63	75%	71	0.42	84%	71	0.59	77%	71	0.64	75%	71	0.51	80%
72	0.59	77%	72	0.63	75%	72	0.52	80%	72	0.53	79%	72	0.56	78%
73	0.61	76%	73	0.61	76%	73	0.48	81%	73	0.49	81%	73	0.70	72%
74	0.65	74%	74	0.60	76%	74	0.62	76%	74	0.64	75%	74	0.53	79%
75	0.58	77%	75	0.56	78%	75	0.63	75%	75	0.65	75%	75	0.70	72%
76	0.56	78%	76	0.66	74%	76	0.52	79%	76	0.63	75%	76	0.61	76%
77	0.51	80%	77	0.59	77%	77	0.47	81%	77	0.51	80%	77	0.67	74%
78	0.64	75%	78	0.61	76%	78	0.39	85%	78	0.75	71%	78	0.78	69%
79	0.60	77%	79	0.66	74%	79	0.61	76%	79	0.81	68%	79	0.53	79%
80	0.67	74%	80	0.61	76%	80	0.57	78%	80	0.48	81%	80	0.55	78%
81	0.50	80%	81	0.66	74%	81	0.50	81%	81	0.63	75%	81	0.46	82%
82	0.59	77%	82	0.62	76%	82	0.55	78%	82	0.52	79%	82	0.42	83%
83	0.53	79%	83	0.58	77%	83	0.61	76%	83	0.52	79%	83	0.62	76%
84	0.46	82%	84	0.47	81%	84	0.68	73%	84	0.84	67%	84	0.51	80%

85	0.64	75%	85	0.55	78%	85	0.69	73%	85	0.63	75%	85	0.47	81%
86	0.61	76%	86	0.73	71%	86	0.58	77%	86	0.48	81%	86	0.53	79%
87	0.42	83%	87	0.60	76%	87	0.70	72%	87	0.55	78%	87	0.57	77%
88	0.60	76%	88	0.38	85%	88	0.66	74%	88	0.55	78%	88	0.65	74%
89	0.54	79%	89	0.60	76%	89	0.68	73%	89	0.51	80%	89	0.59	77%
90	0.69	73%	90	0.61	76%	90	0.57	78%	90	0.61	76%	90	0.46	82%
91	0.43	83%	91	0.60	76%	91	0.71	72%	91	0.57	78%	91	0.59	77%
92	0.77	70%	92	0.55	78%	92	0.64	75%	92	0.56	78%	92	0.54	79%
93	0.62	76%	93	0.49	81%	93	0.75	71%	93	0.54	79%	93	0.64	75%
94	0.54	79%	94	0.49	81%	94	0.60	76%	94	0.58	77%	94	0.51	80%
95	0.66	74%	95	0.63	75%	95	0.40	84%	95	0.50	80%	95	0.82	68%
96	0.50	80%	96	0.58	77%	96	0.63	75%	96	0.55	78%	96	0.62	76%
97	0.58	77%	97	0.45	82%	97	0.91	64%	97	0.59	77%	97	0.44	83%
98	0.55	78%	98	0.67	74%	98	0.57	78%	98	0.47	81%	98	0.38	85%
99	0.45	82%	99	0.50	80%	99	0.61	76%	99	0.46	82%	99	0.54	79%
100	0.53	79%	100	0.56	78%	100	0.67	74%	100	0.60	76%	100	0.57	78%

H-1			**H-2**			**H-3**		
Clast #	**Density**	**Vesicularity**	**Clast #**	**Density**	**Vesicularity**	**Clast #**	**Density**	**Vesicularity**
1	0.51	80%	1	0.52	79%	1	0.68	73%
2	0.62	76%	2	0.56	78%	2	0.53	79%
3	0.54	79%	3	0.48	81%	3	0.73	71%
4	0.53	79%	4	0.60	76%	4	0.64	75%
5	0.68	73%	5	0.54	79%	5	0.44	83%
6	0.56	78%	6	0.54	79%	6	0.50	80%
7	0.58	77%	7	0.61	76%	7	0.60	76%
8	0.71	72%	8	0.62	76%	8	0.51	80%

9	0.58	77%	9	0.49	81%	9	0.69	73%
10	0.68	73%	10	0.40	84%	10	0.59	77%
11	0.57	78%	11	0.50	81%	11	0.89	65%
12	0.67	74%	12	0.46	82%	12	0.47	81%
13	0.62	76%	13	0.59	77%	13	0.56	78%
14	0.68	73%	14	0.57	78%	14	0.54	79%
15	0.50	80%	15	0.50	80%	15	0.62	76%
16	0.61	76%	16	0.49	81%	16	0.69	73%
17	0.98	61%	17	0.78	69%	17	0.66	74%
18	0.43	83%	18	0.41	84%	18	0.68	73%
19	0.66	74%	19	0.68	73%	19	0.50	80%
20	0.71	72%	20	0.42	84%	20	0.66	74%
21	0.54	79%	21	0.55	79%	21	0.46	82%
22	0.61	76%	22	0.55	78%	22	0.67	74%
23	0.57	78%	23	0.71	72%	23	1.09	57%
24	0.73	71%	24	0.53	79%	24	0.58	77%
25	0.64	75%	25	0.35	86%	25	0.58	77%
26	0.43	83%	26	0.67	74%	26	0.79	69%
27	0.57	78%	27	0.60	76%	27	0.34	87%
28	0.63	75%	28	0.60	76%	28	0.69	73%
29	0.53	79%	29	0.64	75%	29	0.58	77%
30	0.50	80%	30	0.57	78%	30	0.63	75%
31	1.03	60%	31	0.55	78%	31	0.49	81%
32	0.51	80%	32	0.62	75%	32	0.53	79%
33	0.64	75%	33	0.58	77%	33	0.42	84%
34	0.57	77%	34	0.58	77%	34	0.65	75%
35	0.59	77%	35	0.43	83%	35	0.61	76%
36	0.47	81%	36	0.74	71%	36	0.76	70%
37	0.58	77%	37	0.62	76%	37	0.60	76%

38	0.60	76%	38	0.47	81%	38	0.74	71%
39	0.63	75%	39	0.67	73%	39	0.04	98%
40	0.38	85%	40	0.61	76%	40	0.54	79%
41	0.54	79%	41	0.48	81%	41	0.60	76%
42	0.51	80%	42	0.73	71%	42	0.61	76%
43	0.53	79%	43	0.72	72%	43	0.54	79%
44	0.49	81%	44	0.57	77%	44	0.64	75%
45	0.42	84%	45	0.53	79%	45	0.48	81%
46	0.54	79%	46	0.63	75%	46	0.36	86%
47	0.57	77%	47	0.58	77%	47	0.73	71%
48	0.61	76%	48	0.62	76%	48	0.52	79%
49	0.64	75%	49	0.47	82%	49	0.59	77%
50	0.51	80%	50	0.56	78%	50	0.62	76%
51	0.54	79%	51	0.54	79%	51	0.66	74%
52	0.62	76%	52	0.47	82%	52	0.64	75%
53	0.60	76%	53	0.71	72%	53	0.67	74%
54	0.40	84%	54	0.63	75%	54	0.71	72%
55	0.47	82%	55	0.73	71%	55	0.52	80%
56	0.35	86%	56	0.61	76%	56	0.59	77%
57	0.63	75%	57	0.53	79%	57	0.62	76%
58	0.73	71%	58	0.59	77%	58	0.74	71%
59	0.64	75%	59	0.56	78%	59	0.42	83%
60	0.52	80%	60	0.61	76%	60	0.59	77%
61	0.52	79%	61	0.58	77%	61	0.72	72%
62	0.50	80%	62	0.45	82%	62	0.56	78%
63	0.51	80%	63	0.64	75%	63	0.49	81%
64	0.63	75%	64	0.60	76%	64	0.70	72%
65	0.74	71%	65	0.62	76%	65	0.45	82%
66	0.68	73%	66	0.35	86%	66	0.56	78%

67	0.62	76%	67	0.62	76%	67	0.40	84%
68	0.71	72%	68	0.56	78%	68	0.57	77%
69	0.61	76%	69	0.88	65%	69	0.50	80%
70	0.55	78%	70	0.66	74%	70	0.61	76%
71	0.44	83%	71	0.62	76%	71	0.63	75%
72	0.52	80%	72	0.54	79%	72	0.67	74%
73	0.55	78%	73	0.50	80%	73	0.59	77%
74	0.54	79%	74	0.65	74%	74	0.61	76%
75	0.64	75%	75	0.50	80%	75	0.65	75%
76	0.52	80%	76	0.58	77%	76	0.70	72%
77	0.44	83%	77	0.46	82%	77	0.56	78%
78	0.64	75%	78	0.39	85%	78	0.66	74%
79	0.59	77%	79	0.47	82%	79	0.58	77%
80	0.64	75%	80	0.62	76%	80	0.62	76%
81	0.45	82%	81	0.71	72%	81	0.48	81%
82	0.64	75%	82	0.58	77%	82	0.69	73%
83	0.71	72%	83	0.60	77%	83	0.71	72%
84	0.86	66%	84	0.45	82%	84	0.63	75%
85	0.54	79%	85	0.49	81%	85	0.63	75%
86	0.40	84%	86	0.53	79%	86	0.64	75%
87	0.55	78%	87	0.50	80%	87	0.37	85%
88	0.62	75%	88	0.61	76%	88	0.47	81%
89	0.52	79%	89	0.76	70%	89	0.59	77%
90	0.43	83%	90	0.61	76%	90	0.48	81%
91	0.67	74%	91	0.49	81%	91	0.63	75%
92	0.82	68%	92	0.54	79%	92	0.93	63%
93	0.67	74%	93	0.60	76%	93	0.57	78%
94	0.63	75%	94	0.56	78%	94	0.59	77%
95	0.70	72%	95	0.52	79%	95	0.56	78%

96	0.57	77%	96	0.62	76%	96	0.57	77%
97	0.80	69%	97	0.55	78%	97	0.50	80%
98	1.00	61%	98	0.56	78%	98	0.60	76%
99	0.39	85%	99	0.67	74%	99	0.67	74%
100	0.62	75%	100	0.43	83%	100	0.53	79%

H-4			**H-10**			**H-15**		
Clast #	**Density**	**Vesicularity**	**Clast #**	**Density**	**Vesicularity**	**Clast #**	**Density**	**Vesicularity**
1	0.66	74%	1	0.67	74%	1	0.62	76%
2	0.51	80%	2	0.54	79%	2	0.70	73%
3	0.53	79%	3	0.39	85%	3	0.66	74%
4	0.68	73%	4	0.17	93%	4	0.62	75%
5	0.61	76%	5	0.68	73%	5	0.82	68%
6	0.67	73%	6	0.56	78%	6	0.64	75%
7	0.59	77%	7	0.69	73%	7	0.59	77%
8	0.69	73%	8	0.65	74%	8	0.71	72%
9	0.58	77%	9	0.62	76%	9	0.74	71%
10	0.65	74%	10	0.65	74%	10	0.84	67%
11	0.67	74%	11	0.53	79%	11	0.52	80%
12	0.68	73%	12	0.59	77%	12	0.69	73%
13	1.00	61%	13	0.39	85%	13	0.71	72%
14	0.58	77%	14	0.49	81%	14	0.82	68%
15	0.57	78%	15	0.57	78%	15	0.47	81%
16	0.64	75%	16	0.71	72%	16	0.54	79%
17	0.63	75%	17	0.59	77%	17	0.60	76%
18	0.59	77%	18	0.57	78%	18	0.63	75%
19	0.75	70%	19	0.48	81%	19	0.59	77%

20	0.63	75%	20	0.56	78%	20	0.63	75%
21	0.53	79%	21	0.74	71%	21	0.68	73%
22	0.41	84%	22	0.52	80%	22	0.75	70%
23	0.54	79%	23	0.67	74%	23	0.52	80%
24	0.50	80%	24	0.74	71%	24	0.69	73%
25	0.66	74%	25	0.72	72%	25	0.56	78%
26	0.66	74%	26	0.67	74%	26	0.70	72%
27	0.60	76%	27	0.43	83%	27	0.46	82%
28	0.61	76%	28	0.69	73%	28	0.62	76%
29	0.61	76%	29	0.60	76%	29	0.38	85%
30	0.58	77%	30	0.62	76%	30	0.69	73%
31	0.54	79%	31	0.66	74%	31	0.67	74%
32	0.53	79%	32	0.75	70%	32	0.56	78%
33	0.50	80%	33	0.64	75%	33	0.39	84%
34	0.53	79%	34	0.66	74%	34	0.61	76%
35	0.59	77%	35	0.65	75%	35	0.36	86%
36	0.47	81%	36	0.37	85%	36	0.58	77%
37	0.69	73%	37	0.43	83%	37	0.55	78%
38	0.50	80%	38	0.51	80%	38	0.53	79%
39	0.50	80%	39	0.72	72%	39	0.67	74%
40	0.53	79%	40	0.70	72%	40	0.54	79%
41	0.59	77%	41	0.82	68%	41	0.59	77%
42	0.48	81%	42	0.64	75%	42	0.41	84%
43	0.58	77%	43	0.53	79%	43	0.65	74%
44	0.47	82%	44	0.58	77%	44	0.31	88%
45	0.47	82%	45	0.64	75%	45	0.46	82%
46	0.68	73%	46	0.65	75%	46	0.51	80%
47	0.64	75%	47	0.64	75%	47	0.55	78%
48	0.48	81%	48	0.67	74%	48	0.64	75%

49	0.64	75%	49	0.58	77%	49	0.61	76%
50	0.90	65%	50	0.59	77%	50	0.52	80%
51	0.60	76%	51	0.50	80%	51	0.70	72%
52	0.66	74%	52	0.58	77%	52	0.77	70%
53	0.71	72%	53	0.54	79%	53	0.62	76%
54	0.66	74%	54	0.56	78%	54	0.47	81%
55	0.58	77%	55	0.54	79%	55	0.70	72%
56	0.52	80%	56	0.56	78%	56	0.78	69%
57	0.67	73%	57	0.81	68%	57	0.57	77%
58	0.62	75%	58	0.62	76%	58	0.41	84%
59	0.71	72%	59	0.71	72%	59	0.59	77%
60	0.63	75%	60	0.64	75%	60	0.68	73%
61	0.51	80%	61	0.73	71%	61	0.64	75%
62	0.73	71%	62	0.69	73%	62	0.62	76%
63	0.61	76%	63	0.67	74%	63	0.64	75%
64	0.63	75%	64	0.56	78%	64	0.57	78%
65	0.63	75%	65	0.60	76%	65	0.73	71%
66	0.59	77%	66	0.64	75%	66	0.69	73%
67	0.55	78%	67	0.48	81%	67	0.78	69%
68	0.59	77%	68	0.53	79%	68	0.69	73%
69	0.53	79%	69	0.62	76%	69	0.54	79%
70	0.48	81%	70	0.57	77%	70	0.68	73%
71	0.66	74%	71	0.53	79%	71	0.67	73%
72	0.54	79%	72	0.77	70%	72	0.67	74%
73	0.73	71%	73	0.56	78%	73	0.60	76%
74	0.58	77%	74	0.47	81%	74	0.62	76%
75	0.70	73%	75	0.74	71%	75	0.61	76%
76	0.49	81%	76	0.67	74%	76	0.65	75%
77	0.64	75%	77	0.74	71%	77	0.55	78%

78	0.49	81%	78	0.53	79%	78	0.76	70%
79	0.71	72%	79	0.58	77%	79	0.54	79%
80	0.71	72%	80	0.65	74%	80	0.60	76%
81	0.58	77%	81	0.52	80%	81	0.63	75%
82	0.66	74%	82	0.40	84%	82	0.61	76%
83	0.63	75%	83	0.44	83%	83	0.58	77%
84	0.54	79%	84	0.63	75%	84	0.65	75%
85	0.79	69%	85	0.38	85%	85	0.66	74%
86	0.64	75%	86	0.73	71%	86	0.53	79%
87	0.65	75%	87	0.75	70%	87	0.66	74%
88	0.62	76%	88	0.63	75%	88	0.59	77%
89	0.49	81%	89	0.67	73%	89	0.67	74%
90	0.59	77%	90	0.44	83%	90	0.63	75%
91	0.64	75%	91	0.54	79%	91	0.46	82%
92	0.55	78%	92	0.48	81%	92	0.66	74%
93	0.45	82%	93	0.57	77%	93	0.70	72%
94	0.52	80%	94	0.57	78%	94	0.56	78%
95	0.55	78%	95	0.78	69%	95	0.61	76%
96	0.65	74%	96	0.75	70%	96	0.70	72%
97	0.54	79%	97	0.66	74%	97	0.52	80%
98	0.70	72%	98	0.70	72%	98	0.52	80%
99	0.50	80%	99	0.57	78%	99	0.56	78%
100	0.61	76%	100	0.64	75%	100	0.60	76%

Appendix J: Isopachs

Thicknesses of the lower, middle, and upper Y4-G, and Y5-Base in cm, where *t* means trace deposit found and *a* means absent. The location coordinates are in WSG84 UTM.

Lower Y4-G	Middle Y4-G	Upper Y4-G	Y5-Base	UTM	East	North
a	a	a	a	60S	414554	5697305
a	a	a	a	60S	412353.2	5694018
a	a	a	a	60S	407939	5692179
a	a	a	80	60S	422804.2	5715369
a	a	a	5	60S	432428	5714449
a	a	a	5	60S	447997.6	5707219
t	5	a	40	60S	432845.6	5702797
t	5	a	30	60S	431162.4	5702728
t	5	a	30	60S	430625.1	5702498
t	t	a	5	60S	429863.9	5702079
a	a	a	20	60S	437176	5702578
5	5	4	20	60S	437998	5706484
5	a	a	a	60S	435386	5705323
5	5	11	30	60S	438388.9	5713268
5	a	t	15	60S	437396.8	5714045
a	a	a	20	60S	433897.7	5714422
a	a	a	t	60S	423996.4	5725835
a	a	a	a	60S	417455.5	5726931
a	a	a	a	60S	412030.1	5720669
a	a	a	60	60S	429039.4	5719158
5	10	6	40	60S	429992.6	5703849
t	10	a	20	60S	427670.2	5704253
10	t	11	75	60S	427255.6	5704225
5	5	11	40	60S	427643.9	5704256
t	t	6	30	60S	425555.6	5702188
3	15	7	30	60S	430455	5710938
30	45	15	40	60S	419917	5704781
10	25	20	50	60S	428674	5706559
20	30	40	50	60S	426988	5707485
40	50	20	50	60S	421445	5705812
a	a	a	50	60S	414727	5715310

Appendix K: MP ML

Maximum pumice (MP) and maximum lithic (ML) measurements (mm) from the 5 largest pumice and lithics in the Exposure D samples with their averaged measurements in mm.

Sample	5 MP (mm)	Av MP (mm)	5 ML (mm)	Av ML (mm)
D-15	41	47	27	30.8
	48		27	
	46		34	
	58		35	
	42		31	
D-14	50	50	19	18
	62		20	
	48		14	
	47		14	
	43		23	
D-13	69	51.2	18	18.4
	58		17	
	41		18	
	48		18	
	40		21	
D-12	52	47.2	13	13.8
	54		16	
	40		17	
	42		10	
	48		13	
D-11	64	59.2	59	28.2
	63		35	
	61		16	
	56		16	
	52		15	
D-10	64	50.8	15	20.8
	54		21	
	47		19	
	44		13	
	45		36	
D-9	47	38.8	16	15.2
	40		16	
	35		12	
	37		10	
	35		22	
D-8	61	52.6	27	22.8
	45		19	

	61		16	
	52		28	
	44		24	
D-7	52	41.6	24	22.2
	47		19	
	34		19	
	37		22	
	38		27	
D-6	68	43.2	18	16.4
	40		16	
	41		17	
	37		15	
	30		16	
D-5	8	6.8	10	7.8
	6		11	
	5		6	
	8		6	
	7		6	
D-4	23	25.2	14	11.4
	29		10	
	29		11	
	24		11	
	21		11	
D-3	14	9.2	11	7.8
	10		8	
	7		7	
	7		7	
	8		6	
D-2	4	3.4	6	3.2
	3		4	
	4		2	
	3		2	
	3		2	
D-1	8	3.4	3	1.6
	3		2	
	2		1	
	2		1	
	2		1	

Supplementary Material: Figure 4.13 repeated